On The Variability of Mineral Dust and the Intertropical Convergence Zone Over West Africa: A synthesis of observations, climate models and geochemical analysis

A Dissertation Presented

by

Owen Doherty

to

The Graduate School

in Partial Fulfillment of the

Requirements

for the Degree of

Doctor of Philosophy

in

Marine and Atmospheric Science

Stony Brook University

December 2012

Stony Brook University

The Graduate School

Owen Doherty

We, the dissertation committee for the above candidate for the
Doctor of Philosophy degree, hereby recommend
acceptance of this dissertation.

Nicole Riemer – Dissertation Co-Advisor
Assistant Professor, Department of Atmospheric Science, University of Illinois at Urbana-Campaign

J. Kirk Cochran – Dissertation Co-Advisor
Professor, School of Marine and Atmospheric Sciences, Stony Brook University

Sultan Hameed – Chairperson of Defense
Professor, School of Marine and Atmospheric Sciences, Stony Brook University

E. Troy Rasbury
Associate Professor, Department of Geosciences, Stony Brook University

William K.-M. Lau
Chief of Atmospheres, NASA Goddard Space Flight Center

This dissertation is accepted by the Graduate School

Charles Taber
Interim Dean of the Graduate School

Abstract of the Dissertation

On The Variability of Mineral Dust and the Intertropical Convergence Zone Over West Africa: A synthesis of observations, climate models and geochemical analysis

by

Owen Doherty

Doctor of Philosophy

in

Marine and Atmospheric Science

Stony Brook University

December 2012

Mineral dust in the atmosphere is of great importance through its impacts on climate, atmospheric chemistry and biogeochemical processes. The year-to-year and season-to-season variability of mineral dust transport are not well understood. This work focuses on investigating and explaining the inter-annual variability of mineral dust transport by an approach that combines data analysis from in-situ observations, global climate models, multiple reanalysis products and geochemical laboratory analysis. Linking a 38-year record of mineral dust concentration at Barbados to variations in position and intensity of the zone of near-surface convergence over West Africa, a part of the Intertropical Convergence Zone (ITCZ) a relationship between the latitude of the ITCZ over West Africa and mineral dust at Barbados is demonstrated during winter ($r = -0.69$) and summer ($r = -0.47$). This finding represents an improvement over previous studies, which related mineral dust transport to changes in the NAO and ENSO. Southward displacement of the ITCZ leads to favorable winds for dust emission near the surface in both seasons, and in summer also leads to reductions in precipitation over the Sahel, which in turn increases aridity. The newly developed climate index that quantifies the variability of the ITCZ is then used to assess the performance of a suite of 11 global climate models (from CMIP3) in both hindcasts of the 20th century and predictions of the 21st century. A northward trend in the position of the ITCZ is observed in the summer of the 20th century, and predicted in both summer and winter of the 21st century. Northward migration of the ITCZ in the 21st century is expected to reduce dust load by $-1.9\ \mu g\,m^{-3}$ to $-3.8\ \mu g\,m^{-3}$ in summer and by $-1.5\ \mu g\,m^{-3}$ to $-2.2\ \mu g\,m^{-3}$ in winter. To establish provenance of mineral dust the mineralogy and elemental composition of dust samples collected from four continents are analyzed and via principle component analysis it is demonstrated that continental sources can be separated.

Dedication Page

Churn, churn.

Forward and onward!

Contents

List of Figures

List of Tables

Acknowledgements

Thanks are extended to the dissertation committee responsible for this document including Sultan Hameed, Troy Rasbury and William K.-M. Lau. Special thanks to co-advisors Nicole Riemer and J. Kirk Cochran for their tireless support.

Appreciation is extended to the faculty of the School of Marine and Atmospheric Sciences for lessons learned in and out of the classroom. In particular thanks are due to the faculty of ITPA; Edmund Chang, Brian Colle, Daniel Knopf and Minghua Zhang. Many faculty in MSRC were instrumental in my education as well; Bob Aller, Bruce Brownawell, Jackie Collier, Chris Gobler, Kamazima Lwiza, Anne McElroy, Mary Scranton, Gordon Taylor, Joe Warren and Robert Wilson.

The author wishes to thank Ms. Carol Dovi, Ms. Gina Gartin, Ms. Eileen Goldsmith, Mr. John Graham, Ms. Kim Knoll, Mr. Cliff Jones, Ms. Stefanie Massucci, Mr. Steve Ortega and Ms. Bonnie Stephens for their help, support and assistance in navigating university bureaucracy.

The author is grateful to Dr. Wuyin Lin for his help accessing and interpreting climate model data. The author is indebted to Dr. Joe Olson, Dr. Matt West, Mr. Mark Lang and Mr. Mike Charles for their assistance and instruction on computational problems.

Dr. Sidney Hemming and Dr. Aaron Beck were instrumental in experimental design and analysis. The author is grateful for the assistance provided by Dr. Christina Heilbrun, Mr. David Hirschberg and Mr. William Wise with sample preparation and transportation. Mr. Aaron Frodsham, Ms. Rachel Guryn and Ms. Carol Lee helped greatly in the laboratory of Dr. Troy Rasbury.

The author is grateful to the following for their help in acquiring samples: Prof. Jordi Garcia-Orellana of Universitat Autnoma de Barcelona; Prof. Shuxian Fan, Nanjing University of Information Science & Technology; Prof. N. Gary Hemming, Queens University; Prof. Minghua Zhang, Stony Brook University; and Mr. Ken Faile, Australia.

Mr. Eric Edgerton of Atmospheric Research Inc. provided the filter samples analyzed in this study.

Portions of this work were performed at Beamline X26A, National Synchrotron Light Source (NSLS), Brookhaven National Laboratory. X26A is supported by the Department of Energy (DOE) - Geosciences (DE-FG02-92ER14244 to The University of Chicago - CARS). Use of the NSLS was supported by DOE under Contract No. DE-AC02-98CH10886.

We acknowledge and thank Prof. Joe Prospero and his staff for producing and sharing the record of mineral dust concentrations at Barbados.

We acknowledge the modeling groups, the Program for Climate Model Diagnosis and Intercomparison (PCMDI) and the WCRP's Working Group on Coupled Modelling (WGCM) for their roles in making available the WCRP CMIP3 multi-model dataset. Support of this dataset is provided by the Office of Science, U.S. Department of Energy.

UK Met Office / Hadley Center Climate Model data provided by the Met Office Hadley Centre.

NCEP Reanalysis and GPCP Precipitation data provided by the NOAA/OAR/ESRL PSD, Boulder, Colorado, USA, from their Web site at http://www.esrl.noaa.gov/psd.

ERA-40 and ERA Interim data provided by the European Center for Medium Range Forecasts, Shinfield Park, Reading, United Kingdom, from their website at http://data-portal.ecmwf.int/.

GIMMS NDVI produced by the Global Land Cover Facility (www.landcover.org) and the University of Maryland Department of Geography.

Chapter 1

Introduction

1.1 Background

1.1.1 Importance of Mineral Dust

Mineral dust, particles of Earth derived material suspended in the atmosphere, has been of interest to the scientific community since the 19th century. The record of mineral dust in modern scientific literature begins with Darwin's observations aboard the H.M.S. Beagle [*Darwin*, 1846]. Mineral dust transport did not receive attention again until the 1960's when Joseph Prospero began his seminal work on Saharan Mineral Dust in the Tropical North Atlantic Ocean [*Prospero and Carlson*, 1972]. Recently, as the importance of mineral dust to many natural systems (climate, chemical, geological and biological) has become clear, the number of papers published on mineral dust has grown exponentially as seen in Figure 1.1.

Implications for Climate

Recent IPCC reports have identified mineral dust aerosols as a major source of uncertainty in climate predictions [*Solomon et al.*, 2007]. Much of this uncertainty extends from mineral dust exerting both a direct radiative forcing on climate as it interacts with solar and longwave radiation [*Andreae*, 1996; *Sokolik and Toon*, 1996; *Tegen et al.*, 1996; *Miller et al.*, 2004] and an indirect forcing on climate as dust particles play an important role for various aspects of the microphysics of clouds [*Wurzler et al.*, 2000; *Rosenfeld et al.*, 2001; *Mahowald et al.*, 2003; *Levin et al.*, 2005], including mixed-phase clouds [*DeMott et al.*, 2003], thin ice clouds [*Sassen et al.*, 2003; *DeMott et al.*, 2003] and warm clouds [*Levin et al.*, 2005]. By affecting cloud microphysics, mineral dust may impact climate indirectly, as it alters the cloud lifetime and their reflectivity. In summary, depending on the conditions, these forcing mechanisms can impart a positive (warming) or a negative (cooling) forcing on the climate system as mineral dust both absorbs and reflects radiation, and by changing the properties and lifetime of clouds can either warm or cool the planet. The overall effect of mineral dust on the climate system varies with a number of factors, including the composition, size distribution and shape of the dust particles, composition of underlying surface, the quantity and the vertical profile of the mineral dust and the strength of solar insolation.

The largest source of mineral dust globally is the Sahara Desert [*Prospero et al.*, 2002; *Washington et al.*, 2003]. Mineral dust originating from this region, so called “Saharan mineral dust”, impacts the adjacent tropical climates. Saharan mineral dust has been linked with the frequency and intensity of Atlantic hurricanes [*Dunion and Velden*, 2004; *Evan et al.*, 2006; *Lau and Kim*, 2007b,a; *Braun*, 2010]. Radiative forcing from mineral dust has been shown to shift the location and strength of the tropical rainband over the Atlantic Ocean [*Huang et al.*, 2009] and may impact the ITCZ-monsoon circulation over Africa [*Lau et al.*, 2009a; *Kim et al.*, 2010; *Wilcox et al.*, 2010]. Changes in the conditions of the tropics have been shown to impact the mid-latitudes of the globe, thus a forcing from the presence of mineral dust in the tropics may have global impacts. As mineral dust abundance impacts regional climate, and regional climate in turn impact the abundance of mineral dust, there is potential for a dust feedback loop [*Rosenfeld et al.*, 2001].

Implications for Atmospheric Chemistry

Mineral dust particles in the atmosphere have a large impact on atmospheric chemistry. Dust particles provide a large surface area on which heterogeneous chemical reactions may occur [*Dentener et al.*, 1996; *Grassian*, 2002; *Bian and Zender*, 2003; *Krueger et al.*, 2004]. Heterogeneous reactions involving sulfur dioxide on mineral dust may result in an important sink for atmospheric sulfur. Sulfur dioxide and sulfides often become deposited on the surface of mineral dust particles, increasing the hygroscopicity of the dust particles and reducing the sulfur load of the atmosphere [*Bauer et al.*, 2004; *Bian and Zender*, 2003]. This reduction in atmospheric sulfur, and thus atmospheric scattering, acts as a positive radiative forcing [*Bauer et al.*, 2004]. Atmospheric chemistry also impacts mineral dust, by coating mineral dust particles in turn reducing the ability of mineral dust to act as an ice nucleus. Photolysis rates, important in many chemical reactions in the atmosphere are affected by the presence of mineral dust [*Dickerson et al.*, 1997].

Biogeochemistry

As discussed, mineral dust has large impacts on the atmosphere while it is airborne. Once deposited, mineral dust has similarly large impacts on biological, chemical and geological systems. Mineral dust is rich in silicon, calcium, iron and aluminum [*Prospero and Savoie*, 1989; *Jickells*, 1999] as well as other trace nutrients, which may be important in many regions of the global ocean that are considered to be nutrient-limited [*Fung et al.*, 2000; *Meskhidze et al.*, 2003, 2005]. These regions feature a physical environment that is conducive to planktonic growth but lack essential macro or micro nutrients [*Jickells*, 1999]. Iron has been shown to be a common limiting micronutrient that is prevalent in mineral dust, and in turn mineral dust deposition onto the global ocean has been shown to be an important source of iron to the surface ocean [*Jickells*, 1999]. As a result, understanding the atmospheric distribution of mineral dust is important to understanding primary production in the ocean. Encountering suitable circumstances the deposition of mineral dust can lead to algal blooms

[*Walsh and Steidinger*, 2001]. The long-range transport of mineral dust from the Sahara across the Atlantic is significant enough to be responsible for the formation of the soils of many Caribbean islands and the Amazon Basin [*Borg and Banner*, 1996; *Herwitz et al.*, 1996; *Muhs et al.*, 2007; *Muhs et al.*, 2012]. Saharan mineral dust is an important supplier of both phosphate and potasium for the Amazon Basin [*Swap et al.*, 1992; *Koren et al.*, 2006].

1.1.2 Global Sources and Transport Routes of Mineral Dust

This study focuses on mineral dust reaching the North American continent. Mineral dust reaches North America primarily from two major sources, multiple deserts in Asia and the Sahara Desert in North Africa.

Arid and semi-arid regions represent potential sources for mineral dust. The majority of mineral dust emitted into the atmosphere originates from the arid Sahara Desert and the surrounding semi-arid Sahel [*Prospero et al.*, 2002; *Washington et al.*, 2003], with the highest concentrations of mineral dust occurring in the summer season of June through September. Mineral dust from Asian deserts is the second largest source of mineral dust with emissions maximized in spring [*Massie et al.*, 2004]. Arid regions in North America, South America, South Africa and Australia represent lesser sources of mineral dust to the atmosphere.

Saharan mineral dust in summer is transported long distances, often traveling at least 5,000 km and persisting in the atmosphere for periods in excess of a week [*Prospero et al.*, 1970] before reaching the Americas. Saharan mineral dust is able to persist in the atmosphere for long periods of time due to the formation of Saharan Air Layer. The Saharan air layer forms as hot, dry air from the Sahara moves over the comparatively cool, damp air of the Tropical North Atlantic [*Carlson and Prospero*, 1972]. The elevated Saharan airmass has very high static stability, resulting in little or no vertical mixing and reduced probabilities of precipitation [*Carlson*, 1979]. As such, mineral dust aerosols in this layer tend to be longer lived than aerosols emitted from other deserts, allowing for increased transport downwind. The occurrence of Saharan air layers is found dominantly in the summer months, occurring less frequently in the spring and fall, and infrequently in the winter [*Chiapello and Moulin*, 2002; *Karyampudi and Pierce*, 2002]. This layer can extend to about 5000 m vertically, resulting in elevated transport [*Petit et al.*, 2005].

While summer is the peak season for mineral dust transport from the Sahara, dust emissions form the deserts in central Asia are maximized in spring when meteorological conditions are dry and windy [*Sun et al.*, 2001]. Strong westerlies during spring across the Pacific allow for inter-continental transport of dust [*Merrill et al.*, 1989]. However, as generally less dust is emitted in the Gobi, Taklamakan and other Asian sources the distance between the Asian deserts to North America is greater, and the atmospheric stability over the Pacific is lower than in the Saharan case, thus smaller quantities of dust are expected to reach other continents.

1.2 Mineral Dust Variability

Using both sediment and ice cores, reconstructions of mineral dust over geologic time indicates variability on the order of 2 to 4 fold increases [*McGee et al.*, 2010] from interglacial to glacial periods. Some of this variability could be tied to additional sources of mineral dust emerging during glacial periods over such regions as North America, Europe and Siberia [*Mahowald et al.*, 2006]. Recently *McGee et al.* [2010] show that wind gustiness controls the quantity of mineral dust emitted to the atmosphere over geologic time. Changes in precipitation between glacial and interglacial periods over semi-arid and arid regions like the Sahara have also been shown to be important in controlling mineral dust emission over geologic time [*Stuut et al.*, 2002].

More recently, during the instrumental record mineral dust has been estimated or measured via satellite and by surface based stations, respectively. For example, much attention has been paid to a long-term record of mineral dust at Barbados where dust concentrations have been measured from 1965 through present [*Rydell and Prospero*, 1972; *Prospero and*

Nees, 1977; *Glaccum and Prospero*, 1980; *Prospero and Carlson*, 1980; *Prospero and Nees*, 1986; *Savoie et al.*, 1987; *Moulin et al.*, 1997; *Chiapello et al.*, 1999; *Prospero and Lamb*, 2003; *Ginoux et al.*, 2004; *Chiapello et al.*, 2005; *Prospero et al.*, 2008; *Trapp et al.*, 2010]. Long-range transport of mineral dust, such as that to Barbados, is subject to considerable inter-annual and intra-annual variability due to a number of physical factors. Winds over the Sahara and Sahel control emissions of mineral dust [*Washington et al.*, 2003; *Washington and Todd*, 2005], and winds downstream of the emission region affect subsequent transport [*Chiapello et al.*, 1995; *Riemer et al.*, 2006; *Doherty et al.*, 2008]. Precipitation and vegetation in the Sahel have been suggested as key factors in the dust emission process [*Evan et al.*, 2006a]. Precipitation over the source region can modulate dust emission, and precipitation over the transport region can remove dust from the atmosphere [*Tegen and Fung*, 1994; *Zender et al.*, 2003]. While this system has been studied in detail in the past 50 years, two key factors, wind and precipitation, have emerged as being critical in both geologic and contemporary time.

Understanding the year-to-year variability of this dust load is critical as mineral dust originating from the Sahara is the dominant aerosol type over much of West Africa and the Tropical North Atlantic [*Formenti et al.*, 2008] and in turn has complex impacts on the climate and biogeochemistry of the region. The focus of this dissertation is in explaining the year-to-year variability of mineral dust reaching North America over the recent past and near future, focusing on the Caribbean and Southeastern United States.

While the long-term average quantity of mineral dust emitted in Africa and transported over the Tropical North Atlantic Ocean is at its peak in summer, this quantity varies greatly from year to year. Much effort has gone into improving our understanding of the processes that are responsible for this variability. Observations of Saharan mineral dust over the Atlantic Ocean and at Barbados have been related to variability in the North Atlantic Oscillation (NAO) [*Moulin et al.*, 1997], particularly in the winter season [*Chiapello and Moulin*, 2002]. Similar relationships have been diagnosed from global chemistry and transport model results [*Ginoux et al.*, 2004]. *Prospero and Lamb* [2003] related mineral dust in Barbados and an El Niño-Southern Oscillation (ENSO) index. Dust transport to the Americas has been liked to the position of the Azores High in winter [*Riemer et al.*, 2006] and in summer to the position of the Azores High and Hawaiian High [*Doherty et al.*, 2008]. *Schwanghart and Schütt* [2008] found no connection between regional weather systems and dust emission in summer, instead suggesting that dust emission in West Africa is connected to regional convection.

In this work we show that the mechanisms causing variability of mineral dust concentration at Barbados depend on the season and are linked to the migration of the ITCZ over West Africa. During winter the variability can be attributed to changes in emissions [*Doherty et al.*, 2012a]. In contrast, during summer the variability can be explained by increased aridity driven by reductions in precipitation in the Sahel, leading to increased emissions. In both seasons it is the southward migration of the ITCZ that leads to increased dustload at Barbados through changes in near surface wind and precipitation, respectively. To obtain these results it was necessary to develop a framework to quantify the movements of the ITCZ over West Africa.

1.3 Intertropical Convergence Zone Over West Africa

In this work we present a new perspective on mineral dust transport in the region by focusing on the role of the Intertropical Convergence Zone (ITCZ) over Africa rather than on global teleconections indices as has previously been done. The ITCZ is a global belt of inclement weather that generally occurs where the trade winds converge and form the ascending branch of the Hadley Circulation. Annually the ITCZ moves north and south following the progression of annual solar maximum [*Folland et al.*, 1991]. Over the ocean the ITCZ circulation is relatively simple whereas over land the structure of the ITCZ becomes more complicated. When the ITCZ occurs over land it can be referred to as a monsoon. For example over Africa parts of the ITCZ are referred to as the West Africa Monsoon (WAM). Much ambiguity exists in terminology regarding the ITCZ [*Nicholson*, 2009], owing to the increased complexity of the system over land. Over West Africa the annual northward migration of the ITCZ-WAM brings critical seasonal rainfall to areas of the Sahel and southern Sahara [*Nicholson*, 2009]. As such the location and strength of the ITCZ has implications for seasonal soil and vegetative conditions, and likely dust emission and transport.

It has been previously noted that a relationship between the ITCZ and mineral dust likely exists. The tradewind circulation associated with the ITCZ blows through the area downwind of the Sahara and Sahel where mineral dust loads are the highest [*Prospero and Carlson*, 1972; *Moulin et al.*, 1997]. *Prospero and Carlson* [1972] first showed in a field experiment that the dust belt was located directly to the north of the ITCZ. *Moulin et al.* [1997] and later *Evan et al.* [2006b] showed using satellite observations of mineral dust that the dust belt moves north blowing dust into the Caribbean ahead of the ITCZ in summer, and returns south blowing dust into South America in winter. Precipitation in the tropical North Atlantic basin and surrounding locations have been shown to be dependent on the location of the ITCZ [*Kapala et al.*, 1998] and multiple studies have linked mineral dust in Barbados with precipitation in the Sahel region of Africa [*Prospero and Nees*, 1986; *Chiapello et al.*, 2005]. Although work has been done linking the movement of the ITCZ to changes in dust load locally in Africa [*Engelstaedter and Washington*, 2007; *Schwanghart and Schütt*, 2008; *Sunnu et al.*, 2008; *Lau et al.*, 2009b; *Wilcox et al.*, 2010], this is the first study that addresses how the movement of the ITCZ has implications for the amount of dust that extends over the Atlantic and reaches the Americas. Specifically we examine how changes in the ITCZ effect wind and precipitation patterns over both the North Africa and the Tropical North Atlantic and in turn control the amount of mineral dust that reaches Barbados.

1.4 Statement of Problem

This work addresses the question of what controls the annual transport of mineral dust. Here we hypothesize that the position of the ITCZ over West African controls the quantity of mineral dust reaching the Caribbean and North America. To test this hypothesis we ask and answer four major questions. (1) How does the movement of the ITCZ over West Africa impact mineral dust emission and transport in winter and summer? (2) How do global climate models recreate the ITCZ over West Africa over the 20th century? (3) Do global climate models predict major changes to the ITCZ over West Africa in the 21st century and how would this impact mineral dust emission and transport? (4) Can we use geochemical tracers of mineral dust source on transported mineral dust samples to confirm our ITCZ over West Africa hypothesis? To answer these questions we utilize multiple data-sources including in situ observations, climate reanalysis products, satellite observations and a novel geochemical analysis of mineral dust samples taken from five continents.

1.5 Approach

1.5.1 Quantification of the ITCZ and the Center of Action Approach

Before quantitative analysis involving the position of the ITCZ can be made, first we must develop an index to track the movement of the ITCZ. To accomplish this we utilize the "Center of Action" approach. Centers of Action (COA) refer to seasonal large-scale systems with occur annually in nearly the same geographic regions [*Rossby*, 1939; *Angell and Korshover*, 1974, 1982; *Hurrell*, 1995; *Kapala et al.*, 1998; *Mächel et al.*, 1998]. In the mid-latitudes examples of such systems include the Azores High and the Icelandic Low. Over West Africa, the ITCZ can be thought of as a "center of action" as annually it appears in nearly the same position, moving with solar heating over the course of the year. The Center of Action approach identifies where the center of mass of the semi-permanent action center is position, yielding a latitude and longitude position. Similarly, an intensity of the center is calculated. We can then relate the positions of the Center of Action to geophysical quantities [*Christoforou and Hameed*, 1997; *Croke et al.*, 1999; *Piontkovski and Hameed*, 2002; *Hameed and Piontkovski*, 2004; *Riemer et al.*, 2006; *Kolker and Hameed*, 2007; *Bakalian et al.*, 2007; *Doherty et al.*, 2008; *Jordi and Hameed*, 2009; *Doherty et al.*, 2012a; *Taylor et al.*, 2012], in this case mineral dust, to establish relationships.

1.5.2 Application: Relating the ITCZ to mineral dust and atmospheric variables

Using the COA approach and reanalysis data, latitude, longitude and intensity of the ITCZ over West Africa can be calculated from 1948 to the present. We compare values of latitude, longitude and intensity of the ITCZ over West Africa to surface based measurements of mineral dust at Barbados [*Prospero and Carlson*, 1972] and satellite measurements of mineral dust to note how changes in the position of the ITCZ over West Africa changes mineral dust loads. It is desirable and necessary to physically explain observed relationships between the ITCZ over West Africa and mineral dust. To do this we examine winds over West Africa and Tropical Atlantic in reanalysis products, as well as precipitation estimates, vegetation and drought indices to assess changes in aridity.

1.5.3 Application: GCM hindcast of ITCZ in 20th century

Global climate models (GCM) are now ubiquitous in atmospheric science. In order to use GCM models to make future predictions, first the models must show they have skill to recreate past climate. Here we compare GCM output from the Climate Model Intercomparison Project 3 (CMIP3) to multiple reanalysis datasets to quantify the errors from GCM using the newly defined ITCZ index as a metric. Differences from reanalysis are calculated for spatial fields and temporal trends of the ITCZ over West Africa.

1.5.4 Application: GCM predictions of ITCZ in 21st century

Next the climate models are evaluated in the 21st century. Deviations from the 20th century are noted, and trends in the 21st century are calculated. Changes in the positions of the ITCZ over West Africa in the 21st century are used to estimate changes in mineral dust emission and transport.

1.5.5 Geochemical Analysis

Changes in precipitation and wind patterns driven by the ITCZ over West Africa lead to key mineral dust hot-spots over West Africa becoming more or less active. Each such hot-spot has a unique geochemical fingerprint, a combination of mineralogy, elemental composition and isotopic ratios. Here we attempt to use these fingerprints on both samples acquired close to mineral dust source regions and filter samples of unknown sources to differential source regions. To accomplish this samples representative of source regions are acquired from four continents, and sensitive analysis techniques are developed to be applied trace quantities of dust.

Source regions important to mineral dust emissions have unique geological histories, for example the Bodele Depression is a dried lakebed. In turn this geological history dictates the mineral composition of the surface soils which once eroded are lifted and transported by the atmosphere. The extent of prevalence of which a mineral or a group of minerals appear in a given location can be used as a proxy [*Formenti et al.*, 2011]. Elemental ratios also vary from location to location, for example the Ca to Al ratio has been used to apportion aerosol provenance in the Southeastern United States [*Perry et al.*, 1997]. Lastly the isotopic ratios of Pb, Nd, Sr can be used to determine the source of mineral dust and other crustal materials [*Grousset and Biscaye*, 2005].

1.5.6 Application: Apportionment of Unknown Samples in the Southeastern United States

As we seek to use such fingerprints to detect changes in source regions, we must fully characterize source regions. To this end samples have been acquired and analyzed from four continents; Europe, Asia, Australia and Africa. Additionally to test our hypothesis samples of unknown provenance were acquired from Pensacola, FL and are analyzed for two purposes; first to demonstrate if we can clearly separate continental sources and secondly for samples with African sources if changes in the position of the ITCZ over West Africa drives is reflected in the mineralogy, elemental composition or isotopic ratios of the samples. Geochemical analysis produces a large quantity of data, signals in which may not be clearly evident. For example, the elemental composition of mineral dust in this analysis are calculated for 26 elements. To parse signals out of large datasets we apply principle component analysis. Using a simple framework identified from the mineralogy, we construct a framework by which continental source apportionment can easily be made.

1.6 Unique Contributions of the Work

This dissertation consists of two complimentary components advancing our understanding of the controls of mineral dust transport by combining atmospheric sciences and geochemistry. (1) A synergistic data analysis component: Central to this is the development of a new climate index quantifying the movement and intensity of the ITCZ. This new climate index is then applied in three novel ways: to explain dust transport mechanisms where the new framework proves to be superior in comparison to the ones previously used; to assess skill of GCM in the 20th century; and to predict future trends in the ITCZ in the 21st century. (2) A lab component developing geochemical techniques, which allow for the differentiation of mineral dust sources. Geochemical tracers are then applied to unknown samples taken from the Southeastern United States. In sum, this work produces a new conceptual model for explaining year-to-year variability of mineral dust concentration and a novel multidisciplinary approach to apportioning mineral dust sources.

1.7 Dissertation Outline

The structure of the dissertation is as follows. The role of the ITCZ over West Africa in controlling mineral dust transport in winter is explored in Chapter 1. These results are presented as published in *Doherty et al.* [2012a]. Chapter 2 presents the results of a similar experiment, here we asses the role of the ITCZ over West African in controlling mineral dust transport in summer. These results are presented as a manuscript in preparation for submission [*Doherty et al.*, 2012b]. The ability of global climate models to accurately capture the position of the ITCZ over West Africa is assessed and presented in Chapter 3. Model trends and projections for the ITCZ over West Africa and the implications for mineral dust transport in the coming century are presented in Chapter 4. The geochemical analysis and framework for continental apportionment are presented in Chapter 5. Chapter 5 is presented here as a dissertation chapter but is anticipated to be published with co-authors A. Beck, J.K. Cochran and E.T. Rasbury. The dissertation is concluded in Chapter 6 by summarizing the results, discussing the results in context of previous work, the implications of this study and possible continuation of this work in future studies.

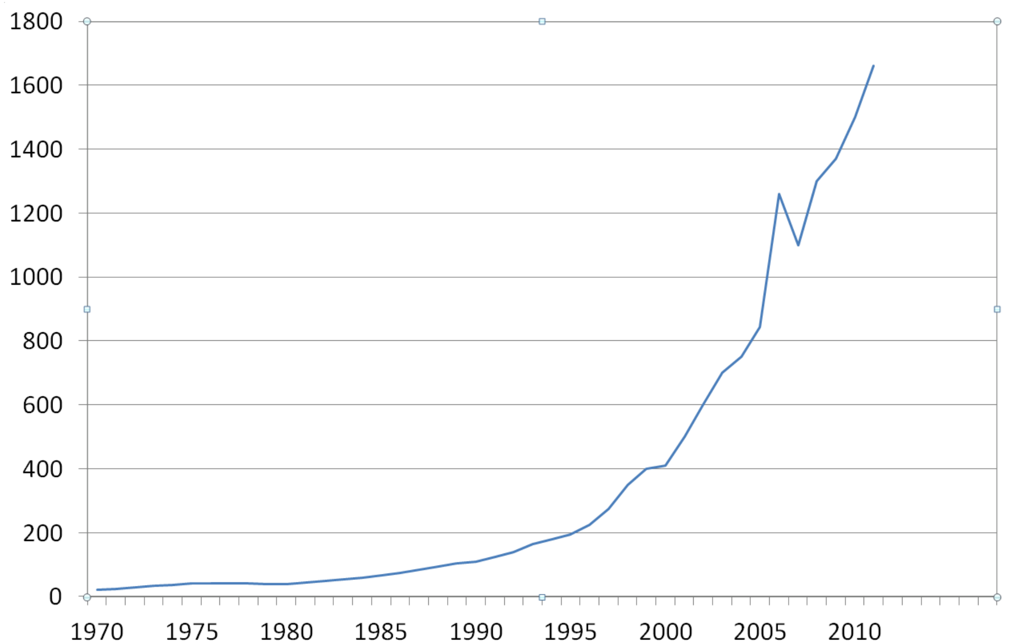

Figure 1.1: Number of publications related to keyword search "Saharan Mineral Dust" in Google Scholar by year, 1965 to present. After *Kaufman et al.* [2005].

Chapter 2

Control of Saharan Mineral Dust Transport to Barbados in Winter by the Intertropical Convergence Zone over West Africa

2.1 Introduction

The largest source of mineral dust globally is the Saharan desert [*Prospero et al.*, 2002; *Washington et al.*, 2003]. Dust from this region is transported long distances over the North Atlantic Ocean [*Darwin*, 1846; *Prospero et al.*, 1970] and plays an important role in the climate system [*Arimoto*, 2001]. It exerts a direct radiative forcing on climate as it interacts with solar and longwave radiation [*Sokolik and Toon*, 1996; *Tegen et al.*, 1996]. Moreover, dust particles play an important role for various aspects of the microphysics of both mixed-phase clouds [*DeMott et al.*, 2003] and warm clouds [*Levin et al.*, 2005] and hence are an important contributor to the aerosol indirect effect. Saharan dust has been linked with the frequency and intensity of Atlantic hurricanes [*Dunion and Velden*, 2004; *Evan et al.*, 2006; *Lau and Kim*, 2007b,a] and has been found to fertilize ocean waters with iron and other micronutrients [*Jickells*, 1999; *Baker et al.*, 2006], to promote algal blooms [*Walsh and Steidinger*, 2001], and to provide phosphate and potassium to the Amazon Basin [*Swap et al.*, 1992]. The long-range transport of mineral dust from the Sahara across the Atlantic is significant enough to be responsible for the formation of the soils of many Caribbean islands and the Amazon Basin [*Herwitz et al.*, 1996; *Muhs et al.*, 2007].

This long-range transport of mineral dust is subject to considerable inter-annual and intra-annual variability due to a number of physical factors. Winds over the Sahara and Sahel control emissions of mineral dust [*Washington et al.*, 2003; *Washington and Todd*, 2005], and winds downstream of the emission region affect subsequent transport [*Chiapello et al.*, 1995; *Riemer et al.*, 2006; *Doherty et al.*, 2008]. Precipitation and vegetation in the Sahel has been suggested as a key factor in dust emission processes [*Evan et al.*, 2006a]. Precipitation over the source region can modulate dust emission, and precipitation over the transport region can remove dust from the atmosphere [*Tegen and Fung*, 1994; *Zender et al.*, 2003].

The variability of mineral dust transport from Africa across the Atlantic is documented in the long-term mineral dust record measured at Barbados. Dust concentrations have been measured and published at this locations from 1965 through 2003 and have been studied extensively by the community [*Rydell and Prospero*, 1972; *Prospero and Nees*, 1977; *Glaccum and Prospero*, 1980; *Prospero and Carlson*, 1980; *Prospero and Nees*, 1986; *Savoie et al.*, 1987; *Moulin et al.*, 1997; *Chiapello et al.*, 1999; *Prospero and Lamb*, 2003; *Ginoux et al.*, 2004; *Chiapello et al.*, 2005; *Prospero et al.*, 2008; *Trapp et al.*, 2010]. Several studies focused on explaining this variability by linking the observed dust load with climate indices. For example, a qualitative link relating mineral dust in Barbados and an El Niño-Southern Oscillation (ENSO) index has been suggested by *Prospero and Lamb* [2003]. *Moulin et al.* [1997] demonstrated a statistical relationship between mean annual dust load at Barbados and the mean value of the North Atlantic Oscillation (NAO) index, while *Chiapello and*

Moulin [2002] linked variability in satellite observations of dust over the tropical North Atlantic Ocean off the coast of Africa to variability of the NAO during winter. *Ginoux et al.* [2004] showed a weak statistical relationship between the winter NAO index and the observed surface dust at Barbados as well as in simulated mineral dust concentration in the region. *Doherty et al.* [2008] demonstrated an improvement upon the relationship of NAO and mineral dust by showing an even stronger relationship between the location of the Azores High in the Atlantic and the Hawaiian High in the Pacific and dust in the Caribbean.

In this work we present a new perspective on mineral dust transport in the region by focusing on the role of the Intertropical Convergence Zone (ITCZ) over Africa rather than on global teleconections indices as has previously been done. Here we consider the ITCZ to represent the zone of near-surface convergence over continental West Africa that is sometimes referred to as the West African monsoon trough [*Sultan et al.*, 2003]. Year-to-year and decade-to-decade variability of the ITCZ has been observed over Africa and the Atlantic [*Mächel et al.*, 1998; *Kapala et al.*, 1998], with differences in the intensity and location noted. Some variability of the ITCZ can likely be ascribed to changes in sea surface temperature [*Folland et al.*, 1986; *Hoerling et al.*, 2006] as precipitation in the Sahel has been linked to sea surface temperature changes [*Folland et al.*, 1986; *Giannini et al.*, 2003]. *Tomas et al.* [1999] present theoretical evidence for the location of the ITCZ also being a function of the cross-equatorial pressure gradient.

It has been previously noted that a relationship between the ITCZ and mineral dust likely exists. The tradewind circulation associated with the ITCZ blows through the area downwind of the Sahara and Sahel where mineral dust loads are the highest [*Prospero and Carlson*, 1972; *Moulin et al.*, 1997]. *Prospero and Carlson* [1972] first showed in a field experiment that the dust belt was located directly to the north of the ITCZ. *Moulin et al.* [1997] and later *Evan et al.* [2006b] showed using satellite observations of mineral dust that the dust belt moves north blowing dust into the Caribbean ahead of the ITCZ in summer, and returns south blowing dust into South America in winter. Precipitation in the tropical

North Atlantic basin and surrounding locations have been shown to be dependent on the location of the ITCZ [*Kapala et al.*, 1998] and multiple studies have linked mineral dust in Barbados with precipitation in the Sahel region of Africa [*Prospero and Nees*, 1986; *Chiapello et al.*, 2005].

Although work has been done linking the movement of the ITCZ to changes in dust load locally in Africa [*Engelstaedter and Washington*, 2007; *Schwanghart and Schütt*, 2008; *Sunnu et al.*, 2008; *Lau et al.*, 2009b; *Wilcox et al.*, 2010], this is the first study that addresses how the movement of the ITCZ has implications for the amount of dust that extends over the Atlantic and reaches the Americas. Specifically we examine how changes in the ITCZ effect wind and precipitation patterns over both the North Africa and the Tropical North Atlantic and in turn control the amount of mineral dust that reaches Barbados. We focus in this paper on the winter season to compare to more well known teleconnections such as the NAO and ENSO. Although less dust reaches Barbados in winter than does in summer [*Kaufman et al.*, 2005], dust continues to reach Barbados in winter in appreciable quantities as Barbados lies on the northern edge of this dust plume. The dustier summer season will be the focus of a forthcoming paper.

The structure of this paper is as follows. In Section 2.2 we describe how we quantify the variability of the ITCZ. We will introduce the various data sets used in this study in Section 2.3. In Section 2.4 we will then explore the long-term relationship between mineral dust in Barbados and the ITCZ , and we will compare the physical mechanisms by which the ITCZ impact the mineral dust concentrations in Barbados. Section 2.5 concludes our findings.

2.2 The ITCZ over West Africa as a Center of Action

Year-to-year and decade-to-decade [*Mächel et al.*, 1998; *Kapala et al.*, 1998] variability of the ITCZ has been observed, with differences in the intensity and location noted. To compare to the record of mineral dust at Barbados, a time series of the position and intensity of the

ITCZ is necessary. Here we develop such a time series by utilizing the "Center of Action" (COA) approach. This provides us with three indices, one for the latitudinal position, one for the longitudinal position, and one for the intensity of the system.

The concept of an atmospheric "Centers of Action" (COA) was first suggested by *Rossby* [1939] and used by others since [*Angell and Korshover*, 1974, 1982; *Hurrell*, 1995; *Kapala et al.*, 1998; *Mächel et al.*, 1998]. A COA is a seasonal large-scale system which occurs annually in nearly the same geographic region. Examples of such COA are the Azores High COA or the Icelandic Low COA. While each of these COA have a well established and well understood long-term mean location, on a monthly or seasonal basis there is a large amount of variability in its exact location. As each of these COA are often the major climatic feature of a given region for a given season, this short-term location variability can be extremely important in terms of dictating the weather for a given season. Similarly each COA can vary in terms of its strength or intensity from month to month or season to season.

Once the position and intensity is quantified by the COA indices, those indices can be related to geophysical variables to investigate their relationships. Such an approach in the mid-latitudes has been successfully applied to many geophysical systems, e.g. solar cycle variability [*Christoforou and Hameed*, 1997], cloud cover and global temperature [*Croke et al.*, 1999], zooplankton in the Gulf of Maine [*Piontkovski and Hameed*, 2002], location of the Gulf Stream northwall [*Hameed and Piontkovski*, 2004], mineral dust transport [*Riemer et al.*, 2006; *Doherty et al.*, 2008], variability in sea level [*Kolker and Hameed*, 2007], frequency of Greenland tip jet events [*Bakalian et al.*, 2007] and sea-surface temperatures in the Gulf of Lion [*Jordi and Hameed*, 2009]. As we will describe shortly, in this paper we apply this framework to the ITCZ over West Africa.

In the literature there is some ambiguity regarding the definition of the term ITCZ [*Nicholson*, 2009]. The term ITCZ has been applied to both the tropical rain belt over West Africa [*Sultan et al.*, 2003] and the region of near-surface convergence, sometimes referred to at the Inter Tropical Front (ITF). As explained below, we define our index of convergence to be the center of mass of the low level (925 hPa) convergence as described in NCEP Reanalysis over West Africa. We refer to this as the West Africa Convergence Zone (WACZ) to avoid any confusion with terminology associated with the ITCZ in the literature. Defined in this way, the WACZ is observed to be north of the African Easterly Jet as described in *Mohr and Thorncroft* [2006], consistent with the conceptual model presented in *Nicholson* [2009]. It is shown to be associated with large scale changes in circulation and precipitation both locally in West Africa and regionally over the Tropical Atlantic.

While pressure has previously been used as the field to quantify the COA [*Hameed and Piontkovski*, 2004; *Riemer et al.*, 2006; *Doherty et al.*, 2008], in the tropics the gradient of sea level pressure is very small, and so we follow after *Kapala et al.* [1998] and use divergence as the reference field. Specifically, we define the WACZ to be the center of mass of the low level (925 hPa) convergence as described in NCEP Reanalysis [*Kalnay et al.*, 1996] over West Africa (15° S to 20° N and 20° W to 20° E). Figure 2.1 shows the climatological mean of divergence at 925 hPa from NCEP Reanalysis from 1965-2003 during the boreal winter including the months December to March. The three WACZ COA indices identify the position and intensity of the center of mass of the band of convergence extending between 5° N and 10° N from the West African coast east across the continent.

The intensity index W_i is defined as an area-weighted divergence departure from a threshold value over the domain (I, J)

$$W_\mathrm{i} = \frac{\sum_{i,j=1}^{I,J}(D_{i,j} - D_\mathrm{t})\cos\phi_{i,j}(-1)^M\delta_{i,j}}{\sum_{i,j=1}^{I,J}\cos\phi_{i,j}\delta_{i,j}}, \tag{2.1}$$

where $D_{i,j}$ is the divergence value at 925 hPa at a grid point (i, j), D_t is the threshold divergence value ($D_\mathrm{t} = -1.8 \times 10^{-6}$ s^{-1}), $\phi_{i,j}$ is the latitude of grid point (i, j), $M = 0$ for divergent systems and 1 for convergent systems, $\delta = 1$ if $(-1)^M(D_{i,j} - D_\mathrm{t}) > 0$, and $\delta = 0$ if $(-1)^M(D_{i,j} - D_\mathrm{t}) < 0$.

The latitudinal index W_ϕ is defined as:

$$W_\phi = \frac{\sum_{i,j=1}^{I,J}(D_{i,j} - D_{\mathrm{t}})\phi_{i,j}\cos\phi_{i,j}(-1)^M\delta_{i,j}}{\sum_{i,j=1}^{I,J}(D_{i,j} - D_{\mathrm{t}})\cos\phi_{i,j}(-1)^M\delta_{i,j}}. \quad (2.2)$$

The longitudinal index W_λ is defined analogously. The location indices thus give divergence-weighted mean latitudinal and longitudinal positions of the WACZ.

As a result we obtain time series of monthly values for latitude (W_ϕ), longitude (W_λ) and intensity (W_{i}) that characterize the WACZ. The indices are available from January 1948 to the present. Results were not significantly sensitive to changes in box size, the box location or the divergence threshold. This work focuses on the seasonal variability of mineral dust and the WACZ in boreal winter, and to represent this we use the average of four months December ($Y - 1$), January (Y), February (Y) and March (Y) where Y represents the year of the winter season. Our choice of DJFM is motivated by the work of *Ben-Ami et al.* [2011] who find that dust transport of Africa enters its southerly or winter mode from the end of November through the end of March. Values of the WACZ presented in this work are for the period December 1965 to March 2003, concurrent with the mineral dust record at the surface.

2.3 Datasets

In this study we utilize the mass concentration of mineral dust as recorded in Barbados. Barbados is an ideal location for observing mineral dust as it is the first land mass encountered by mineral dust traveling over the North Atlantic from Africa. Mineral dust at the surface at Barbados has been the subject of previous studies [*Prospero et al.*, 1970; *Carlson and Prospero*, 1972; *Prospero and Nees*, 1986; *Moulin et al.*, 1997; *Prospero and Lamb*, 2003; *Ginoux et al.*, 2004; *Chiapello et al.*, 2005] and is the longest continuous record of surface mineral dust concentrations. The record of monthly mineral dust at Barbados is available from August 1965 through December 2003. Data is collected near the surface at Barbados, located at 13° 10' N and 50° 30' W.

We use NCEP/NCAR Reanalysis wind data from NOAA/ESRL PSD [*Kalnay et al.*, 1996] to calculate the WACZ COA indices. Data is available from January 1948 to present, although we only consider the period of 1965–2003 to be consistent with the mineral dust record at Barbados. We compared the WACZ COA index from NCEP/NCAR Reanalysis to one calculated from ERA-40 (not shown), and for the winter season we found the two were not statistically different. NCEP/NCAR Reanalysis winds were also used to compute composite images, as described in Section 2.4.2.

Two traditional teleconnection climate indices are used in this study for comparison purposes, the NAO and ENSO. Monthly values of the NAO are from the Climate Prediction Center of NCEP/NOAA (`http://www.cpc.ncep.noaa.gov`). ENSO monthly values are also from the Climate Predictions Center of NCEP/NOAA who computes the ENSO indices from NOAA OI SST product over multiple regions in the Pacific.

The GPCP Dataset (v 2.1) [*Adler et al.*, 2003] is used for precipitation data in this study. Data is available from January 1979 - April 2008, however data after 2003 is not used in this study to be consistent with the mineral dust record at Barbados.

We use TOMS Aerosol Index (AI, v 8.0) as a measure of aerosol load [*Herman et al.*, 1997]. Data is available for the period 1979-1993 and 1996-2005. As described in *Kiss et al.* [2007] some calibration and instrument errors exist for this instrument. To this end we do not use the AI in any quantitative way, but present it as a qualitative aid in understanding how dust load changes with variation in the WACZ.

2.4 Results

2.4.1 Climatology of West Africa Convergence Zone

As shown in Figure 2.2 the WACZ (as defined in Section 2.2) displays a clear seasonal latitudinal migration from its southernmost point in January to its northernmost point in

August. The latitudinal index W_ϕ is thus consistent with the conventional understanding that the WACZ's location is seasonal and that the WACZ moves to follow the solar heating [*Folland et al.*, 1991]. The index W_ϕ reaches its northernmost position over Africa in July and August, trailing the movement of the solar heating maxima by one to two months. *Nicholson* [2009] notes that August also represents the period of maximum rainfall in the Sahel region and the period of maximum variability associated with the WACZ.

The movement of the WACZ is not a simple north-to-south migration, but rather is a two-dimensional migration. W_λ reaches its most westward point in the spring and moves towards the east in the fall. Coupled with the annual latitudinal migration, this means the WACZ moves on a NW to SE axis from spring/summer into fall/winter. Maximal convergence occurs in the spring and decreases to a minimum in fall, and is thus more intense in its north and west mode than its south and east mode.

While the long-term mean of the indices shows a clear annual cycle with an obvious seasonal migration, both the inter- and intra-annual variability of the WACZ is large. In the summer, when W_ϕ reaches its northernmost maximum there are large differences in the latitudinal position from year to year, ranging from 16 to 19 degrees north. In semi-arid locations such as the Sahel, a large shift in the location of the WACZ can be the difference between flooding and drought, and in turn can greatly effect soil conditions and ultimately dust mobilization. Additionally the latitudinal intra-annual variability plays a major role in controlling regional climate. Some years the WACZ remained in a northward phase for multiple consecutive months, leading to an extended rainy season for the Sahel, while in other years the northward phase and hence the rainy season is very short. The duration of the northward rainy phase may be critical in determining soil characteristics for the semi-arid Sahel, particularly in the summer when strong solar insolation can quickly dry out soils.

2.4.2 Relationship of Mineral Dust at Barbados and WACZ and ENSO during winter

To establish a relationship we correlated mean winter (DJFM) dust load at Barbados with the mean winter (DJFM) WACZ COA indices (W_ϕ, W_λ and W_i). Winter season mineral dust load at Barbados is significantly correlated with the location of the WACZ in terms of both the latitude (W_ϕ) and longitude (W_λ) of the WACZ at an α of at least 0.01 as shown in Table 2.1. No statistical relationship between the intensity of the WACZ (W_i) and mineral dust at Barbados was observed. Since the W_ϕ index increases in value as the WACZ moves north, the negative correlation observed between dust and W_ϕ suggests that as the WACZ moves south dust load at Barbados increases. Likewise the positive correlation between dust and W_λ suggests that as the WACZ moves eastward dust load at Barbados increases.

Traditionally a Pearson product-moment correlation coefficient is used to represent co-variance between two datasets. The Pearson product-moment correlation coefficient is not robust as it requires a normal distribution for both datasets nor resistant to outliers [*Wilks*, 1995]. Both the seasonally mean DJFM mineral dust at Barbados and ENSO climate indices used in this work are not normally distributed, and in the case of the ENSO dataset include multiple outliers. To reduce the impacts of outliers between datasets we use the Spearman rank correlation as shown in *Wilks* [1995]. It should be noted that using either the Pearson or the Spearman correlation coefficients the correlations between dust and W_ϕ, W_λ and E_{1+2} are statistically significant, but the Spearman correlation coefficient gives a more representative reflection of the covariance between datasets.

The indices W_ϕ and W_λ are not independent of one another as shown in Table 2.2. The WACZ is located further east in winters when it is in its south phase, and further west in winters when it is in its north phase, suggesting that in the winter season the WACZ varies along a NW to SE axis. This NW to SE axis is clearly visible in Figure 2.3a where during seasons in which the WACZ is north (blue diamonds) it also tends to be west and vice versa. Hence the NW location correlates to a reduction of mineral dust in Barbados and the

SE location correlates to an increase in mineral dust at Barbados. Figure 2.3b shows the magnitude of change in divergence at 925 hPa that accompanies the NW to SE shift, and a clear dipole pattern emerges. To produce this figure we subtracted the seasonal winter mean (DJFM) of divergence of the northernmost WACZ seasons (75th percentile) from the seasonal winter mean (DJFM) of the southernmost WACZ seasons (25th percentile). The black contour indicates a significant difference at 10%. The box over which the WACZ COA is computed is shown in black.

Figure 2.4 shows the temporal relationship between W_ϕ and mineral dust load at Barbados. Mineral dust load at Barbados reached its lowest value during the mid-1960's when W_ϕ is found to be at its most northward location, and it reached its peak in the mid-1980's when W_ϕ was in its most southward location.

Also shown in Table 2.1 is that the south and east migration of the WACZ explains more of the variability of the mineral dust than traditional climate indices such as the NAO or ENSO do. The ENSO Region 1+2 (E_{1+2}) is located along the coastline of Ecuador and Peru, ENSO 3 (E_3) is located just to the north and west of ENSO 1+2 spanning the central Pacific, and ENSO 4 (E_4) is the westernmost box approaching Papua New Guinea. We observe that the largest correlation between mineral dust and ENSO occurs for the ENSO index closest to South America (E_{1+2}), with the correlation coefficient attenuating moving into the Central Pacific. The relationship between ENSO and mineral dust is statistically significant at 5% close to the coast of South America (E_{1+2}) and not significant for the eastern Pacific (E_3), central Pacific ($E_{3.4}$) and central-west Pacific (E_4). This is consistent with *Mahowald et al.* [2003] who did not find widespread correlations in and around West Africa between dust and $E_{3.4}$ using a combination of modeling results and station observations. Our results suggest that statistical correlations between mineral dust transport and ENSO are sensitive to choice of ENSO domain.

As E_{1+2} and W_ϕ are not independent ($r = 0.80$), we apply a partial correlation analysis to account for their covariance and assess the relationship between each and mineral dust as if they were independent [*Wilks*, 1995]. There is precedent for using a partial correlation analysis to remove an ENSO signal. *Sankar-Rao et al.* [1996] use partial correlation to evaluate the signal of the Indian Monsoon on Eurasian seasonal snowfall without the influence of ENSO. More recently partial correlation was used similarly in a paper on mineral dust, tropical cyclone activity and ENSO [*Evan et al.*, 2006]. If we evaluate the rank correlation between mineral dust and W_ϕ with E_{1+2} held constant, the correlation coefficient decreases only slightly from $r = -0.69$ to $r = -0.66$, remaining significant at α of <0.001. The rank correlation between mineral dust and E_{1+2} with W_ϕ held constant decreases from $r = 0.30$ to $r = 0.06$, which is statistically insignificant. Much of the statistical relationship between E_{1+2} and mineral dust is a mathematical artifact caused from E_{1+2} varying in time with W_ϕ. We confirmed this in a separate composite analysis and find no physical relationship between E_{1+2} and wind or precipitation over emission, transport and deposition regions (not shown).

To corroborate our findings on the statistical relationships of Barbados mineral dust and the WACZ, we present the appropriate composite figures of the TOMS Aerosol Index (AI) data from NIMBUS-7 (1979-1993) and Earth Probe (1996-2005) as a semi-quantitative proxy for dust load over the entire Tropical North Atlantic. We analyze AI data to assess if the relationship between the WACZ and mineral dust at Barbados is reflective of larger scale changes in mineral dust load over the North Atlantic and Caribbean. AI measures absorbing particles in the atmosphere by comparing observed UV measurements to an idealized UV profile of the atmosphere. TOMS AI is not able to differentiate between types of absorbing aerosols, in particular particles from biomass burning register similarly to mineral dust aerosols. During boreal winter biomass burning is at a maximum [*Formenti et al.*, 2008] in North Africa, and a mix of mineral dust and biomass burning aerosols are likely. TOMS AI has known biases due to the height of the aerosol layer [*Herman et al.*, 1997; *Mahowald and Dufresne*, 2004], calibration drift errors [*Kiss et al.*, 2007] and cloud contamination issues [*Torres et al.*, 1998, 2002]. Here we only seek to verify the relationships of mineral dust surface observation and WACZ index, and so a qualitative use of the TOMS data is appropriate.

We use composites to represent seasonal conditions in which an index is in a positive or negative phase. The index W_ϕ is ranked in ascending order, the lowest quartile (q25) of data is identified as the negative phase and the highest quartile (q75) of data is identified as the positive phase. The years used to compute the seasonal composites are shown in Table 2.3. For W_ϕ the negative phase (q25) corresponds to periods in which the WACZ is in a south mode, and the positive phase (q75) corresponds to periods in which the WACZ is in a north mode. All seasons of AI data that have been selected as negative (q25) or positive (q75) phases are then averaged together to form a composite.

Figure 2.5 shows composites of TOMS AI with respect to the northward (minimum dust in Barbados) and southward phase (maximum dust at Barbados) of W_ϕ. We restrict our analysis to the period 1979-1993, 1996-2003 to included all AI data that is concurrent with the dust record at Barbados. Barbados is observed to be in a plume of dust entering the Caribbean in the southward phase of the WACZ (Figure 2.5a). When the WACZ is south (Fig. 2.5a), the greatest values of AI occur between 15° and 20° N, from the Atlantic Coastline east to 20° E. A very large plume of mineral dust is also evident over the Tropical North Atlantic centered between 15° and 20° N, which extends into the Caribbean Sea. The largest AI values of greater than AI = 3.0 occur near the Bodele Depression, a known hot-spot for mineral dust emission in Africa [*Washington et al.*, 2003]. Along the Gulf of Guinea values of AI are modest, near AI = 1.0 and likely reflect a mix of mineral dust and biomass burning aerosols.

In contrast, when W_ϕ is in its northward phase, the highest values of AI occur along the Gulf of Guinea, extending westward into the Tropical North Atlantic, centered at about 7.5° N. While some of this plume may be the result of biomass burning, *Formenti et al.* [2008] found that more than 70% of this material is mineral dust. A peak in AI (AI= 2.5) is observed near the Bodele Depression. Over much of the Sahara values of AI are modest, coming in around 1.0.

Comparing the north and south phases of the WACZ, a clear dipole in AI is evident in the composite difference image (Fig. 2.5c), similar to the dipole pattern in the composite difference for divergence as shown in Figure 2.3b. As the WACZ moves southward a large increase in AI is seen over the Sahara Desert, with increasing value of AI extending over a broad geographical area northward to the Mediterranean and eastward to the Red Sea, suggesting a robust response in dust emission to southward movement of the WACZ.

Higher values of AI are observed across nearly all of the Tropical North Atlantic north of 10° N suggesting a large increase in westward transport of mineral dust. Increases in AI are visible into the Caribbean. This analysis supports the conclusion drawn from the observed correlations, that mineral dust at the surface at Barbados increases as the WACZ moves southward.

Over Africa south of the Sahel and in particular south of 12° N a decrease in AI is observed as the WACZ moves southward. It is not clear if this is due to a decrease in mineral dust transport into this region or a reduction in biomass burning aerosols as TOMS AI cannot differentiate between mineral dust and biomass burning aerosols. This reduction in AI over this region is not likely due to precipitation as DJFM is the dry season in the Sahel, where precipitation is very low.

Our results are similar to those of *Engelstaedter and Washington* [2007] who find a spatial correlation between 10 m-divergence in ERA-40 and TOMS-AI over much of North Africa. Our results differ from the findings of *Ben-Ami et al.* [2011] who argue that during the boreal winter season that the dust plume across the Atlantic is constrained to a band centered on 4° N. However when the WACZ is in its north phase our results support the finding of *Ben-Ami et al.* [2011] as maximum aerosol load does appears to be near 4° N. We find that the location of the dust belt in TOMS-AI measurements is sensitive to the latitudinal position of the WACZ during the boreal winter, shifting northward to include Saharan sources when the WACZ is south phase. We find a plume of most likely mixed dust-biomass smoke is found near to 4° N only when the WACZ is in a north phase. It should be noted that the studies focus on different time periods. This analysis includes years over the period 1979-1993/1996-2004, whereas the Ben-Ami data is from the 21st century only.

2.4.3 Physical Mechanisms for Observed Correlation

The strong correlation between W_ϕ and mineral dust at Barbados and mineral dust at Barbados must be explained physically. Next we will examine how changes in W_ϕ impact wind and precipitation in the region, which in turn control the emission and transport of mineral dust from the Sahara.

Strong northeast winds over the Sahel have been shown to increase mineral dust emissions [*Engelstaedter and Washington*, 2007; *Schwanghart and Schütt*, 2008; *Doherty et al.*, 2008]. Figure 2.6 shows the composite difference in winds for the 25th percentile W_ϕ (southern most) winter (DJFM) seasons minus the 75th percentile W_ϕ (northern most) winter (DJFM) seasons over the period December 1965 - March 2003. This represents the difference in flow from the southern mode in which mineral dust is maximized at Barbados and the northern mode in which such dust is minimized. Figure 2.6a shows a strengthening of near-surface northeasterly winds during these conditions. This strengthening occurs over much of the Sahel and the Eastern Sahara, which are important source regions for mineral dust [*Washington and Todd*, 2005; *Engelstaedter and Washington*, 2007]. We hypothesize that the location of these strengthening winds is important in increasing dust emissions.

Northeastern winds in this region are typical in winter [*Engelstaedter and Washington*, 2007]. These winds known as the Harmattan winds transport mineral dust from the Sahara and Sahel regions southwards into sub-Saharan Africa in winter. The Harmattan winds are effective at emitting dust not only because of their strength but because of where they occur. The area around Lake Chad is a major source of mineral dust emissions [*Washington and Todd*, 2005] and just downwind of this region the largest increase in northeastern flow (Figure 2.6a and b) is observed as the WACZ changes phase. *Ben-Ami et al.* [2011] suggest that the Bodele Depression, which lies just north and east of Lake Chad, is the primary source of mineral dust during the boreal winter, where dust emissions are highly dependent on near-surface wind speeds [*Koren and Kaufman*, 2004]. Again near to the Bodele Depression we note increases in NE winds as the WACZ changes phase.

Our results support the hypothesis of *Schwanghart and Schütt* [2008] who noted the role of Harmattan winds which blow over the Bodele Depression, emitting large quantities of mineral dust in the boreal winter. In their study *Schwanghart and Schütt* [2008] observed that the strength of NE winds at 850 and 925 hPa near the Bodele was tightly correlated to the amount of mineral dust emitted in winter. *Schwanghart and Schütt* [2008] suggested that northward movement of the ITCZ had the capacity to diminish the NE winds. Our results here confirm their hypothesis.

In summary the strength of the NE Harmattan winds are an important control on the amount of mineral dust that is emitted in the boreal winter. We hypothesize that shifts in the WACZ controls dust emission not only by increasing wind speeds over much of West Africa, but does so by focusing these increases in critical locations such as the Sahel, Lake Chad and the Bodele Depression. Similar near-surface wind increases are observed from the composites for W_λ (not shown).

Wind increases in the Sahel, Lake Chad and Bodele Depression, known dust hot spots, are a means of relating changes in position of the W_ϕ to a third key physical parameter, soil texture. Mineral dust originating in dried lake beds (e.g. areas surrounding Lake Chad, Bodele Depression) are composed of vastly different minerals than that of sand (e.g. Sahara Desert) [*Cole et al.*, 2009]. Such lake bed derived minerals are known to be more easily emitted as windborne mineral dust [*Koren and Kaufman*, 2004]. In turn incorporation of soil texture databases (such as `http://daac.ornl.gov/cgi-bin/dataset_lister_new.pl?p=19`) in climate models is known to be of importance to accurately predict mineral dust emission. As the location of wind augmentation is shown to be critical in this work, we successfully link W_ϕ to soil texture.

Steering winds aloft at the base of the Saharan Air Layer show an increase in east to west flow, increasing trans-Atlantic transport of emitted particles (Figure 2.6b). The height of the Saharan Air Layer depends on the season [*Carlson and Prospero*, 1972], and satellite observations suggest that mineral dust transport is constrained to heights below 700 hPa in boreal winter over the Tropical North Atlantic [*Ben-Ami et al.*, 2009]. Figure 2.6b both show an increase in trans-Atlantic transport, although this increase is not statistically significant.

Figure 2.7a shows the winter (DJFM) mean precipitation for years in which the WACZ is in its south phase. Maximum precipitation rates are observed south of the equator, with the highest values observed in Brazil south of the Amazon River. In Africa precipitation is highest in Central Africa, south of the equator. Moderate precipitation is observed between the equator and 9° N over West Africa. No precipitation occurs over the Sahel or Sahara, as winter is the dry season. Differences in precipitation between the south phase conditions of the WACZ (Figure 2.7a) and the north phase conditions are shown in Figure 2.7a. Composite differences are calculated in such a way to show conditions that lead to maximized dust load at Barbados. We do not see a shift in the location of precipitation as the phase of W_ϕ changes, but rather a large scale drying across the Central Africa, the equatorial Atlantic and the Amazon Basin.

Precipitation over mineral dust source regions is not affected by changes in W_ϕ. No change in the amount of precipitation over the Sahel or Sahara regions occurs as W_ϕ changes phase from south to north, as no precipitation falls in this region during either phase. Wet deposition, vegetation, soil moisture in source regions are therefore not related to W_ϕ in winter.

In contrast to the Sahel and Sahara, over the tropical North Atlantic Ocean precipitation is non-zero. Mineral dust reaching Barbados and the Caribbean encounters precipitation in these regions as it is transported. Figure 2.7b suggests that dust maximization at Barbados is consistent with drier conditions in the tropical North Atlantic region, however. Although dust transport to the Americas could be increased in seasons when W_ϕ is in its south phase as less precipitation and therefore less wet deposition occurs, the observed change in precipitation here is too small to support this conclusion. Based on changes in precipitation in source and transit regions we conclude that changes in precipitation driven by variability W_ϕ are not important for mineral dust emission and transport to Barbados. Interestingly, Figure 2.7 shows significant precipitation occurring during the winter season across the equatorial Atlantic into South America, suggesting the wet deposition may be an important removal process in this region. As the W_ϕ changes to the southern phase, significant drying is observed across the equatorial Atlantic into South America (Figure 2.7b). While this is not relevant for the dust transport processes that are the focus of this paper, we hypothesize that this drying would reduce wet deposition of mineral dust that is transported to the Amazon Basin during winter from the Sahara and Sahel by way of the equatorial Atlantic (Figure 2.5).

Table 2.1 shows the near-zero correlation coefficient between intensity of WACZ (W_i) and mineral dust at Barbados ($r = 0.13$). This finding may seem surprising and counterintuitive, hence deserves further analysis. For this “null case” we produced composite images as was done for the latitude index W_ϕ. The weak (q25 of W_i) and intense (q75 of W_i) years used in these composite images are listed in Table 2.4. Here we note that since the correlation coefficient between W_i and dust at Barbados is near zero, the direction of the difference has no physical meaning. This is in contrast to the composites based on W_ϕ, which were built to highlight conditions that lead to dust maximization at Barbados.

The differences in the wind field at both 925 hPa (Figure 2.8a) and 850 hPa (Figure 2.8b) are not statistically significant between intense and weak WACZ seasons over source regions of the Sahel or Sahara. Over the Tropical North Atlantic a few patches of increased east to west flow are observed, suggesting a slight increase in transport when the WACZ is weak compared to the strong phase. These patches of increased flow do not appear to be large enough in scale to increase mineral dust transport to Barbados. We attribute a lack of change in wind over source regions as an explanation for why the intensity of the WACZ is not correlated with mineral dust load at Barbados.

As no precipitation falls in the source regions of the Sahel and Sahara and winter, the strength of the WACZ does not impact precipitation in these regions. Mineral dust emission is thus not impacted via precipitation as a function of WACZ intensity. Over the Tropical North Atlantic a general increase in precipitation is observed in years in which the WACZ is weak, with significant changes observed near to the African coastline. Mineral dust being transported to the Caribbean and Barbados could encounter more precipitation, and thus be impacted by wet deposition. Large changes in precipitation are observed over the equatorial Atlantic and Amazon Basin. Here precipitation is increased in the weak WACZ phase, potentially increasing removal of mineral dust via wet deposition.

To summarize we observe no changes in near surface flow or precipitation over the source regions of the Sahel and Sahara as the WACZ changes phase from weak to strong. Hence no physical mechanisms for increased dust emission are tied to changes in the WACZ intensity. We do observe some changes in the transport region of the tropical North Atlantic Ocean, specifically favorable winds for transport are increased while removal by precipitation also increases in the weak phase of the WACZ. We conclude that (1) processes in the source region are more important than processes in the transport region for mineral dust transport to Barbados and the Caribbean and (2) increased transport via enhanced advection is compensated for by increased removal in the weak phase resulting in no significant change in transport.

In summary, we note that increases in dust at Barbados during the winter season are associated with the WACZ moving south and that the underlying physical process is a change in winds in particular over the source region, not a change in precipitation. This is in agreement with the findings of *Sunnu et al.* [2008] who performed a field experiment and observed increased concentrations of mineral dust at the surface in Ghana when the ITCZ was south of the observing station in boreal winter.

2.5 Conclusions

The relationship between convergence over West Africa, referred to as the ITCZ or West Africa Monsoon, and mineral dust in the Tropical North Atlantic has long been discussed, and in this paper we quantified the relationship for the winter season. We constructed three climate indices that quantify the variability of the convergence over West Africa by applying the Centers of Action approach to wind divergence at 925 hPa from NCEP Reanalysis. We demonstrated the utility of such indices by relating them to the quantity of mineral dust reaching Barbados over the period from 1965 to 2003.

Southward and eastward movement of the WACZ is associated with an increase of the quantity of mineral dust reaching the surface at Barbados. This increase can be explained by increases in near-surface NE Harmattan winds over the Sahel. The location of the increase in wind is critical with increases in NE flow observed near the key Lake Chad and Bodele Depression region. Combined this leads to increases in emission of mineral dust when the WACZ is in its south phase. Once emitted, mineral dust aerosols encounter an increase in the east-to-west trade wind flow over across much of the Saharan Air Layer over West Africa. This increase in advective flow could increase mineral dust transport towards the Americas.

The latitude of the WACZ does not change dust emission or transport in winter by precipitation-driven effects. No changes in precipitation over the source regions of the Sahel or Sahara are noted, nor are significant changes observed in the transport zone between West Africa and Barbados. Although not related to transport of mineral dust to Barbados, we note a distinct drying over much of Central Africa, the tropical Atlantic and parts of South America associated with southward movement of the WACZ.

No relationship between the intensity of the WACZ and mineral dust was observed. We note that wind strength and direction does not change over key source regions between intense and weak phases of the WACZ. We hypothesize that this lack of change in winds explains why no relationship is observed between intensity of WACZ and mineral dust at Barbados. Although not related to transport of mineral dust to Barbados, weakening of the WACZ over Africa is shown to lead to drying over the equatorial Atlantic and Amazon Basin.

Studies looking for links between naturally varying systems and the atmosphere often refer to familiar indices such as for example the NAO or ENSO. We show that the location and intensity of the WACZ is a strong alternative to other common indices, with clear links to changes in circulation in the region.

Table 2.1: Spearman rank correlation coefficients between mean DJFM mineral dust at Barbados and climate indices for DJFM season 1965 to 2003. $\diamond$,† and $*$ represent significance at <0.001, 1% and 5% respectively.

	W_ϕ	W_λ	W_i	NAO	E_{1+2}	E_3	E_4	$E_{3.4}$
Dust at Barbados	$-0.69^\diamond$	$0.51^\dagger$	-0.13	0.18	0.30^*	0.18	0.11	0.15

Table 2.2: Cross correlation Spearman rank coefficient between mean winter (DJFM) WACZ COA indices for DJFM season 1965 to 2003. The $\diamond$ represents statistical significance at $\alpha < 0.001$.

	W_ϕ	W_λ	W_i
W_ϕ	-	$-0.73^\diamond$	-0.08
W_λ	$-0.73^\diamond$	-	0.06
W_i	-0.08	0.06	-

Table 2.3: Years that were used to generate seasonal mean composite images of AI, wind and precipitation based on W_ϕ. Each season mean was calculated using the average of four individual months of data; December $(Y-1)$, January (Y), February $(Y)$and March (Y) where Y represents the year of the winter season.

	q25	q75
AI	1983, 1998, 1989, 1992, 2000, 2001	1984, 1985, 1986, 1988, 1991
Wind	1977, 1983, 1989, 1992, 1993, 1995, 1998, 1999, 2000, 2001	1966, 1967, 1968, 1969, 1973, 1974, 1979, 1986, 1991, 1996
Precipitation	1983, 1989, 1992, 1998, 2000, 2001	1982, 1984, 1986, 1988, 1991, 1996

Table 2.4: Years that were used to generate seasonal mean composite images wind and precipitation based on W_i. Each season mean was calculated using the average of four individual months of data; December $(Y-1)$, January (Y), February $(Y)$and March (Y) where Y represents the year of the winter season.

	q25	q75
Wind	1996, 1990, 1995, 1968, 1985, 1981, 1984, 1989, 1997, 1970	1969, 1967, 2003, 1966, 1999, 2000, 2002, 1979, 1998, 1992
Precipitation	1996, 1990, 1995, 1985, 1981, 1984	2003, 1999, 2000, 2002, 1998, 1992

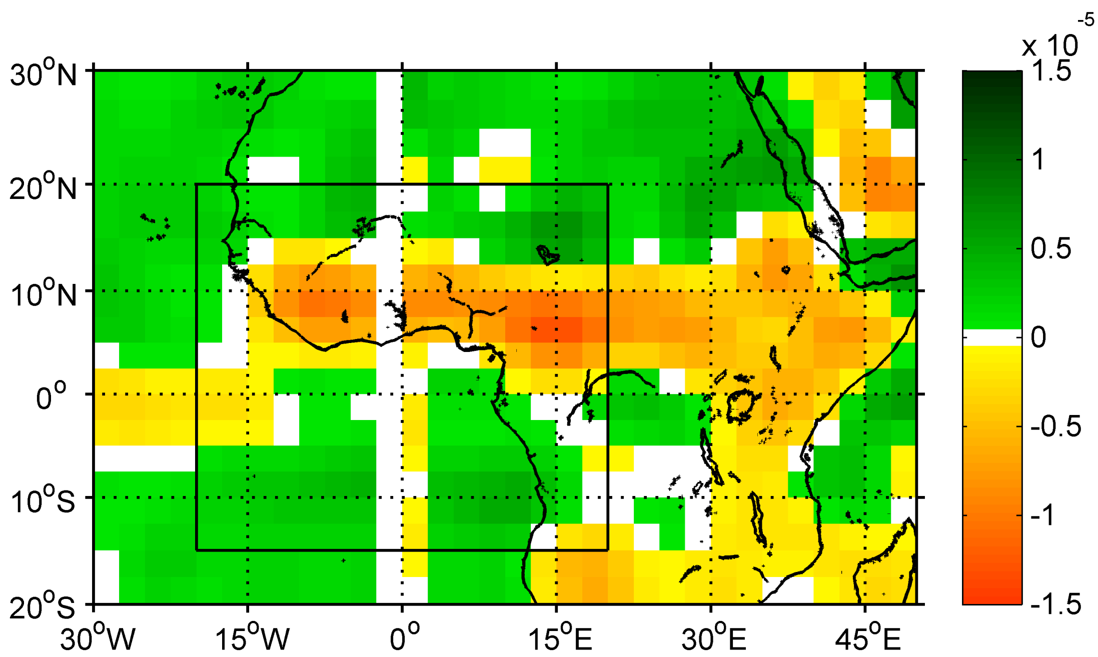

Figure 2.1: Mean winter (DJFM) divergence at 925 hPa as computed from NCEP Reanalysis winds. The box over which the WACZ COA is computed is shown in black.

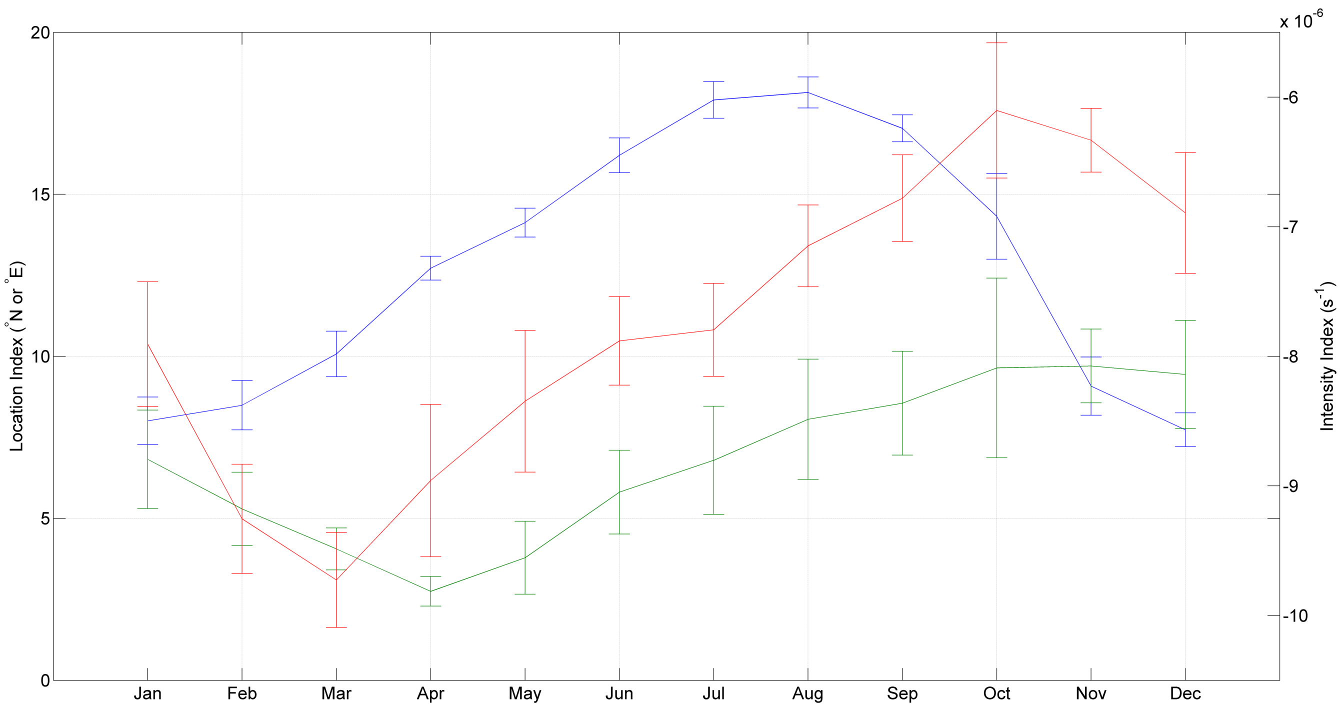

Figure 2.2: The long-term mean (1965-2003) of the WACZ latitude (W_ϕ) (blue line, left axis), longitude (W_λ) (green line, left axis) and intensity (W_{i}) (red line, right axis). Error bars represent the standard deviation based on the monthly average for each index.

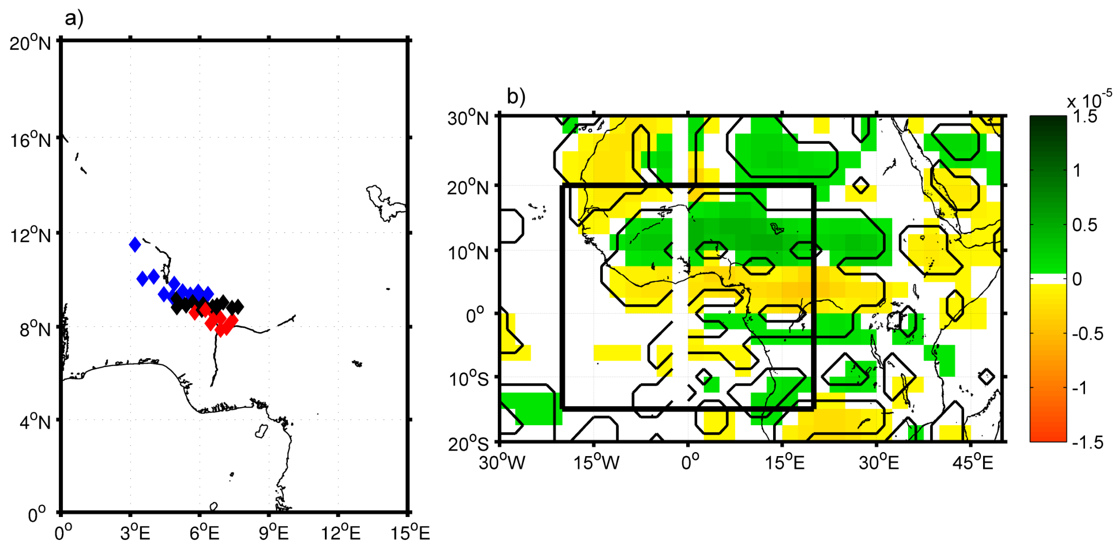

Figure 2.3: (a) Location of seasonal winter (DJFM) mean of WACZ COA over the period 1965 to 2003. Blue dots represent the northern (75th percentile) phase of WACZ COA, red dots represent southern (25th percentile) phase of WACZ COA. Black dots represent the middle 50 percent seasons of WACZ COA. (b) Difference in divergence of NCEP Reanalysis at 925 hPa during winter (DJFM) over the period 1965 to 2003. Differences are calculated by subtracting the seasonal winter mean (DJFM) of the northern most WACZ seasons (75th percentile) from the seasonal winter mean (DJFM) of southern most WACZ seasons (25th percentile). The difference represents the conditions of the WACZ latitude index for which dust is maximized at Barbados. Black contour represent a significant difference at 10%. The box over which the WACZ COA is computed is shown in black.

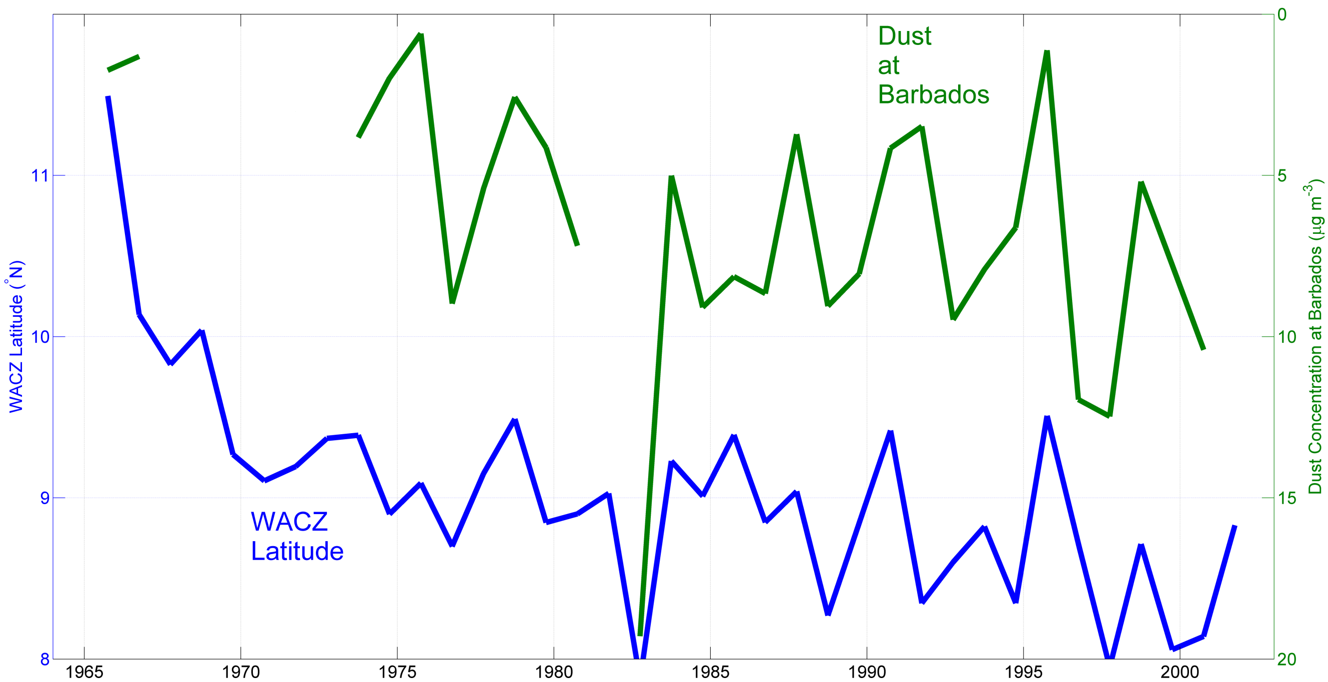

Figure 2.4: Comparison of the position of the mean DJFM WACZ latitude (left axis) and mean DJFM dust load at Barbados (right axis, inverted) over the period 1965 to 2003. Seasonal averages are calculated only for seasons that contain concentration data for all months of the season. Both time series are averaged over the winter months of December-March.

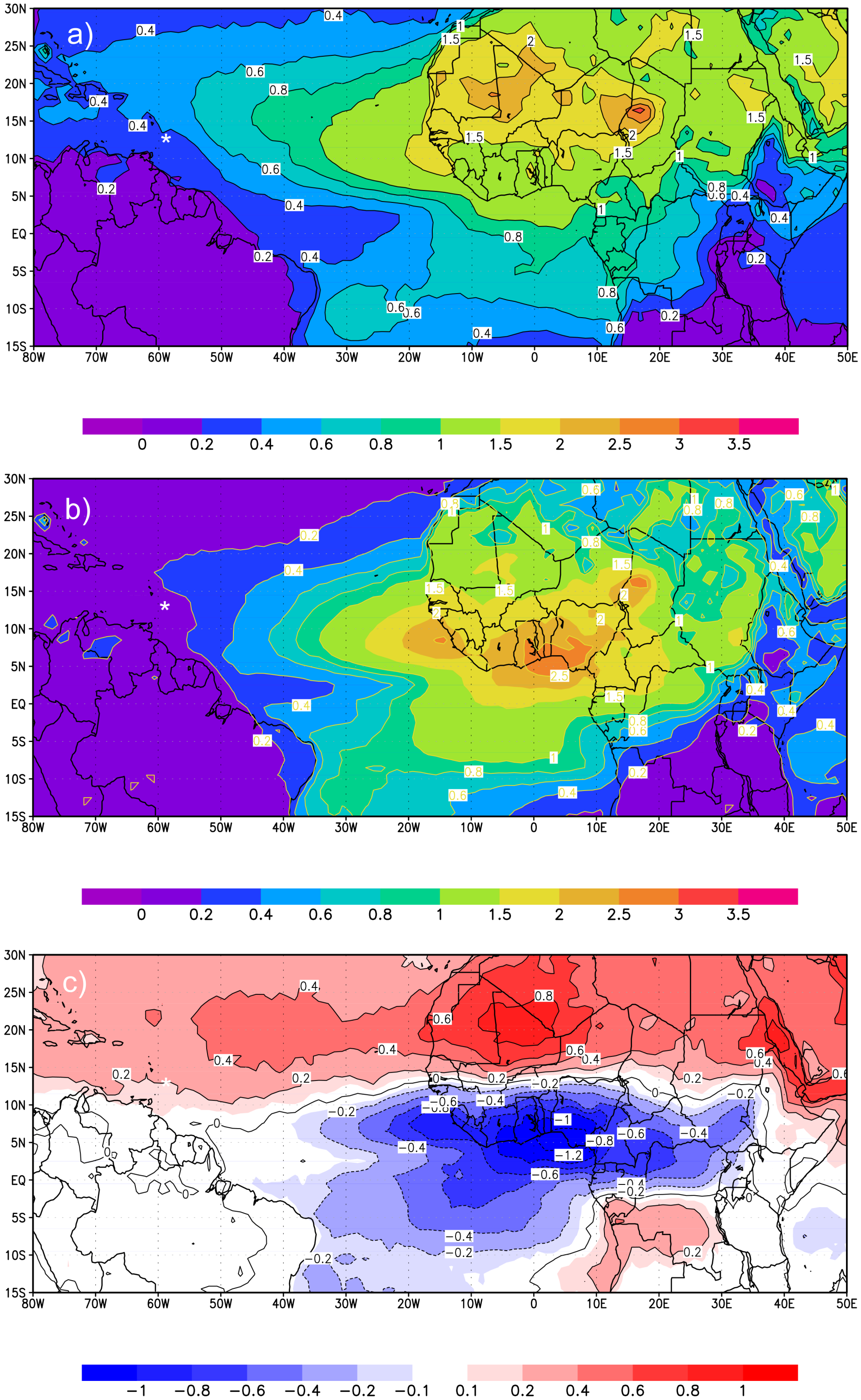

Figure 2.5: (a) Composite mean of TOMS AI for the southernmost winter (DJFM) seasons (25th percentile) of the WACZ. (b) As in (a) but for the northernmost WACZ latitude (75th percentile) winter (DJFM) seasons. Seasons with missing AI data are excluded from the composite. (c) The difference (a) minus (b), i.e. conditions of the WACZ latitude index for which dust load is maximized at Barbados. All composites are calculated over the period 1979-93; 1996-2003. Asterisks represent the location of Barbados.

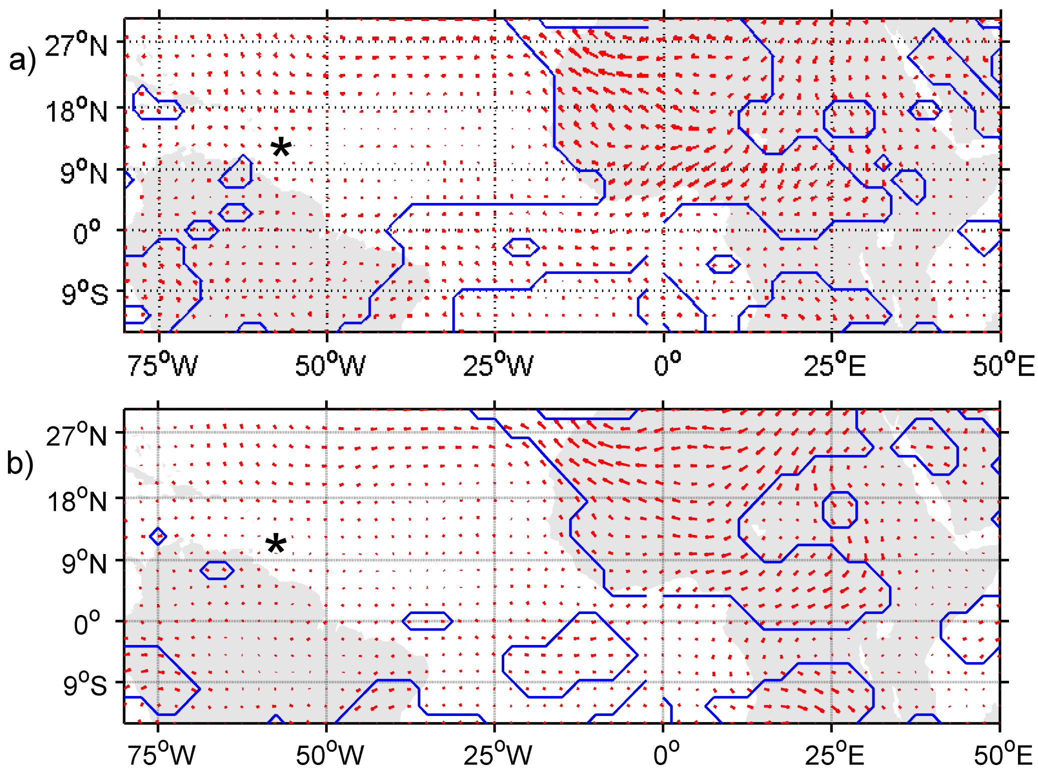

Figure 2.6: Difference in composite mean of NCEP Reanalysis winds at (a) 925 hPa and (b) 850 hPa. Differences are calculated by subtracting the seasonal winter mean (DJFM) of the northern most WACZ seasons (75th percentile) from the seasonal winter mean (DJFM) of southern most WACZ seasons (25th percentile). The difference represents the conditions of the WACZ latitude index for which dust is maximized at Barbados. All composites are calculated over the period 1965-2003; Blue contour represent a significant difference at 10%. Asterisks represent the location of Barbados.

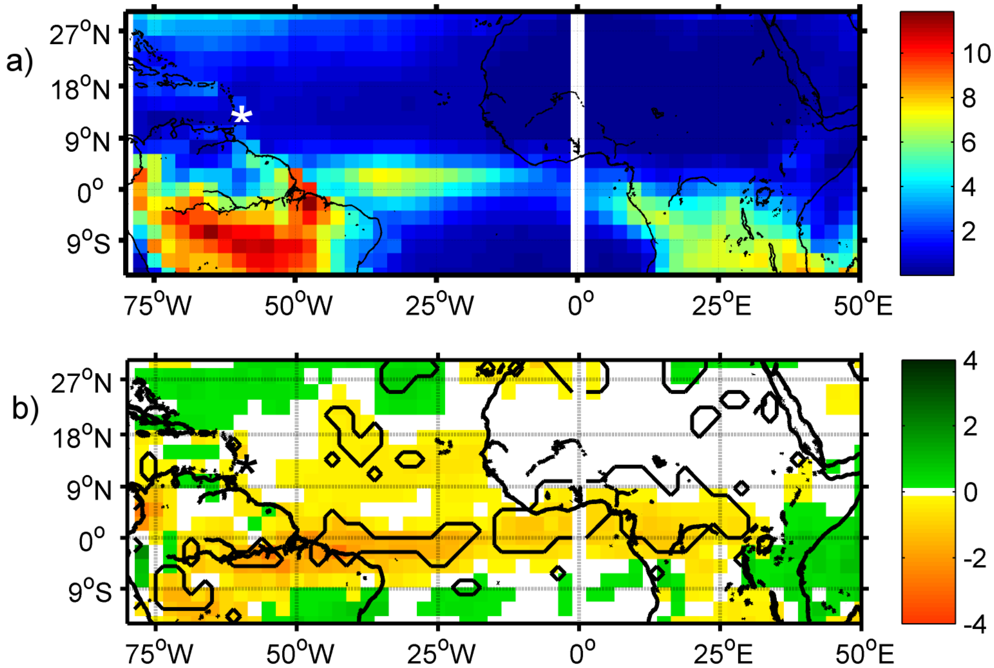

Figure 2.7: (a) Composite mean of GPCP precipitation for the southernmost winter (DJFM) seasons (25th percentile) of the WACZ over the period 1979 to 2003. (b) Difference in composite mean of GPCP precipitation over the period 1979 to 2003. Differences are calculated by subtracting the seasonal winter mean (DJFM) of the northern most WACZ seasons (75th percentile) from the seasonal winter mean (DJFM) of southern most WACZ seasons (25th percentile). The difference represents the conditions of the WACZ latitude index for which dust is maximized at Barbados. Black contour represent a significant difference at 10%. Units are mm day^{-1} from GPCP. Asterisks represent the location of Barbados.

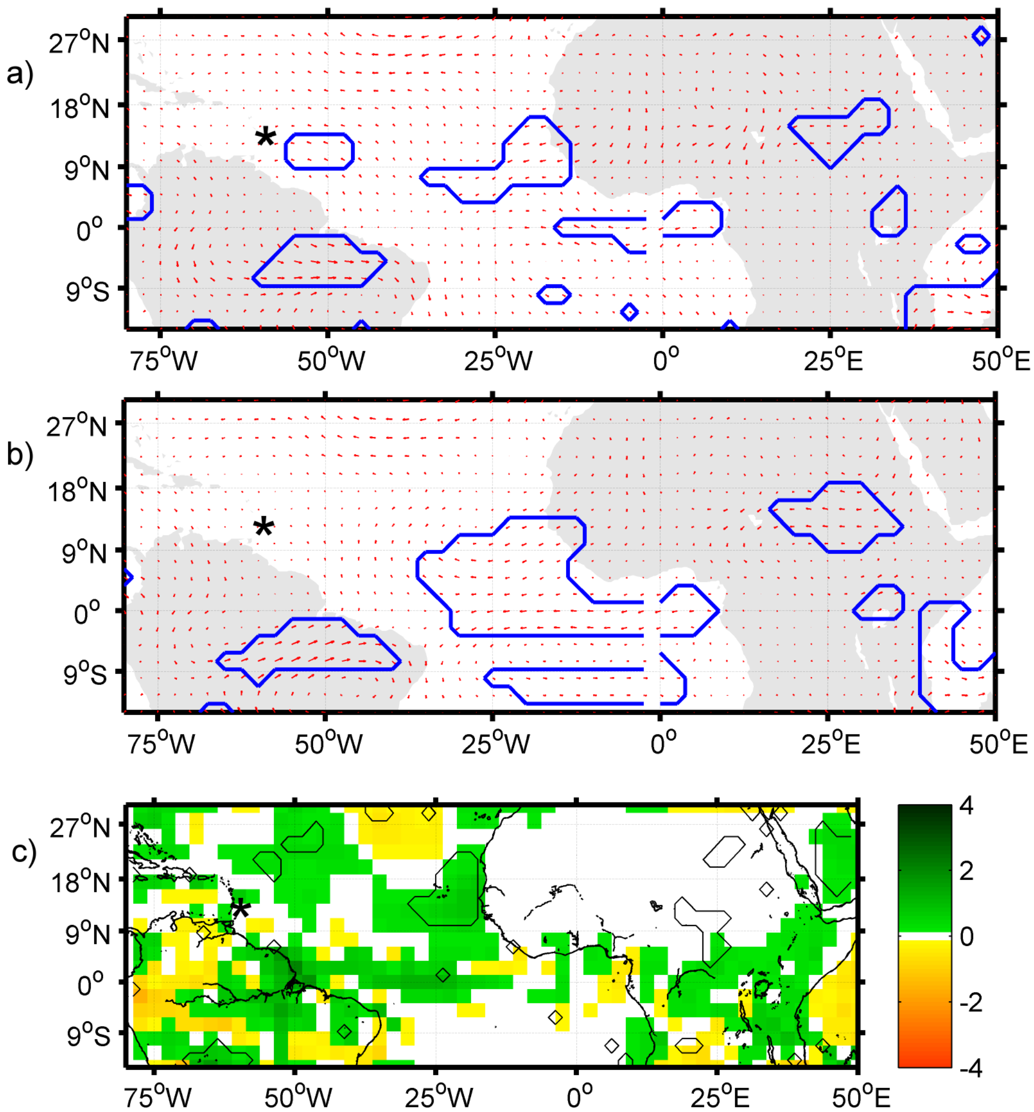

Figure 2.8: Difference in composite mean of NCEP Reanalysis winds at (a) 925 hPa and (b) 850 hPa. Differences are calculated by subtracting the seasonal winter mean (DJFM) of the weakest WACZ seasons (75th percentile) from the seasonal winter mean (DJFM) of strongest WACZ seasons (25th percentile). Wind composites are calculated over the period 1965-2003; Blue contour lines represent a significant difference at 10%. (c) As (a) and (b) but for GPCP precipitation (mm day^{-1}) over the period 1979 to 2003. Black contour lines represent a significant difference at 10%. Asterisks represent the location of Barbados.

Chapter 3

Role of the Intertropical Convergence Zone Over West Africa in Controlling Saharan Mineral Dust Transport to the Caribbean in the Dusty Season

3.1 Introduction

The majority of mineral dust emitted into the atmosphere originates from the arid Sahara Desert and the surrounding semi-arid Sahel [*Prospero et al.*, 2002; *Washington et al.*, 2003], with the highest concentrations of mineral dust occurring in the summer season of June through September. Understanding the year-to-year variability of this dust load during summer is critical as mineral dust originating from the Sahara is the dominant aerosol type over much of West Africa and the Tropical North Atlantic [*Formenti et al.*, 2008] and has complex impacts on the radiation budget and cloud properties of the region [*Arimoto*, 2001]. Mineral dust directly impacts the radiation by absorbing and reflecting incoming shortwave radiation and absorbing outgoing longwave radiation [*Sokolik and Toon*, 1996; *Tegen et al.*, 1996]. Like other aerosols, mineral dust indirectly impacts radiation by increasing droplet concentration [*Twomey*, 1977], and by altering the precipitation efficiency, albedo and lifetime of rain clouds [*Albrecht*, 1989]. Mineral dust has been shown to act as condensation nucleus for ice nucleation [*Sassen et al.*, 2003; *DeMott et al.*, 2003], potentially increasing the abundance of cirrus clouds and thereby warming the climate. On the other hand it has been shown that during particularly dusty summers a cooling of the tropical North Atlantic Ocean can occur [*Lau and Kim*, 2007b] as a result of the sum of direct and indirect effects.

Saharan mineral dust has also been linked to tropical cyclone formation over the tropical North Atlantic [*Dunion and Velden*, 2004; *Evan et al.*, 2006; *Lau and Kim*, 2007b,a; *Braun*, 2010], which is located downwind of the Sahara Desert. Radiative forcing from mineral dust has been shown to shift the location and strength of the tropical rainband over the Atlantic Ocean [*Huang et al.*, 2009] and may impact the ITCZ-monsoon circulation over Africa [*Lau et al.*, 2009a; *Kim et al.*, 2010; *Wilcox et al.*, 2010].

Saharan mineral dust in summer is transported long distances, often traveling at least 5,000 km and persisting in the atmosphere for periods in excess of a week [*Prospero et al.*, 1970] before reaching the Americas. The quantity of mineral dust transported to the Americas is important for many biogeochemical [*Swap et al.*, 1992; *Jickells*, 1999; *Baker et al.*, 2006; *Koren et al.*, 2006] and geological processes [*Herwitz et al.*, 1996; *Muhs et al.*, 2007].

Dust emission in North Africa is paradoxically maximized in the summer season when the annual northward migration of the Intertropical Convergence Zone (ITCZ) results in the maximum annual rainfall in the semi-arid lands of the Sahel [*Moulin et al.*, 1997; *Evan et al.*, 2006b]. Precipitation reduces dust load in multiple ways [*Tegen and Fung*, 1994; *Zender et al.*, 2003] both directly and indirectly. Where precipitation occurs concurrently with mineral dust aerosols the dust is removed by wet deposition. Precipitation leads to plant growth [*Eklundh and Olsson*, 2003; *Olson et al.*, 2005; *Herrmann et al.*, 2005], which in turn increases root activity, reduces soil mobility, improves soil quality and ultimately decreases dust emission [*Nicholson et al.*, 1998]. Hence, increased summer dust load over

West Africa occurs in spite of increases in precipitation, not due to it.

Amongst the atmospheric conditions responsible for maximum dust concentrations during summer are African Easterly Waves, the existence of the Saharan Air Layer [*Karyampudi et al.*, 1999] and increased easterly winds. African Easterly Waves produce strong gusty winds near the surface as they move from east to west over West Africa, resulting in dust emission [*Jones et al.*, 2003]. The Saharan Air Layer (SAL) has long been known to be a key factor in increasing stability and thus allowing mineral dust to travel long distances to reach the Americas [*Carlson and Prospero*, 1972; *Prospero and Carlson*, 1972]. In the summer the SAL exhibits its greatest vertical extent and is more prevalent. Lastly, north of the ITCZ, easterly winds increase in the summer months resulting in a higher probability of emitted dust reaching the Americas.

While the long-term average quantity of mineral dust emitted in Africa and transported over the tropical North Atlantic Ocean is at its peak in summer, this quantity varies greatly from year to year. Much effort has gone into improving our understanding of the processes that are responsible for this variability. Observations of Saharan mineral dust over the Atlantic Ocean and at Barbados have been related to variability in the North Atlantic Oscillation (NAO) [*Moulin et al.*, 1997], particularly in the winter season [*Chiapello and Moulin*, 2002]. Similar relationships have been diagnosed from global chemistry and transport model results [*Ginoux et al.*, 2004]. *Prospero and Lamb* [2003] related mineral dust in Barbados and an El Niño-Southern Oscillation (ENSO) index. Dust transport to the Americas has been linked to the position of the Azores High in winter [*Riemer et al.*, 2006] and in summer to the position of the Azores High and Hawaiian High [*Doherty et al.*, 2008]. *Schwanghart and Schütt* [2008] found no connection between regional weather systems and dust emission in summer, instead suggesting that dust emission in West Africa is connected to regional convection. More recently the variability of dust concentration at Barbados during winter has been attributed to changes in emissions driven by changes in the latitude of the ITCZ over West Africa [*Doherty et al.*, 2012a].

In this paper we show that the ITCZ is an atmospheric center of action directly related to all key processes affecting mineral dust emission and transport during summer and that the variability of mineral dust concentration in the atmosphere can be attributed to a large extent to the variability in the ITCZ. The ITCZ is a global belt of inclement weather that generally occurs where the trade winds converge and form the ascending branch of the Hadley Circulation. Annually the ITCZ moves north and south following the progression of annual solar maximum [*Folland et al.*, 1991]. Over the ocean the ITCZ circulation is relatively simple whereas over land the structure of the ITCZ becomes more complicated. When the ITCZ occurs over land it can be referred to as a monsoon. For example over Africa parts of the ITCZ are referred to as the West Africa Monsoon (WAM). Much ambiguity exists in terminology regarding the ITCZ [*Nicholson*, 2009], owing to the increased complexity of the system over land. Over West Africa the annual northward migration of the ITCZ-WAM brings critical seasonal rainfall to areas of the Sahel and southern Sahara [*Nicholson*, 2009]. As such the location and strength of the ITCZ has implications for seasonal soil and vegetative conditions, and likely dust emission and transport.

In this paper we explore how the variability of the ITCZ impacts summer dust emission and transport to the Caribbean. We introduce the data sets used in this study in Section 3.2. In Section 3.3 we describe the quantification of the variability of the ITCZ. In Section 3.4 we demonstrate the long-term relationship between mineral dust in Barbados and the ITCZ during the dusty season, and we compare the physical mechanisms by which the ITCZ impacts the mineral dust concentrations at Barbados. In section 3.5 we conclude our findings.

3.2 Datasets

3.2.1 Mineral Dust

To quantify the amount of mineral dust in the atmosphere we utilize two datasets; a long term surface based record of dust concentrations at Barbados (1965 - 2003) and a satellite derived measure of optical thickness from the Advance Very High Resolution Radiometer (AVHRR) instrument over the tropical North Atlantic (1982 - 2010).

The surface record of mineral dust concentrations in Barbados is regarded as the longest continuous observation of aerosols and its record has been extensively studied [*Rydell and Prospero*, 1972; *Prospero and Nees*, 1977; *Glaccum and Prospero*, 1980; *Prospero and Carlson*, 1980; *Prospero and Nees*, 1986; *Savoie et al.*, 1987; *Moulin et al.*, 1997; *Chiapello et al.*, 1999; *Prospero and Lamb*, 2003; *Ginoux et al.*, 2004; *Chiapello et al.*, 2005; *Prospero et al.*, 2008; *Trapp et al.*, 2010]. Barbados is an ideal location to study mineral dust transport as the island is the easternmost point of the Americas in the Caribbean, and thus the first land encountered by mineral dust that has traversed the North Atlantic Ocean. Barbados is situated approximately 4,800 km west of the western-most point of Africa. Monthly values of mineral dust concentrations in $\mu g\,m^{-3}$ are available from August 1965 through September 2003. In this study, only the years in which all four months (JJAS) of the summer season have data are used in the calculation.

To determine how the spatial distribution of mineral dust responds to changes of the location and intensity of the ITCZ we utilize an AVHRR-based dust aerosol optical thickness (AOT) [*Evan et al.*, 2006]. The dataset provides monthly mean AOT with a resolution of $1° \times 1°$ over the tropical North Atlantic Ocean (0° N to 25° N and 65° W to 10° W). The algorithm used to create the dataset is described fully in *Evan et al.* [2006] and a general discussion and climatology of the dataset is presented in *Evan et al.* [2006b]. This dataset was chosen as it has been calibrated for the tropical North Atlantic Ocean to detect optically thick dust over ocean surfaces, was cross-platform calibrating using AERONET, Metosat and TOMS-AI and is of a long record (1982–2010) coincident with much of the Barbados record. The major advantage of this product is that it is able to detect optically thick dust storms (AOT > 2) which many algorithms incorrectly identify as clouds [*Evan et al.*, 2006]. This feature is particularly important in summer (JJAS) when optically thick dust storms are most prevalent.

3.2.2 Gridded Datasets

In this study we use several gridded reanalysis products to characterize atmospheric and surface conditions. Wind data in this work is taken from NCEP Reanalysis [*Kalnay et al.*, 1996]. NCEP Reanalysis data is available monthly from 1948 to the present, although we constrain our analysis to the period 1965–2010, and has a resolution of $2.5° \times 2.5°$. Monthly averages of winds at 925 hPa from NCEP Reanalysis are used to calculate divergence, which is needed for the ITCZ Center of Action approach as described in Section 3.3.

To represent precipitation we use Global Precipitation Climatology Project (GPCP) Version 2.1 Combined Precipitation Data Set [*Adler et al.*, 2003]. GPCP precipitation data is available from 1979 to 2010, with a resolution of $2.5°\times2.5°$.

The Palmer Drought Severity Index (PDSI) dataset is used to represent soil conditions [*Dai et al.*, 2004]. PDSI data is available from 1870 to 2005, although we constrain our analysis to the period 1965–2003. PDSI has a resolution of $2.5° \times 2.5°$. A PDSI value of 0 represents the mean state of soil moisture. Negative values represent drought, with values of -3 and -4 representing severe and extreme droughts respectively. Positive values of PDSI represent greater moisture than average soil conditions.

To represent vegetation at the surface the GIMMS Normalized Difference Vegetation Index (NDVI) dataset is used [*Tucker et al.*, 2005]. The NDVI is calculated using irradiance data from the AVHRR instrument carried aboard NOAA satellites. NDVI data is available over the period July 1981–December 2002 at a resolution of $0.25°\times0.25°$. Values of NDVI near zero represent surface conditions of barren rock or sand, with increasing values of NDVI representing more lushly vegetated surfaces. For example brush and savannah-like terrains may have an NDVI value of between 0.2 to 0.4, and a tropical rainforest a value between 0.8 and 1.0.

Data was acquired from Physical Sciences Divsion of the Earth System Research Laboratory of NOAA (`http://www.esrl.noaa.gov/psd/`) with the exception of the AVHRR AOT record which was acquired from the University of Virginia (`http://trane.evsc.virginia.`

edu/Data.html) and GIMMS NDVI which was acquired from the Asia-Pacific Data-Research Center (http://apdrc.soest.hawaii.edu/) via OPeNDaP.

3.3 Methods

3.3.1 ITCZ as a Center of Action

Introduced by *Rossby* [1939] and used by others since [*Angell and Korshover*, 1974, 1982; *Hurrell*, 1995] an atmospheric "Center of Action" (COA) refers to semi-permanent atmospheric systems which persist for long periods of time, regularly appear in the same location year after year, and have impacts on regional climate. Some well known COA include the Azores High and Icelandic Low.

Here we treat the ITCZ over West Africa as a COA and seek to quantify its variability. Over West Africa much ambiguity exists regarding the use of the phrases "Intertropical Convergence Zone" and "monsoon". The system of interest consists of two zones of convergence and uplift, a northern convergence associated with the African Easterly Jet and a southern band of convergence associated with the Tropical Easterly Jet. To highlight the ambiguity of the use of the term ITCZ in the literature we note that *Sultan et al.* [2003] and *Parker et al.* [2005] and references therein refer to the southern convergence as the ITCZ, while *Nicholson* [2009] refer to the northern zone of convergence as the ITCZ.

As shown shortly, our approach considers the center of mass of convergence over West Africa and so as to avoid any ambiguity regarding the terms "Intertropical Convergence Zone" or "West African Monsoon" in this work we refer to this band of convergence as the West Africa Convergence Zone (WACZ).

The Center of Action approach is explained fully in *Doherty et al.* [2012a], but here we will briefly review the key components. In the traditional Center of Action approach the center of mass of a pressure system is identified and quantified by three indices, its longitudinal and latitudinal position and its intensity. For each index time series are generated, which characterize the variability of the COA under consideration which then can be used to explain the variability of a geophysical system of interest. This approach has been successfully applied globally to explain the variability in many geophysical systems [*Christoforou and Hameed*, 1997; *Croke et al.*, 1999; *Piontkovski and Hameed*, 2002; *Hameed and Piontkovski*, 2004; *Riemer et al.*, 2006; *Doherty et al.*, 2008; *Kolker and Hameed*, 2007; *Bakalian et al.*, 2007; *Jordi and Hameed*, 2009; *Hameed et al.*, 2011].

Here we seek to generate similar time series of location and intensity indices that quantify the variability of the WACZ. In the aforementioned studies pressure has been used as the field to quantify the COA, however in the tropics the gradient of sea level pressure is very small, and so we follow after *Kapala et al.* [1998] and use divergence as the reference field, as described in *Doherty et al.* [2012a].

We define the WACZ by computing convergence at 925 hPa using winds from NCEP Reanalysis [*Kalnay et al.*, 1996] over West Africa (0° N to 25° N and 20° W to 20° E). This domain is outlined in black in Figure 3.1a. Figure 3.1a also shows the climatological mean of JJAS divergence from 1965 to 2003, the center of the WACZ is just north of 18° N across much of West Africa before dipping southward near Lake Chad.

The intensity index of the WACZ W_i is defined as an area-weighted divergence departure from a threshold value over the domain (I, J):

$$W_\mathrm{i} = \frac{\sum_{i,j=1}^{I,J}(D_{i,j} - D_\mathrm{t})\cos\phi_{i,j}(-1)^M\delta_{i,j}}{\sum_{i,j=1}^{I,J}\cos\phi_{i,j}\delta_{i,j}}, \tag{3.1}$$

where $D_{i,j}$ is the divergence value at 925 hPa at a grid point (i, j), D_t is the threshold divergence value ($D_\mathrm{t} = -5.0 \times 10^{-5}$ s^{-1}). $\phi_{i,j}$ is the latitude of grid point (i, j). $M = 0$ for divergent systems and 1 for convergent systems. $\delta = 1$ if $(-1)^M(D_{i,j} - D_\mathrm{t}) > 0$ and $\delta = 0$ if $(-1)^M(D_{i,j} - D_\mathrm{t}) < 0$. The latitudinal index W_ϕ is defined as:

$$W_\phi = \frac{\sum_{i,j=1}^{I,J}(D_{i,j} - D_\mathrm{t})\phi_{i,j}\cos\phi_{i,j}(-1)^M\delta_{i,j}}{\sum_{i,j=1}^{I,J}(D_{i,j} - D_\mathrm{t})\cos\phi_{i,j}(-1)^M\delta_{i,j}}. \tag{3.2}$$

The longitudinal index W_λ is defined analogously. The location indices thus give divergence-weighted mean latitudinal and longitudinal positions of the WACZ. The physical location of the WACZ COA for mean JJAS seasons from 1965 to 2003 is shown in Figure 3.1b.

3.3.2 Composite Imaging Analysis

We use composite images to show changes in environmental conditions associated with a change in phase of W_ϕ, W_λ or W_i. For example to see how changes in the latitudinal position index W_ϕ impact regional wind circulation, the seasonal mean values of W_ϕ are ranked in ascending order. The lowest quartile (q25) of seasonal data is identified as the "south phase", which corresponds to the seasons when the WACZ was in a southerly position. The highest quartile (q75) of seasonal data is identified as the "north phase", which corresponds to the seasons when the WACZ was in a northerly position. All seasons of wind data that have been selected as southern (q25) or northern (q75) phases are then averaged to form a wind composite representing wind conditions for the south phase or the north phase, respectively. This approach can be repeated for other WACZ indices (W_i, W_λ) instead of W_ϕ, and other environmental variables (e.g. AVHRR AOT, GPCP Precipitation, GIMMS NDVI, PDSI) instead of wind. Years used to generate the individual composite images are shown in Table 3.3 and Table 3.4.

3.3.3 Empirical Orthogonal Function Analysis

We use Empirical Orthogonal Function (EOF) analysis to identify the key spatial patterns evident in the variability of environmental data and link the time series of principle components of these key spatial patterns to the time series of the WACZ latitude index. In essence EOF reduces temporally variant gridded data with internal variability to a small number of spatial patterns which represent the maximum possible quantity of the variability of the original data [*Wilks*, 1995]. In this analysis we use singular value decomposition on the covariance matrices of our gridded data to produce eigenvectors. For each pattern identified by the EOF a spatial map can be generated by multiplying the anomalies of the original data by the eigenvector, this spatial patterns shows what regions vary in the same or opposing directions to maximize the variance of the original data. The principle components, or the time series related to each spatial pattern can be generated by multiplying the anomalies of the original data by the eigenvalues. Principle component time series can be related to other physical quantities to determine what outside factors may give rise to observed spatial patterns in the data. Each mode generated in this way is orthogonal to the others and the cross-correlations of the principle components are zero. Each mode explains a fraction of the variance of the original data, the first mode controls the most variance with each subsequent mode controlling a smaller fraction of the variance of the original data.

3.4 Results

3.4.1 Climatology of WACZ Index During the Dusty Season

Figure 3.2a shows the latitudinal position of the WACZ (W_ϕ) during the summer season and adjacent months. The median value is indicated by a horizontal red bar. Skewness and spread are shown by the position of the 25th and 75th percentiles indicated by edges of the central box. Whiskers denote the spread of all non-outlying data with outliers indicated by red crosses. The WACZ moves steadily northward over West Africa in spring and summer, reaching its northernmost location on average in August. After September the WACZ shifts rapidly southward. Maximum year-to-year variability in the WACZ latitude index is observed in autumn.

Figure 3.2b represents mean Sahel precipitation averaged over the domain 15° N to 25° N and 0° to 25° E over the same time period. Precipitation begins as the WACZ moves northward in late spring and summer, and ends as the WACZ begins to move southward in fall. The WACZ latitude index appears to capture the seasonal precipitation cycle well, and our results are consistent with those presented in *Nicholson* [2009].

3.4.2 Relationship Between Mineral Dust in the Caribbean and Climatic Indices

Barbados Mineral Dust

Calculating the correlation coefficients between the time series of mineral dust concentration at Barbados and the three WACZ indices, we find that summer season mineral dust load is significantly correlated with both the latitudinal and longitudinal location index of the WACZ at $\alpha = 0.01$ as shown in Table 3.1. Since the WACZ index W_ϕ increases with latitude, the observed negative correlation of W_ϕ and mineral dust means that seasonal mineral dust load increases as the WACZ is displaced southward and seasonal mineral dust load decreases as the WACZ is displaced northward. Likewise mineral dust increases as the WACZ moves eastward and decreases as the WACZ moves westward.

The latitude and longitude indices of the WACZ are not independent of one another (Table 3.2). As seen in Figure 3.1b the WACZ is found to be further east when it is in its south phase and further west when it is in its north phase, suggesting that in the summer season the WACZ varies along a NW to SE axis. The NW location correlates to a reduction of mineral dust in Barbados and the SE location correlates to an increase in mineral dust at Barbados.

Figure 3.3 shows the temporal relationship between the latitude index of the WACZ and mineral dust load at Barbados. The scale for mineral dust concentration at Barbados has been inverted for visual ease of comparison. Mineral dust load at Barbados reaches its lowest value during the mid-1960's when the WACZ is found to be at its most northward location. Mineral dust reaches its peak in the mid-1980's when the WACZ reaches its most southward location.

Table 3.1 also includes the correlation coefficients of summer season mineral dust concentration at Barbados and traditional climate indices such as the NAO or ENSO. Only statistically insignificant correlations are observed.

AVHRR AOT

The long-term record at Barbados (1965 to 2003) is of great value as its length allows us to examine inter-annual variability of dust transport to the Caribbean region. Having established the relationship between increase in dust concentration at Barbados and a southward displacement of the WACZ, next we seek to determine if this relationship exists over the rest of the Caribbean. For greater spatial coverage we utilize the North Atlantic mineral dust AVHRR aerosol optical thickness product as described in *Evan et al.* [2006], which is available for the period 1982 to 2010. For winter we utilized TOMS AI data to represent mineral dust over the Caribbean. Here for the summer season we use the Evan AOT dataset instead, as instrument drift in later years makes TOMS AI data unreliable [*Kiss et al.*, 2007]. Seasons in which the WACZ is north in summer are dominated by later years (see Table 3.3), meaning for TOMS the composite difference compares years in which the instrument drifted (WACZ north, later years) and years in which the instrument did not drift (WACZ south, early years). In winter TOMS AI is an appropriate choice because north and south years are evenly distributed, reducing impacts of drift on composite images. Here we use the Evan AOT instead to ensure difference plots show changes driven by geophysical mechanisms rather than instrument drift.

Figure 3.4a shows the composite mean in AOT of JJAS seasons in which the WACZ was in its south phase, as described in Section 3.3.2. A plume originating over Mauritania is evident, which extends west towards the Americas centered at or just slightly north of 16° N. Figure 3.4b shows the corresponding composite mean of AOT in which the WACZ was in its north phase. Here we again note a plume forming west of Mauritania, extending westward towards the Americas centered near to 16° N. Figure 3.4c is the difference in AOT, subtracting the north phase conditions shown in Figure 3.4b from the south phase conditions shown in Figure 3.4a representing conditions that lead to dust maximization at Barbados. Figure 3.4c shows no shift in the location of the dust belt, but rather an increase in AOT over nearly all of the Tropical North Atlantic. In the center of the dust belt the AOT increases by

0.2 to 0.3 as the WACZ shifts southward. The lack of movement in the dust belt; rather an increase during seasons in which the WACZ moves southward is confirmed by the first mode EOF analysis (Figure 3.4d). At all points the relative magnitude of the first EOF mode (which explains 36% of the total variance in the AOT record) are negative, suggesting that the AOT responds unidirectionally, either increasing or decreasing over the Tropical North Atlantic. The principle component of this first EOF is statistically significantly correlated with the WACZ latitude at $\alpha \leq 0.01$ ($r = 0.51$), suggesting that southward movement of the WACZ is indeed coupled with the basin-wide increase in mineral dust.

The observed relationship of a southward movement of the WACZ and increases both in dust concentration at the surface at Barbados and in the wide-spread mineral dust observed in the AVHRR record suggests a robust link between the position of the WACZ and mineral dust reaching the Caribbean. In the remainder of this section we will investigate the physical mechanisms by which the WACZ impacts mineral dust emission on the one hand and transport to the Caribbean on the other hand.

In particular we will analyze how changes in the WACZ impact winds near the surface, precipitation, soil conditions and vegetation over West Africa, which in turn impact mineral dust emission. We will also analyze winds aloft and precipitation over the North Atlantic to see how changes in the WACZ may impact transport of mineral dust across the Atlantic.

3.4.3 Mechanisms Impacting Emission

Winds and Precipitation in Source Regions

Figure 3.5 shows the difference in 925 hPa winds between conditions when the WACZ is in the south mode and conditions when the WACZ is in the north mode. These differences represent conditions that lead to dust maximization at Barbados. An increase in the strength of the trade winds across the Sahel is evident, including a maximum strengthening near Lake Chad which is a major source for mineral dust aerosols [*Washington et al.*, 2006]. Winds aloft (not shown) over West Africa show a similar increase in NE to SW flow leading to an increase of export of emitted mineral dust particles.

Figure 3.6a shows the JJAS mean composite of precipitation for the northern phase of the WACZ. Maximum precipitation is observed in a band stretching from East Africa west across the Atlantic into South America. However when the WACZ moves southward, so does the band of precipitation, and a general drying across Africa is evident as seen in Figure 3.6b. This figure shows the difference in precipitation between conditions when the WACZ is in the south mode (not shown) and conditions when the WACZ is in the north mode (Figure 3.6a), i.e. conditions which lead to dust maximization at Barbados. Significant drying occurs over all of Africa between 10° N and 20° N. Just north of the equator a slight increase in precipitation is noted, related to the southward shift of the WACZ. We note that the strongest drying occurs over the semi-arid Sahel region. Comparison with Figure 3.5 shows that the area of reduced precipitation is coincident with the area of increased winds, resulting in an ideal scenario favoring dust emission.

EOF analysis suggests that the north-to-south movement of the precipitation belt represents the majority of variance in the GPCP precipitation product for the summer season (JJAS). Figure 3.7a shows the first mode (which represents 42% of the total variance) and Figure 3.7b the second mode (12% of variance). The first mode shows a clear north-south dipole in precipitation, the second mode features a NE to SW dipole. Both the first and second modes are significantly correlated with the WACZ latitude index at or below an $\alpha = 0.01$. Regressing the first and second mode of precipitation together onto the WACZ latitude index results in a correlation of $r = 0.66$ (Figure 3.7c). The WACZ latitude index appears tightly related to the major modes of variability in precipitation over West Africa.

While a widespread reduction in precipitation in the sensitive Sahel region is clearly observed, it is not immediately clear how exactly this reduction in precipitation leads to changes in mineral dust load. Reduced precipitation can reduce wet deposition of mineral dust. In addition reduced precipitation can lead to reductions in soil moisture and vegetation, both of which can allow for increased emission of mineral dust. Hence we next examine changes in vegetation and soil moisture tied to latitudinal shifts in the movement of the WACZ.

Vegetation and Soil Conditions in the Source Region

GIMMS NDVI is used as a high-resolution proxy for surface vegetation. Reductions in vegetation are observed in the Sahel in Figure 3.8 which is the composite difference in NDVI for the south phase of the WACZ minus the north phase of the WACZ which show changes that lead to dust maximization in Barbados. Vegetation is reduced in a band between 12° N and 18° N extending from the Atlantic Ocean to the Red Sea, suggesting a robust response in vegetation due to shifts in the latitudinal position of the WACZ. Figure 3.9a and b show the first and second modes of the EOF analysis on NDVI for JJAS summer seasons. Mode 1 (39% of the variance) shows a clear north to south dipole, in which vegetation increases in the Sahel while decreasing to the south, or vice-versa. Mode 2 (12% of the variance) is related to variance in the vegetation of the very southern extent of the Sahara Desert. The principle components of both mode 1 and mode 2 are significantly correlated with the WACZ latitude index at $\alpha = 0.01$. Regressing the first and second modes of NDVI together onto the WACZ latitude index results in a correlation of $r = 0.68$ (Figure 3.9c), i.e. changes in vegetation are directly related to the latitudinal position of the WACZ.

PDSI is used to represent soil moisture conditions. Figure 3.10a shows the composite of PDSI during JJAS seasons in which the WACZ is in its south mode, and Figure 3.10b shows the composite of the north mode. Both north and south phases show drought-like conditions, reflecting the extreme drought that occurred from the 1970's through the early 1990's in sub-Saharan Africa. However the south phase shows more extreme drying, with much of the Sahel experiencing values of -3 to -4 PDSI which represent severe to extreme drought. Subtracting the composite shown in Figure 3.10(b) from the one in Figure 3.10(a) we see over much of the Sahel and southern Sahara desert that drying of this region occurs concurrently with dust maximization, as the WACZ moves into its south phase. We are not able to present an EOF analysis of the PDSI due to many missing data points.

In summary we note that southward movement of the WACZ leads to increases in near-surface flow in key emission locations. These key emission locations also receive significantly reduced precipitation in seasons in which the WACZ is in its south phase, reducing wet deposition removal of mineral dust in these regions. Reductions in vegetation and soil moisture also follow the southern migration of the WACZ. Thus we hypothesize that southern displacement of the WACZ is critical in increasing mineral dust emission by degradation of the surface soils and increased opportunities for emission via increases in near surface wind.

3.4.4 Mechanisms Impacting Transport

Mineral dust emitted over Africa travels nearly 5,000 km to reach Barbados and the Caribbean. Steering winds over the tropical North Atlantic control where the dust is transported once emitted, and stronger winds result in quicker transport to the Americas reducing gravitational settling and the chance of removal via wet deposition. Next we examine how changes in the latitudinal position of the WACZ impact steering currents aloft and precipitation over the tropical North Atlantic.

Figure 3.11a (850 hPa), 3.11b (700 hPa) and 3.11c (500 hPa) show composite differences of the wind conditions aloft, which are calculated in the same manner as for Figure 3.5 to represent conditions in which dust is maximized at Barbados. While just south of the dust belt (around 16° N) there is significant strengthening of easterly winds between the equator and 10° N, in the center of the dust belt we see no significant change in transport winds. The spatial mismatch of the wind augmentation and the location of maximum dust concentration suggests that the impacts of the movement of the WACZ on circulation are more important via the emission process. As shown in Section 3.4.3 and Figure 3.5, increases in dust emission can be linked to increased winds in the important source regions of the Sahel and southern Saharan desert.

Precipitation changes that occur as the WACZ shifts from the south phase to the north phase, representing conditions in which mineral dust levels are maximized at Barbados, are shown in Figure 3.11d. Between 15° N and 25° N a drying of the region is noted with statistical significance over limited areas. Between the equator and 15° N we note an increase in precipitation, with statistical significance over limited areas. However in contrast to the extreme drying of the Sahel region (Figure 3.6b) as the WACZ shifts south, no clear statistically significant pattern emerges over the tropical North Atlantic. We conclude that precipitation processes in the transport region play a much smaller role in modulating dust transport to Barbados than does the extreme drying noted over source regions.

3.4.5 Physical Mechanisms for the Null Case

Table 3.1 shows a near-zero correlation between the intensity of the WACZ (W_{i}) and mineral dust at Barbados, which means that there is no observed relationship between the WACZ intensity and dust load at Barbados from 1965 to 2003. This may come as a surprising result, and in comparing this "null case" to the WACZ latitude case discussed in Section 3.4.2, we look for differences between the two cases to further elucidate which processes are important for dust emission and transport and which processes are irrelevant.

For the W_{i} case we again build composite images of wind, precipitation and AVHRR aerosol load for changes in phase of the WACZ intensity to identify reasons which may explain why W_{i} has apparently no role to play in governing the variability of mineral dust. As the correlation coefficient between W_{i} and mineral dust is near zero, the choice in direction of difference in composites is trivial.

Figure 3.12a shows the composite difference of 925 hPa winds based on W_{i}. Here we see a west flow in the Sahel west and south of Lake Chad, which represents a decrease in the near-surface easterly winds. This suggests a reduction in surface dust emission when the WACZ is in a weaker phase. A strong, statistically significant drying occurs over the Sahel and south Sahara (Figure 3.12c), suggesting that a weaker WACZ is associated with decreased precipitation in this region. A similar drying occurs for the W_ϕ case (Figure 3.6), however as W_{i} and W_{ϕ} are not significantly correlated (Table 3.2) these drying patterns are physically independent of each other. In summary over West Africa we see reduced near-surface winds combined with decreased precipitation as the WACZ enters its weaker phase. These changes have opposing effects on dust emission as reduced winds reduce dust emission whereas reduced precipitation increases dust emission. This is consistent with the low correlation coefficient between dust and W_{i}.

Figure 3.12b shows the composite difference of 850 hPa winds based on W_{i}. Wind vectors point west to east over the mineral dust source regions of the Sahel and Sahara, resulting in a decrease in easterly winds in these locations. Over the tropical North Atlantic an increase in east to west flow is observed between the equator and 12° N. Changes in precipitation over the North Atlantic Ocean are mixed (Figure 3.12c), with decreases in precipitation near to Africa and increases in precipitation observed over Barbados southward into South America. This suggests a varied wet depositional change, with reductions near to Africa and increases near to the Caribbean. The implications for transport to the Americas are mixed. Reduced precipitation near Africa could increase the lifetime of mineral dust, and increases in cross-Atlantic flow near the equator could increase transport. However increases in precipitation over the western tropical North Atlantic could remove mineral dust. The AVHRR AOT composite difference of the W_{i} case is shown in Figure 3.12d. An increase in mineral dust is observed over the North Atlantic, however this increase is constrained only near to Africa. This response is small compared to the response to changes in W_{ϕ} (Figure 3.4).

From this it becomes clear that changes in intensity of the WACZ do result in changes in wind and precipitation, but for a given phase of intensity one augments, and the other decreases mineral dust emission and transport. This interplay explains the lack of a robust mineral dust response in the Caribbean to changes in WACZ intensity. Table 3.5 summarizes and contrasts the case of W_{ϕ} in the south phase (left column) in which dust is increased at Barbados and the null case of W_{i} in the weak phase (right column). In both cases reduced precipitation over the source region and steering winds over the tropical North Atlantic act in a way that would increase dust load in Barbados. In both cases there is no clear signal from precipitation over the tropical North Atlantic. However in the W_ϕ case winds over the source regions respond in a way that would increase dust emission, whereas the opposite applies in the W_i case. Our interpretation is that the reduction in surface winds over the Sahel and Sahara is a key reason that mineral dust load does not increase in the W_i case, and conversely the increase in surface winds is a key reason that dust load increases in the W_ϕ case.

3.5 Conclusions

While drought conditions in the Sahel, favorable transport circulations, and increased near-surface winds have long been known to increase dust transport to the Americas, no unified mechanism had hitherto been identified which could explain changes in key variables. Here we present the utility of the WACZ as a center of action, which proves capable of explaining the inter-annual seasonal variability of mineral dust transport to Barbados and to the Caribbean in summer and of separating out the relative importance of transport and emission. We found that the latitudinal shift of the WACZ controls much of the variability of mineral dust over the Caribbean region, and that processes in the source regions over Africa are more important than processes over transport regions.

The WACZ latitude index is significantly correlated with the mineral dust concentration at Barbados, precipitation in the Sahel, soil moisture and vegetation. Through composite imaging we showed that the southward movement of the WACZ is associated with marked increases in near-surface winds over important dust emitting regions and also with decreases in precipitation over the Sahel, which in turn reduces soil moisture and vegetation. EOF analysis of precipitation and vegetation show that the dominant principle components are statistically significantly correlated to the WACZ latitude. EOF loading patterns resemble composite images, showing the robustness of the WACZ latitude index signal.

In contrast to the WACZ latitude index the intensity index is not significantly correlated with mineral dust at Barbados. The corresponding composite analysis reveals that changes in the WACZ intensity do result in characteristic changes in precipication patterns and wind patterns. However it turns out that increased winds over source regions conincide with increased precipitation and vice versa, hence the two processes counteract each other in their impact on mineral dust in the atmosphere.

In summary, the coupling of changes in near-surface winds with changes in precipitation in emission regions driven by the latitudinal movement of the ITCZ is key in explaining the variability of mineral dust over the tropical North Atlantic, Barbados, and the Caribbean.

Table 3.1: Pearson product moment correlation coefficients between mean JJAS mineral dust at Barbados and climatic indices for JJAS season 1965 to 2003. $\diamond$ represent significance at $< 0.1\%$. W_ϕ is the WACZ latitude index, W_λ is the WACZ longitude index, W_{i} is the WACZ intensity index, E_{1+2} is ENSO over the ENSO 1+2 box, E_3 is ENSO over the ENSO 3 box, E_4 is ENSO over the ENSO 4 box and $E_{3.4}$ is ENSO over the ENSO 3.4 box.

	W_ϕ	W_λ	W_{i}	NAO	E_{1+2}	E_3	E_4	$E_{3.4}$
Dust at Barbados	$-0.49^\diamond$	$0.46^\diamond$	-0.04	-0.16	0.24	0.08	-0.01	-0.02

Table 3.2: Cross correlation Pearson product moment coefficient between mean summer (JJAS) WACZ COA indices for JJAS season 1965 to 2003. The $\diamond$ represents statistical significance at $\alpha < 0.1\%$. W_ϕ is the WACZ Latitude, W_λ is the WACZ longitude and W_{i} is the WACZ intensity.

	W_ϕ	W_λ	W_{i}
W_ϕ	-	$-0.67^\diamond$	0.20
W_λ	$-0.67^\diamond$	-	-0.06
W_{i}	0.20	-0.06	-

Table 3.3: Years that were used to generate seasonal mean composite images of wind, AOT, precipitation and PDSI based on W_{ϕ}. The lowest quartile (q25) of seasonal data is identified as the "south phase," which corresponds to the seasons when the WACZ was in a southerly position. The highest quartile (q75) of seasonal data is identified as the "north phase," which corresponds to the seasons when the WACZ was in a northerly position. Each season mean was calculated using the average of four individual months of data; June, July, August and September.

	q25	q75
Wind	1984, 1973, 1990, 1989, 1982, 1987, 1972, 1981, 1991, 1986	1999, 1976, 1979, 1978, 2001, 1977, 1967, 1974, 1966, 1965
AOT	1984, 1990, 1989, 1982, 1987, 1991, 1986	2005, 2003, 2002, 1999, 2001, 2008, 2007
Precipitation	1984, 1990, 1989, 1982, 1987, 1981, 1991	1995, 2003, 1980, 2002, 1999, 1979, 2001
PDSI	1984, 1973, 1990, 1989, 1982, 1987, 1972, 1981, 1991, 1986	1999, 1976, 1979, 1978, 2001, 1977, 1967, 1974, 1966, 1965

Table 3.4: Years that were used to generate seasonal mean composite images of wind, AOT and precipitation on based on W_{i}. Each season mean was calculated using the average of four individual months of data; June, July, August and September.

	q25	q75
Wind	1984, 1969, 1983, 1990, 1991, 1981, 1992, 1994, 1965, 1976	1997, 1980, 1979, 1971, 2000, 1998, 1999, 2001, 1968, 1974
AOT	1984, 1983, 1990, 1991, 1994, 1986	2006, 2000, 2003, 2007, 1998, 2001
Precipitation	1984, 1983, 1990, 1991, 1981, 1992, 1994	1980, 1979, 2000, 2003, 1998, 1999, 2001

Table 3.5: Summary of factors impacting emission and transport for changes in phase of W_ϕ and W_i.

	W_ϕ South Phase	W_i Weak Phase
Wind over Source Regions	Increases Emission	Reduces Emission
Precipitation over Source Regions	Increases Emission	Increases Emission
Wind over North Atlantic	Limited Increase in Transport	Limited Increase in Transport
Precipitation over North Atlantic	Inconclusive	Varies by Location

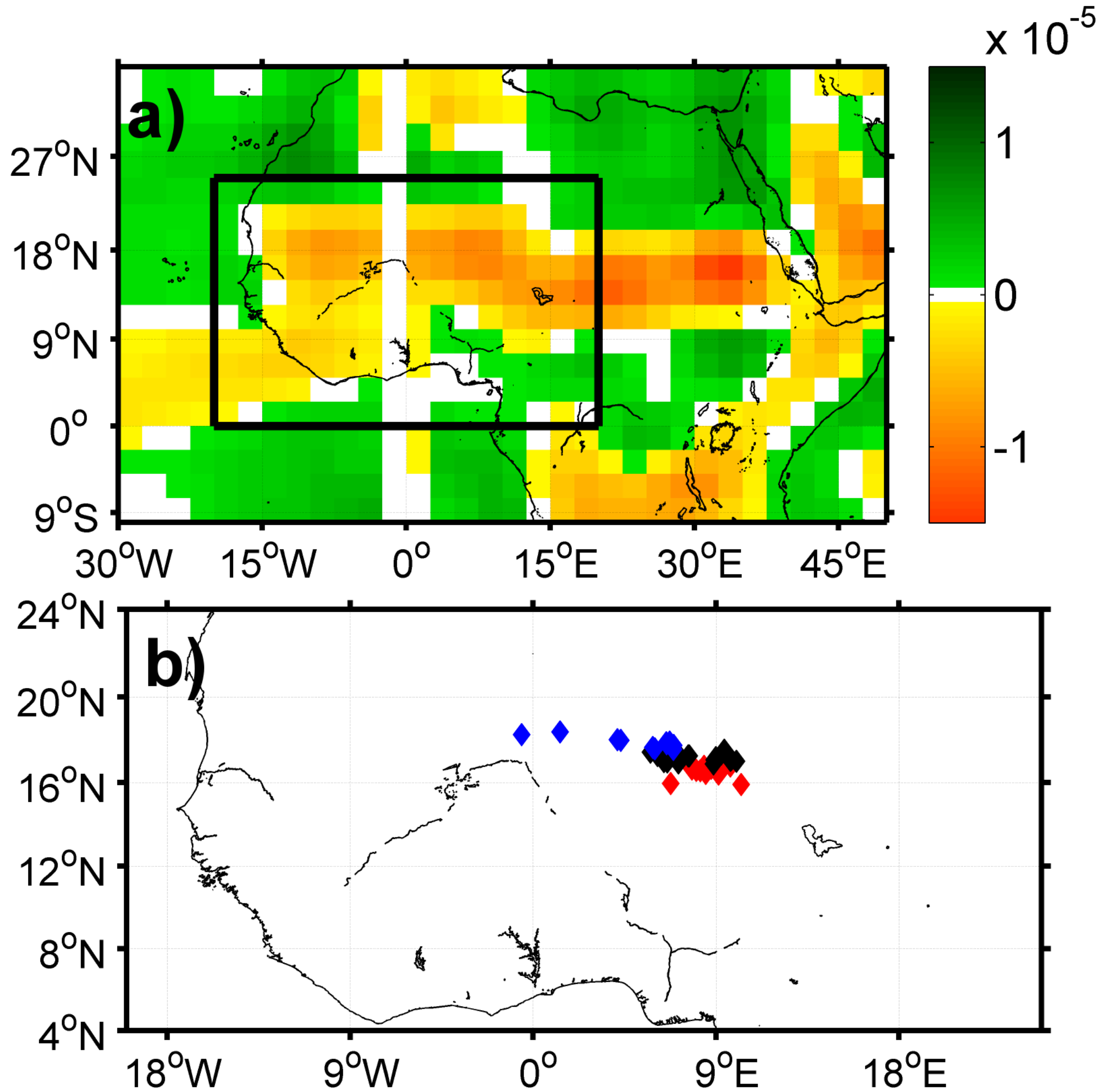

Figure 3.1: (a) Mean summer (JJAS) divergence (s^{-1}) at 925 hPa as computed from NCEP Reanalysis winds. The box over which the WACZ COA is computed is outlined in black. (b) Location of seasonal summer (JJAS) mean of WACZ COA over the period 1965 to 2003. Blue diamonds represent the northern (q75) phase of WACZ COA, red diamonds represent southern (q25) phase of WACZ COA. The lowest quartile (q25) of seasonal data is identified as the "south phase", which corresponds to the seasons when the WACZ was in a southerly position. The highest quartile (q75) of seasonal data is identified as the "north phase", which corresponds to the seasons when the WACZ was in a northerly position. Black diamonds represent the middle 50 percent seasons of WACZ COA.

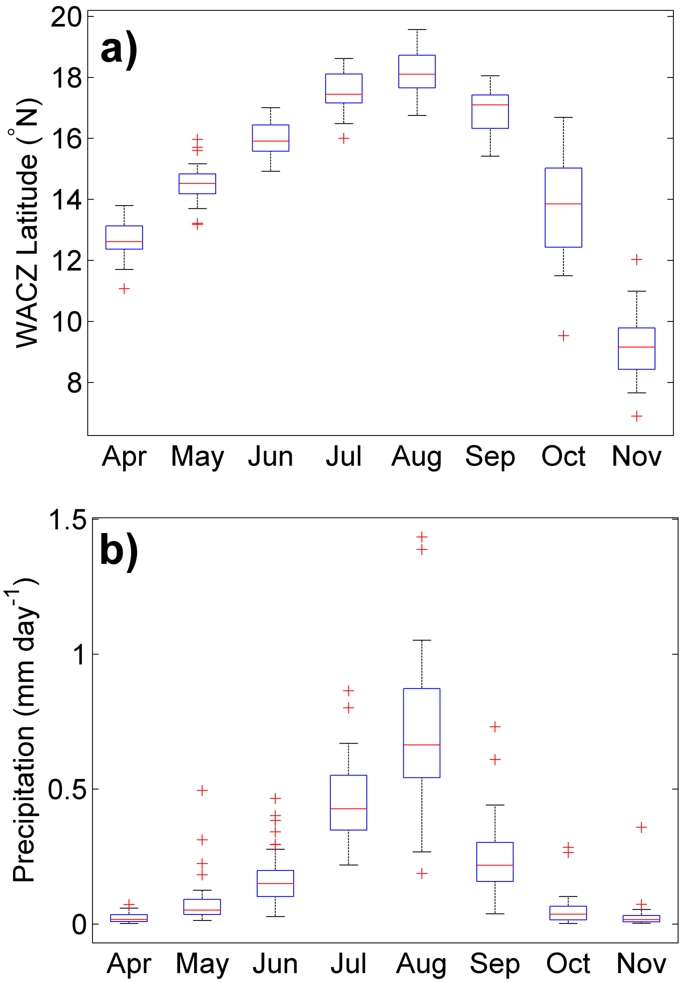

Figure 3.2: Box-plot of monthly of the WACZ Latitude index (W_ϕ, top) and precipitation over the Sahel (15° N to 25° N and 0° to 25° E) from GPCP (bottom) for the summer season of June, July, August, September and adjacent months over the period of 1979 to 2010. Median value indicated by a horizontal red bar, edges of the central box represent the 25th and 75th percentiles. Whiskers denote the spread of all non-outlying data. Outliers are indicated with red crosses.

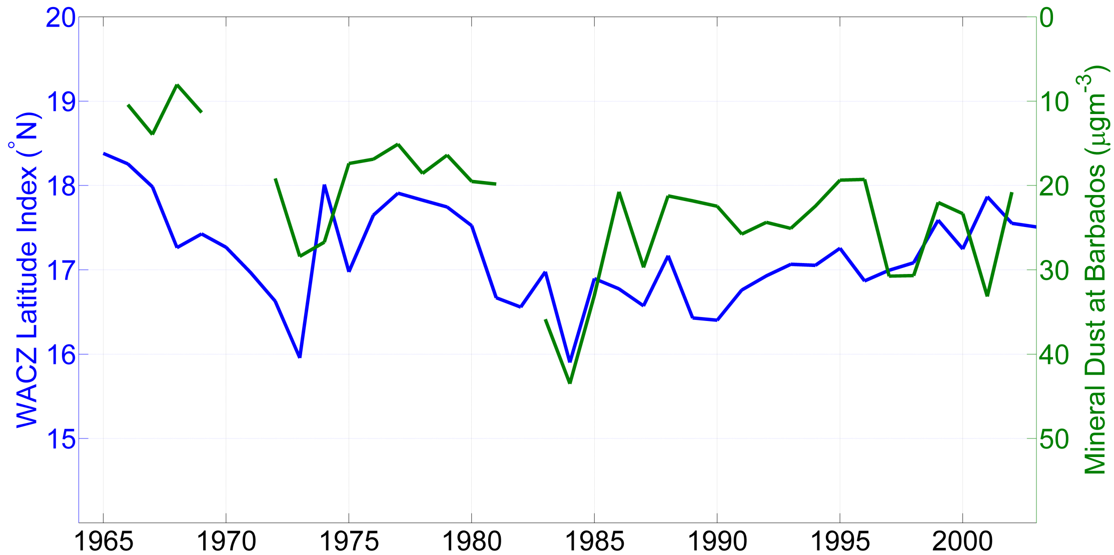

Figure 3.3: Time-series of JJAS seasonal WACZ Latitude index (W_ϕ, blue) and mineral dust concentration at Barbados (green) over the period 1965 to 2003. Seasons in which a month or more of data is missing are ignored.

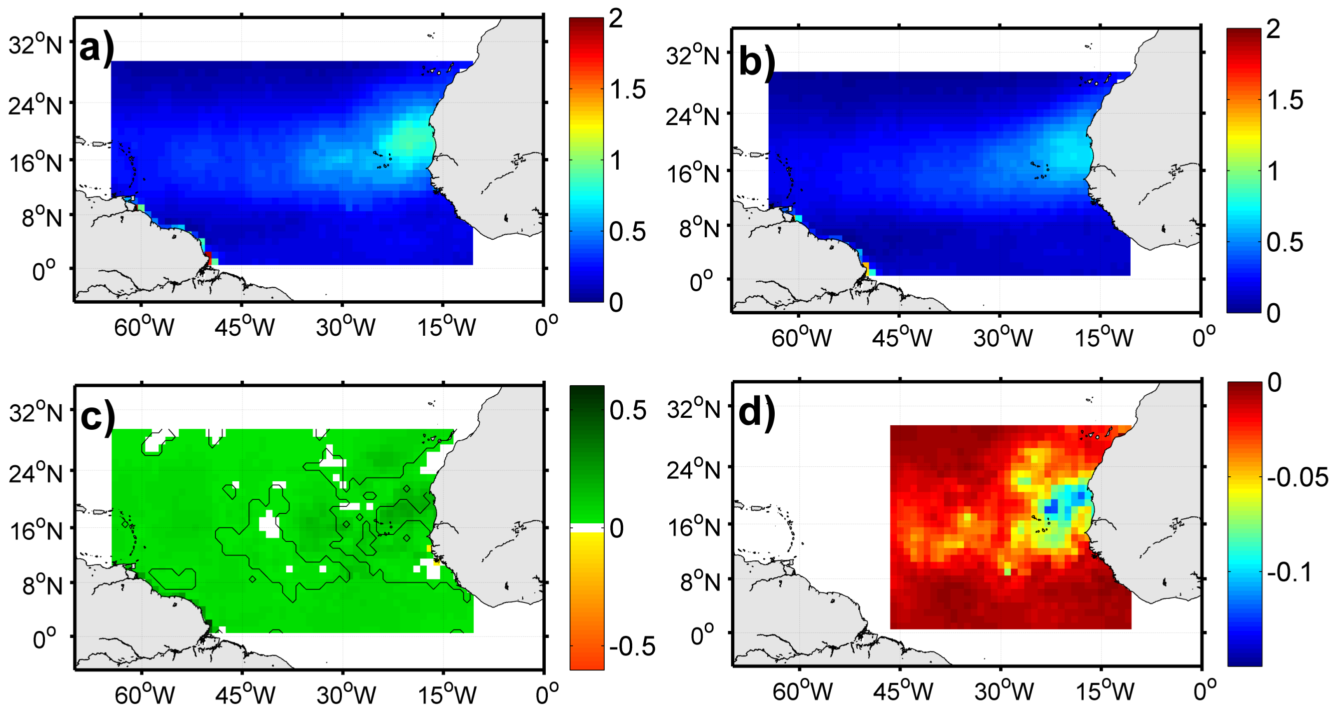

Figure 3.4: (a) Composite mean of Evan AOT for the southernmost summer (JJAS) seasons (25th percentile) of the WACZ. (b) As in (a) but for the northernmost WACZ latitude (75th percentile) summer (JJAS) seasons. (c) The difference (a) minus (b), i.e. conditions of the WACZ latitude index for which dust load is maximized at Barbados. (d) First EOF mode of Evan AOT summer means, which explains 36% of total variance in the Evan AOT record. All composites and principle components are calculated over the period 1982 to 2010.

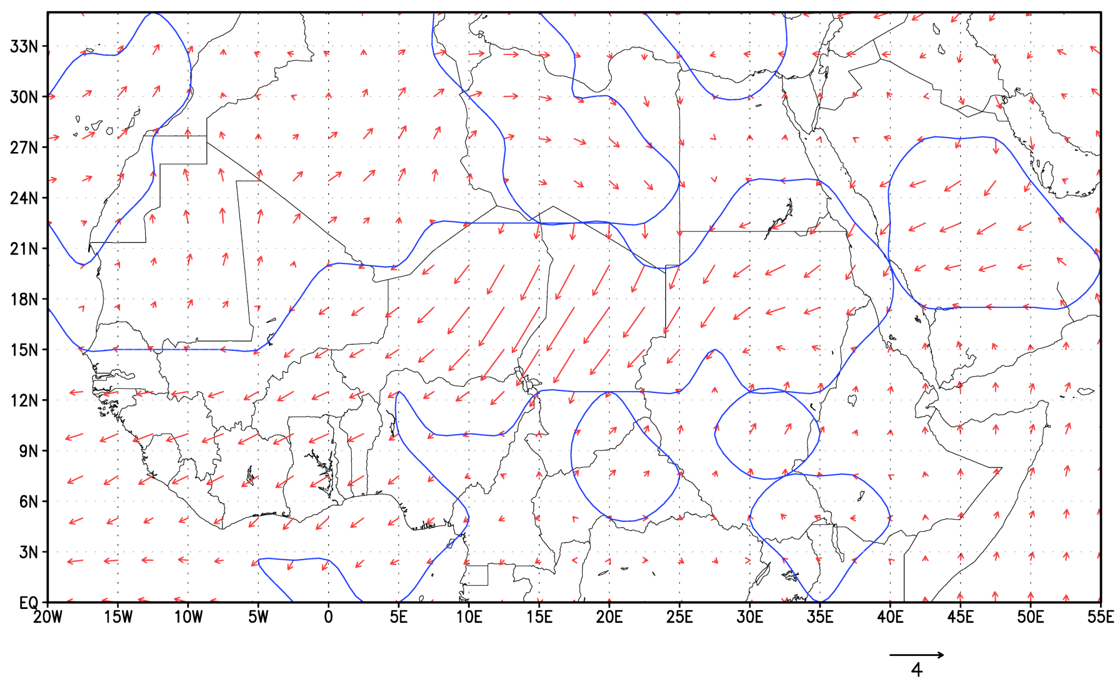

Figure 3.5: Difference in composite mean of NCEP Reanalysis winds (ms^{-1}) at 925 hPa. Differences are calculated by subtracting the seasonal summer mean (JJAS) of the northern most WACZ seasons (75th percentile) from the seasonal summer mean (JJAS) of southern most WACZ seasons (25th percentile). The difference represents the conditions of the WACZ latitude index for which dust is maximized at Barbados. All composites are calculated over the period 1965 to 2003; blue contour represent a significant difference at 10%.

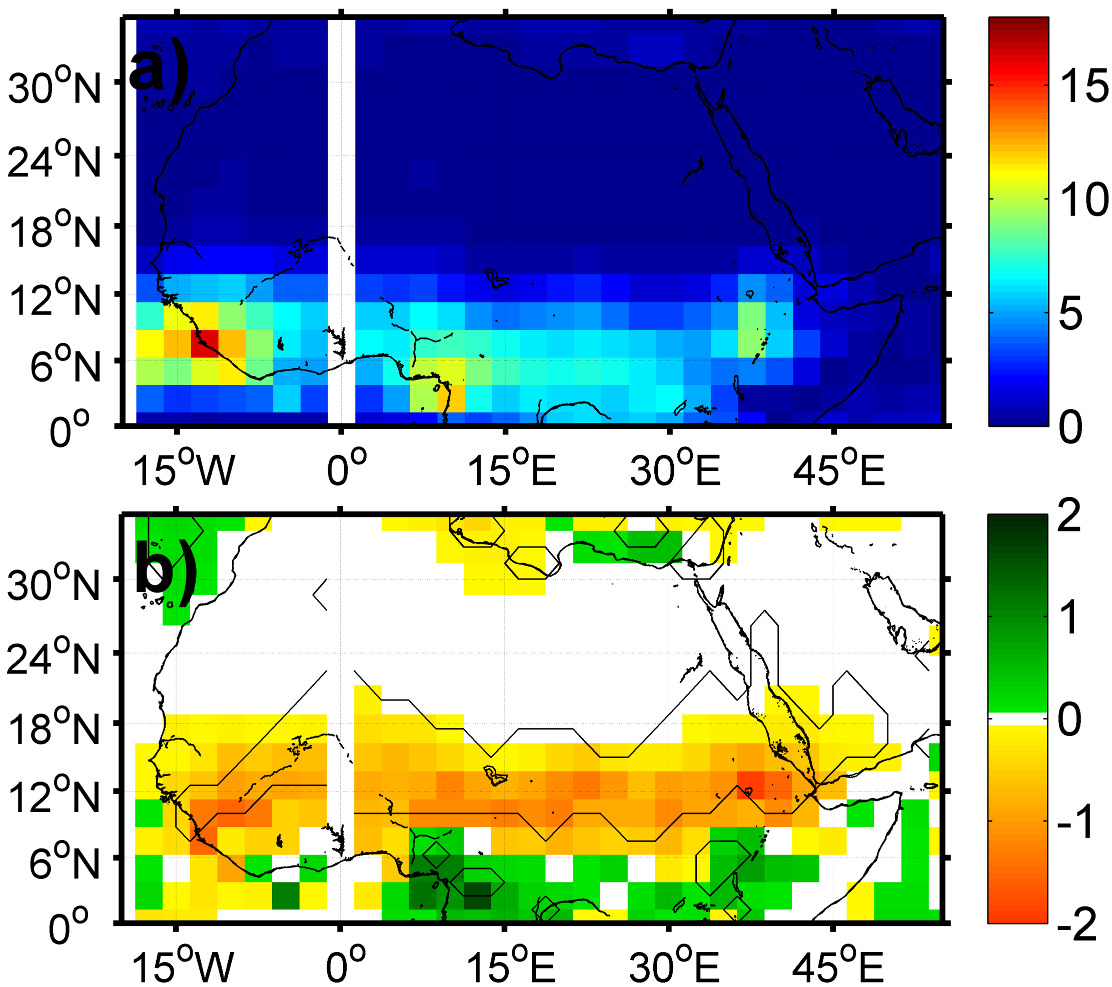

Figure 3.6: (a) Composite mean JJAS precipitation during the southernmost latitude years of the WACZ (q25). (b) Difference in composite mean of GPCP precipitation. Differences are calculated by subtracting the seasonal summer mean (JJAS) of the northern most WACZ seasons (75th percentile) from the seasonal summer mean (JJAS) of southern most WACZ seasons (25th percentile). The difference represents the conditions of the WACZ latitude index for which dust is maximized at Barbados. Units are mm day^{-1} from GPCP. All composites calculated over the period 1979 to 2003, black contour represent a significant difference at 10%.

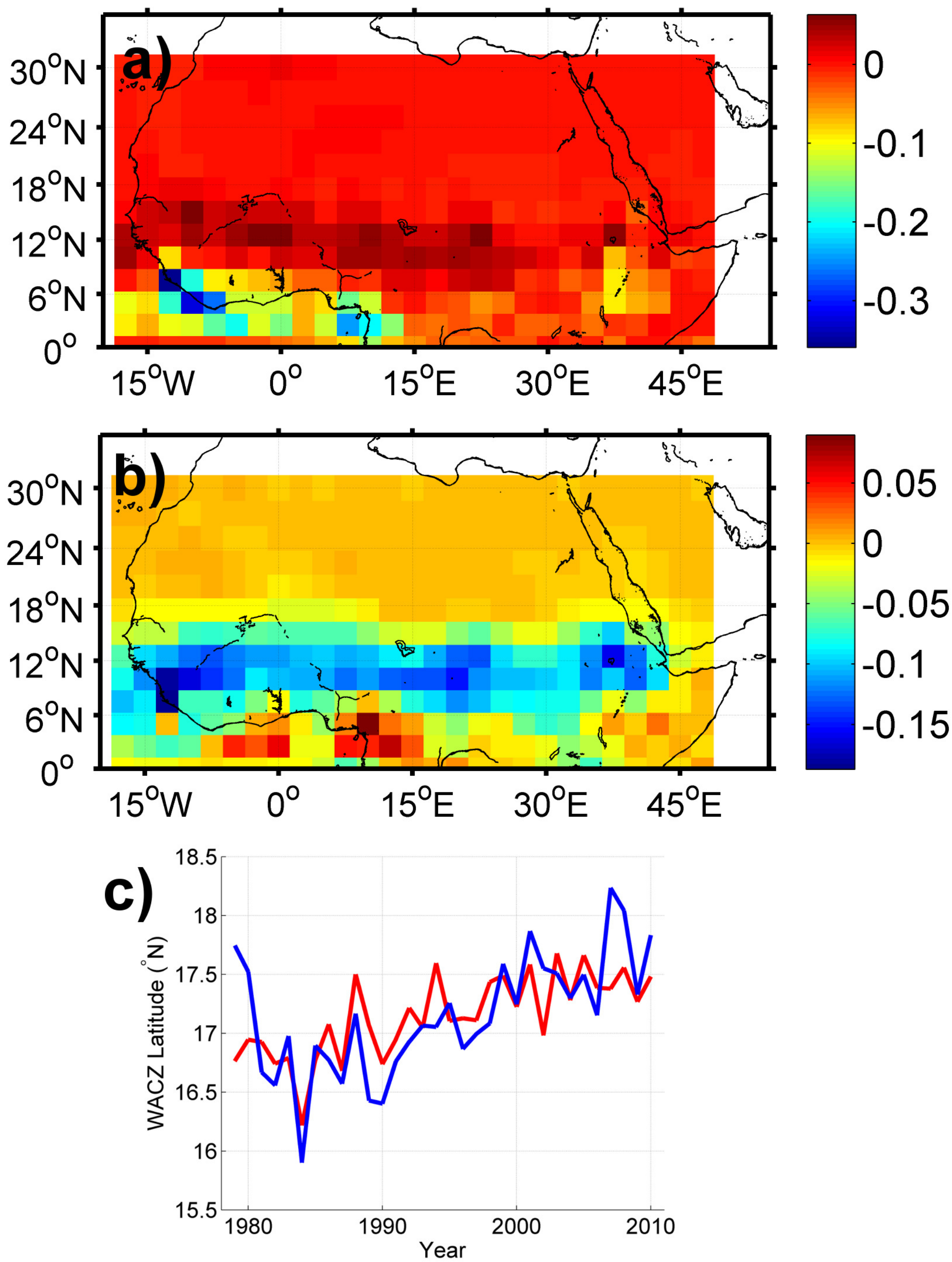

Figure 3.7: (a) First EOF mode of GPCP seasonal JJAS precipitation over the period 1979-2010, mode one explains 42% of total GPCP variance. (b) As in (a) but for second mode of GPCP precipitation, which explains 12% of total GPCP variance. (c) Linear regression of the principle component of the first two modes (red line) onto the WACZ latitude index (W_ϕ, blue line).

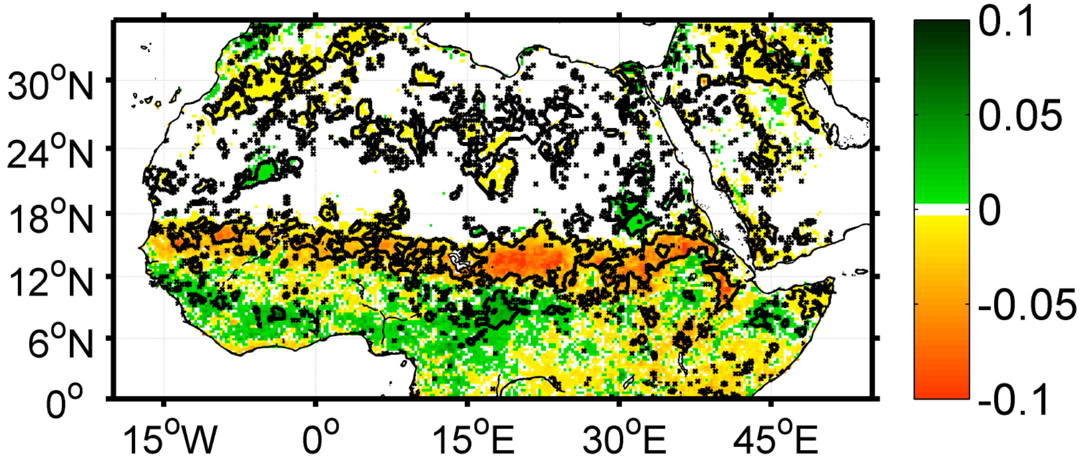

Figure 3.8: Difference in composite mean of GIMMS Normalized Difference Vegetation Index (NDVI). Differences are calculated by subtracting the seasonal JJAS mean of the northern most WACZ seasons (75th percentile) from the seasonal JJAS mean southern most WACZ seasons (25th percentile). The difference represents the conditions of the WACZ latitude index for which dust is maximized at Barbados. The NDVI is positive when more vegetation is present than the long-term mean and negative when there is less vegetation than the long-term mean. Composite difference calculated over the period 1982 to 2002. Black contour represent a significant difference at 10%.

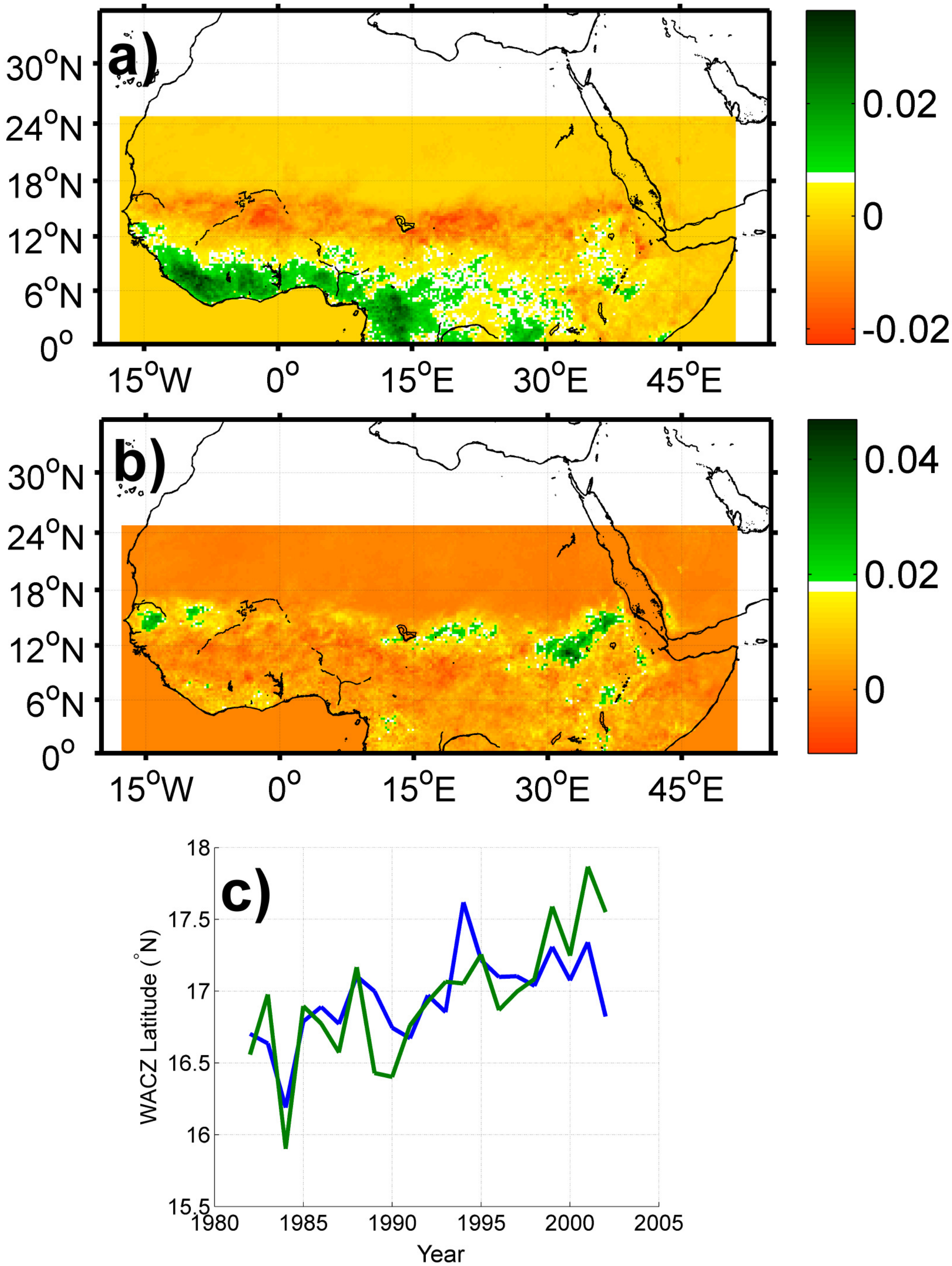

Figure 3.9: (a) First EOF mode of NDVI seasonal JJAS mean over the period 1979-2010, mode one explains 39% of total NDVI variance. (b) As in (a) but for second mode of NDVI, which explains 12% of total NDVI variance. (c) Linear regression of the principle component of the first two modes (green line) onto the WACZ latitude index (W_ϕ, blue line).

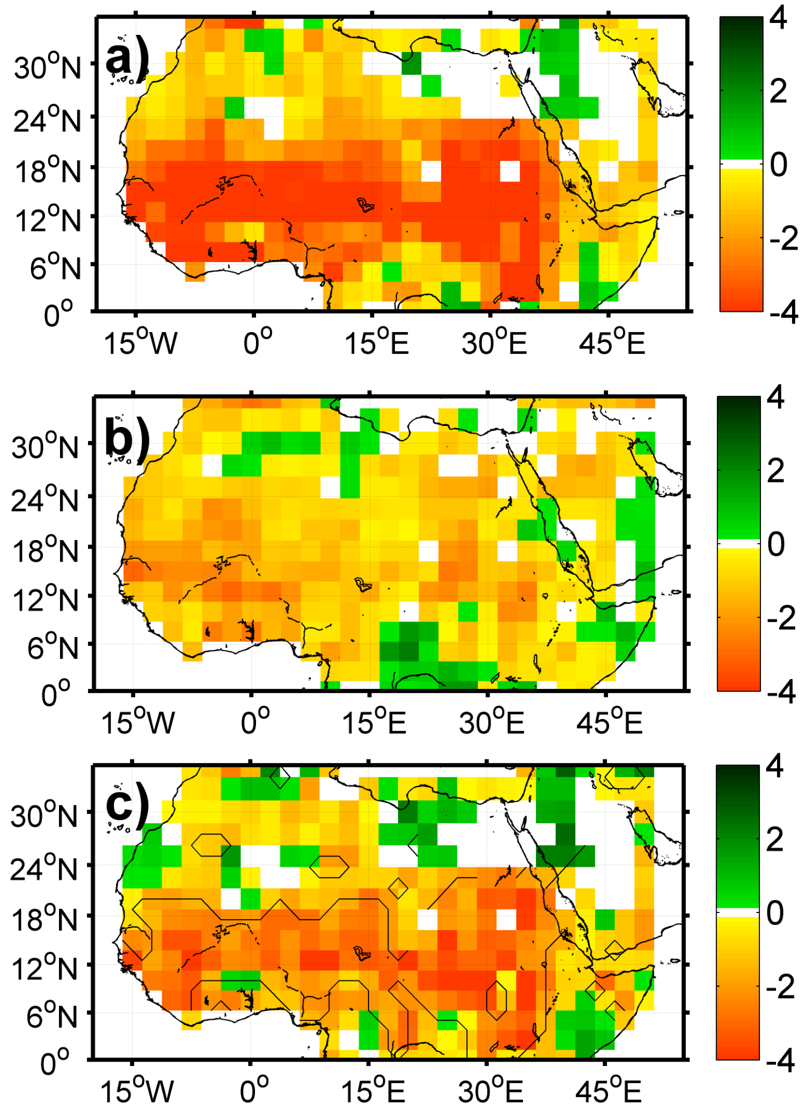

Figure 3.10: (a) Composite mean of Palmer Drought Severity Index for south mode of WACZ (q25). (b) As in (a) but for north mode of WACZ (q75). (c) Composite difference of south mode - north mode. Differences are calculated by subtracting the seasonal summer mean (JJAS) of the northern most WACZ seasons (75th percentile) from the seasonal summer mean (JJAS) of southern most WACZ seasons (25th percentile). The Palmer Drought Severity Index is negative during drought conditions. The difference represents the conditions of the WACZ latitude index for which dust is maximized at Barbados. All composites calculated over the period 1965 to 2003. Black contour represent a significant difference at 10%.

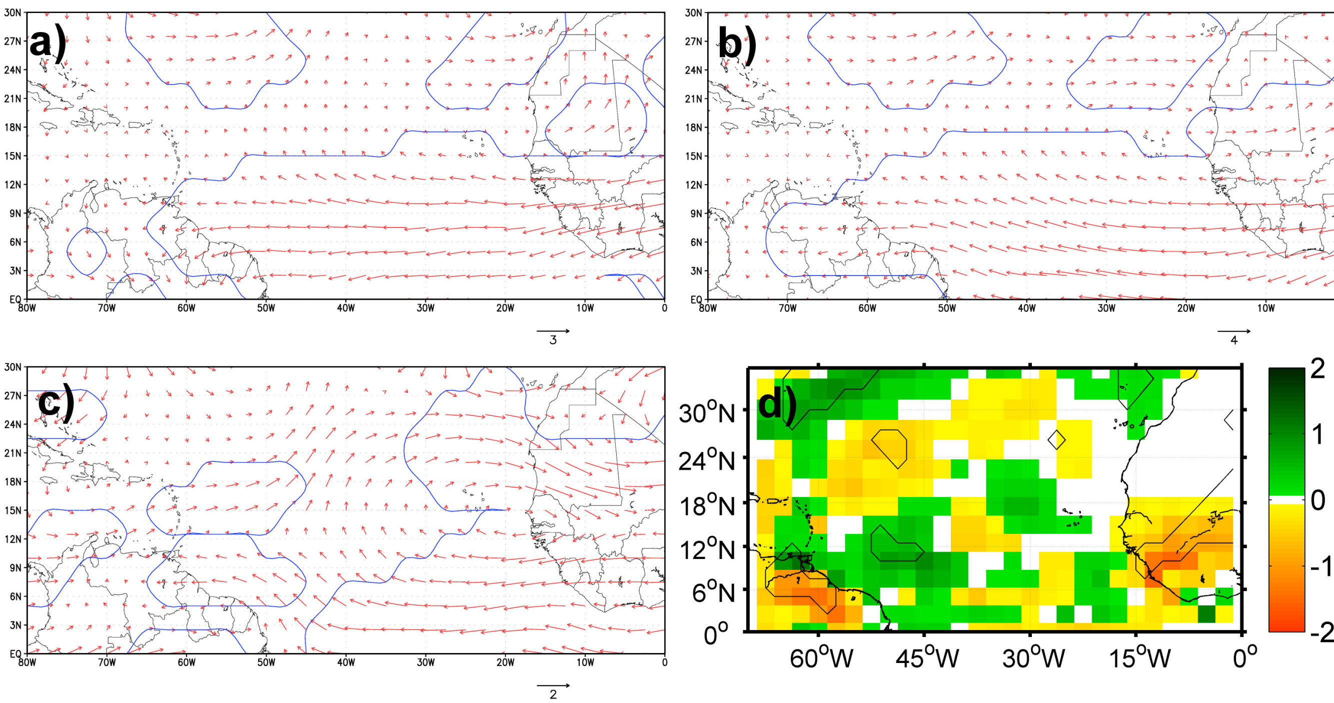

Figure 3.11: Difference in composite mean of NCEP Reanalysis winds at (a) 850 hPa, (b) 700 hPa and (c) 500 hPa. Differences are calculated by subtracting the seasonal summer mean (JJAS) of the northern most WACZ seasons (75th percentile) from the seasonal summer mean (JJAS) of southern most WACZ seasons (25th percentile). The difference represents the conditions of the WACZ latitude index for which dust is maximized at Barbados. Wind composites are calculated over the period 1965 to 2003; blue contour represent a significant difference at 10%. (d) Difference in composite mean of GPCP precipitation. Differences are calculated by subtracting the seasonal summer mean (JJAS) of the northern most WACZ seasons (75th percentile) from the seasonal summer mean (JJAS) of southern most WACZ seasons (25th percentile). Units are mm day^{-1} from GPCP. Precipitation composites calculated over the period 1979 to 2003.

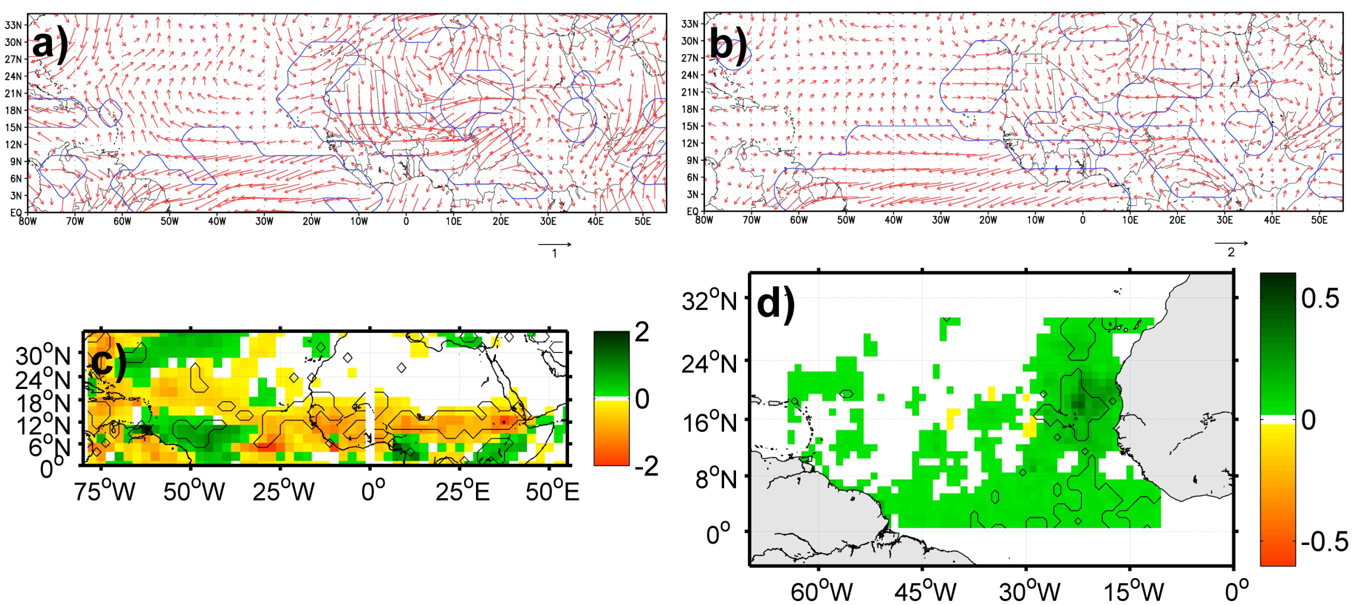

Figure 3.12: Composite mean of difference of JJAS seasonal means from weak intensity (q25) WACZ seasons minus strong intensity (q75) WACZ seasons. Difference in wind (ms^{-1}) (a) 925 hPa and (b) 850 hPa over the period 1965 to 2003. (c) Difference in precipitation ($mmday^{-1}$) from 1979 to 2003. (d) Difference in AVHRR AOT over the period 1982 to 2003 .

Chapter 4

Latitudinal Position of the Intertropical Convergence Zone over West Africa: A Comparative Study in Reanalysis and Global Climate Models of the 20th Century

4.1 Introduction

The importance of the position of the Intertropical Convergence Zone (ITCZ) over West Africa in controlling dust emission and transport has been established for both winter and summer in previous chapters. Additionally the ITCZ and West African Monsoon circulation has been shown elsewhere [*Diedhiou et al.*, 1999; *Hsieh and Cook*, 2005; *Jenkins et al.*, 2005; *Nicholson*, 2008; *Sylla et al.*, 2010], to be of critical importance in determining precipitation patterns in drought-sensitive regions in sub-Saharan Africa. Motivated to consider how the position of the ITCZ may change as the Earth's climate warms in the coming century, here we first assess general circulation models (GCM) hindcasts of the 20th century. As the latitude of the ITCZ has been shown to be of critical importance our analysis focuses on this metric.

Accurately predicting year-to-year and decade-to-decade variability of the position and intensity of the ITCZ over West Africa remains a computational challenge [*Sylla et al.*, 2011]. The structure of the ITCZ and West African Monsoon is directly impacted by vigorous convection which varies in size and scale from individual cells (micro-scale) to well organized convective clusters such as African Easterly Waves (synoptic scale) [*Redelsperger et al.*, 2002]. Global climate models used in this study vary in resolution as coarse as 4° or 400km to as fine as 1° or 100km both of which are insufficient to resolve small scale convection. Additionally global climate models may not have the temporal resolution necessary to initiate and sustain physically reasonable convection. Variability of the ITCZ over West Africa has been linked to SST changes in far away ocean basins including the North and South Atlantic, Mediterranean and Indian Oceans[*Giannini et al.*, 2003]. The ability of climate models to accurately predict such SST changes is also limited. Furthermore land-surface changes and aerosol loading (including dust) have been shown to impact the circulation of West Africa [*Kim et al.*, 2010; *Wilcox et al.*, 2010], again providing a significant forecast challenge for climate models. Evaluation of convectively driven systems over West Africa has been performed in reanalysis [*Diedhiou et al.*, 1999; *Ruti and DellAquila*, 2010] and in regional climate models [*Sylla et al.*, 2010, 2011], but the ability of GCM's to represent these systems has not yet been demonstrated.

Before we focus our attention on GCM projections for the 21st century climate, we first determine if the models are able to predict the known position and strength of the ITCZ over West Africa in the 20th century. This assessment is the focus of this chapter. To assess model quality we compare model output from the Atmospheric Model Intercomparison Project (AMIP) [*Gates*, 1992] scenario from 11 individual models to reanalysis products from the 20th century. In the AMIP scenario GCMs are constrained by realistic observations of sea surface temperature and sea ice coverage. In each model run the atmosphere is able to respond freely to these oceanographic constraints. AMIP scenario data is available for each of our eleven models, and is available over the period 1978 to 2002. We compare this model output to NCEP, ERA-40 and ERA Interim reanalysis products which are also available over the 1978 to 2002 period.

The structure of our comparison is as follows. (1) We qualitatively compare the spatial fields of divergence in GCM's to the spatial fields of divergence in reanalysis products. First the difference between GCM divergence output and the median value of three reanalysis products is analyzed to assess model deviations from observations. Secondly we compute and compare the EOF pattern for each GCM divergence output and each reanalysis divergence output. Our qualitative analysis is performed on annual, summer and winter means of divergence. (2) Next we quantify differences betweens models and reanalysis by applying the COA approach, focusing on how well the models are able to reproduce the previously defined WACZ latitude index. A climatological overview using boxplots of latitude and a direct comparison of time-series are made for this purpose. Scalar accuracy measures are then taken, quantifying the mean absolute error of each model and its bias. (3) Last we perform linear regression to assess trends in the WACZ latitude index. To determine the significance of observed trends a resampling technique is used, specifically bootstrapping of residuals.

The utility of looking at multiple GCM models to asses synoptic scale systems is demonstrated in *Sheridan and Lee* [2010]. However analysis using the "Center of Action" approach with GCM is novel, although some work has been done looking at more traditional climate teleconnection indicies such as the NAO. As both the ITCZ over West Africa and the NAO represent spatially variant patterns which are summarized but numerical indicies, we model our approach after work that has been done on the NAO in GCM. *Osborn et al.* [1999] separated analysis into two sections, a more qualtitative analysis of spatial variability and a quantitative analysis of the derived climate index. Here we follow this approach and divide this study in a similar manner. Following after *Osborn et al.* [1999] we use EOF analysis as the focus of our spatial analysis. Multiple studies of the NAO in GCM use time-series filtering on the NAO indices to remove noise from the signal [*Osborn et al.*, 1999; *Schoof and Pryor*, 2006; *McKendry et al.*, 2006] however seasonal means of the ITCZ already have most of the noise removed thus filtering is not applied in this work. *Stoner et al.* [2009] looks at both spatial and temporal variability of systems like the NAO and finds that while GCMs are able to recreated the general pattern, their ability to correctly place the system zonally and their ability to replicate the temporal variability is limited. In this work we are able to quantify spatial variability through the "Center of Action" approach. In this way our work demonstrates a simple framework as to how track three-dimensional variability through a simple index.

A complete discussion of the global climate models, the climate model scenarios and the reanalysis products used in this study is provided in Section 4.2: Datasets. We follow this with an explanation of the statistical techniques performed in Section 4.3: Methods. We document and explain the results in Section 4.4: Results. We place the results in the context of mineral dust transport and using these GCM in 21st century scenarios in Section 4.5: Discussion.

4.2 Data

4.2.1 Reanalysis Data

Reanalysis data is used frequently in atmospheric science applications, as it represents the best current effort to represent historical global atmospheric conditions. However reanalysis products are not pure observations or truth, but rather derived from incomplete observations put through data assimilation and alteration in physically realistic computational models of the atmosphere. They contain biases and errors derived from a lack of observations, erroneous observations, imperfect data assimilation techniques and computational limitations

Dee [2012]. The Sahara Desert and sub-Saharan Africa are among the least sampled global land regions, featuring low spatial and temporal density of meteorological observations. As such a larger than average degree of uncertainty exists with respect to atmospheric observations and in turn reanalysis products. To account for potential uncertainty three reanalysis products are used here; NCEP Reanalysis, ERA 40 and ERA Interim. NCEP Reanalysis and ERA 40 have a horizontal resolution of $2.5° \times 2.5°$, and ERA Interim features a slightly higher resolution of $1.5° \times 1.5°$. The reanalysis products are available over the entire record of our comparison (1978 to 2002) with the following exceptions; the ERA Interim record begins in January 1979, and the ERA 40 record ends in August 2002. In either case any month with missing data is ignored in any calculations.

Each reanalysis product has unique strengths and weaknesses. NCEP Reanalysis was one of the first reanalysis products produced and as such has been extensively studied, at the time of this writing the *Kalnay et al.* [1996] reference has been cited nearly 14,000 times. It has been shown that NCEP Reanalysis exhibits reduced spatial and temporal moisture variability particularly over oceans and is less reliable over the Southern Hemisphere [*Simmonds and King*, 2004]. Additionally as an older reanalysis product its data assimilation model is somewhat outdated compared to newer data assimilation products. Two studies have documented potential errors in NCEP Reanalysis over West Africa. *Poccard et al.* [2000] identified a problem in early years of the NCEP Reanalysis in which inexplicable shifts in precipitation occurred over West Africa, particularly prior to 1967. Later similar shifts in geopotential height, temperature, humidity and winds were also observed over West Africa [*Camberlin et al.*, 2001]. These studies concluded that NCEP Reanalysis data over West Africa was unreliable before 1967. This study begins in 1978, during a period in which additional information from remote sensing platforms greatly enhanced information about conditions over data sparse regions such as the Sahel and Sahara. NCEP Reanalysis is used as our primary reanalysis product as it is the most widely used dataset and also because it is the best studied reanalysis product and we are confident that major errors have already been identified.

ERA-40 is the replacement for and extension of the older ERA-15 reanalysis product [*Uppala et al.*, 2005]. ERA-40 was revised to include additional sources of atmospheric data including remote sensing platforms, and has undergone assimilation and model upgrades during the process. ERA-40 has been shown to have a strong positive bias in overproducing tropical precipitation and total column water vapor, which may have direct impacts on the WACZ given that it is a tropical feature impacted by latent heating from precipitation.

ERA Interim is the newest reanalysis product used in this work and as such has the highest spatial resolution. ERA Interim is the next generation of the ERA-40 and has been modified to improve the hydrological cycle problems in ERA-40. However *Dee et al.* [2011] suggest that precipitation, particularly over oceans, has been shifted as a result of problems with satellite assimilation.

Realizing that each reanalysis product is imperfect, we frequently calculate the median monthly values and compare the renalysis products amongst themselves as well as to output from climate models to this median value to assess error. Here we note that the median of the reanalysis product is not perfect, and likely contains errors itself. At present it represents the best available estimate to assess atmospheric conditions, in particular in this case divergence at 925 hPa.

4.2.2 CMIP3 and AMIP

CMIP3 or Climate Model Intercomparision Project 3 is part of the well known Intergovernmental Panel on Climate Chance (IPCC) and the data from this project was utilized in the most recent (Fourth Assessment Report (AR4)) IPCC 2007 report [*Solomon et al.*, 2007]. CMIP3 existed to form a repository for research groups to contribute their climate model results and in turn for climate scientists to access said model results [*Meehl et al.*, 2007]. For ease of inter-comparison each model is forced with the same external conditions, defined as climate scenarios. In this chapter we compare model performance in the AMIP scenario to reanalysis products over the period 1979-2002. In the AMIP scenario ocean surface and sea ice conditions are set to match observations and the atmosphere is allowed to respond to this forcing. As such it is the scenario most easily compared to reanalysis products.

Many models from varied international research groups were submitted for included in the CMIP3 project. In this work models were only included if they were run for the 20th century comparison scenario AMIP and future scenarios SRESA1B and SRESB1. Models were excluded if they did not contain projections for the entirety of the 21st century or if they did not provide u and v component winds at 925 hPa. For this reason the number of models for inclusion in this work was limited to eleven. Full details of each model included in this work are contained in Table 4.1. Years included in the AMIP comparison scenario vary from model to model, and any season or year containing missing data is excluded from the analysis. Here we note that the version of the UKMO GCM used in the AMIP and SRESA1B was altered slightly for the SRESB1 scenario and thus omitted. For each model used and selected u and v wind components were extracted and analyzed in the same way as reanalysis products, as described in Section 4.3.

4.3 Methods

4.3.1 Calculation of Divergence

As in previous chapters divergence is used as a references field for assessing the WACZ. Divergence is calculated locally from the horizontal wind (u and v) components at 925 hPa. Divergence is calculated following *Holton and Staley* [1996].

$$\nabla \cdot \hat{V}_{925} = \frac{1}{r\cos\phi}\left(\frac{\partial u}{\partial \lambda} + \frac{v\cos\phi}{\partial \phi}\right) \tag{4.1}$$

Here ∇ is the gradient operator $(\frac{\partial}{\partial x} + \frac{\partial}{\partial y})$, $\hat{V}_{925}$ is the wind at 925 hPa height, u is the meridional component of the wind, v is the zonal component of the wind, r is the radius of the Earth, ϕ is the latitude and λ is the longitude.

4.3.2 Center of Action Approach

To quantify the location and strength of the WACZ the "Center of Action" (COA) approach is applied to GCM and reanalysis divergence fields. The Center of Action is fully described in prior chapters, the same technique is used with only minor changes. For simplicity and ease of comparison a T_{h} of -5×10^{-6} s^{-1} is used for all seasons, and the domain over which the COA is calculated is set to 0 to 25 °N and −20 °W to 20 °E.

4.3.3 Statistical Approaches

To quantify how well model predictions match with observations we define two statistical metrics; mean absolute error (MAE) and bias (B) [*Wilks*, 1995]. MAE determines the average absolute deviation from observation, and B notes the direction of the deviation. The specific equations follow:

$$\mathrm{MAE} = \frac{1}{n}\sum_{k=1}^{n} \|y_k - o_k\|. \tag{4.2}$$

$$\mathrm{B} = \frac{1}{n}\sum_{k=1}^{n}(y_k - o_k). \tag{4.3}$$

Here n represents the number of samples, y is the model or reanalysis value and o is the observation value. When calculating mean absolute error and bias we consider the median value of the reanalysis products to be the observation.

4.3.4 Bootstrapping for Trends

Linear trend analysis is a statistical method for determining rates of change in time-series that is ubiquitously applied in atmospheric science. However a simple linear trend analysis can be misleading. Linear trend analysis is not robust nor resistant, as it requires a time-series to be linear and is sensitive to outliers, particularly at the start or end of the time-series. To reduce the potential impacts of outliers here we apply a bootstrap, a common resampling technique, to assess the uncertainty of observed trends.

Resampling represents an alternative to more traditional frequentist or non-parametric testing[*Wilks*, 1995]. In a traditional frequentist approach a statistical test, such as linear regression, is applied and a test statistic is produced. This test statistic is then compared to an idealized distribution to assess how significant the test result is. For example a correlation coefficient obtained from a Pearson-product moment test is then compared to a distribution based on sample size to determine the correlations significance. With a resampling technique such as the bootstrap analysis used here an observation (or model output) is perturbed a large number of times ($n = 100,000$) to reflect uncertainty in the observation and the statistical test is performed once for each resampling. Instead of comparing the results to a hypothetical distribution the results of each of the 100,000 tests are used to determine significance.

In this way resampling can be used to account for uncertainty in observations and accounts for outliers. We note that in this application the requirement that data be linear is not addressed by the resampling method, meaning the linearity assumption for regression still holds. For this analysis we resampled each reanalysis product and model 100,000 times using the data's internal variability. Each statistical test was also performed 100,000 times, and the results summarized in Section 4.4.

4.4 Results

Next we focus on how well the climate models are able to reproduce divergence patterns at 925 hPa over the period 1978 to 2002. We begin with a qualitative assessment of similarity between model output divergence and reanalysis, examining differences in long-term means for assessing central tendency and empirical orthogonal function (EOF) loading patterns for assessment of variance.

4.4.1 Qualitative Analysis of Divergence Spatial Pattern

Annual

On an annual basis the south (near equator) to north (near 16° to 18° N) seasonal migration of the WACZ from winter to summer is the dominant feature as shown in Figure 4.1. All three reanalysis products show a dipole-like feature over West Africa, with a positive mode centered between 16° and 20° N and a negative mode centered between 6° and 10° N. This dipole feature suggests that convergence and divergence are coupled in this region, with convergence associated with the WACZ and divergence of an opposing magnitude in the opposite season. For example in winter between 6° and 10° N divergence is occurring concurrently with convergence 16° and 20° N, and vice versa in summer. This annual oscillation, or the south to north migration of the WACZ is well established in the literature as well as reanalysis products and the primary source of variability that a GCM must be able to reproduce in order to be considered successful.

As seen in Figure 4.1 models had varying success replicating the EOF pattern observed in reanalysis. Each model, most generally speaking, was able to identify a north-south movement of the WACZ, however the location of the oscillation and its magnitude often differed from reanalysis. The relative magnitude of the dipole pattern tells us what fraction of the total variance in divergence over Africa is associated with the annual migration of the WACZ. For example, if a model produced a lower value of relative magnitude in the dipole structure than reanalysis this would indicate that less of the total variance of divergence is controlled by the annual south to north migration of the WACZ and more of the variance is controlled by shorter term variability (either synoptic or meso- scale disturbances) or locally, topographically induced divergence.

The three reanalysis products Figure 4.1a–c exhibit nearly identical spatial loading patterns. Some differences are evident in relative magnitude; NCEP and ERA-40 have nearly the same relative magnitude while ERA Interim produces a weaker EOF pattern. Spatially NCEP is nearly evenly distributed east to west, while both ERA 40 and ERA Interim show a slightly stronger response in east Africa.

The models (Figure 4.1d–n) were successful identifying the dipole associated with south to north migration of the WACZ. CCSM (Figure 4.1d) and GISS (Figure 4.1g) least resemble the reanalysis products with both models showing asymmetric and longitudinally offset dipole patterns. However all models do at a base level identify a positive north phase and a negative south phase. Most models had relative magnitudes of similar values to reanalysis products, however both CCSM (Figure 4.1d) and MIROC-h (Figure 4.1j) show weaker relative magnitudes than reanalysis, and GISS (Figure 4.1g) shows a higher relative magnitude than reanalysis. We hypothesize that this is related to resolution (see Table 4.1 for resolution details) as both CCSM and MIROC-h feature a higher resolution than ERA-40 and NCEP, while GISS has a significantly lower resolution than all reanalysis products. A model with coarser resolution would be unable to resolve local weather and climate features so larger scale patterns like the annual migration of the WACZ would control a larger fraction of variance, and thus a larger relative magnitude. We note the higher resolution models featured relative magnitudes closer to the higher resolution reanalysis product, ERA-Interim (Figure 4.1c).

Next we shift from looking at how well the models are able to replicate variability of divergence to how well they are able to recreate the mean state of divergence. To assess this, median monthly values of reanalysis products were calculated and then averaged annually. This quantity was then subtracted from each model's annual mean and the differences averaged and plotted in Figure 4.2. The individual reanalysis products (Figures 4.2a–c) show very small differences from the median of reanalysis products. NCEP shows a northward movement of the ITCZ relative to the two other reanalyses, as well as more convergence in West Africa than the median of reanalysis products. ERA-40 most closely resembles the median of reanalysis products. Small-scale effects, some likely driven by topography are evident in the ERA Interim which shows the largest difference from the median of reanalysis products.

Most models differ appreciably from the median of reanalysis products. CCSM, GFDL, MIROC hres and UKMO (Figure 4.2c,f,j,n) all feature topographic discrepancies similar to ERA Interim, but generally with greater deviations from the median reanalysis. Two models, MRI and UKMO (Figure 4.2m–n), displayed a northward bias (divergence north of the median of reanalysis) while the CCSM (Figure 4.2d) displayed a southward bias. Models in general underrepresented the quantity of divergence associated with the WACZ including CNRM, GFDL, IAP, IPSL, MIROCm (Figure 4.2e,f,h,i,j) with only the UKMO (Figure 4.2n) producing larger divergence than the median of reanalysis products. We note that nearly all models, even those which are too weak generally show greater divergence over coastal Kenya than reanalysis products. Overall we find that many models have a geographical bias either in latitude or longitude in their placement of the WACZ and models in general display a weak bias with respect to the intensity of divergence. These biases are quantified in Section 4.44.4.2.

Summer (JJAS)

Next we qualitatively examine how well the models are able to reproduce divergence over West Africa in the summer (JJAS). In contrast to the annual EOF analysis which includes all months and is indicative of the annual migration of the WACZ, this analysis only includes the summer months of JJAS. Here a north to south dipole signal would indicate that the dominant variability in the divergence data is annual differences in which the WACZ is in a "north phase" versus a "south phase". Figure 4.3 shows the first mode of the EOF analysis. In reanalysis Figures (4.3a–c) it appears that the majority of variability occurs over central and east Africa. A north-south pattern emerges around Lake Chad in each of the three reanalysis products.

Models have widely varying loading patterns, many of which do not resemble reanalysis products. CNRM, IAP, MRI and UKMO (Figures 4.3e,h,m,n) all have the dominant pattern settled to the west compared to the reanalysis products. GFDL, GISS, IPSL, MIROC-m, and MPI (Figures 4.3f,g,i,j,l) all show an eastward positioning of the mode of greatest variability, similar to reanalysis but often of with varied latitudinal displacement of the patterns. Lastly CCSM and MIROC-h (Figures 4.3d,k) show an asymmetric pattern that is dissimilar to any of the reanalysis products. We note that this pattern appears to be strongly influenced by topographically generated divergence.

Despite geographic shifts in the loading patterns between models, most models have a similar relative magnitude to reanalysis products. Only the GISS model (Figure 4.3g) was stronger than all reanalysis products, wheras the CCSM and MIROC-h (Figures 4.3d,k) are both significantly weaker than reanalysis products.

Figure 4.4 shows the long term mean of divergence in summer. Each reanalysis product shows an east to west band of divergence between 16° and 18° N, each showing the band drawn further north over West Africa. ERA Interim is most dissimilar to the other two reanalysis products with additional local features evident, likely as a function of the local topography. CCSM and MIROC-h (Figures 4.4d,k) again stand out with neither featuring the expected east to west band of divergence anticipated from reanalysis, rather in both local features dominate the signal, to a larger extent that the ERA Interim product. Other models show the expected band of divergence over West Africa, similar to reanalysis. We note that CNRM, GFDL and IAP (Figures 4.4c,f,h) are each clearly north of the reanalysis products.

To quantify the differences from reanalysis we again calculate the median of summer months of divergence, calculate a seasonal mean of reanalysis products and then subtract reanalysis mean divergence from the model mean, results are shown in Figure 4.5. NCEP reanalysis (Figure 4.5a) shows a NW to SE difference, with more convergence over the Niger River basin and more divergence south of Lake Chad relative to median reanalysis. ERA-40

(Figure 4.5b) shows a similar but weaker W-E dipole between the Niger River and south of Lake Chad, suggesting that again the ERA-Interim is different from the other two reanalysis products.

CCSM and MIROC-hres (Figures 4.5d,k) show significant differences from median reanalysis, again due to topographical influence. Here we confirm the northward bias in CNRM, GFDL and IAP (Figures 4.5c,f,h) as indicated in Figure 4.4. IPSL exhibit a southward bias (Figures 4.5i). While the models closely approximate the intensity of the divergence in reanalysis, GISS, IAP and MPI (Figures 4.5g,h,l) appear to have too little convergence while UKMO (Figure 4.5n) appear to have too much convergence. We again note models overestimate divergence near the Kenyan coast.

Winter (DJFM)

For winter in reanalysis products the first mode of the EOF of divergence is a zonally symmetric dipole focused over west Africa, as seen in Figures 4.6a–c. We note the strongest relative magnitudes associated with this pattern are found in the COA box. The magnitude of the loading pattern is largest in NCEP (Figure 4.6a), followed by decreasing magnitudes in ERA-40 (Figure 4.6b) and the lowest magnitude in ERA Interim (Figure 4.6c). We note the same pattern for latitudinal displacement, NCEP is furthest north, ERA-40 slightly offset to the south, and ERA Interim furthest south.

Few models are able to replicate the first EOF geographic positioning of reanalysis products. CNRM, GISS, IAP, MRI (Figures 4.6e,h,m) locate the first mode too far east relative to reanalysis. GFDL, IPSL, MIROC-m, MPI, UKMO (Figures 4.6f,i,j,l,n) hint at the maximum variability shifting to West Africa, but in general are also located to the east of reanalysis. Figures 4.6d,k again suggest that topography induced divergence plays an important role in the CCSM and MIROC-hres model, but we note that relative to summer in winter topographic influences are reduced as the WACZ moves southward.

Models in general produce similar relative magnitudes to reanalysis products, in particular CNRM, GFDL, IAP, IPSL (Figures 4.6e,f,h,i). We note again that higher resolution models like CCSM and MIROC-h, as well as UKMO have lower relative magnitudes (Figures 4.6 d,k,n). Low resolution models, such as the GISS model (Figure 4.6g) appear to have relative magnitudes greater than reanalysis.

The long term mean of divergence in winter is shown in Figure 4.7. Each of the reanalysis products shows a clear zonal band of divergence between 6° and 12° N. ERA Interim (Figure 4.7c) features a narrower, tighter band closer to the Gulf of Guinea than either NCEP Reanalysis (Figure 4.7a) or ERA-40 (Figure 4.7b). Models appear to do a satisfactory job with the placement of the WACZ, although in general they tend to produce lower values of divergence than reanalysis.

As with summer (in Figure 4.5) for winter we again compute the mean of the difference between median reanalysis and model results in Figure 4.8. NCEP reanalysis (Figure 4.8a) shows a clear northward shift in the WACZ relative to the median of reanalysis products, while ERA Interim (Figure 4.8c) shows a southward shift relative to the median of reanalysis products. ERA-40 (Figure 4.8b) is closest to the median of reanalysis products. We note that differences between individual reanalysis products in winter are larger than those seen in summer (Figure 4.8).

In winter each model has significant differences compared to the median of the reanalysis products. Many models appear to have features consistent with topographically induced discrepancies, e.g. CCSM, GFDL, MIROC hres, UKMO (Figure 4.8d,f,j,n). Latitudinal displacements relative to reanalysis products were observed with models exhibiting both northward (GFDL, MRI and UKMO in Figures 4.8f,m,n) and southward biases (CCSM, CNRM, MIROC (both) in Figures 4.8d,e,j,k). In general many models under represented convergence near to the WACZ, e.g CNRM, IAP, IPSL, MIROC (both), MPI (Figures 4.8e,h,i,j,k,l) while none appear to over represent convergence near to the WACZ. Again as before in summer and for the annual mean each model generates strong divergence near to the coastline of Kenya relative to reanalysis.

To summarize a number of results emerged consistently throughout each season and annually. Both low resolution and high resolution models are markedly different than reanalysis products. The lowest resolution model (GISS) underestimated variability across the domain as a whole and exhibited large differences from reanalysis products in the placement and strength of the WACZ. High resolution models such as the MIROC-hres and CCSM each have more noisy divergence patterns, much of which emerging from topographic features not resolved in reanalysis. All models produce a convergence along the Kenya coastline not seen in any reanalysis product. While individual models can show large biases from season to season, these biases are not necessarily consistent across seasons. As such we need to quantify the bias of each model as a function of season. In the next section we apply the "Center of Action" approach to each model and quantitatively assess each performance.

4.4.2 Quantitative Analysis of WACZ COA Indices

Annual Mean Position of WACZ Latitude

To assess both the temporal and spatial variability of the WACZ latitude W_ϕ here we present boxplots of monthly values of the WACZ latitude in Figure 4.9. Red lines in the center of the box represent the median value, and blue lines above and below represent the 75th and 25th percentiles respectively. Blue lines extending out from the center of the box extend 1.5 times the interquartile range from the median. Outliers are denoted by red plus symbols. Thus boxplots show skewness, spread and central tendency of W_ϕ. A companion statistical summary of Figure 4.9 is shown in Table 4.2. Reanalysis products (Figures 4.9a–c) clearly shows the annual cycle, with a maximum value of W_ϕ in July to August of 16° to 18° N and a minimum value of W_ϕ in December to January of 7° to 9° N. In fall months and to a lesser extent spring months, year-to-year variability is maximized, leading to the largest spread. From January through June W_ϕ undergoes slow and gradual northward migration. In contrast from September through November W_ϕ experiences a very rapid southward transition. The slow and steady northward transition followed by a rapid southward transition leads to an asymmetric temporal migration on an annual basis. Models all capture winter to summer migration observed in reanalysis however subtle, yet important differences emerge. Most models replicate the mean annual position of the WACZ within range of the reanalysis products (8 of 11 in Table 4.2). The MIROC-mres model is nearly 2 degrees south of the reanalysis product, while both GISS and IAP are approximately 1 degree north of the reanalysis products. The majority of models (8 of 11) contain less variance in the latitudinal position of the WACZ than the reanalysis products. The remaining three models (CNRM, GISS and IPSL) exceed reanalysis variance, while no model produced variance within the range of reanalysis variance.

Mean annual conditions are important in assessing the models ability to replicate the movement of the WACZ but to be considered effective the model must also exhibit similar temporal variability compared to observations. Absolute error and bias of the model latitude are calculated relative to the reanalysis latitude. Individual reanalysis latitudes (NCEP, ERA-40, ERA Interim) are significantly correlated with the mean and median of the reanalysis products as shown in Table 4.3, although NCEP and ERA-Interim are not correlated with each other on an annual basis. To simplify the analysis we use the median latitude of the reanalysis to compare to model latitude. To assess the temporal variability of the models we first correlate the model latitude (W_ϕ) to the reanalysis latitude. Although generally the models are able to capture the mean position of the WACZ successfully, the models fail to replicate the change in WACZ with time as in the reanalysis. Only the MIROC-mres shows any skill at replicated in the annual mean position of the WACZ. Here we note that MIROC both qualitatively and quantitatively does a poor job replicating the mean position of the WACZ latitude compared to other models, so this result is surprising. MRI and CCSM show anti-correlation with reanalysis products.

The fact that 10 of 11 models cannot replicate the annual position of the WACZ latitude (Table 4.2) suggests that the models are missing a key component of internal variability needed to accurately predict the mean location on an annual basis, although they do show some skill in replicating the WACZ latitudes' long term mean position.

Mean Summer (JJAS) Position of WACZ Latitude

Figure 4.10 shows the position of the WACZ as determined by the latitude and longitude index of the WACZ COA. Table 4.5 presents statistics summarizing W_ϕ in summer, which are supported with bias and error statistics in Table 4.7. Each reanalysis product places the WACZ north and east of the bend in the Niger River. ERA-40 (Figure 4.10b) appears to be the furthest south of the three reanalysis products, and ERA Interim (Figure 4.10c) is furthest north. NCEP Reanalysis (Figure 4.10a) shows extensive longitudinal variability. Models place the WACZ with varying degrees of success. IAP, MIROC-hres and UKMO (Figure 4.10h,k,n) are tightly clustered, suggesting less variability than reanalysis. CNRM and GFDL (Figure 4.10e–f) each appear to have more scatter than reanalysis.

Most models are close to the reanalysis position while only one model was north of all reanalysis products (GISS) and only two models were found south of all reanalysis products (MIROC-mres and UKMO). A majority of models in Table 4.5 (9 of 11) display less variance in the latitudinal position of the WACZ than the median of reanalysis products, while the CNRM experienced significantly more variance than the median of reanalysis. Only the GISS produced a variance consistent with reanalysis products. The time-series of all W_ϕ are shown in Figure 4.11, and the correlation between the median of reanalysis and each model and reanalysis product W_ϕ are shown in Table 4.6. Visual inspection of the Figure 4.11 suggests limited temporal coherence between models and reanalysis. No model shows significant correlation with the median of reanalysis. Again we note models are unable to replicate the temporal variability observed in reanalysis during the summer.

Mean Winter (DJFM) Position of WACZ Latitude

In winter the WACZ COA in reanalysis tends to be clustered near the intersection of the Niger and Benue Rivers as seen in Figures 4.12a–c. Differences in position between the reanalysis products are smaller in winter compared to summer. This is confirmed in Table 4.8 which shows the median and interquartile range of reanalysis products are similar in winter. In general models place the winter WACZ COA near to reanalysis products, although again we note some models (CCSM, MIROC-hres and UKMO; Figures 4.12d,k,n) appear tightly cluster compared to reanalysis and others (MRI and MPI; Figures 4.12l–m) appear too scattered relative to reanalysis. We note in Table 4.8 that for 5 of 11 models (CCSM, GFDL, IAP, MIROC-hres, UKMO) the median W_ϕ positions were north of all reanalysis products, and for 3 of 11 models (CNRM, MIROC-mres, MPI) median W_ϕ were south of all reanalysis products. Models tended to exhibit a larger latitudinal spread than reanalysis with 5 of 11 models (CNRM, GISS, IAP, MPI, MRI) having a larger interquartile range (IQR) than all reanalysis products and only the CCSM model having less spread than reanalysis.

Figure 4.13 shows the timeseries of reanalysis products and models for W_ϕ. Reanalysis products (bold lines) covary tightly in time, as shown by high correlation co-efficients in Table 4.9. We note more agreement in winter between reanalysis than in summer (Table 4.6), which is reflected in bias and mean absolute error calculations as well (Table 4.10). Models are largely unable to reproduce the temporal variability seen in the reanalysis with only IAP and MIROC-hres significantly correlated with reanalysis. 9 of 11 models show no significant correlation with reanalysis products.

Despite differences in model physics, data assimilation techniques, observations and resolution the reanalysis products are qualitatively similar in their handling of the divergence of the WACZ, although minor differences emerge. Models show a mixed ability to replicate the central tendency and spread of reanalysis products, with models doing better in winter and showing larger differences in summer. No model is able to replicate the temporal variability of reanalysis. As the climate warms the Hadley cell is expected to drift northward [*Gastineau et al.*, 2008], and with it perhaps the WACZ. In the next section we assess the trend in reanalysis and CMIP models.

4.4.3 Trend Analysis of WACZ Latitude

In this section we apply bootstrapping to linear trend analysis of our COA data. To summarize the results we present four figures. The first figure summarizes the mean (x-axis) and standard deviation (y-axis) of the resampled data. The next two figures assess the trend, first by calculating the linear trend ($^\circ yr^{-1}$) in each resampled set of data and then by calculating the correlation coefficient between the W_ϕ and time for each resampled set of data. Last the probability of a significant trend (p-value) is assessed for each resampled set of data.

Trend in Annual Mean

The mean and standard deviations of resampled annual means are shown in Figure 4.14. Both ERA-40 and ERA Interim show a strong majority of resamplings exhibit a northward annual trend as evident in Figure 4.15. NCEP reanalysis shows a southward trend, with a similarly significant quantity of resamples showing this southward trend. While both ERA-40 and ERA Interim show nearly all resamplings have a positive correlation (northward trend) with time in Figure 4.16, the relationship is not statistically significant for NCEP reanalysis. The model response is also varied in sign. CNRM, GFDL, GISS, MIROC-hres all suggest a possible northward trend (Figure 4.15e–g,k and 4.16e–g,k) while MRI and UKMO (4.15m–n and 4.16m–n) are suggestive of a southward trend. While more reanalysis products and models suggest a northward trend in the annual mean W_ϕ the results are overall inconclusive.

Table 4.11 shows an overview of trend statistics for summer. Interestingly reanalysis products show contradictory evidence of statistically significant northward and southward trends. NCEP Reanalysis shows a southward trend that is statistically significant with a p-value of 0.031. ERA-40 and ERA-Interim show a northward trend that are statistically significant with a p-value of 0.042 and 0.017 respectively (also seen in Figure 4.17). No clear result is obvious from this analysis or reanalysis. Three models produce a statistically significant northward trend (CNRM, GFDL, MIROC-hres).

Trend in Summer (JJAS) Mean

The mean of resampled summer means is shown in Figure 4.18. In summer all three reanalysis products show evidence of a northward trend in Figures 4.19a–c. ERA Interim has no resamplings with a non-positive (non-northward) trend, while ERA-40 and ERA Interim include a few non-positive trends. A similar result is shown in Figures 4.20a–c, with a large majority of resamplings for each reanalysis product showing a positive (northward) correlation with time. Extrapolating each trend over the period 1979 to 2002 suggests a northward shift of nearly 1°. Models suggested both northward (CNRM, GFDL, MRI; Figures 4.19e–f,m) and southward trends (IAP, UKMO; Figures 4.19h,n). Reanalysis products conclusively suggest a robust and significant northward movement in the WACZ from 1979 to 2002, while some models captured this trend, most did not.

Table 4.12 shows an overview of trend statistics for summer. ERA-40 ($r = 0.35, p < 0.03$) and ERA Interim ($r = 0.70, p < 0.01$) each have a significant trend as indicated by time-series correlation and p-values (significance is seen graphically in Figure 4.21). NCEP Reanalysis ($r = 0.28, p = 0.116$) fell just short of significance, but we note it does have an insignificant northward trend. Two models, CNRM and CCSM, each showed a significant northward trend as well and the UKMO showed a significant southward trend. Much as the models could not capture the interannual variability of the WACZ, here they appear to not capture the temporal trend with any skill either.

Trend in Winter (DJFM) Mean

The mean of resampled winter means is shown in Figure 4.22. In winter all three reanalysis products show evidence of a southward trend in Figures 4.23a–c. NCEP shows the strongest southward trend, with ERA-40 and ERA-Interim each successively showing less of a trend. Four models hint at a southward trend as well (IPSL, MPI and MRI, UKMO) in Figures 4.23i,l–n, while three models suggest the opposite, northward trend (CCSM, GFDL, MIROC-hres) in Figures 4.23d,f,k. Time-series correlation suggest a similar result in Figure 4.20.

Table 4.13 shows an overview of trend statistics for winter. Each of the three reanalysis products shows a negative or southward trend, however based on median correlation and median p-values of the resampled tests only the NCEP Reanalysis is statistically significant ($r = -0.486$, $p < 0.01$). Significance is shown graphically in Figure 4.25. A negative trend was only found to be statistically significant in two models, MRI and UKMO. Two other models had statistically significant northward or positive trends, GFDL and MIROC-hres.

The summary of the trend analysis is shown in Table 4.15. Overall from reanalysis we find a statistically significant northward trend of the WACZ in summer in 2 of 3 reanalysis products, and in winter we find some evidence of a southward trend of the WACZ but this is only statistically significant in 1 of 3 reanalysis products. On an annual basis results are mixed with NCEP suggesting a significant southward trend of the WACZ, and ERA-40 and ERA Interim suggesting a significant northward trend of the WACZ. We conclude from this that in summer the WACZ is likely moving northward, and in winter the WACZ is possibly drifting southward, thus potentially increasing the annual range of the WACZ, although this is not shown to be statistically significant. We note GFDL and MIROC-hres each produces trends in the opposite direction of reanalysis in both winter and summer.

4.5 Discussion

Each of the eleven models used in this study have been spatially and temporally analyzed for mean position, variance and trend of W_ϕ compared to reanalysis products. Table 4.14 shows model absolute error (MAE) of W_ϕ relative to median reanalysis for each season and annual mean, as well as the total of each season and annual mean. As the latitude of the WACZ is the focus of this work the sum of MAE is used to rank models from best to worst. Below we discuss and summarize each models strengths and weaknesses as previously shown in Section 4.4. Models are divided into three sections, the strongest performing models had MAE similar to reanalysis products, the middling performing models had MAE over two times as large as reanalysis products and the poor performing models had MAE three times as large as reanalysis products. IAP and MIROC-mres are rated as poor performing models. IPSL, MIROC-hres and MPI are rated as the best performing models.

Strong Performing Models

IPSL IPSL was the best performing model, comparable in skill with the ERA Interim model at determining the position of W_ϕ. While overall IPSL did well, the absolute convergence it generated in the WACZ was less than reanalysis, particularly in winter and the annual mean, and experienced less variance than the median in summer. IPSL's EOF loading pattern was slightly east of reanalysis in winter.

MIROC-hres MIROC-hres performed well in spite of including topographically induced divergence features not included in reanalysis. We note that the majority of these topography-induced features were outside of the domain in which the COA is calculated over West Africa. This increased variance induced by local topography resulted in EOF patterns that were weaker than reanalysis in all seasons for MIROC-hres. In summer the EOF pattern in MIROC-hres was asymmetric, and W_ϕ experienced less variance than any reanalysis product. Although MIROC-hres displayed a southward bias in its position of W_ϕ in winter, it was able to recreate annual variability as seen in reanalysis.

MPI MPI performed just as well as MIROC-hres overall, performing very well in summer. MPI displayed a weak bias, that is to say it produced less convergence in the WACZ than did reanalysis products in both summer and winter. MPI underrepresented variance of W_ϕ in both winter and summer, and its EOF loading pattern was shifted east in winter relative to reanalysis.

CNRM CNRM, as did MIROC-hres and MPI, performed very well in summer, outperforming its winter placement despite summer in general having more variability and less predictability. CNRM displays a weak bias, but under representing convergence in the WACZ relative to reanalysis in winter and annual means. CNRM is biased in both winter and summer, with a north bias in winter and a south bias in winter. CNRM's EOF loading pattern is shifted east of reanalysis in winter. Unlike most other models CNRM has more variance in W_ϕ than reanalysis products in both summer and winter.

Middling Performing Models

MRI MRI experienced bias in each season, north in annual mean and winter, and a south bias in summer. EOF loading patterns were longitudinally offset, west in summer and east in winter. The W_ϕ from MRI experience more variance than reanalysis in winter and less variance in summer. The annual mean of MRI was anti-correlated with reanalysis products, suggesting poor skill at representing interannual variability.

GFDL GFDL had the lowest resolution of any model in the study, and visual inspection of its divergence fields suggested poor skill with the WACZ, but in terms of total error from reanalysis the model is in the middle of the pack. GFDL placed the WACZ north of reanalysis products in both winter and summer and underestimated the strength of convergence in the WACZ, particularly in annual means. In summer this model produced less variance than reanalysis. We also noted that GFDL produced an EOF loading pattern east of reanalysis in winter.

UKMO UKMO performed poorly in summer compared to winter, with a nearly four times larger error in summer, resulting in a moderate overall performance. UKMO showed marked differences from reanalysis in EOF loading patterns, for example it was west of reanalysis in summer, east of reanalysis in winter and generally of lower relative magnitudes, particularly in winter. UKMO showed a northward bias in its position in both winter and annual means. Topographic induced disturbances were evident, causing differences from reanalysis products, although mainly north and east of the domain over which W_ϕ was calculated. UKMO was one of the only models to produce convergence in excess of that observed in reanalysis, particularly in summer and annual means. Variability associated with W_ϕ was lower in summer in UKMO.

CCSM CCSM struggled to predict W_ϕ in summer. The EOF loading pattern in CCSM varied from reanalysis in all seasons, we note that the relative magnitude for CCSM was less than reanalysis in every season. In summer and on an annual basis the EOF pattern is asymmetric. W_ϕ showed reduced variance compared to reanalysis in both summer and winter. We note that CCSM showed anti-correlation with reanalysis for annual means. Topographically induced divergence patterns are evident in CCSM that do not appear in reanalysis.

GISS GISS showed a consistent MAE in every season, including the annual mean. GISS underestimated convergence in the WACZ relative to reanalysis, particularly in summer. W_ϕ is found to be 1° north of reanalysis in the annual mean. GISS shows marked divergence from reanalysis in its EOF loading pattern in winter as it is too far east, and asymmetric for the annual mode. GISS had relative magnitudes larger than that found in reanalysis in all seasons. The variability of W_ϕ in GISS was lower than that of reanalysis in both summer and winter.

Poor Performing Models

MIROC-mres MIROC-mres had large MAE in each season, but performed particularly poorly in summer. MIROC-mres produced less convergence in the WAC in winter and for annual means. The loading pattern of the MIROC-mres EOF was too far east in winter. MIROC-mres had a significant south bias in winter and was nearly 2° south of the annual mean of reanalysis. However despite its south bias of annual mean, it was correlated with reanalysis. In summer the W_ϕ of MIROC-mres had less variance than reanalysis in summer.

IAP IAP was the worst performing model, faring particularly poorly in summer. IAP underestimated convergence relative to reanalysis in every season. The loading pattern of EOF for IAP displayed a west bias in summer and an east displacement in winter. A north bias was evident in both summer and annual value. W_ϕ of IAP showed less variance than reanalysis in both summer in winter. Despite its overall poor performance IAP was correlated with the time-series of reanalysis in winter.

4.6 Conclusions

Models were able to recreate the annual south to north migration of the WACZ successfully, but many models struggled to replicate seasonal mean positions, seasonal variability and all models were unable to replicate temporal variability. The inability of the models to replicate temporal variability may limit the utility of model projections for the 21st century. While in summer clear northward trends were observed in reanalysis products, models as a whole were unable to simulate this northward migration, although some individual models were able to simulate the northward migration. Three models were identified as performing similarly to reanalysis, while two models were identified as performing poorly.

This study began with a spatial analysis of divergence, looking at changes in mean state and variability. Empirical orthoganal function analysis show that models able to capture the north-to-south migration of the WACZ. However models show appreciable differences in the exact positioning of the oscillation, and its strength. With respect to long-term mean individual models displayed north or south biases, but overall underestimated total convergence in the WACZ.

The models exhibit the least coherence in JJAS with the greatest variability in divergence pattern and largest deviations from reanalysis occurring in summer. Differences between reanalysis products are also maximized in JJAS. The largest fraction of divergence in reanalysis is shifted east of the box over which the COA is calculated. Based on EOF patterns we note that the models generally do a poor job in summer replicating reanalysis variance and long term mean position. We note that higher resolution models and reanalysis products veer from the traditional zonal band image of the WACZ highlighting potential complexities from local/small scale sources.

DJFM highest variance in divergence shifts west over the COA box, and reanalysis products differ slightly in latitudinal position of the WACZ. Models closer to reanalysis in winter, but in general contain less convergence over WACZ.

The utility of the centers of action approach was shown as an strong quantitative measure of model performance. In reanalysis products W_ϕ clearly demonstrates the annual cycle maximizing annually in summer between 16° to 18° N and reaching a minimum in winter between 7° to 9° N. We find an asymmetric migration with a slow steady northward migration in spring and a rapid southward migration in fall. Eight of eleven models place the mean annual position within range of reanalysis products, however only one of eleven models is significantly temporally correlated with reanalysis products suggesting an inability to replicate interannual variability.

The COA approach confirms many of the biases and mean errors suggested in the qualitative approach for the summer season. With respect to the mean positioning of the COA models do well in summer, with only one model north of all reanalysis products and only two models south of all reanalysis products. Likewise models struggle to recreate the variance of W_ϕ with nine of 11 models having less variance than any of the reanalysis products. Similarly to the annual cycle, models show no correlations with any reanalysis product, suggesting in an inability to replicate interannual variability.

In winter, reanalysis products are very similar to each other, with less mean absolute error and bias when compared to summer. Five of eleven models predict latitudinal position of WACZ north of reanalysis, and three of eleven models predict latitudes south of observations in reanalysis products. Again models were unable to recreate the temporal variability, as only 2 of 11 models had any significant correlation with reanalysis products.

The summary of the trend analysis is shown in Table 4.15. Overall from reanalysis we find a statistically significant northward trend of the WACZ in summer in 2 of 3, and in winter we find some evidence of a southward trend of the WACZ but this is only statistically significant in 1 of 3 reanalysis products. On an annual basis results are mixed with NCEP suggesting a significant southward trend of the WACZ, and ERA-40 and ERA Interim suggesting a significant northward trend of the WACZ. We conclude from this that in summer the WACZ is likely moving northward, and in winter the WACZ is possibly drifting southward, thus potentially increasing the annual range of the WACZ, although this is not shown to be statistically significant.

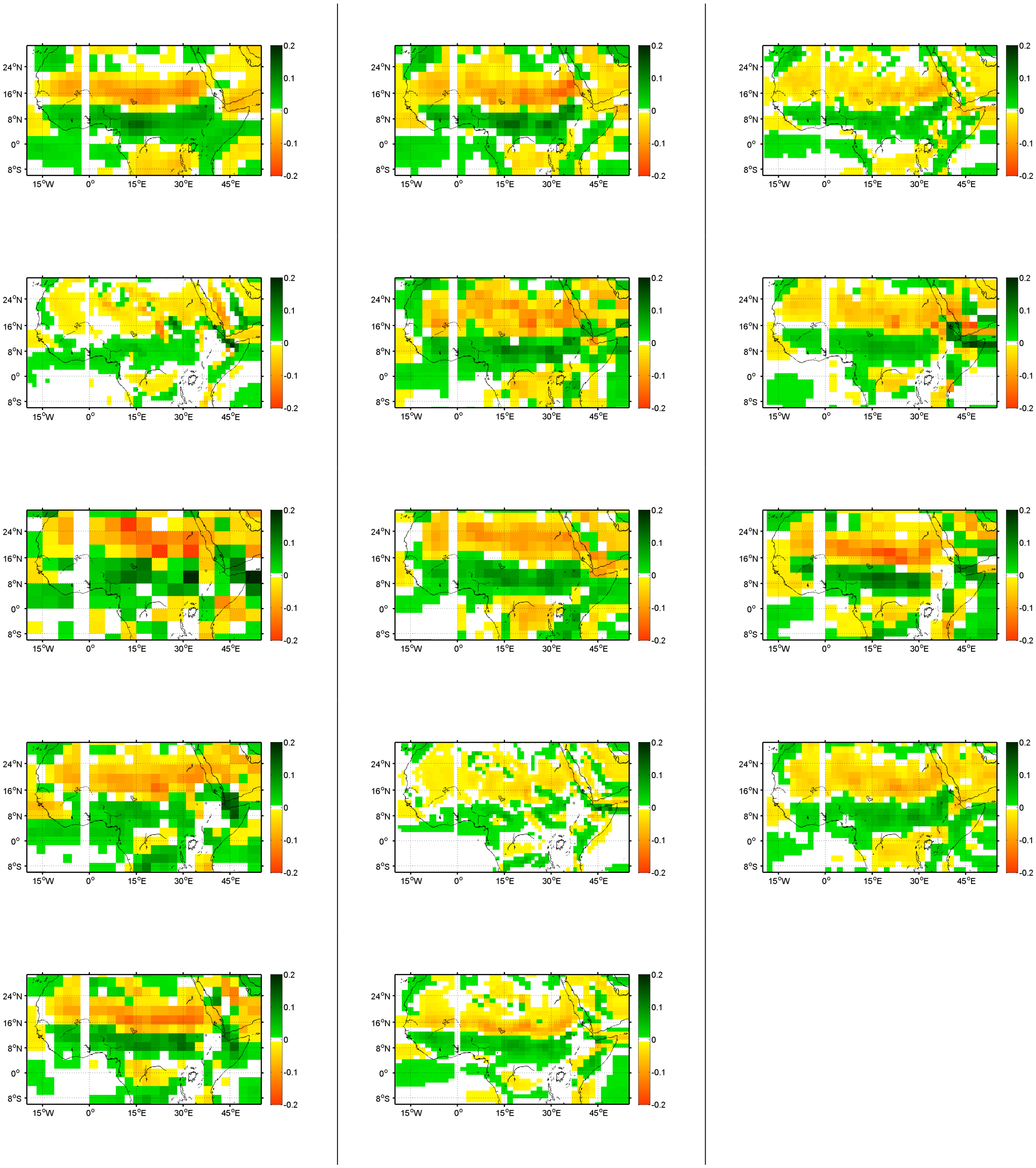

Figure 4.1: First mode of the EOF of 925hPa divergence (all months) from CMIP3-AMIP scenario. Years used in the calculation are shown in in Table 4.1. Top row (reanalysis product): (a) NCEP Reanalysis, (b) ERA-40, (c) ERA Interim. Second row: (d) CCSM, (e) CNRM, (f) GFDL. Third row: (g) GISS, (h)IAP, (i)IPSL Fourth row: (j) MIROC-mres, (k) MIROC-hires, (l) MPI. Fifth row: (m) MRI and (n) UKMO-HADGEM.

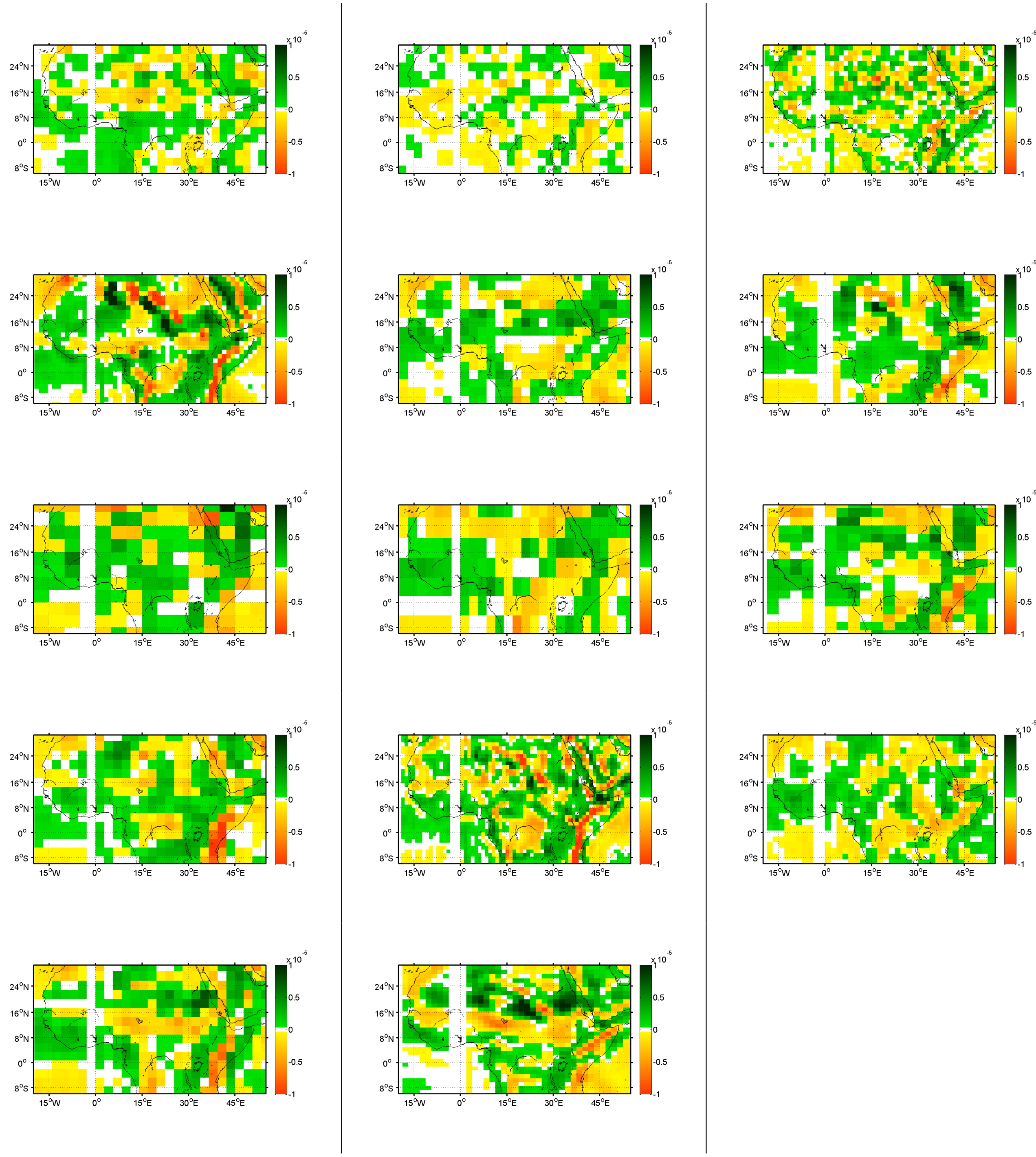

Figure 4.2: Annual model mean divergence from CMIP3-AMIP scenario minus the annual median reanalysis divergence over the period 1978 to 2002. Before differences are calculated all data is regridded to the lowest common resolution between reanalysis products and model. Top row (reanalysis product): (a) NCEP Reanalysis, (b) ERA-40, (c) ERA Interim. Second row: (d) CCSM, (e) CNRM, (f) GFDL. Third row: (g) GISS, (h)IAP, (i)IPSL Fourth row: (j) MIROC-mres, (k) MIROC-hires, (l) MPI. Fifth row: (m) MRI and (n) UKMO-HADGEM.

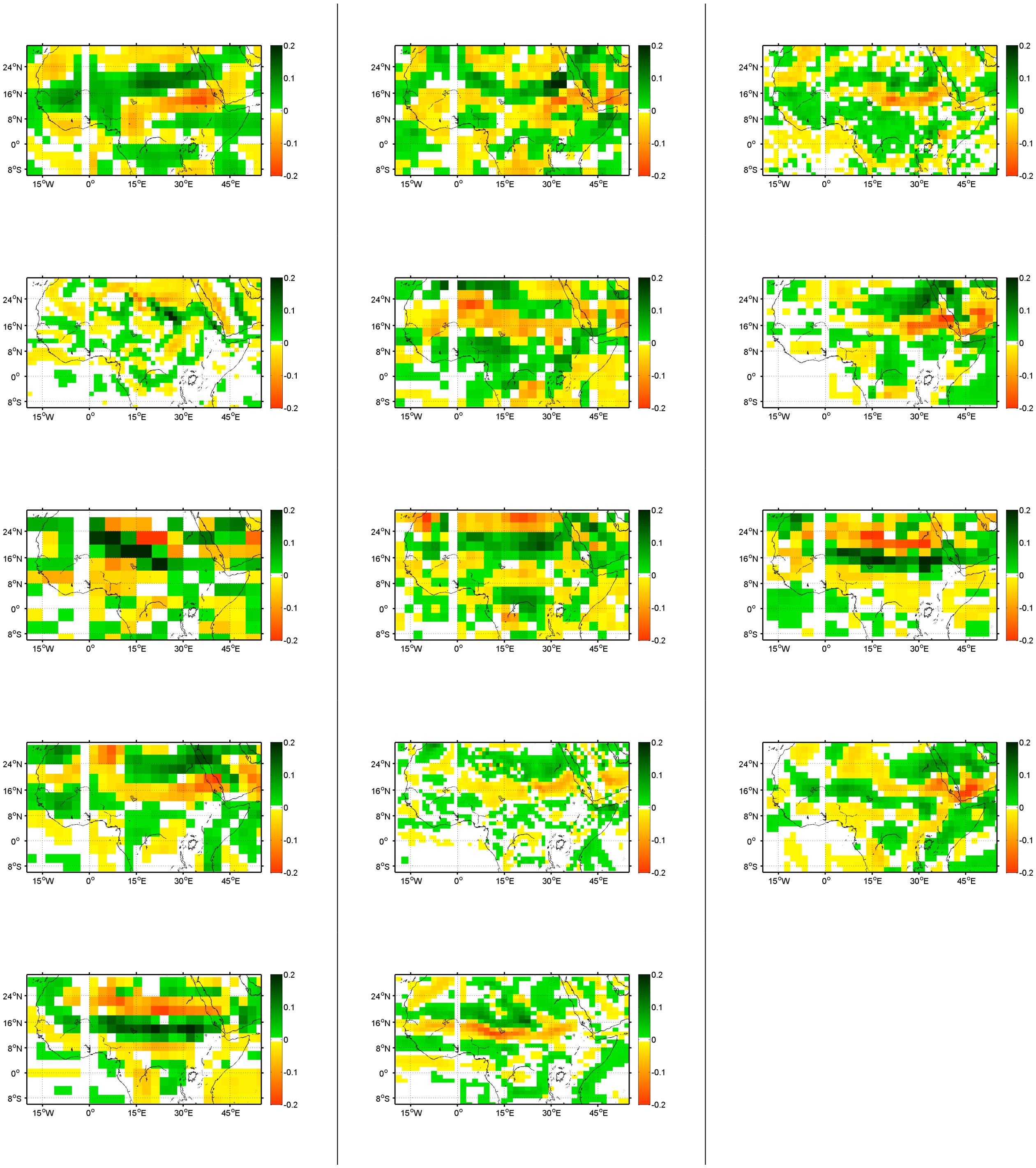

Figure 4.3: First mode of the EOF of 925hPa divergence in summer (JJAS) from CMIP3-AMIP scenario. Years used in the calculation are shown in in Table 4.1. Top row (reanalysis product): (a) NCEP Reanalysis, (b) ERA-40, (c) ERA Interim. Second row: (d) CCSM, (e) CNRM, (f) GFDL. Third row: (g) GISS, (h)IAP, (i)IPSL Fourth row: (j) MIROC-mres, (k) MIROC-hires, (l) MPI. Fifth row: (m) MRI and (n) UKMO-HADGEM.

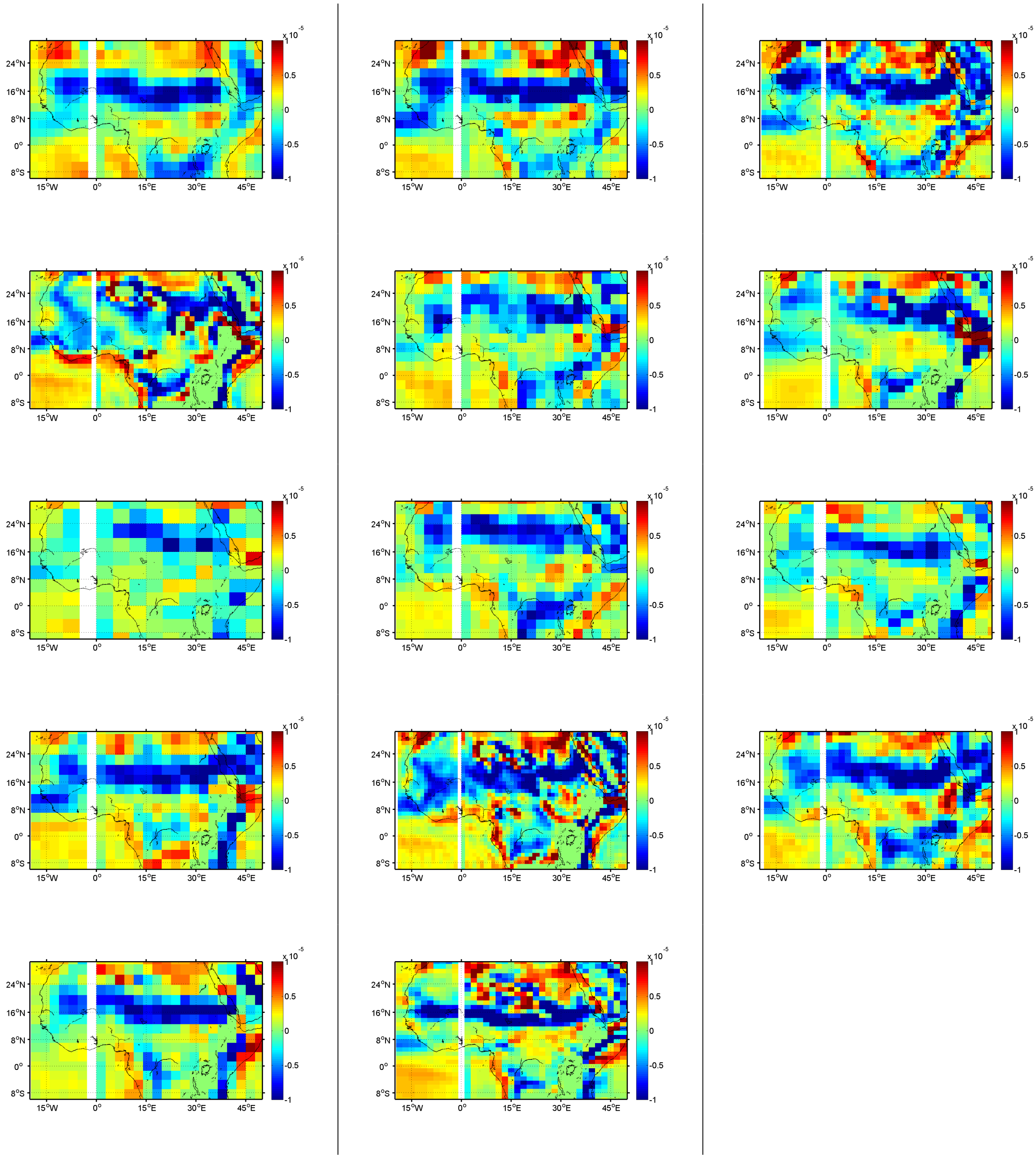

Figure 4.4: Long term mean of 925hPa divergence in summer (JJAS) from CMIP3-AMIP scenario. Years used in the calculation are shown in in Table 4.1. Top row (reanalysis product): (a) NCEP Reanalysis, (b) ERA-40, (c) ERA Interim. Second row: (d) CCSM, (e) CNRM, (f) GFDL. Third row: (g) GISS, (h)IAP, (i)IPSL Fourth row: (j) MIROC-mres, (k) MIROC-hires, (l) MPI. Fifth row: (m) MRI and (n) UKMO-HADGEM.

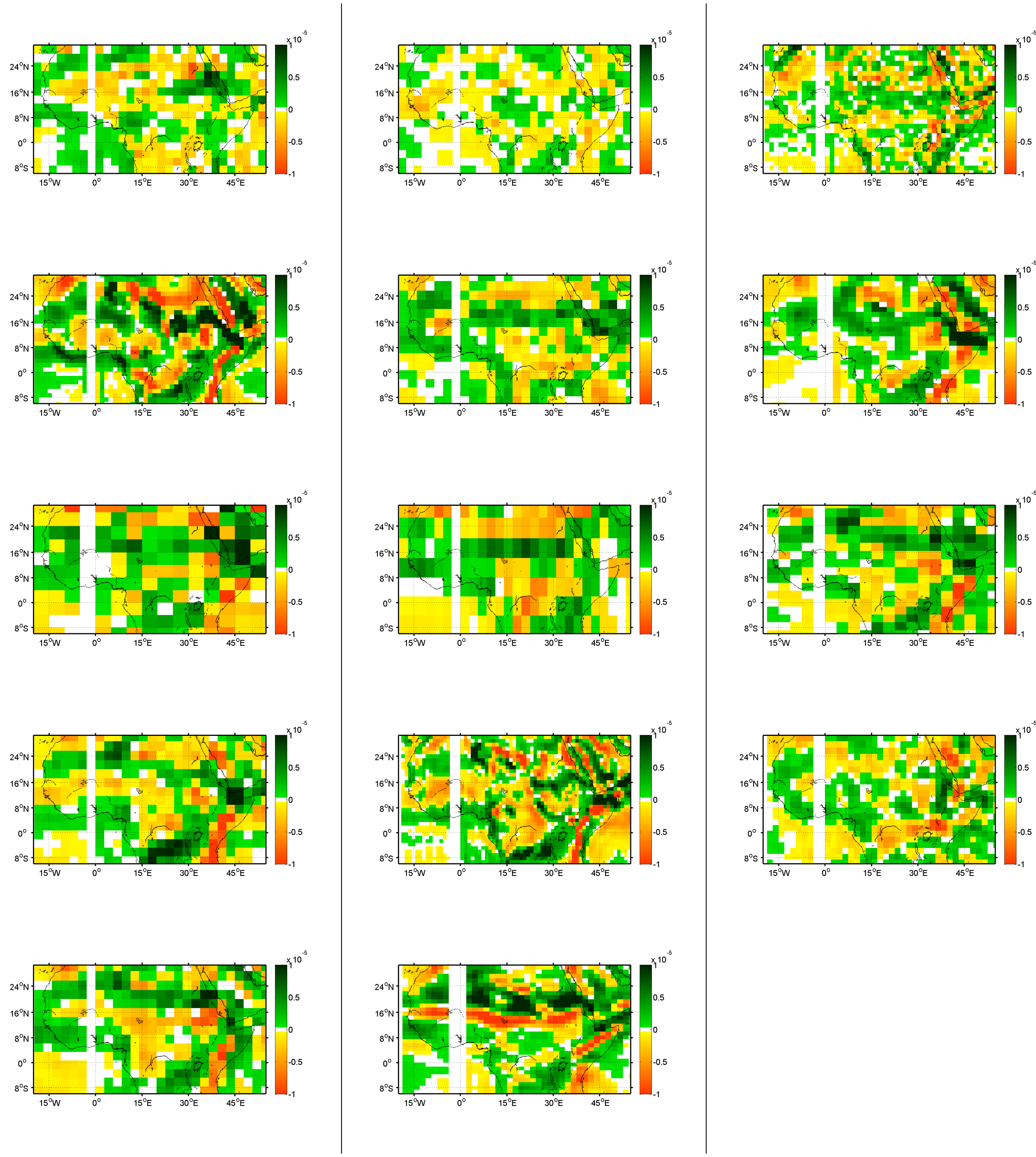

Figure 4.5: Summer (JJAS) model mean divergence from CMIP3-AMIP scenario minus the winter median reanalysis divergence over the period 1978 to 2002. Before differences are calculated all data is regridded to the lowest common resolution between reanalysis products and model. Top row (reanalysis product): (a) NCEP Reanalysis, (b) ERA-40, (c) ERA Interim. Second row: (d) CCSM, (e) CNRM, (f) GFDL. Third row: (g) GISS, (h)IAP, (i)IPSL Fourth row: (j) MIROC-mres, (k) MIROC-hires, (l) MPI. Fifth row: (m) MRI and (n) UKMO-HADGEM.

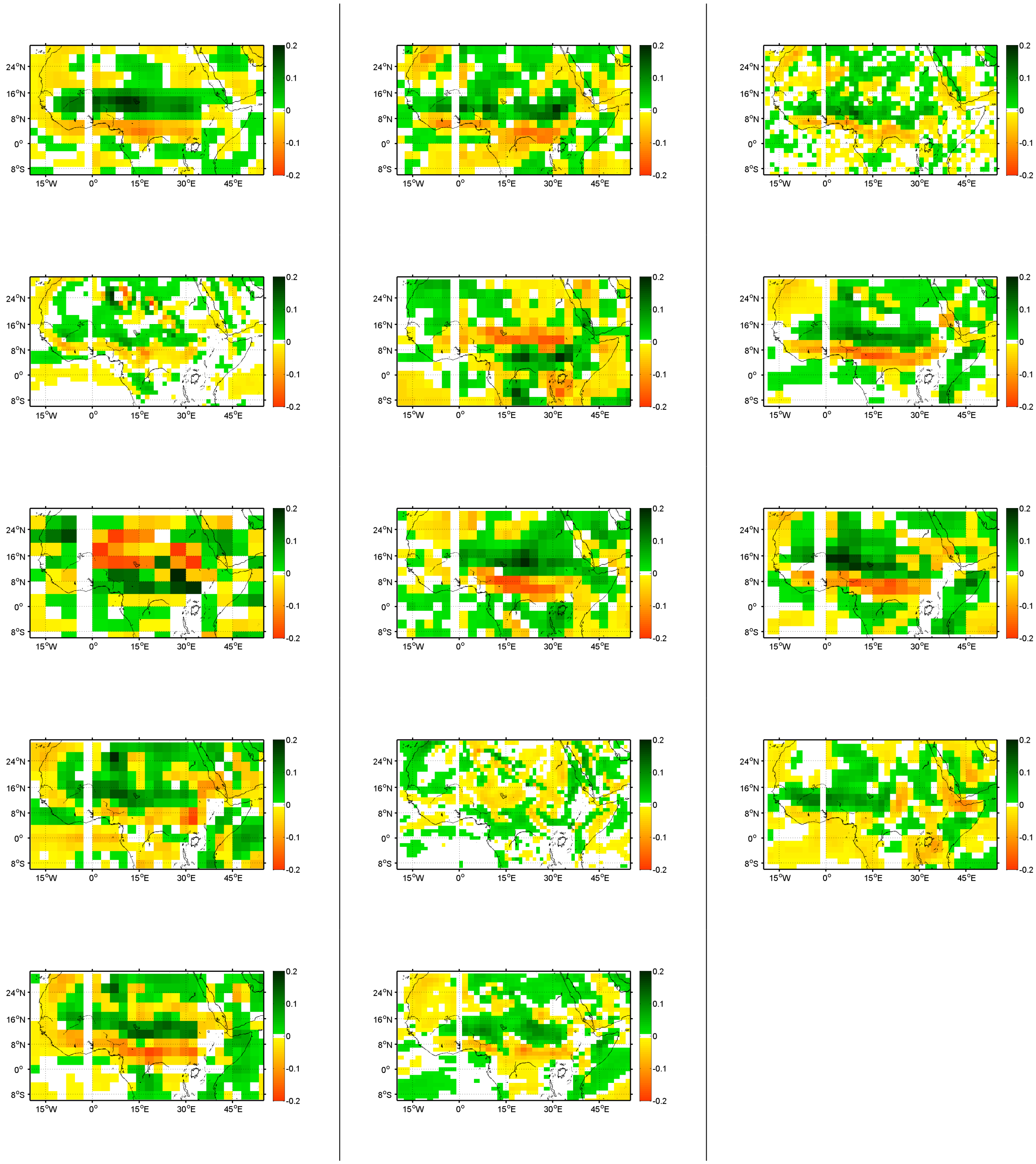

Figure 4.6: First mode of the EOF of 925hPa divergence in winter (DJFM) from CMIP3-AMIP scenario. Years used in the calculation are shown in in Table 4.1. Top row (reanalysis product): (a) NCEP Reanalysis, (b) ERA-40, (c) ERA Interim. Second row: (d) CCSM, (e) CNRM, (f) GFDL. Third row: (g) GISS, (h)IAP, (i)IPSL Fourth row: (j) MIROC-mres, (k) MIROC-hires, (l) MPI. Fifth row: (m) MRI and (n) UKMO-HADGEM.

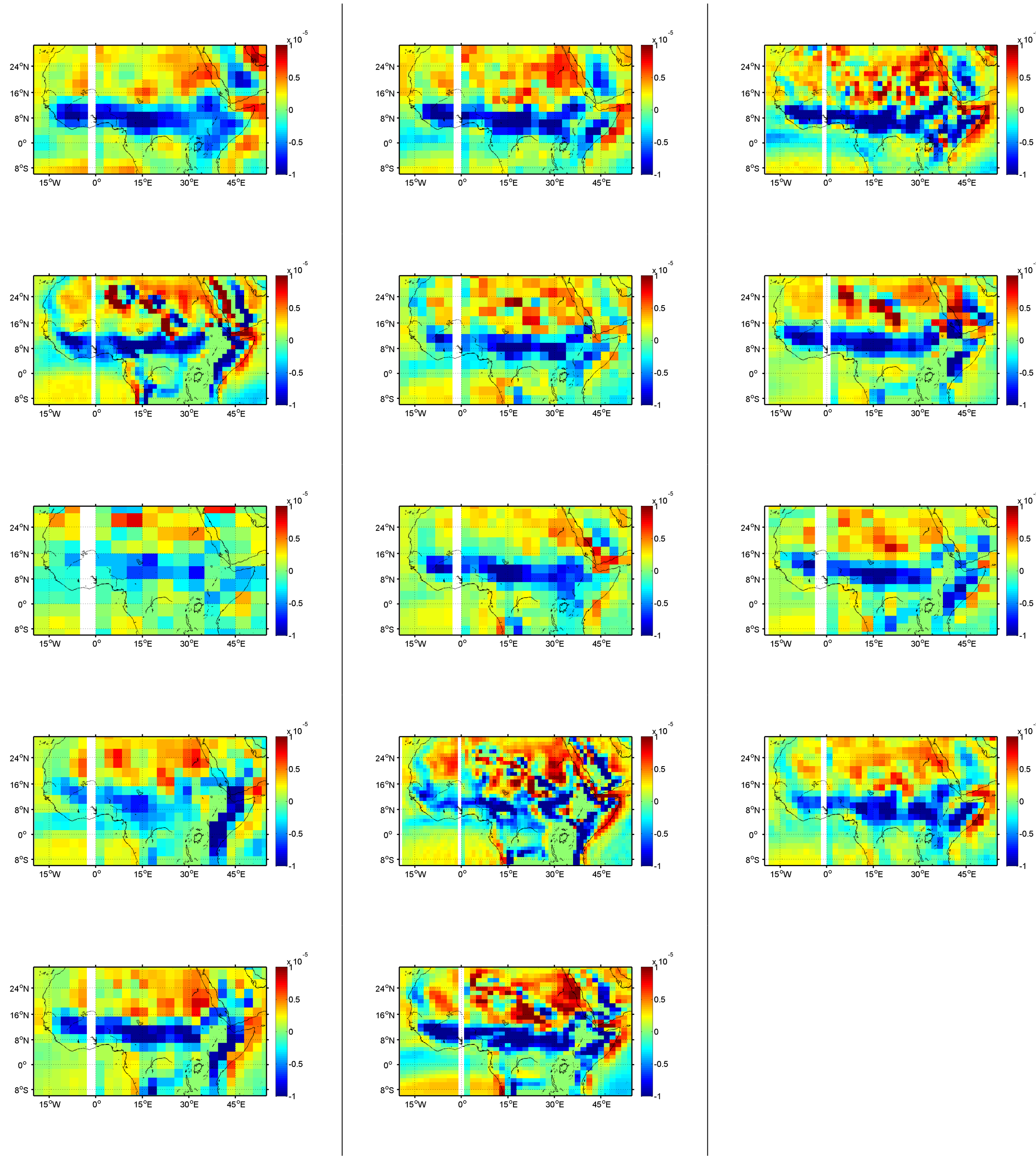

Figure 4.7: Long term mean of 925hPa divergence in winter (DJFM) from CMIP3-AMIP scenario. Years used in the calculation are shown in in Table 4.1. Top row (reanalysis product): (a) NCEP Reanalysis, (b) ERA-40, (c) ERA Interim. Second row: (d) CCSM, (e) CNRM, (f) GFDL. Third row: (g) GISS, (h)IAP, (i)IPSL Fourth row: (j) MIROC-mres, (k) MIROC-hires, (l) MPI. Fifth row: (m) MRI and (n) UKMO-HADGEM.

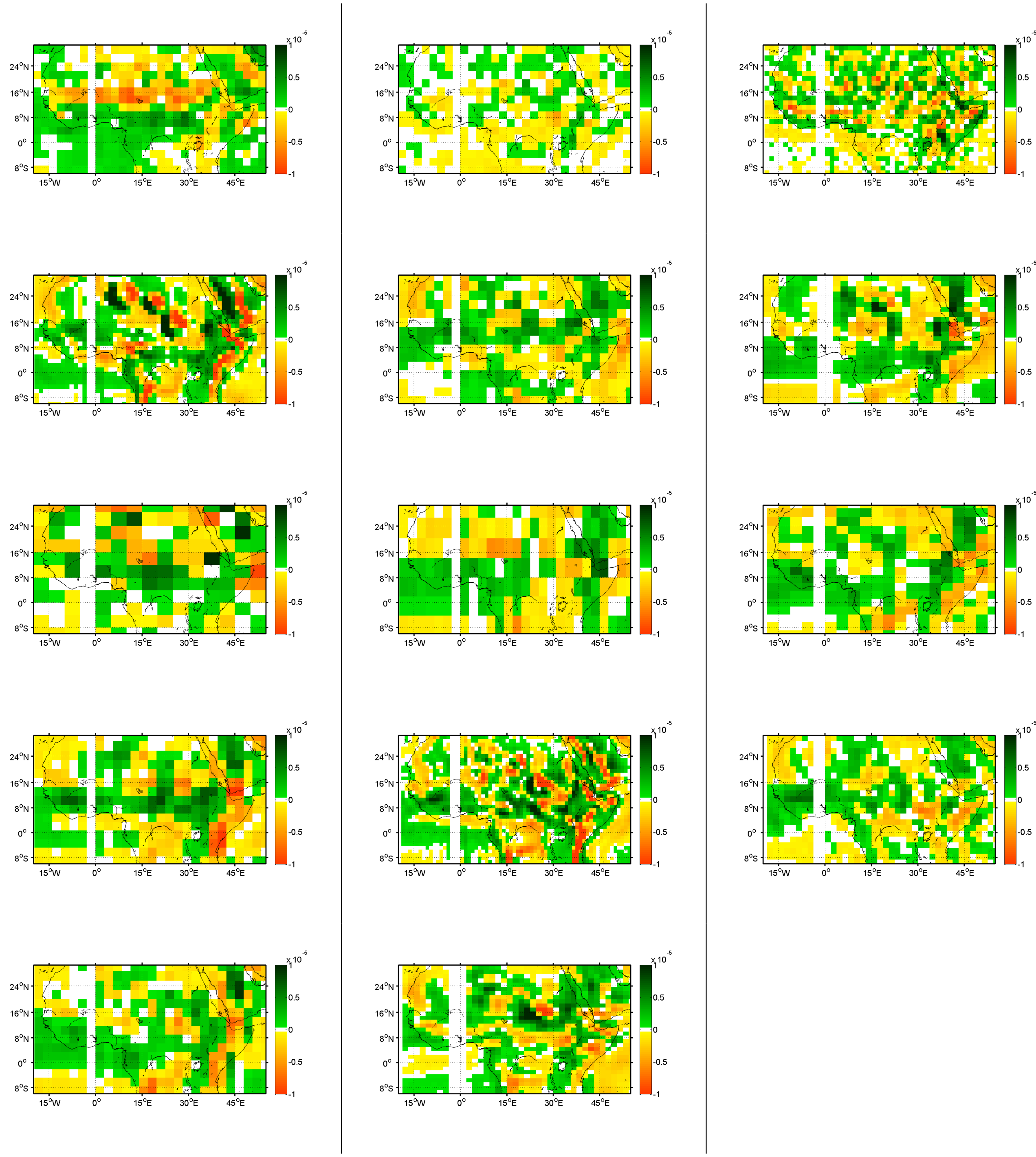

Figure 4.8: Winter (DJFM) model mean divergence from CMIP3-AMIP scenario minus the winter median reanalysis divergence over the period 1978 to 2002. Before differences are calculated all data is regridded to the lowest common resolution between reanalysis products and model. Top row (reanalysis product): (a) NCEP Reanalysis, (b) ERA-40, (c) ERA Interim. Second row: (d) CCSM, (e) CNRM, (f) GFDL. Third row: (g) GISS, (h)IAP, (i)IPSL Fourth row: (j) MIROC-mres, (k) MIROC-hires, (l) MPI. Fifth row: (m) MRI and (n) UKMO-HADGEM.

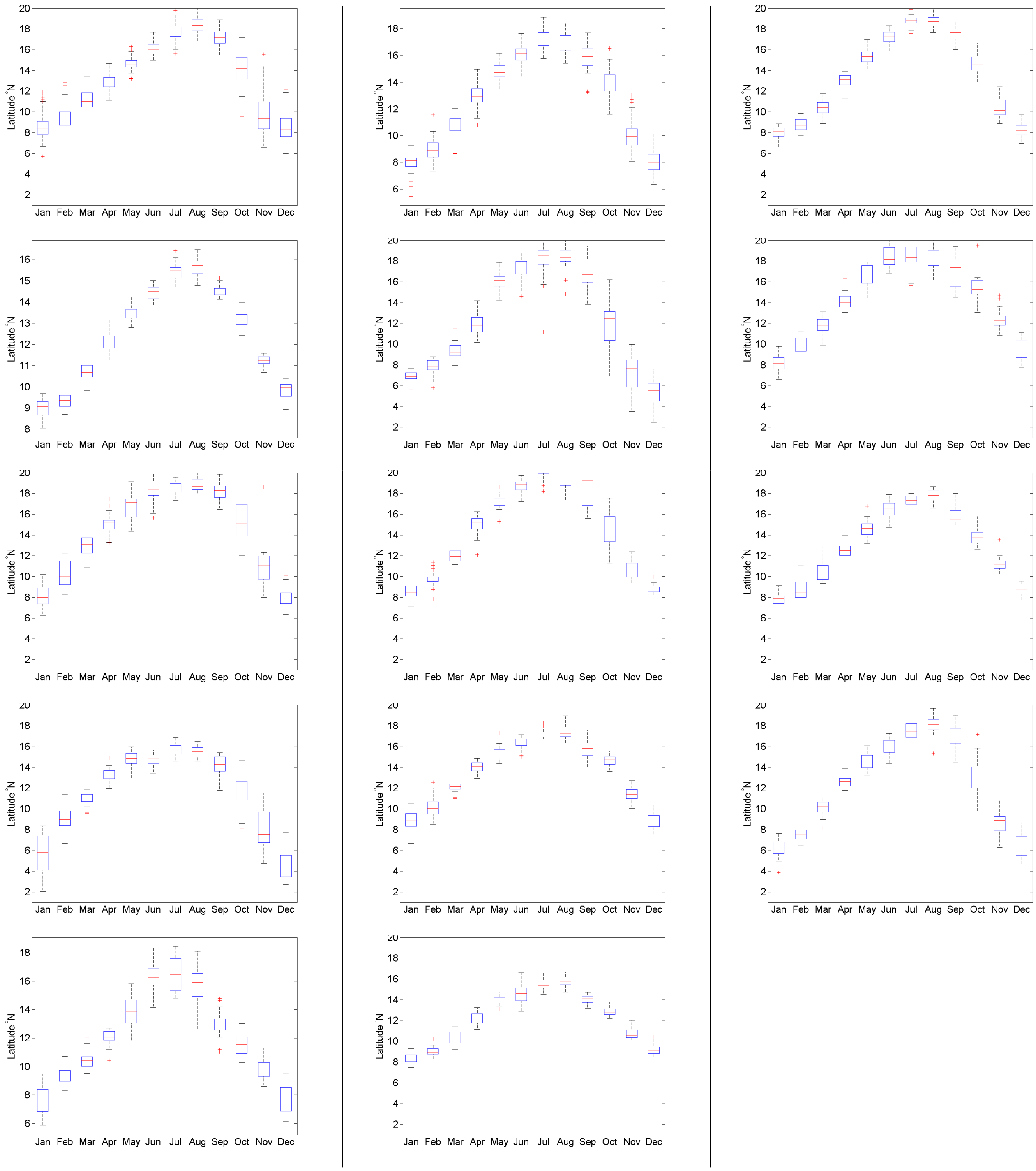

Figure 4.9: Monthly values of WACZ Latitude Index. Red line represent monthly median value, with blue verticle lines representing the 75th and 25th percentiles respectively. Outliers are indicated with an asterisk. Top row (reanalysis product): (a) NCEP Reanalysis, (b) ERA-40, (c) ERA Interim. Second row: (d) CCSM, (e) CNRM, (f) GFDL. Third row: (g) GISS, (h)IAP, (i)IPSL Fourth row: (j) MIROC-mres, (k) MIROC-hires, (l) MPI. Fifth row: (m) MRI and (n) UKMO-HADGEM.

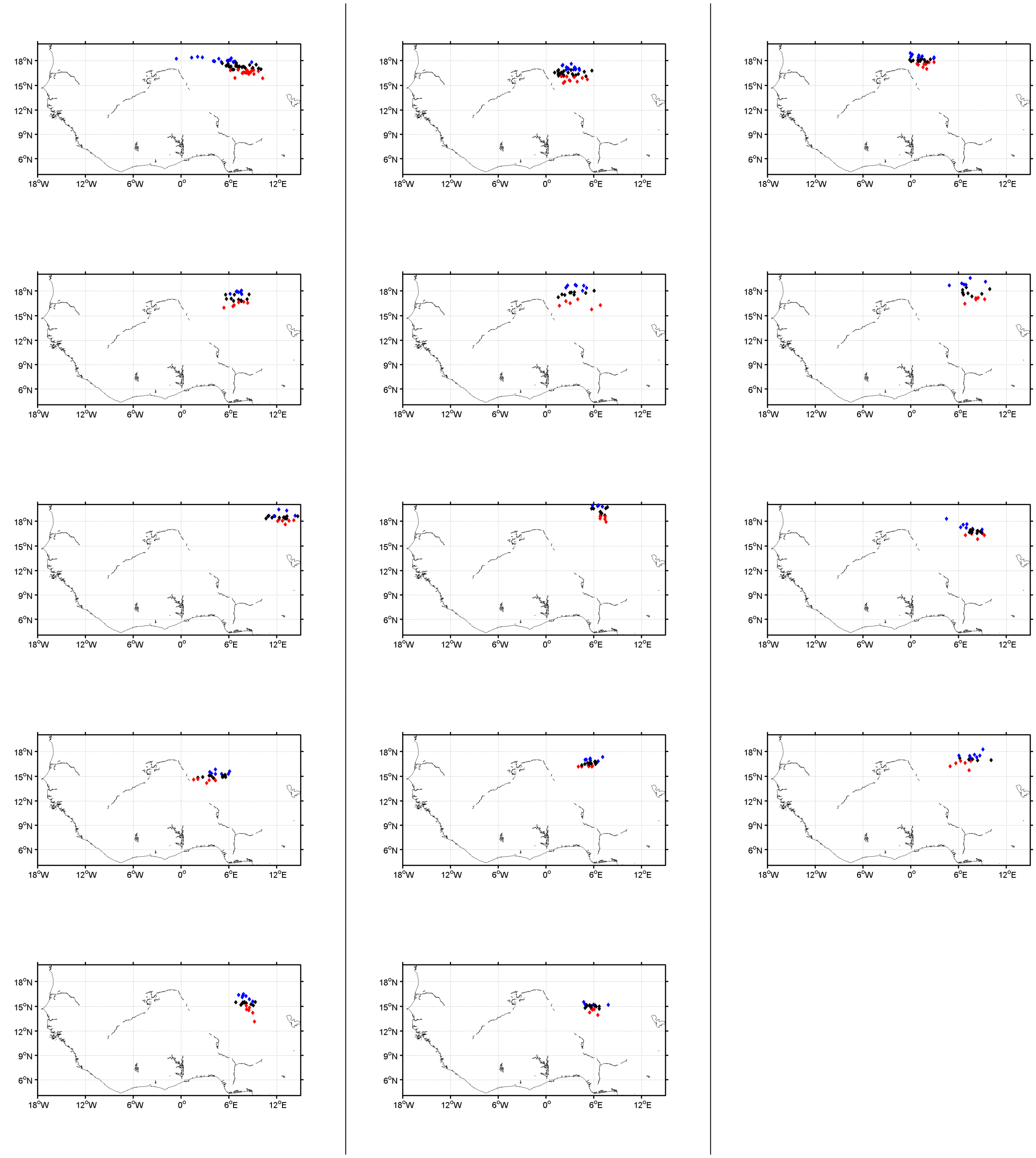

Figure 4.10: Position of WACZ COA in summer (JJAS) from CMIP3-AMIP scenario over the period 1978 to 2002. Blue diamonds represent the 75th northern percentile of WACZ latitude position. Red diamonds represent the 25th southern percentile of WACZ latitude position. Black diamonds represent the middle 50th percentile of WACZ latitude seasons. Top row (reanalysis product): (a) NCEP Reanalysis, (b) ERA-40, (c) ERA Interim. Second row: (d) CCSM, (e) CNRM, (f) GFDL. Third row: (g) GISS, (h)IAP, (i)IPSL Fourth row: (j) MIROC-mres, (k) MIROC-hires, (l) MPI. Fifth row: (m) MRI and (n) UKMO-HADGEM.

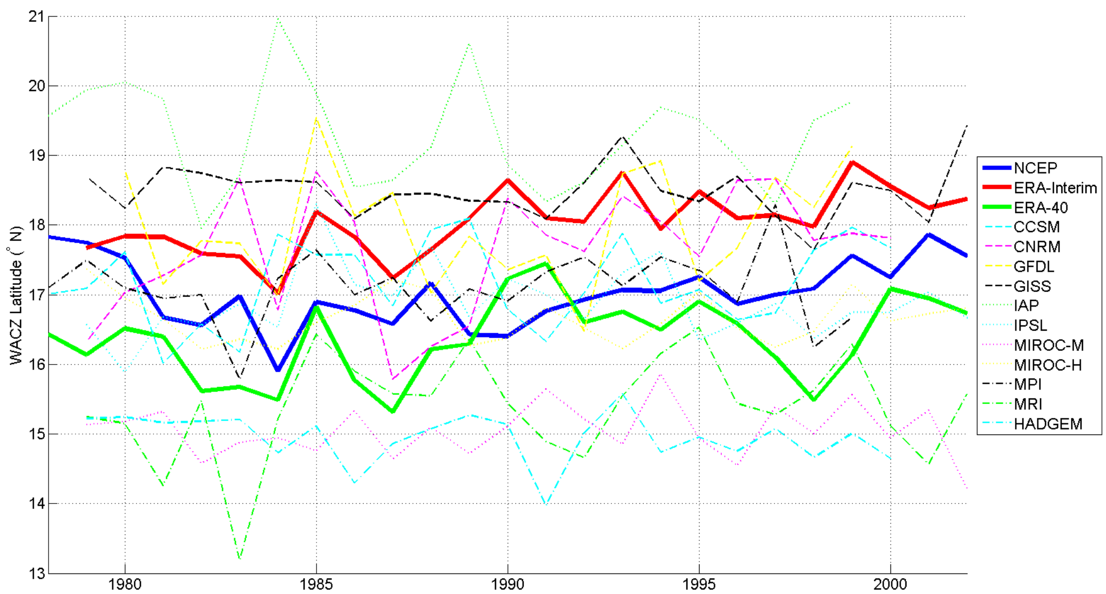

Figure 4.11: Timeseries of summer (JJAS) WACZ Latitude (W_ϕ) for the three reanalysis products and 11 model runs over the period 1978 – 2002.

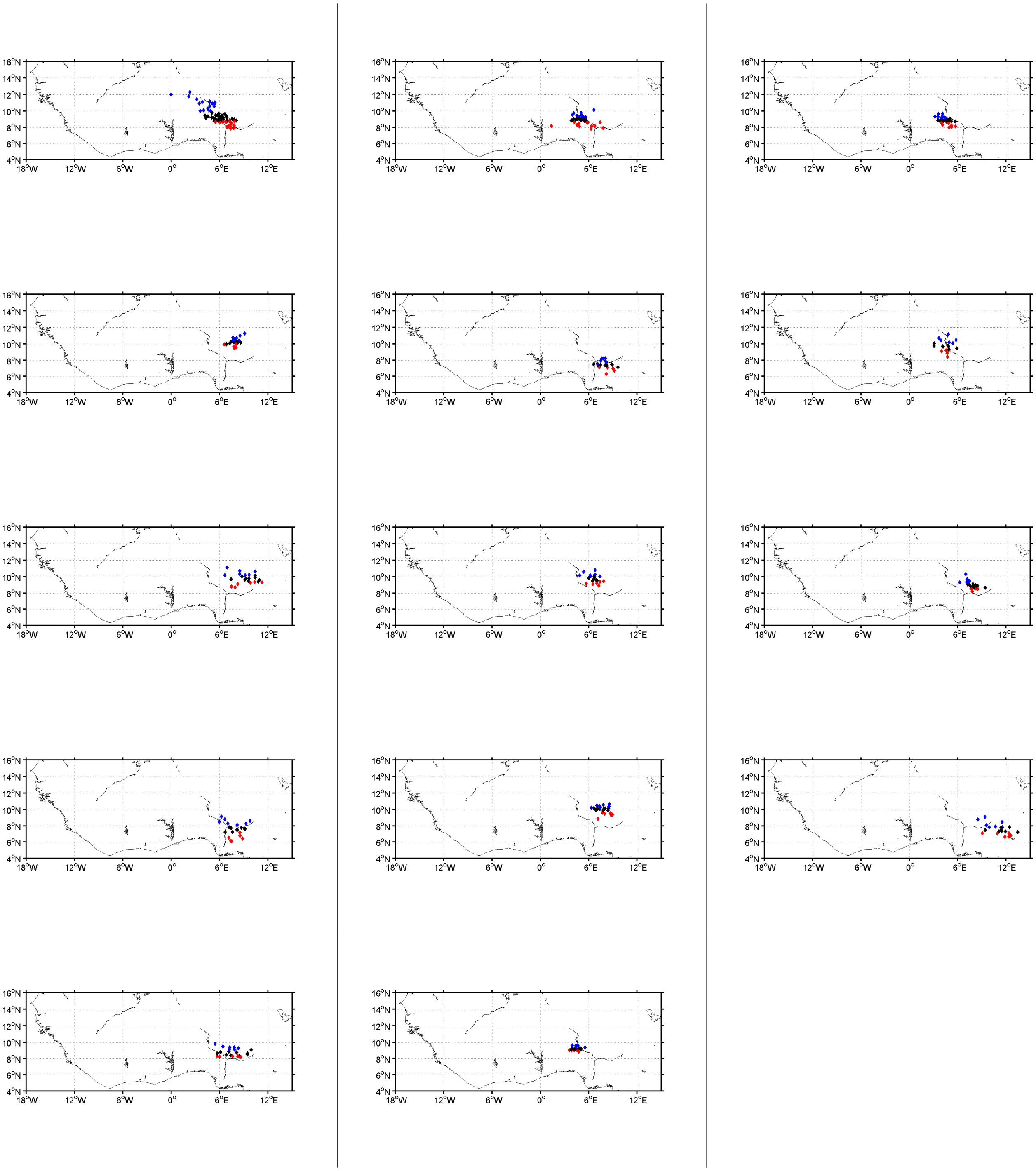

Figure 4.12: Position of WACZ COA in winter (DJFM) from CMIP3-AMIP scenario over the period 1978 to 2002. Blue diamonds represent the 75th northern percentile of WACZ latitude position. Red diamonds represent the 25th southern percentile of WACZ latitude position. Black diamonds represent the middle 50th percentile of WACZ latitude seasons. Top row (reanalysis product): (a) NCEP Reanalysis, (b) ERA-40, (c) ERA Interim. Second row: (d) CCSM, (e) CNRM, (f) GFDL. Third row: (g) GISS, (h)IAP, (i)IPSL Fourth row: (j) MIROC-mres, (k) MIROC-hires, (l) MPI. Fifth row: (m) MRI and (n) UKMO-HADGEM.

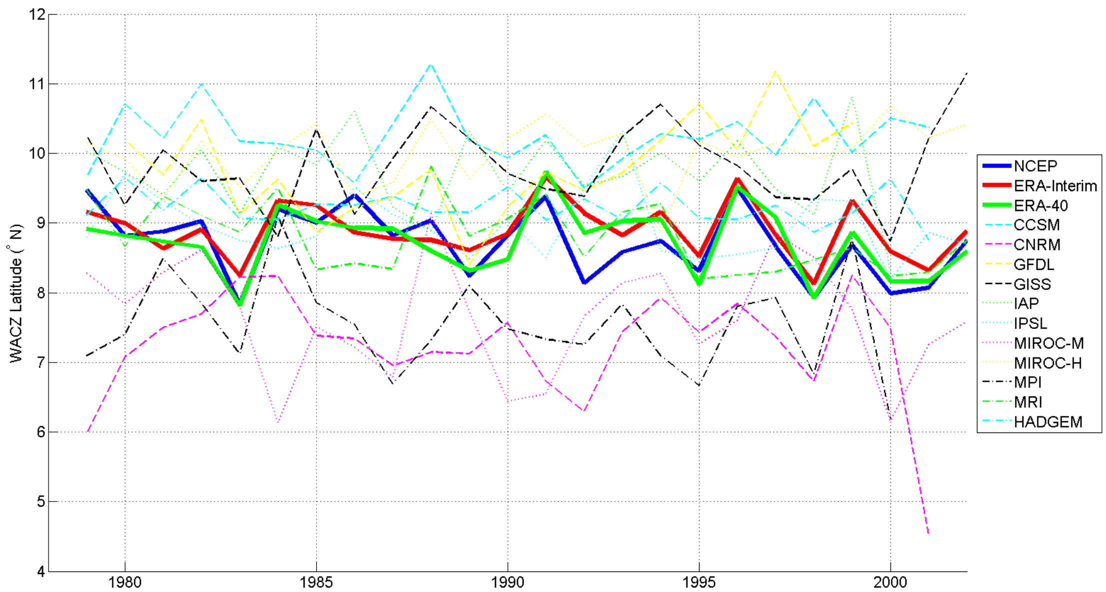

Figure 4.13: Timeseries of winter (DJFM) WACZ Latitude (W_ϕ) for the three reanalysis products and 11 model runs over the period 1978 – 2002.

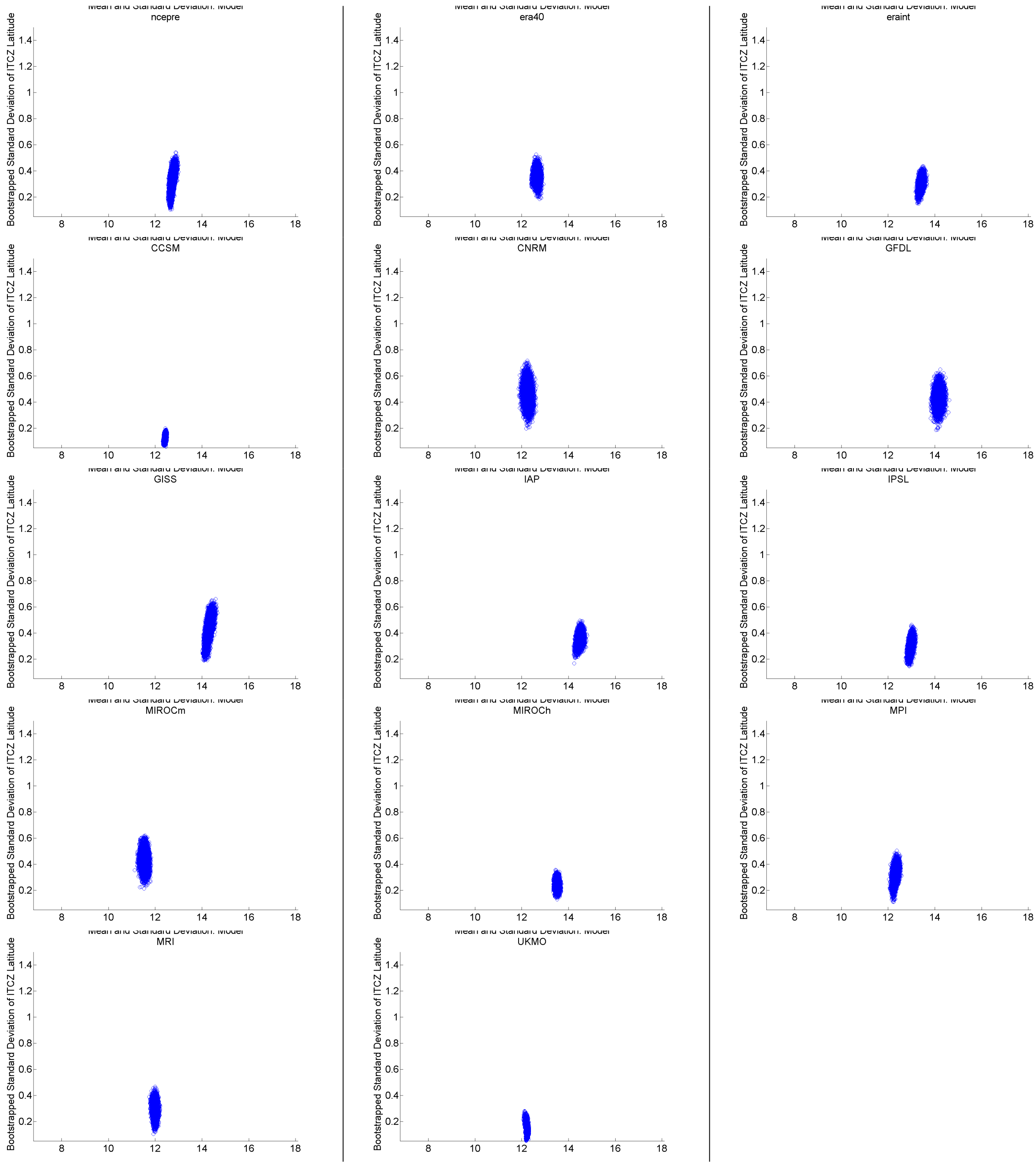

Figure 4.14: Mean and standard deviation of WACZ latitude of annual means from CMIP3-AMIP scenario over the period 1978 to 2002. Top row (reanalysis product): (a) NCEP Reanalysis, (b) ERA-40, (c) ERA Interim. Second row: (d) CCSM, (e) CNRM, (f) GFDL. Third row: (g) GISS, (h)IAP, (i)IPSL Fourth row: (j) MIROC-mres, (k) MIROC-hires, (l) MPI. Fifth row: (m) MRI and (n) UKMO-HADGEM.

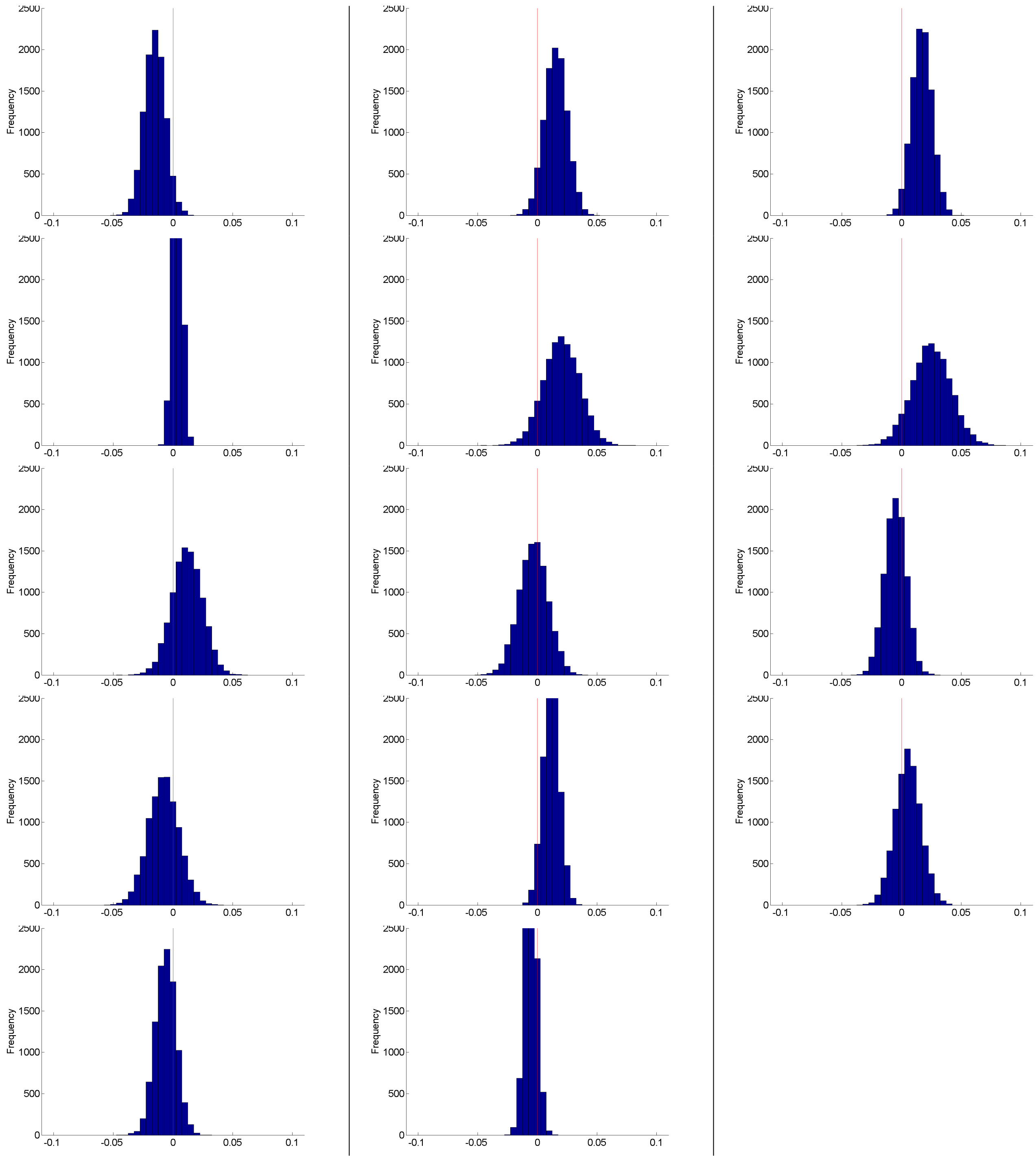

Figure 4.15: Linear trend of WACZ latitude in annual means from CMIP3-AMIP scenario over the period 1978 to 2002. Top row (reanalysis product): (a) NCEP Reanalysis, (b) ERA-40, (c) ERA Interim. Second row: (d) CCSM, (e) CNRM, (f) GFDL. Third row: (g) GISS, (h)IAP, (i)IPSL Fourth row: (j) MIROC-mres, (k) MIROC-hires, (l) MPI. Fifth row: (m) MRI and (n) UKMO-HADGEM.

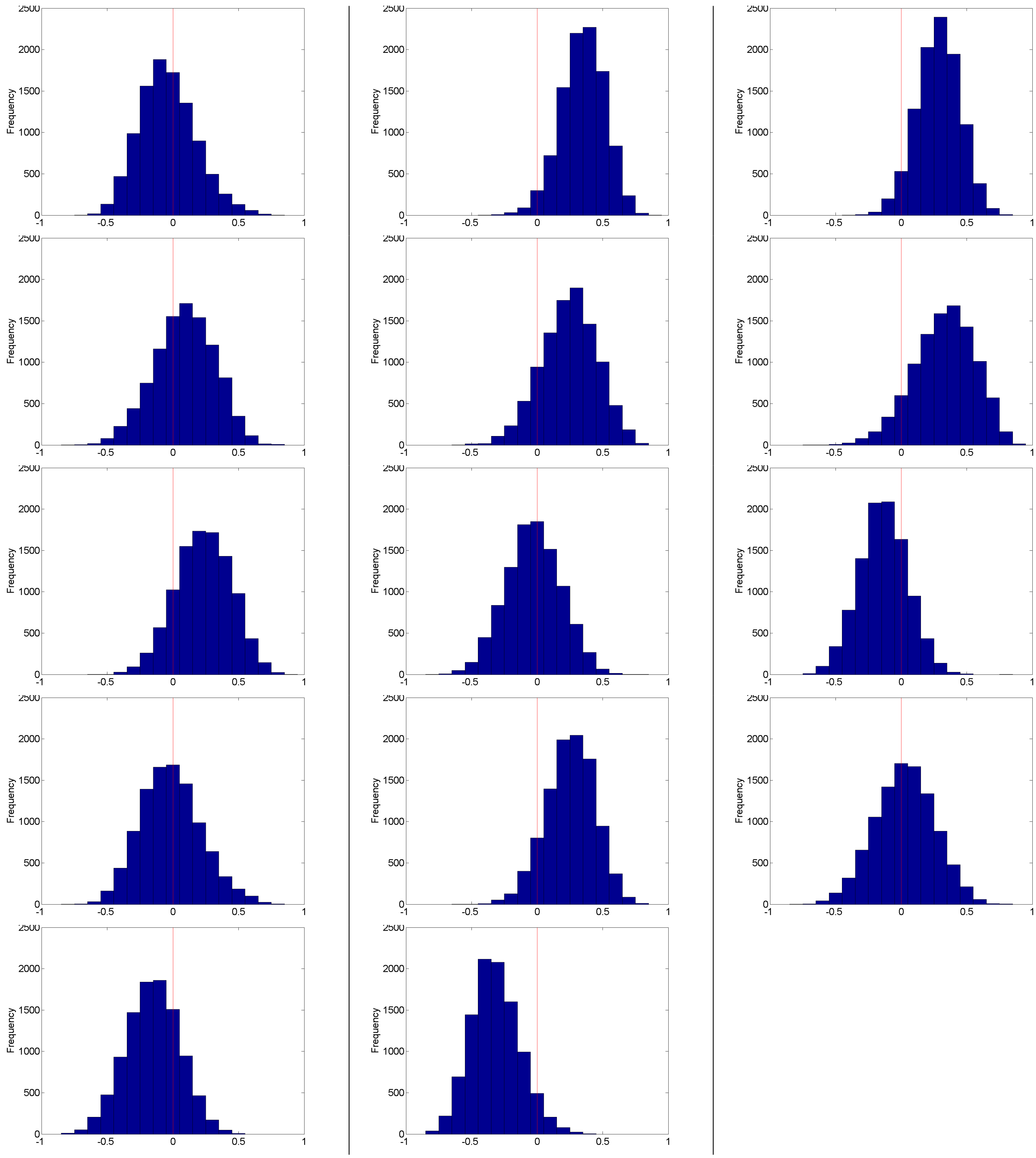

Figure 4.16: Correlation co-efficients between time and WACZ latitude in annual means from CMIP3-AMIP scenario over the period 1978 to 2002. Top row (reanalysis product): (a) NCEP Reanalysis, (b) ERA-40, (c) ERA Interim. Second row: (d) CCSM, (e) CNRM, (f) GFDL. Third row: (g) GISS, (h)IAP, (i)IPSL Fourth row: (j) MIROC-mres, (k) MIROC-hires, (l) MPI. Fifth row: (m) MRI and (n) UKMO-HADGEM.

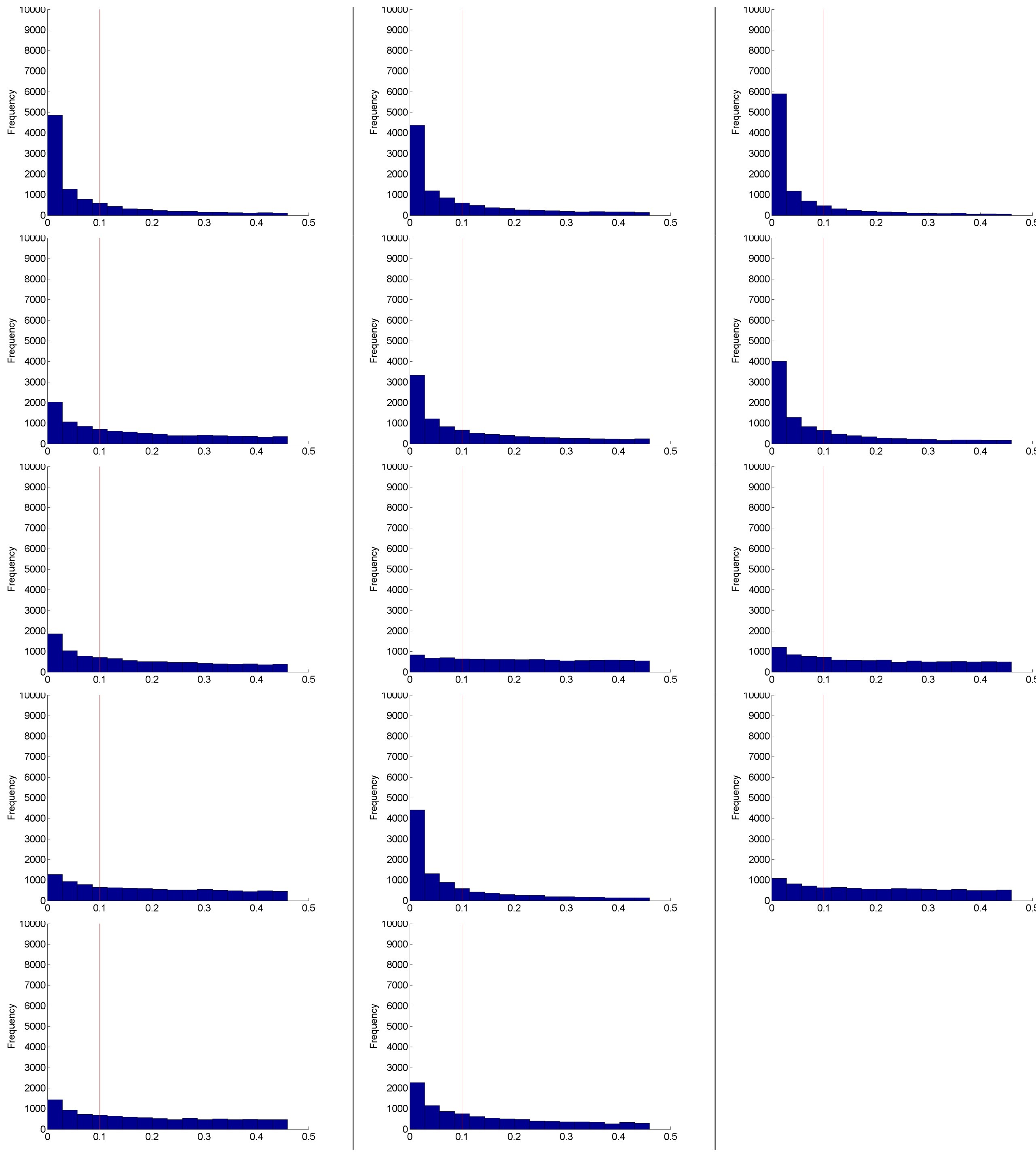

Figure 4.17: *P*-values of significance of trend of WACZ latitude in annual means from CMIP3-AMIP scenario over the period 1978 to 2002. Top row (reanalysis product): (a) NCEP Reanalysis, (b) ERA-40, (c) ERA Interim. Second row: (d) CCSM, (e) CNRM, (f) GFDL. Third row: (g) GISS, (h)IAP, (i)IPSL Fourth row: (j) MIROC-mres, (k) MIROC-hires, (l) MPI. Fifth row: (m) MRI and (n) UKMO-HADGEM.

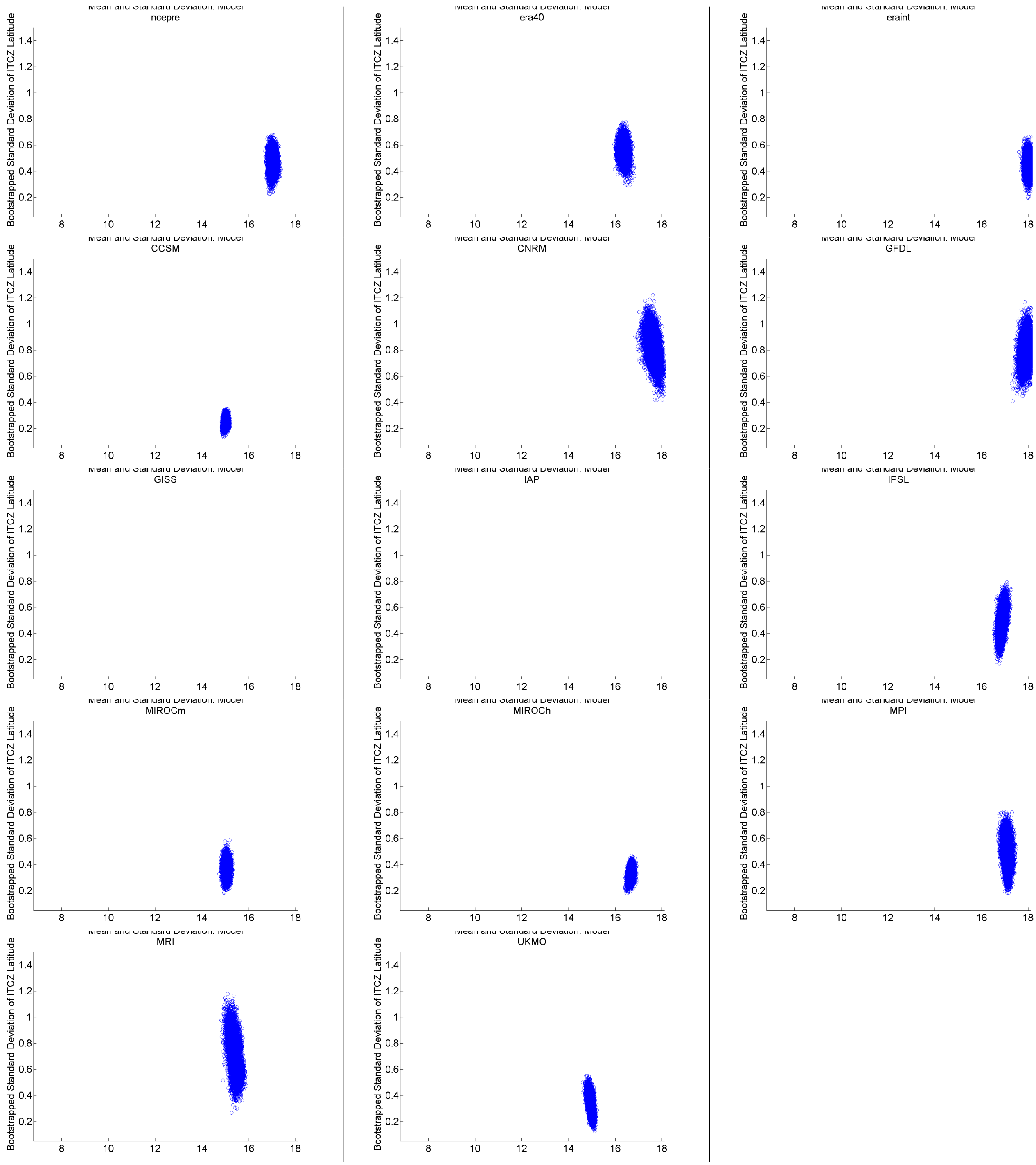

Figure 4.18: Mean and standard deviation of WACZ latitude in summer (JJAS) from CMIP3-AMIP scenario over the period 1978 to 2002. Top row (reanalysis product): (a) NCEP Reanalysis, (b) ERA-40, (c) ERA Interim. Second row: (d) CCSM, (e) CNRM, (f) GFDL. Third row: (g) GISS, (h)IAP, (i)IPSL Fourth row: (j) MIROC-mres, (k) MIROC-hires, (l) MPI. Fifth row: (m) MRI and (n) UKMO-HADGEM.

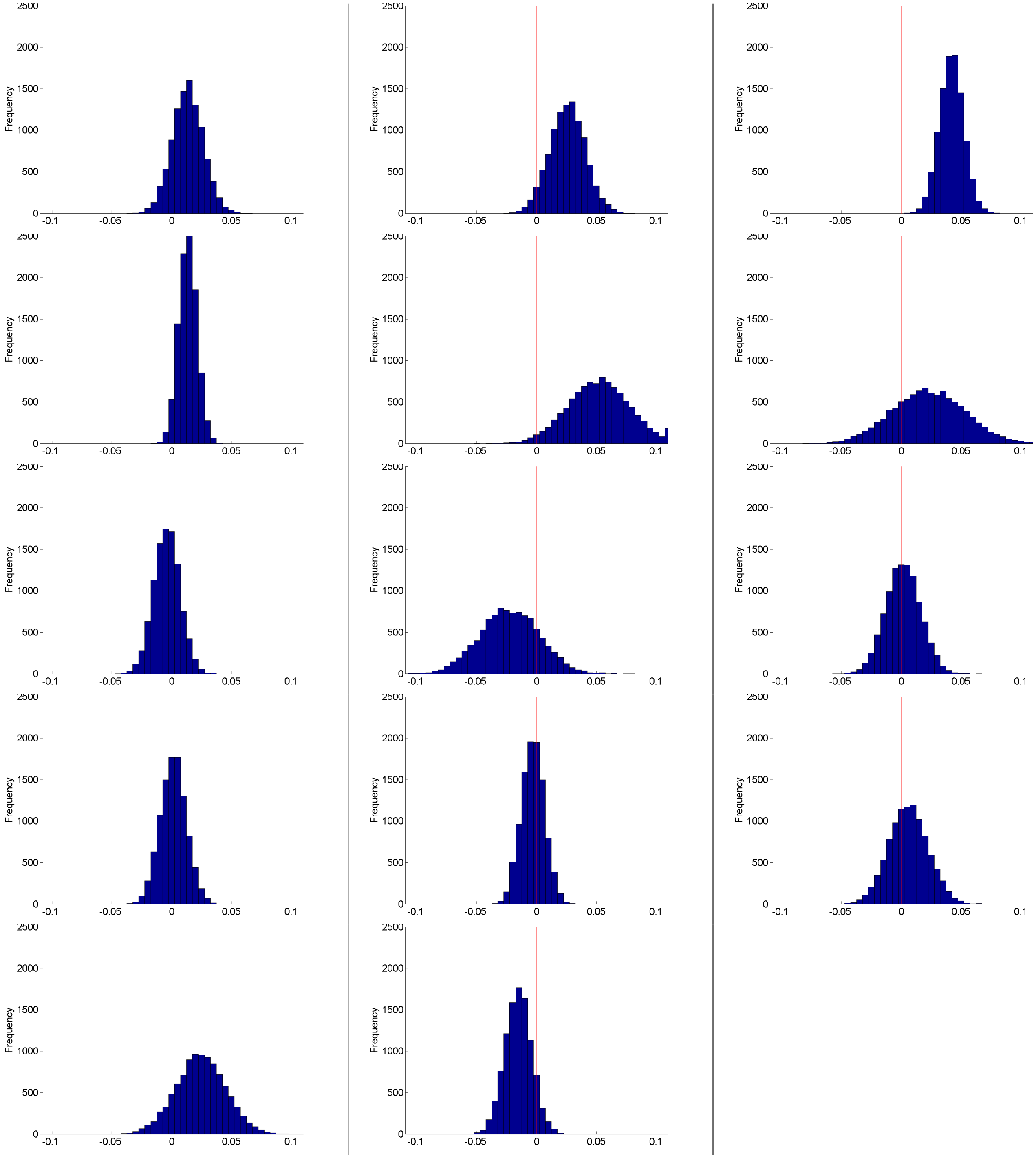

Figure 4.19: Linear trend of WACZ latitude in summer (JJAS) from CMIP3-AMIP scenario over the period 1978 to 2002. Top row (reanalysis product): (a) NCEP Reanalysis, (b) ERA-40, (c) ERA Interim. Second row: (d) CCSM, (e) CNRM, (f) GFDL. Third row: (g) GISS, (h)IAP, (i)IPSL Fourth row: (j) MIROC-mres, (k) MIROC-hires, (l) MPI. Fifth row: (m) MRI and (n) UKMO-HADGEM.

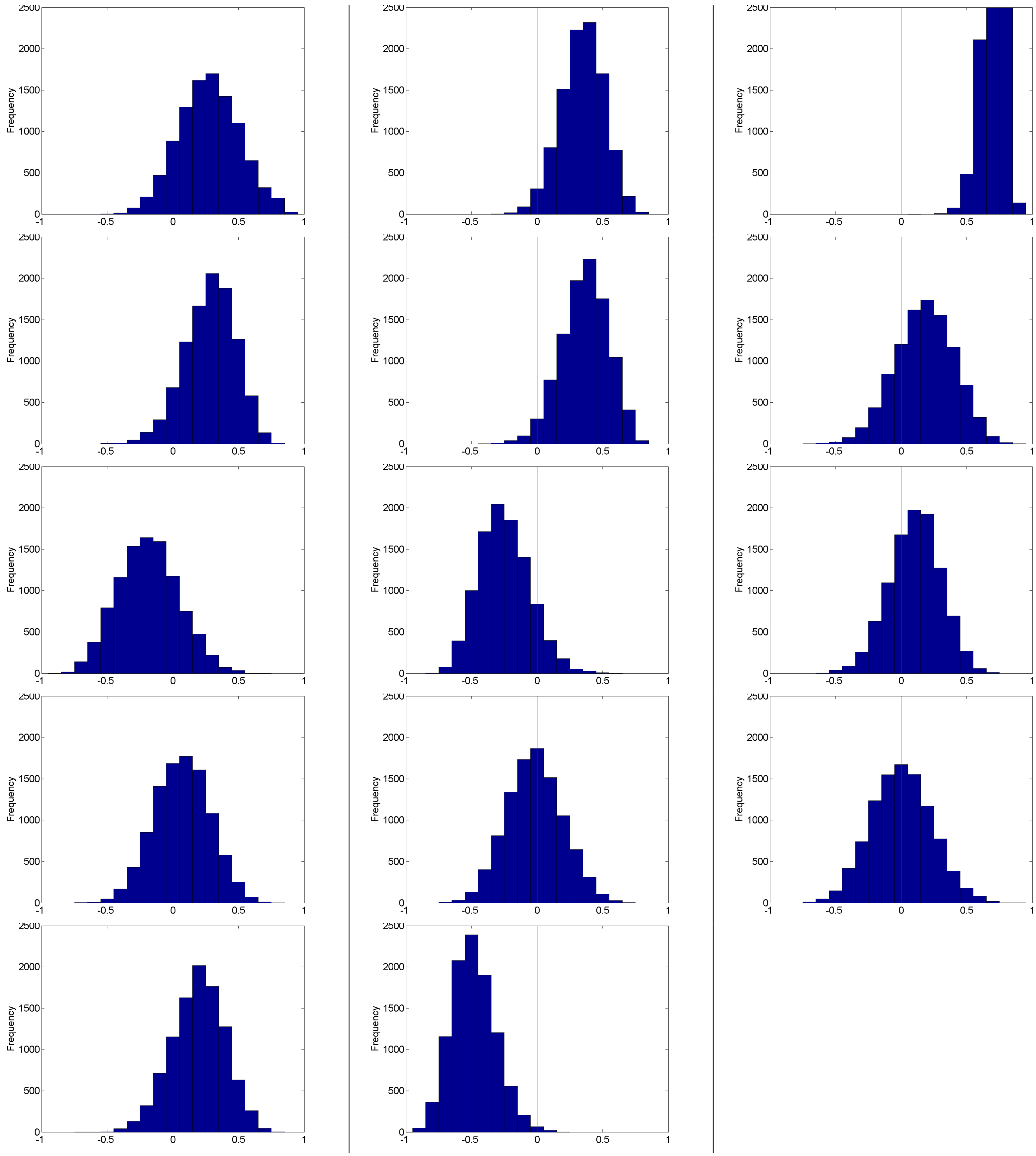

Figure 4.20: Correlation co-efficients between time and WACZ latitude in summer (JJAS) from CMIP3-AMIP scenario over the period 1978 to 2002. Top row (reanalysis product): (a) NCEP Reanalysis, (b) ERA-40, (c) ERA Interim. Second row: (d) CCSM, (e) CNRM, (f) GFDL. Third row: (g) GISS, (h)IAP, (i)IPSL Fourth row: (j) MIROC-mres, (k) MIROC-hires, (l) MPI. Fifth row: (m) MRI and (n) UKMO-HADGEM.

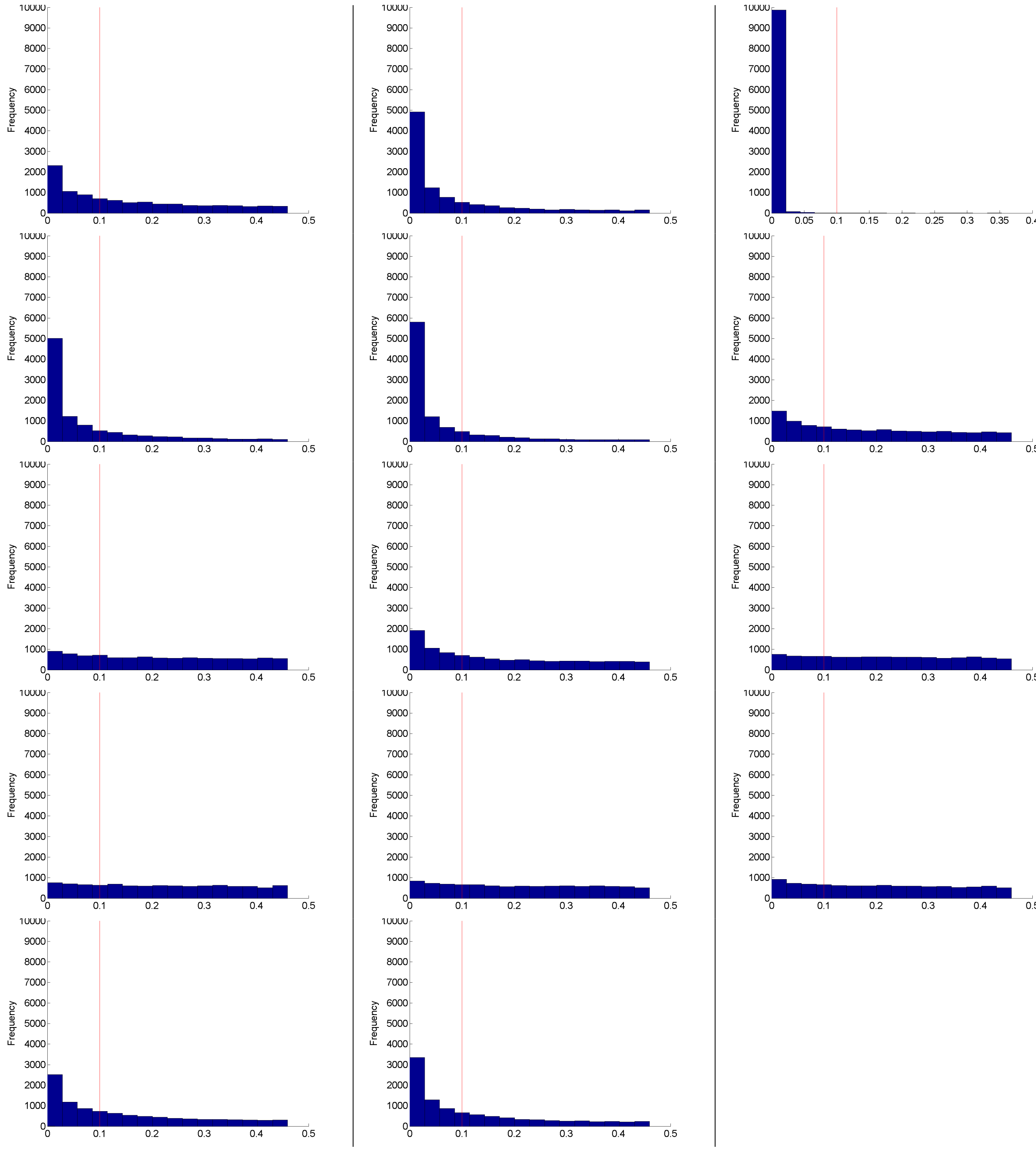

Figure 4.21: P-values of significance of trend of WACZ latitude in summer (JJAS) from CMIP3-AMIP scenario over the period 1978 to 2002. Top row (reanalysis product): (a) NCEP Reanalysis, (b) ERA-40, (c) ERA Interim. Second row: (d) CCSM, (e) CNRM, (f) GFDL. Third row: (g) GISS, (h)IAP, (i)IPSL Fourth row: (j) MIROC-mres, (k) MIROC-hires, (l) MPI. Fifth row: (m) MRI and (n) UKMO-HADGEM.

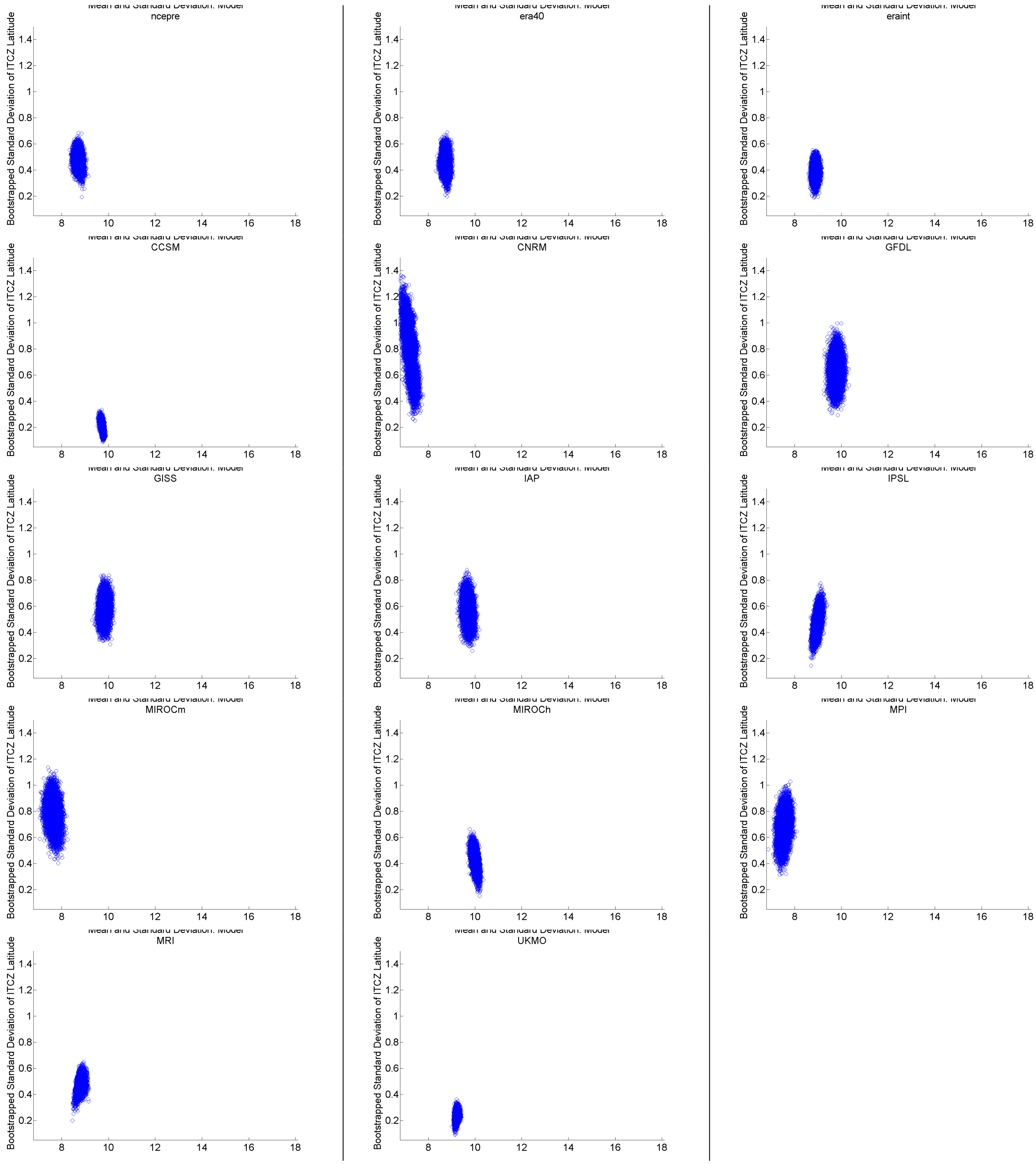

Figure 4.22: Mean and standard deviation of WACZ latitude in winter (DJFM) from CMIP3-AMIP scenario over the period 1978 to 2002. Top row (reanalysis product): (a) NCEP Reanalysis, (b) ERA-40, (c) ERA Interim. Second row: (d) CCSM, (e) CNRM, (f) GFDL. Third row: (g) GISS, (h)IAP, (i)IPSL Fourth row: (j) MIROC-mres, (k) MIROC-hires, (l) MPI. Fifth row: (m) MRI and (n) UKMO-HADGEM.

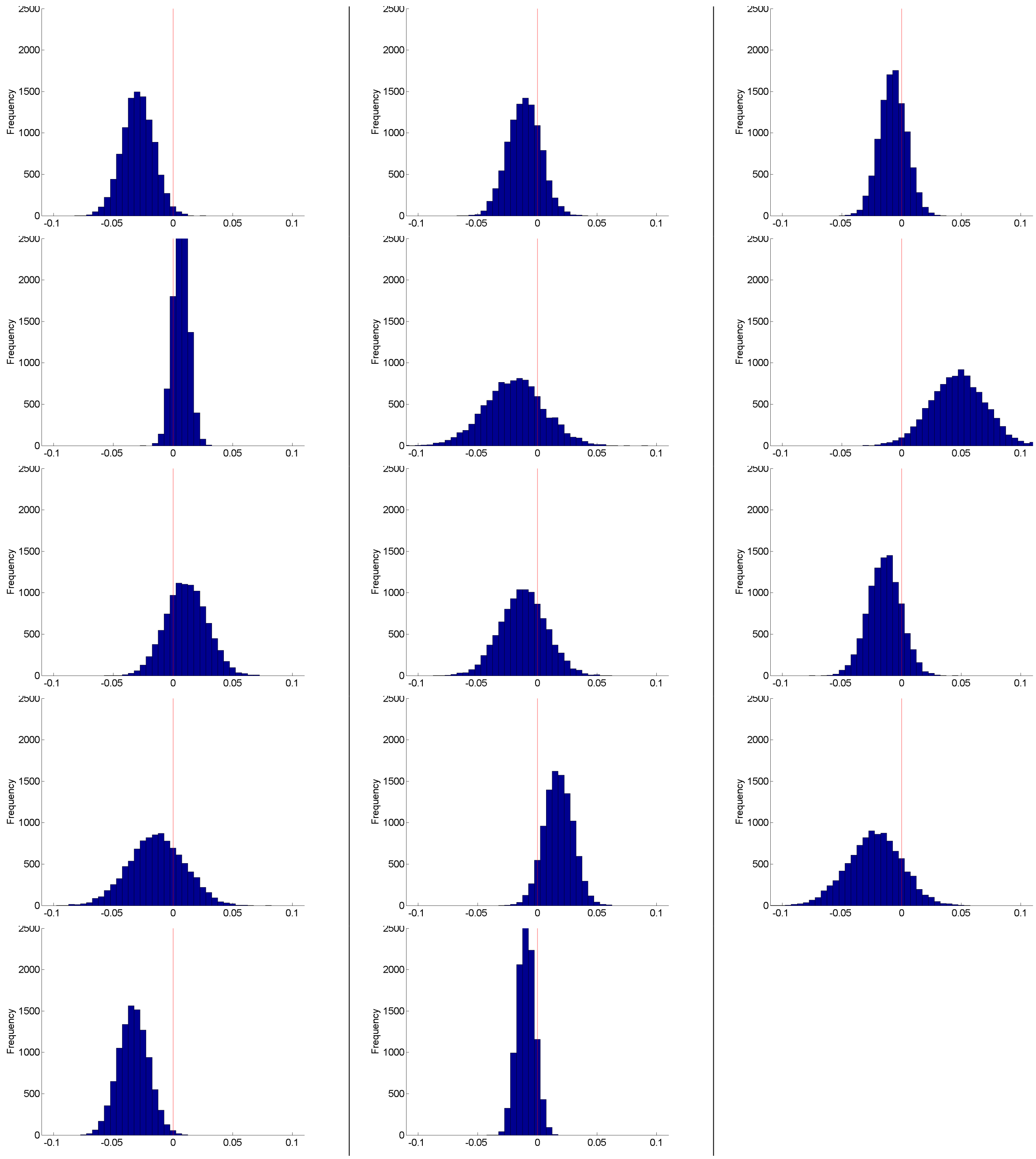

Figure 4.23: Linear trend of WACZ latitude in winter (DJFM) from CMIP3-AMIP scenario over the period 1978 to 2002. Top row (reanalysis product): (a) NCEP Reanalysis, (b) ERA-40, (c) ERA Interim. Second row: (d) CCSM, (e) CNRM, (f) GFDL. Third row: (g) GISS, (h)IAP, (i)IPSL Fourth row: (j) MIROC-mres, (k) MIROC-hires, (l) MPI. Fifth row: (m) MRI and (n) UKMO-HADGEM.

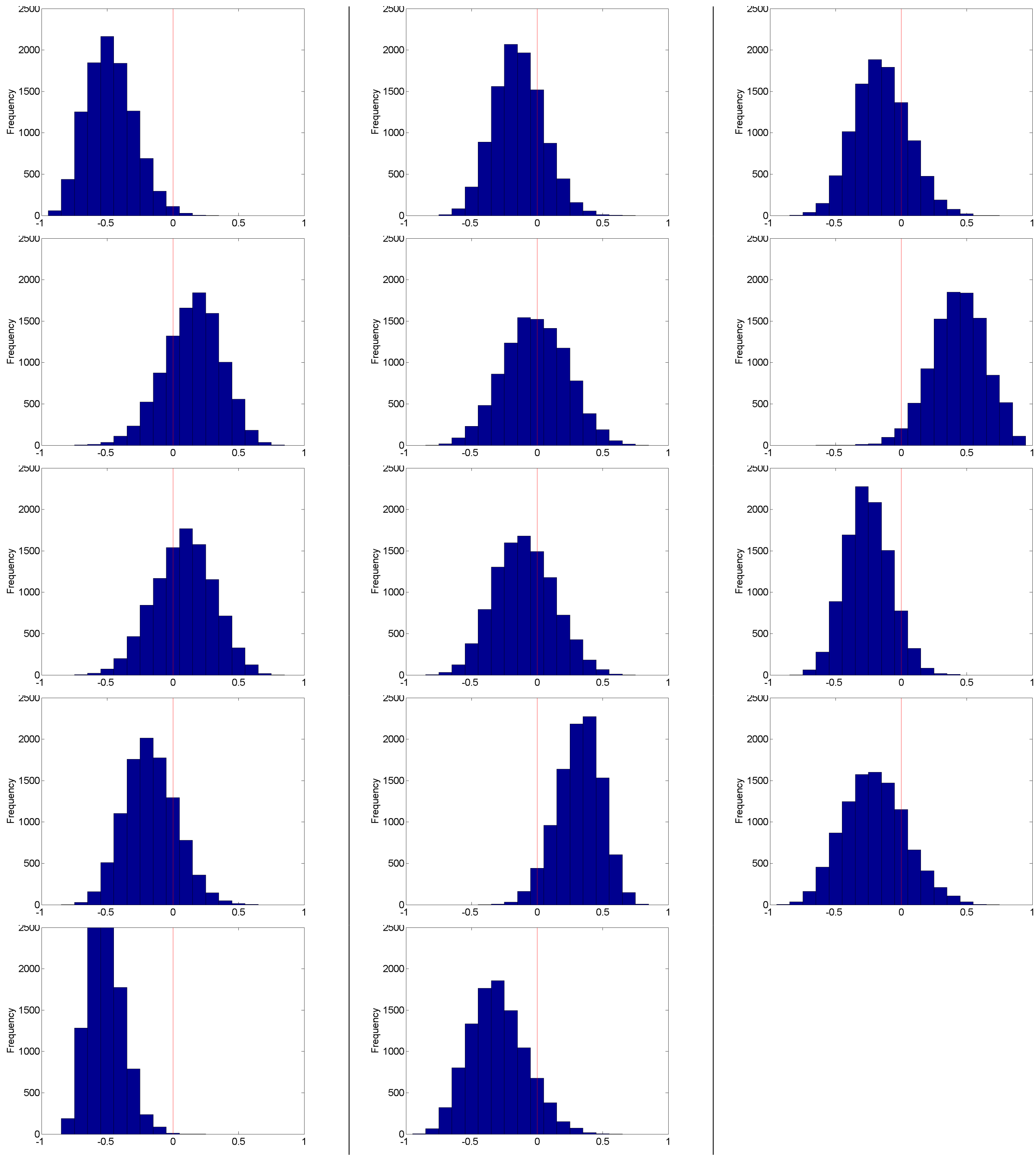

Figure 4.24: Correlation co-efficients between time and WACZ latitude in winter (DJFM) from CMIP3-AMIP scenario over the period 1978 to 2002. Top row (reanalysis product): (a) NCEP Reanalysis, (b) ERA-40, (c) ERA Interim. Second row: (d) CCSM, (e) CNRM, (f) GFDL. Third row: (g) GISS, (h)IAP, (i)IPSL Fourth row: (j) MIROC-mres, (k) MIROC-hires, (l) MPI. Fifth row: (m) MRI and (n) UKMO-HADGEM.

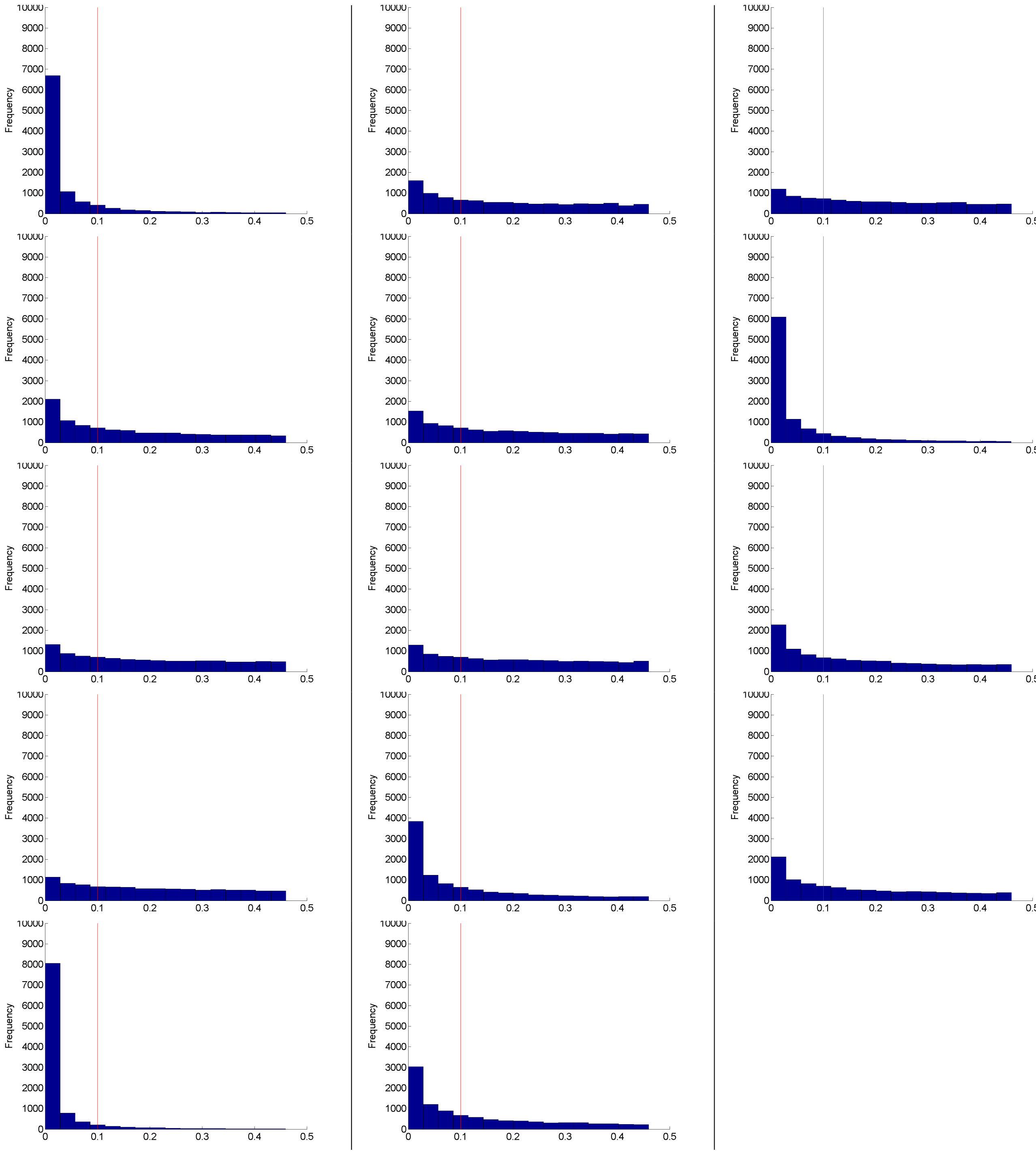

Figure 4.25: P-values of significance of trend of WACZ latitude in winter (DJFM) from CMIP3-AMIP scenario over the period 1978 to 2002. Top row (reanalysis product): (a) NCEP Reanalysis, (b) ERA-40, (c) ERA Interim. Second row: (d) CCSM, (e) CNRM, (f) GFDL. Third row: (g) ISS, (h) IAP, (i) IPSL Fourth row: (j) MIROC-mres, (k) MIROC-hires, (l) MPI. Fifth row: (m) MRI and (n) UKMO-HADGEM.

Table 4.1: Summary of key information on CMIP GCMs and Reanalysis used, including acronyms, host institution, resolution, start and end times for each scenario and the primary reference for each.

Model Acronym	Host Institution	Location	Resolution	Start	End	Reference
NCEP Reanalysis	NCEP NCAR	Boulder, CO, USA	2.5°× 2.5°	Jan 1948	present	*Kalnay et al.* [1996]
ERA-40	European Centre For Medium-Range Weather Forecasts	Reading, United Kingdom	2.5°× 2.5° Sep 1957	Aug 2002	[*Uppala et al.*, 2005]	
ERA-Interim	European Centre For Medium-Range Weather Forecasts	Reading, United Kingdom	1.5°× 1.5°	Jan 1979	present	[*Dee et al.*, 2011]
NCAR CCSM	National Center for Atmospheric Research	Boulder, CO, USA	1.40625°× 1.40625°	Jan 1978	Dec 2000	*Collins et al.* [2006]
CNRM-CM3	Centre National de Recherches Meteorologques, Meteo-France	Toulouse, France	2.8125°× 2.8125°	Jan 1979	Dec 2000	
GFDL AM2.1	NOAA Geophysical Fluid Dynamics Laboratory	Princeton, NJ, USA	2°× 2.5°	Jan 1980	Nov 1999	
GISS ModelE	NASA Goddard Institute for Space Studies	New York, NY, USA	4°× 5°	Jan 1979	Dec 2002	
IAP	Institute for Atmospheric Physics	Beijing, China	3°× 2.8125°	Jan 1978	Dec 1999	*Wang et al.* [2004]
IPSL	Institut Pierre Simon Laplace	Paris, France	2.5°× 3.75°	Jan 1979	Dec 2002	
MIROC (mres)	Center for Climate System Research	Tokyo, Japan	2.8125°× 2.8125°	Jan 1979	Dec 2002	
MIROC (hires)	Center for Climate System Research	Tokyo, Japan	1.125°× 1.125°	Jan 1979	Dec 2002	
MPI-ECHAM5	Max Planck Institute for Meteorology	Hamburg, Germany	1.875°× 1.875°	Jan 1978	Dec 1999	
MRI	Meteorological Research Institute	Tsukuba, Japan	2.8125°× 2.8125°	Jan 1979	Dec 2002	*Yukimoto et al.* [2001]
UKMO-HADGEM	Met Office	Exeter, United Kingdom	1.25°× 1.875°	Jan 1979	Dec 2000	

Table 4.2: Exploratory data analysis overview of annual means of WACZ Latitude W_ϕ using robust and resistant statistical measures. Median (°) is use to represent central tendency. Interquartile Range (IQR) (°) represents spread. Yule-Kendall Index represents skewness.

Model Acronym	Median	Interquartile Range	Skewness Index
NCEP Reanalysis	12.06	0.32	0.52
ERA-40	11.65	0.29	-0.03
ERA-Interim	12.59	0.36	0.20
CCSM	12.43	0.18	0.68
CNRM	11.98	0.41	-0.07
GFDL	12.54	0.21	-0.48
GISS	13.63	0.40	0.17
IAP	13.38	0.26	0.39
IPSL	12.34	0.38	0.51
MIROC-mres	10.99	0.22	-0.67
MIROC-hres	12.96	0.27	-0.14
MPI-ECHAM	12.08	0.26	-0.48
MRI	12.12	0.28	-0.15
UKMO-HADGEM	12.03	0.24	-0.84

Table 4.3: Pearson product-moment correlation coefficient matrix of annual means of WACZ latitude (W_ϕ) COA calculated from reanalysis products and CMIP-AMIP. Column headers abbreviations as follows: NCEP: NCEP Reanalysis, ERA 40: ERA 40, ERA IN: ERA Interim, R_μ: mean of three reanalysis products, and R_{q50}: median of three reanalysis products. An * indicates statistical significance at 10%, † at 5% and $^\diamond$ at 1%.

Model Acronym	W_ϕ				
	NCEP	ERA 40	ERA IN	R_μ	R_{q50}
NCEP Reanalysis	–	$0.52^\diamond$	-0.01	$0.64^\diamond$	$0.85^\diamond$
ERA-40	$0.52^\diamond$	–	$0.63^\diamond$	$0.93^\diamond$	$0.82^\diamond$
ERA-Interim	-0.01	$0.63^\diamond$	–	$0.74^\diamond$	$0.41^\dagger$
R_μ	$0.64^\diamond$	$0.93^\diamond$	$0.74^\diamond$	–	$0.90^\diamond$
R_{q50}	$0.85^\diamond$	$0.82^\diamond$	$0.41^\dagger$	$0.90^\diamond$	–
CCSM	-0.14	-0.40	-0.17	-0.34^*	-0.42
CNRM	-0.12	0.11	0.35^*	0.16	0.03
GFDL	-0.04	-0.36^*	0.11	-0.11	-0.17
GISS	-0.02	-0.01	-0.21	-0.12	-0.06
IAP	-0.01	0.33^*	0.28	0.27	0.16
IPSL	-0.06	0.07	0.09	0.05	-0.07
MIROC-mres	0.21	0.34^*	0.32^*	$0.38^\dagger$	0.37^*
MIROC-hres	0.23	$0.43^\dagger$	0.19	0.37^*	0.29
MPI-ECHAM	-0.02	-0.06	-0.18	-0.11	-0.03
MRI	-0.23	-0.20	-0.24	-0.30	-0.32^*
UKMO-HADGEM	0.14	-0.24	-0.17	-0.12	-0.01

Table 4.4: Mean absolute error and bias of WACZ COA latitude index (W_ϕ) in three reanalysis products and eleven global circulation models. Error and bias are calculated with respect to the median WACZ COA latitude index (W_ϕ) of three reanalysis products.

	W_ϕ MAE	W_ϕ B
NCEP	0.29	-0.19
ERA 40	030	-0.33
ERA I	0.49	0.49
CCSM	0.52	-0.51
CNRM	0.73	-0.66
GFDL	1.25	1.25
GISS	1.38	1.38
IAP	1.55	1.55
IPSL	0.37	0.05
MIROC-m	1.38	-1.38
MIROC-h	0.59	0.59
MPI	0.65	-0.62
MRI	0.94	-0.93
UKMO	0.70	-0.70

Table 4.5: Exploratory data analysis overview of WACZ latitude index for summer season (JJAS) means using robust and resistant statistical measures. Median is use to represent central tendency. Interquartile Range (IQR) represents spread. Yule-Kendall Index represents skewness.

Model Acronym	Median	Interquartile Range	Skewness Index
NCEP Reanalysis	15.03	0.45	-0.10
ERA-40	14.66	0.52	-0.37
ERA-Interim	16.35	0.54	-0.37
CCSM	14.96	0.41	0.18
CNRM	16.09	0.74	-0.28
GFDL	14.87	0.47	0.15
GISS	17.35	0.55	-0.21
IAP	16.24	0.29	1.27
IPSL	14.87	0.36	1.06
MIROC-mres	14.13	0.21	-0.60
MIROC-hres	15.71	0.34	0.39
MPI-ECHAM	16.23	0.37	0.19
MRI	14.97	0.46	-0.98
UKMO-HADGEM	14.47	0.39	0.20

Table 4.6: Pearson product-moment correlation coefficient matrix of summer (JJAS) means of WACZ latitude (W_ϕ) COA calculated from reanalysis products and CMIP-AMIP. Column headers abbreviations as follows: NCEP: NCEP Reanalysis, ERA 40: ERA 40, ERA IN: ERA Interim, R_μ: mean of three reanalysis products and R_{q50}: median of three reanalysis products. An * indicates statistical significance at 10%, † at 5% and $^\diamond$ at 1%.

Model Acronym	W_ϕ				
	NCEP	ERA 40	ERA IN	R_μ	R_{q50}
NCEP Reanalysis	–	$0.56^\diamond$	0.33^*	$0.70^\diamond$	$0.91^\diamond$
ERA-40	$0.56^\diamond$	–	$0.48^\dagger$	$0.83^\diamond$	$0.75^\diamond$
ERA-Interim	0.33^*	$0.48^\dagger$	–	$0.78^\diamond$	$0.41^\dagger$
R_μ	$0.70^\diamond$	$0.83^\diamond$	$0.78^\diamond$	–	$0.85^\diamond$
R_{q50}	$0.91^\diamond$	$0.75^\diamond$	$0.41^\dagger$	$0.85^\diamond$	–
CCSM	-0.18	-0.25	0.17	-0.09	-0.28
CNRM	0.11	0.12	$0.73^\diamond$	$0.42^\dagger$	0.19
GFDL	0.20	-0.08	0.24	0.15	0.15
GISS	0.00	0.22	0.14	0.17	0.06
IAP	-0.28	-0.24	-0.22	-0.34	-0.38
IPSL	0.10	0.03	-0.01	0.05	0.06
MIROC-mres	0.20	0.01	-0.03	0.06	0.07
MIROC-hres	0.23	-0.01	-0.14	0.03	0.15
MPI-ECHAM	-0.10	0.27	0.13	0.14	-0.01
MRI	-0.32	-0.06	0.06	-0.12	-0.25
UKMO-HADGEM	0.37^*	0.01	0.30	0.28	0.26

Table 4.7: Mean absolute error and bias of WACZ latitude index (W_ϕ) in three reanalysis products and eleven global circulation models for summer (JJAS). Error and bias are calculated with respect to the median WACZ latitude index (W_ϕ) of three reanalysis products.

	W_ϕ MAE	W_ϕ Bias
NCEP	0. 21	-0.12
ERA 40	0.78	-0.78
ERA I	0.88	0.88
CCSM	2.07	-2.07
CNRM	0.84	0.53
GFDL	1.04	0.92
GISS	1.35	1.35
IAP	2.22	2.22
IPSL	0.60	-0.27
MIROC-m	2.10	-2.10
MIROC-h	0.57	-0.49
MPI	0.52	0.02
MRI	1.75	-1.75
UKMO	2.14	-2.14

Table 4.8: Exploratory data analysis overview of WACZ COA in winter (DJFM) using robust and resistant statistical measures. Median is use to represent central tendency. Interquartile Range (IQR) represents spread. Yule-Kendall Index represents skewness.

	Median	Interquartile Range	Yule-Kendall Index
NCEP Reanalysis	9.26	0.37	-0.35
ERA-40	8.46	0.30	0.44
ERA-Interim	8.88	0.48	0.07
CCSM	9.74	0.24	-0.76
CNRM	7.73	0.57	-2.19
GFDL	10.37	0.44	0.05
GISS	9.56	0.61	0.74
IAP	10.17	0.68	1.02
IPSL	9.13	0.34	0.58
MIROC-mres	7.69	0.34	0.58
MIROC -hires	9.96	0.37	-1.09
MPI-ECHAM	8.24	0.71	0.40
MRI	9.23	0.72	0.57
UKMO-HADGEM	9.39	0.40	-0.22

Table 4.9: Pearson product-moment correlation coefficient matrix of winter (DJFM) means of WACZ latitude (W_ϕ) COA calculated from reanalysis products and CMIP-AMIP. Column headers abbreviations as follows: NCEP: NCEP Reanalysis, ERA 40: ERA 40, ERA IN: ERA Interim, R_μ: mean of three reanalysis products and R_{q50}: median of three reanalysis products. An * indicates statistical significance at 10%, † at 5% and $^\diamond$ at 1%.

Model Acronym	W_ϕ				
	NCEP	ERA 40	ERA IN	R_μ	R_{q50}
NCEP Reanalysis	–	$0.71^\diamond$	$0.77^\diamond$	$0.88^\diamond$	$0.84^\diamond$
ERA-40	$0.71^\diamond$	–	$0.86^\diamond$	$0.94^\diamond$	$0.88^\diamond$
ERA-Interim	$0.77^\diamond$	$0.86^\diamond$	–	$0.95^\diamond$	$0.97^\diamond$
R_μ	$0.88^\diamond$	$0.94^\diamond$	$0.95^\diamond$	–	$0.98^\diamond$
R_{q50}	$0.84^\diamond$	$0.88^\diamond$	$0.97^\diamond$	$0.98^\diamond$	–
CCSM	-0.24	-0.18	-0.33^*	-0.23	-0.24
CNRM	0.19	0.25	0.30	0.29	0.30
GFDL	-0.31	-0.11	-0.11	-0.18	-0.15
GISS	0.01	-0.19	-0.06	-0.11	-0.10
IAP	$0.45^\dagger$	$0.44^\dagger$	$0.56^\diamond$	$0.52^\diamond$	$0.57^\diamond$
IPSL	0.06	0.09	-0.16	0.01	-0.07
MIROC-mres	-0.04	-0.08	-0.08	-0.08	-0.09
MIROC-hres	$0.41^\dagger$	0.24	0.31	0.33^*	0.36^*
MPI-ECHAM	0.19	-0.08	-0.05	0.01	-0.02
MRI	0.12	-0.07	0.01	-0.01	-0.05
UKMO-HADGEM	0.26	-0.06	0.04	0.08	0.08

Table 4.10: Mean absolute error and bias of ITCZ COA indices in three reanalysis products and eleven global circulation models. Error and bias are calculated with respect to the median ITCZ COA indices of three reanalysis products.

	W_ϕ MAE	W_ϕ Bias
NCEP	0.18	-0.05
ERA 40	0.09	-0.04
ERA I	0.15	0.01
CCSM	0.95	0.95
CNRM	1.48	-1.45
GFDL	0.90	0.88
GISS	1.05	1.00
IAP	0.90	0.90
IPSL	0.51	0.17
MIROC-m	1.16	-1.10
MIROC-h	1.19	1.17
MPI	1.18	-1.18
MRI	0.41	0.02
UKMO	0.59	0.46

Table 4.11: Summary of statistics associated with the bootstrap analysis of linear trend of annual means over the period 1979 to 2002. $\text{Trend}_{0.5}$ is the median of the linear trend ($^\circ\text{yr}^{-1}$). r_{min} and r_{min} are the 95 % confidence interval of the correlation between W_ϕ. $r_{0.5}$ is the median correlation coeffient. $p_{0.5}$ is the median probability to reject the hypothesis that a trend exists using a t-test.

	$\text{Trend}_{0.5}$	r_{min}	r_{max}	$r_{0.5}$	$p_{0.5}$
NCEP	-0.0152	-0.425	0.424	-0.0532	0.031
ERA-40	0.0154	0.00497	0.65	0.355	0.042
ERA Interim	0.0171	-0.0487	0.593	0.287	0.0167
CNRM	0.0203	-0.193	0.637	0.253	0.0716
CCSM	0.00368	-0.367	0.51	0.0963	0.128
GFDL	0.0251	-0.169	0.723	0.342	0.0494
GISS	0.0118	-0.196	0.628	0.236	0.141
IAP	-0.0032	-0.429	0.375	-0.0284	0.212
IPSL	-0.0051	-0.492	0.213	-0.138	0.185
MIROC-hres	0.0116	-0.133	0.595	0.261	0.0395
MIROC-mres	-0.0079	-0.433	0.471	-0.0255	0.178
MPI	0.0054	-0.415	0.471	0.029	0.196
MRI	-0.00598	-0.556	0.244	-0.149	0.171
UKMO	-0.00546	-0.646	0.0775	-0.329	0.113

Table 4.12: Summary of statistics associated with the bootstrap analysis of linear trend in summer (JJAS) over the period 1979 to 2002. $\text{Trend}_{0.5}$ is the median of the linear trend ($^{\circ}\text{yr}^{-1}$). r_{min} and r_{min} are the 95 % confidence interval of the correlation between W_{ϕ}. $r_{0.5}$ is the median correlation coeffient. $p_{0.5}$ is the median probability to reject the hypothesis that a trend exists using a t-test.

	$\text{Trend}_{0.5}$	r_{min}	r_{max}	$r_{0.5}$	$p_{0.5}$
NCEP	0.0134	-0.172	0.744	0.275	0.116
ERA-40	0.0261	0.00833	0.646	0.351	0.0303
ERA Interim	0.0421	0.504	0.833	0.703	0.0000101
CNRM	0.0524	-0.0128	0.684	0.37	0.0174
CCSM	0.0136	-0.141	0.619	0.297	0.0287
GFDL	0.0225	-0.282	0.603	0.185	0.164
GISS	-0.00404	-0.624	0.257	-0.192	0.205
IAP	-0.0227	-0.599	0.15	-0.261	0.137
IPSL	0.00155	-0.289	0.467	0.111	0.217
MIROC-hres	-0.00301	-0.422	0.408	-0.0223	0.213
MIROC-mres	0.00126	-0.349	0.472	0.07	0.217
MPI	0.00595	-0.423	0.477	0.00226	0.209
MRI	0.0243	-0.225	0.559	0.2	0.103
UKMO	-0.0152	-0.78	-0.129	-0.493	0.0694

Table 4.13: Summary of statistics associated with the bootstrap analysis of linear trend of winter (DJFM) means over the period 1979 to 2002. $\text{Trend}_{0.5}$ is the median of the linear trend ($^{\circ}\text{yr}^{-1}$). r_{min} and r_{min} are the 95 % confidence interval of the correlation between W_{ϕ}. $r_{0.5}$ is the median correlation coeffient. $p_{0.5}$ is the median probability to reject the hypothesis that a trend exists using a t-test.

	$\text{Trend}_{0.5}$	r_{min}	r_{max}	$r_{0.5}$	$p_{0.5}$
NCEP	-0.0294	-0.789	-0.102	-0.486	0.00967
ERA-40	-0.0109	-0.491	0.2542	-0.148	0.161
ERA Interim	-0.00711	-0.534	0.266	-0.158	0.182
CNRM	-0.0191	-0.487	0.46	-0.0158	0.163
CCSM	0.00657	-0.308	0.546	0.163	0.128
GFDL	0.0475	0.00421	0.813	0.442	0.0145
GISS	0.0111	-0.368	0.509	0.0881	0.178
IAP	-0.0116	-0.527	0.367	-0.106	0.183
IPSL	-0.0142	-0.58	0.103	-0.258	0.12
MIROC-hres	0.0176	-0.0372	0.619	0.331	0.0551
MIROC-mres	-0.0136	-0.522	0.237	-0.179	0.185
MPI	-0.0223	-0.633	0.293	-0.211	0.129
MRI	-0.0332	-0.739	-0.226	-0.526	0.00269
UKMO	-0.00951	-0.672	0.156	-0.312	0.0813

Table 4.14: Summary of total absolute mean error (MAE) in models and reanalysis relative to median reanalysis values. The models are sorted in ascending order of MAE.

	Annual	DJFM	JJAS	Total
NCEP	0.29	0.18	0.21	0.68
ERA 40	0.30	0.09	0.78	1.17
ERA I	0.49	0.15	0.88	1.52
IPSL	0.37	0.51	0.60	1.48
MIROC-hres	0.59	1.19	0.57	2.35
MPI	0.65	1.18	0.52	2.35
CNRM	0.73	1.48	0.84	3.05
MRI	0.94	0.41	1.75	3.10
GFDL	1.25	0.90	1.04	3.19
UKMO	0.70-	0.59	2.14	3.43
CCSM	0.52	0.95	2.07	3.54
GISS	1.38	1.05	1.35	3.78
MIROC-mres	1.38	1.16	2.1	4.64
IAP	1.55	0.90	2.22	4.67

Table 4.15: Summary of p-value statistics associated with the bootstrap analysis of linear trend of winter (DJFM) means over the period 1979 to 2002. Table counts instances in which a reanalysis product (left) or model (right) expresses a significant trend, as determined by a p-value from a two-tailed asymmetric t-test statistic. P-values of greater than 0.1 are described as an insignificant trend or no trend, p-values below 0.1 but in excess of 0.02 are described as significant trend, and p-values below 0.02 are described as extremely significant.

	Reanalysis					CMIP AMIP Models				
	Ext. Neg. Trend	Sig. Neg. Trend	No Trend	Sig. Pos. Trend	Ext. Pos. Trend	Ext. Neg. Trend	Sig. Neg. Trend	No Trend	Sign. Pos. Trend	Ext. Pos. Trend
	$p < 0.02$	$p < 0.1$	$p \geq 0.1$	$p < 0.1$	$p < 0.02$	$p < 0.02$	$p < 0.1$	$p \geq 0.1$	$p < 0.1$	$p < 0.02$
Annual	0	1	0	1	1	0	0	8	3	0
JJAS	0	0	1	1	1	0	1	8	2	0
DJFM	1	0	2	0	0	1	0	9	1	0

Chapter 5

Predicted Changes in Position of Intertropical Convergence Zone Over West Africa in 21st Century in CMIP3

5.1 Introduction

Precipitation in the tropics, the narrow band between 15° N and 15° S accounts for more than one third of global precipitation [*Simpson et al.*, 1988]. The latent heating resulting from this extreme rate of precipitation is of great importance to global climate; impacting both regional weather and weather in mid-latitude regions. Moreover the radiation of the tropical atmosphere is of great interest and has been studied extensively on decadal timescales [*Chen et al.*, 2002; *Wielicki et al.*, 2002].

A large fraction of the precipitation in the tropics is associated with upward motion in the ascending branch of the Hadley Cell, the dominate feature in the tropical atmosphere [*Oort and Yienger*, 1996]. As such changes in circulation associated with the Hadley Cell have been extensively studied. Multiple studies using observations have suggested that the Hadley Cell has increased in strength towards the end of the 20th century [*Chen et al.*, 2002; *Tanaka et al.*, 2004; *Mitas and Clement*, 2005]. However in contrast most GCMs predict a weakening of the Hadley Cell in recreations of the 20th century [*Mitas and Clement*, 2006]. Both observational and modeling studies have focused on the "strength" of the Hadley Cell to assess variability. For example in both *Mitas and Clement* [2005] and *Mitas and Clement* [2006] streamfunction and velocity potential are used to quantify the strength of the Hadley Cell. While this approach is effective in assessing changes in the mean overturning of the atmosphere, this approach does not provide information about potential changes in the position of the Hadley Cell.

More recently research suggests that the Hadley Cell expanded towards the end of the 20th century and is likely to expand further in the 21st century as the climate warms. *Hu and Fu* [2007] find using outgoing longwave radiation (OLR) data derived from multiple satellite measurements a poleward expansion of the Hadley Cell of 2.4° in winter (DJF) and 2.2° in summer (JJA) over both hemispheres over the period 1979 to 2005. Some of the widening of the Hadley Cell has been attributed to depletion of ozone [*Polvani and Kushner*, 2002] while the pole to equator temperature gradient and mid-latitude storm track activity are also related to the poleward position of the Hadley Cell.

Over West Africa the WACZ represents the ascending branch of the Hadley Cell [*Folland et al.*, 1986]. The position of the WACZ is of great importance in determining the spatial extent of precipitation in sub-Sahran Africa, where northward movement of the WACZ could lead to increases in precipitation in the Sahel and decreases in precipitation in traditionally wetter regions nearer to the equator. Interannual variability of the latitude of the WACZ has been shown previously to be important in determining the annual emission and transport of mineral dust from West Africa to the Americas [*Doherty et al.*, 2012a]. The natural question arises of what are the implications of changes in strength and poleward expansion of the Hadley Cell on the position of the WACZ? While as previously mentioned much attention has been paid to the Hadley Cell in general, less work has been paid to the ascending branch of it in detail. *Gastineau et al.* [2008] looking at multiple GCMs showed that the ascending branch of the Hadley Cell, located near to the equator, may shift in the 21st century, although the direction of the shift was unclear. This work was done examining the streamfunction at 500 hPa.

In this work we apply the COA framework to 21st century projections in CMIP GCMs to assess changes in the latitudinal position of the WACZ focusing on answering three questions. (1) What interannual and decadal variability in the latitude of the WACZ do GCMs predict for the 21st century and how does this compare to 20th century observations and in GCMs from AMIP? (2) Is the northward trend observed in the 20th century (see chapter 4) continued in GCMs in the 21st century? (3) Do models that performed poorly in AMIP perform differently than those models identified as strong performing models in the 21st century?

The structure of this chapter is as follows. In Section 5.2 the models and climate scenarios used in this project are introduced. In Section 5.3 we present the results, divided by scenario. For each scenario annual, summer and winter means are discussed focusing on changes in mean state compared to 20th century, changes in variability of W_ϕ and trends over the 21st century. In Section 5.4 we discuss our results in context of the literature and the implications for mineral dust emission and transport in the 21st century. In Section 5.5 we conclude our findings.

5.2 Data and Methods

5.2.1 CMIP and the SRES Scenarios

For the sake of consistency models used in this analysis are identical to those used in the prior chapter. All models were again taken from the CMIP-3 modeling inter-comparison project. The exact years included in the analysis are contained in Table 5.1. Here we note that the

UKMO model employed in the AMIP analysis in Chapter 4 is only available for one of two climate scenarios analyzed here, it is omitted from the scenario in which it is missing. Table 5.2 provides an overview of the socioeconomic assumptions of the two climate scenarios used in this work (reproduced from *Solomon et al.* [2007]). Each scenario is described in more detail below.

The A1 scenarios are characterized by a world in which rapid economic growth is prioritized within an “integrated world” or one that exchanges new and efficient technological advances freely. In the A1 scenarios global human population continues its exponential growth until reaching a maximum of 9 billion in the year 2050 and then following the demographic transition slowly decreases with time. In this scenario it is assumed that developing countries develop quickly and in time global income and lifestyles become more homogeneous. The specific scenario used in this study (A1B) assumes that energy is derived from a mix of fossil fuel, nuclear and alternative energies. For comparison other A1 scenarios (not used in this study) utilize an either an all fossil fuel energy source (A1FI) or an energy supply focused on alternatives (A1T). As such A1B represents a middle ground between the extremes of energy source scenarios.

In contrast the B1 scenarios reflect a future that is considered to be ecologically friendly in which global attention is paid to solving environmental problems as they emerge. In these scenarios rapid economic growth indeed occurs however the focus of growth is a service and information based economy, demanding less energy use. These scenarios assume reductions in material consumption and development and distribution of clean, resource efficient technologies. Population growth is identical to scenario A1.

Figure 5.1 shows the total emissions in the 21st century associated with both scenarios and additional SRES scenarios. Scenario A1B shows enhanced emissions relative to Scenario B1, but less than other scenarios in which fossil fuels use is encouraged. Likewise Scenario B1 shows a reduction relative to Scenario A1B, but is not the scenario with minimal emissions. As such Scenario A1B and Scenario B1 represent moderate scenarios within the manifold of all expected scenarios. Indeed as the “best estimate” of 21st century warming is given a range of between 0.6°C and 4.0°C in the varied scenarios, the warming expected with A1B and B1 of 2.8°C and 1.8°C, respectively, again places the scenarios toward the middle of possible outcomes.

Otherwise all methods employed in this chapter are identical to those used in Chapter 4, Section 4.3.

5.3 Results

Next we present an overview of the mean state, variability and trends of divergence at 925 hPa and W_ϕ as calculated from divergence in CMIP3 GCM. We compare the output from two scenarios SRES-A1B and SRES-B1 to each other and to 20th century reanalysis and the CMIP3-AMIP scenario as discussed in Chapter 4. The structure of this section is as follows. For each scenario we present a brief overview of how the model handles the annual migration of the WACZ and its interannual variability. Next for both summer (JJAS) and winter (DJFM) we present a detailed overview of how models handle the spatial distribution of divergence, discuss both inter-annual and decedal variability in W_ϕ and conclude with a discussion of trends in each season.

5.3.1 Scenario: SRES-A1B

Annual Means

The primary mode of variability for the ITCZ over West Africa is its annual south to north migration occurring each boreal winter into summer. Figure 5.2 presents the first loading pattern of the EOF of 925 hPa divergence for the eleven CMIP models in scenario SRES-A1B for all months over the period 2000 to 2100. Each model replicates the south-north dipole, with a pattern flipping sign in the latitude belt 8° N to 16° N. We note differences in relative magnitude are proportional to model resolution, with higher resolution models having lower relative magnitudes suggesting that a larger degree of variability in these models is contained in other features.

The seasonal cycle of W_ϕ is shown in Figure 5.3. Again each model captures a south to north migration of the WACZ latitude index however the amplitude (annual range) and phase (timing) of the migration vary from model to model estimation of the oscillation. In the 20th century reanalysis we noted a asymmetric seasonal cycle, with a slow and steady northward migration in boreal spring into early summer, and then a rapid irregular southward migration in autumn. We note that CCSM, IPSL, MIROC-h, MRI and UKMO (Figures 5.3a,f,h,j–k) show a rather steady and smooth southward migration in fall, in contrast to 20th century reanalysis which featured a less symmetric north to south migration. GFDL, GISS and UKMO (Figures 5.3c–d,k) show two annual peaks, an early peak in May and a secondary peak in July–August, this feature was not evident in 20th century reanalysis or in AMIP model scenarios.

The time-series of 21st century W_ϕ in scenario SRES-A1B is shown in Figure 5.4, for comparison 20th century reanalysis products are shown in Figure 5.5. Visual inspection of the time-series of W_ϕ suggest a northward trend with time, later in this section we confirm this trend in a full trend analysis. Accompanying Figure 5.4 is Table 5.3, which shows the median, interquartile range and skewness of W_ϕ annual means. Here we note that the models show reduced interannual variability compared to 20th century reanalysis (Figure 5.5) and do not show any evidence of multi-decadal variability. Figure 5.5 shows evidence of the drought-like conditions in the 1970's and 1980's in which the WACZ was shifted southward, and precipitation was correspondingly reduced in the Sahel. During this period in NCEP Reanalysis the WACZ is on average 2 degrees south of its position in the 1950's and 1960's, and a degree south of its position in the 2000's. Visual analysis of model WACZ in Figure 5.4 shows no similar multi-decadal shifts in the position of the WACZ. Likewise inter-annual variability is reduced in models in the 21st century in Figure 5.4 compared to reanalysis products in the 20th century in Figure 5.5.

In summary, models are able to capture the annual migration of the ITCZ over West Africa, although some irregularities in monthly position are noted as compared to the 20th century. A northward trend is visibly evident in the time-series of W_ϕ. Less variability is produced by models relative to the 20th century observations on both inter-annual and decadal scales. It is not clear if such reductions in variability are related to model error, or rather are prediction for reductions in the 21st century. In the next section we analyze models prediction of the summer season.

Summer Means

We expect, based on 20th century reanalysis, that the first mode of summer (JJAS) means should reflect changes in phase associated with seasons in which the WACZ is north and seasons in which the WACZ is south. Figure 5.6 shows the first mode of annual summer means over the period 2000–2100 in scenario SRES-A1B. In general we note the first loading pattern of the EOF is associated with changes in phase of the WACZ, with a dipole evident about the mean summer position of the WACZ (Figure 5.7, generally 16° N to 18° N). In models with high resolution such as CCSM, MIROC-h (Figures 5.6a,k) we note lower relative magnitudes, suggesting less of total variability is associated with changes in north-south phase.

The long term mean 925 hPa divergence is shown in Figure 5.7. The majority of models show a East-West band of convergence just north of 16° N. Over westernmost Africa, this East-West band experiences a slight bend and slight northward jog relative to central and east Africa (this was also seen in the 20th century). Figure 5.8 shows the difference of individual models in 21st century, scenario SRES-A1B minus the median of 20th century reanalysis products. Under this convention negative values represent increased convergence in the 21st century relative to the 20th, and positive values represent reduced convergence in the 21st century than the 20th century. IAP (Figure 5.8e) is a good example of mean model response, with a reduction in convergence century north of 16° N concurrent with increased convergence south of 16° N, overall suggesting a mean southward shift of the WACZ in SRES-A1B in the 21st century. MIROC-h and UKMO (Figures 5.8h,k) are examples of models that show the opposite, both exhibiting a northward shift of the WACZ in SRES-A1B. The southward shift in position of the zone of convergence associated with the WACZ seen in most models from 20th century to the 21st century could be a result of one of two factors; a net bias in position between scenarios or a shift with time and changing atmospheric forcing. In the case of the former, a large shift in position between the 20th century and 21st century without a trend would be indicative of model induced bias. We examine the latter possibility by looking at trends in the record later in this section.

Figure 5.9 couples W_ϕ with W_λ to show a graphical representation of the position of the WACZ over West Africa. A summary of median of W_ϕ location and spread (interquartile range) are presented in Table 5.5. Comparison with similar plots from the AMIP scenario of the 20th century as shown in Chapter 4 confirms the southward shift as suggested in previous figures. Figure 5.10 shows the boxplot of summer means of W_ϕ in all models, presented next to each other for comparison purposes. Horizontal lines across Figure 5.10 show the maximum and minimum values of median annual values. IAP and IPSL have medians above (north of) the range of the model median, and MIROC-m and UKMO have medians below (south of) the range of model medians. IPSL, MIROC-h and MRI all have reduced ranges compared to other models, suggesting lower seasonal variance. The time-series of W_ϕ in the 21st century for SRES-A1B is presented in Figure 5.11 and for comparison the time-series of W_ϕ in reanalysis products during the 20th century is shown in Figure 5.12. The models produce less inter-annual variability than do 20th century reanalysis products. Again evidence of a southern phase of W_ϕ in the 1970's and 1980's is seen in reanalysis while models do not predict any decadal shifts of similar magnitude in the 21st century. A northward trend over the 21st century is evident in most models.

To assess the significance of the northward trend we employ a bootstrapping technique on linear regression. Our time-series of summer means is re-sampled 10,000 times and the linear trend, correlation with time, a p-value associated with the slope of the linear trend are calculated once for each of our 10,000 time-series. An overview of the median and standard deviation of each re-sampling is shown in Figure 5.13. A summary of key statistics is shown in Table 5.6. Figure 5.14 shows the distribution of linear trends for each of the 10,000 model re-samplings, a clear majority of models exhibit a positive (northward) trend on the order of 0.01 ° yr^{-1}. GISS (Figure 5.14d) is the outlier, indicating a negative (southward) trend. Figure 5.15 shows a positive correlation between W_ϕ and time suggesting a northward, linear trend. Figure 5.16 shows the significance of the trend as assessed by a student's t-test on linear regression co-efficients. Empty histograms show that all tests were near zero, indicating significance of the trend. CCSM, GISS and MRI all contained some samplings that were insignificant, however the majority of cases for each (at least 95%) were significant at $\alpha = 0.1$.

In summary we note in summer that a north-south dipole is the main mode of variability suggesting that north-south changes in phase of W_ϕ is the dominant climate factor associated with 925 hPa divergence. As predicted W_ϕ has little inter-annual and multi-decadal variability, especially when compared to 20th century reanalysis variability, which showed both large interannual and decadal variability. Compared to 20th century reanalysis the majority of models experience a southward shift in mean state, but experience a northward trend in time, suggesting a major southward bias introduced in 21st century model runs which is manifested at year 2000 and reduces over time accounting to the superimposed northward temporal trend.

Winter Means

Most models identify a north-south dipole associated with inter-annual changes in phase of the WACZ during winter? as shown in Figure 5.17. We note the dipole shifts towards West Africa, consistent with 20th century reanalysis. All models feature this dipole pattern, each centered about 8° to 10° N.

The climatological winter mean of 925 hPa divergence as seen in scenario SRES-A1B is shown in Figure 5.18. Clear, consistent east to west bands of convergence are visible between 8° to 12° N in each model, although clear differences in mean state are visible between models. Model-to-model variability appears to be reduced from summer (as it was in the 20th century), a strong example of which is shown in CCSM (Figure 5.18a).

Spatial plots showing the 20th century divergence from median reanalysis minus the 21st century divergence from the models in winter are shown in Figure 5.19. The negative values (yellow) represent increased convergence from the 20th century, and positive values (green) reduced convergence from the 20th century. Thus a green strip north of a yellow strip implies a southward shift and vice-versa. The color shading shows the magnitude of difference, with darker colors representing large difference and white shading representing no difference. Four models suggest a southward shift in the WACZ (CCSM, CNRM, MPI and UKMO; Figures 5.19a,b,i,k) while three models suggest a northward shift (IPSL, IAP, GFDL; Figures 5.19c,e–f). Two models show very little difference between 21st and 20th century runs (GISS, MRI; Figures 5.19d,j). Both MIROC simulations (MIROC-h and MIROC-m; Figures 5.19g–h) show less divergence in 20th century than in simulation over most of the domain. Shifts in mean position could indicate a trend, or a discontinuity or shift in model state between simulations. We further evaluate observe trends later in this section.

Next we examine the geographical placement of the WACZ COA on a year to year basis by coupling W_ϕ and W_λ in Figure 5.20. Information about the mean state, spread and skewness of W_ϕ is shown in Table 5.7. Models place the COA generally in the Niger River basin, on average just to the west of the meeting of the Niger and the Benue River. There are differences between models in placement of the WACZ with the MIROC-mres model placing it near to the Atlantic Ocean (Figure 5.20g) and the IPSL model placing the WACZ just south of the Sahel (Figure 5.20f). This range in latitudinal placement is also seen in Figure 5.21. The horizontal lines represent the maximum and minimum values of the median of winter means of W_ϕ in all model runs over the period 2000 to 2100. IPSL and MIROC-mres are shown to be north and south outliers respectively.

The time-series of W_ϕ in each model run is shown in Figure 5.22, for comparison the time-series of W_ϕ from reanalysis is shown in Figure 5.23. In 20th century reanalysis we note more cohesion between reanalysis products in time and less inter-annual variability than in summer. In winter there is less evidence for decadal variability than in summer, with values in general declining from the 1960's into the drought period of the late 1970's and 1980's, but no northward recovery into the 1990's and 2000's or other oscillations evident. 21st century model runs consistently produce less inter-annual variability than the 20th century and also produce less variability than 20th century reanalysis. We note that while NCEP reanalysis had a range of 2 degrees from 1980 to 2000, few 21st century models replicate this degree of variability. It is unclear if this reduction in variability is a result of model errors or are driven by changes in climate.

A northward progression in the position of W_ϕ is visible in Figure 5.22. To assess the significance of this trend we perform a bootstrap analysis on the linear regression of W_ϕ, the means and standard deviations of which are shown in Figure 5.24. Ten of eleven models indicate a northward trend in time as shown in Figures 5.25 and 5.26 and Table 5.27. Of the ten models with a northward trend all ten are significant at an alpha of 10% and nine of ten are significance at an alpha of 2%. The significance of the trend is summarized in Figure 5.27. Again, similar to the summer means, the outlying model that does not indicate a northward trend is the lower-resolution GISS model.

To summarize, in winter, models identify a north-south dipole as the first EOF mode suggesting that north south variability in the position of the WACZ is the dominant feature of 925 hPa divergence. Models produce less variability of W_ϕ in the 21st century than the 20th century on an annual timescale, but are consistent with 20th century reanalysis for decadal variability. Over the course of the 21st century W_ϕ is shown to significantly increase in time in ten of eleven models.

5.3.2 Scenario: SRES-B1

We repeat the analysis of 925 hPa divergence and W_ϕ in scenario SRES-B1 over the period 2000–2100. As discussed in Section 5.2 the SRES-B1 is a less extreme climate scenario, assuming that some actions are taken to mitigate the release of fossil fuels and in term greenhouse gas forcing on the climate system. Overall results for Scenario SRES-B1 are similar to SRES-A1B (as previously discussed) with only slight changes in strength, position and trends of divergence and W_ϕ observed. In this section we will present a shortened overview of the analysis and a comparison of SRES-B1 to SRES-A1B which has already been discussed.

Annual Means

Figure 5.28 shows the first loading pattern of the EOF of all months over the period 2000 to 2100. Similar to both 20th century reanalysis, AMIP model runs and SRESA1-B scenario runs the dominant feature is a north-south dipole that reflects the annual south to north migration of the WACZ. The relative magnitude of the pattern is inversely proportional to model resolution, that is to say high resolution models have lower relative magnitudes associated with the loading pattern.

The annual latitudinal migration of the WACZ is shown in Figure 5.29, which is a boxplot of W_ϕ. A smother annual cycle is observed compared to SRES-A1B in which a few models had two annual peaks, this double peak phenomena is not present in SRES-B1 (save GFDL model). SRES-B1 models show similarities to 20th century AMIP and reanalysis in that the fall southward migration appears to be more rapid than the spring northward migration.

The time-series of annual means of W_ϕ is shown in Figure 5.30. Similar to SRES-A1B the lack of inter-annual and decadal variability is clearly evident. Information of model median, interquartile range and skewness is shown in Table 5.9. Eight of ten models are south in their median position compared to their position in the 20th century, suggesting a southward shift in WACZ in this scenario relative to AMIP. Some weak trends appear, although they appear to be lower in magnitude than SRES-A1B. Table 5.10 shows a statistical overview of trends in annual mean via a bootstrap analysis of linear regression. Nine of ten models show a positive linear trend and positive correlation with time. Each of these nine models are significant at an alpha of 10% and seven of nine models are significant at an alpha of 2%. We discuss trends in W_ϕ in the following sections.

Summer Means

Figure 5.31 shows the first loading pattern of the EOF associated with mean summer 925 hPa divergence. The dominant pattern is a dipole associated with changes in phase of the WACZ from north to south years. We note the relative magnitudes are lower compared to SRES-A1B in CCSM and MIROCH-h (Figure 5.31a,h).

The long term mean of 925 hPa divergence is shown in Figure 5.32, the climatological statistics on W_ϕ are shown in Table 5.11. As expected an east to west band of divergence is evident across North Africa, centered about 18° N. As in both the 20th century and SRES-A1b the strongest convergence is shifted toward central and eastern Africa. The median summer position of W_ϕ is shown to be south of its position in AMIP, with a southward shift in position on average of $-1.52°$ observed. In Figure 5.33 we present the difference of 20th century models from the AMIP scenario from the long term mean 925 hPa divergence in SRES-B1. Here green (positive values) north of yellow (negative values) suggests a southward shift in the WACZ from the 20th century to the 21st century, which is observed in most models.

The position of the WACZ COA is shown in Figure 5.34, and boxplots of W_ϕ are shown in Figure 5.35. We note the COA varies in both latitudinal and longitudinal placement from model to model, similarly to both the 20th century AMIP scenario and the SRES-A1B scenario. The interquartile range of W_ϕ in Table 5.11 shows a reduction in comparison to SRES-A1B suggesting a reduction in near median inter-annual variability in SRES-B1. This reduction in inter-annual variance in the top and bottom quartiles is seen also in Figure

5.36 which shows the time-series of W_ϕ. A lack of decadal variability is evident, similar to SRES-A1B. A trend is also visible in some models, the significance of which we assess next.

Bootstrapping on linear regression of W_ϕ is performed, the mean and standard deviation of the boostrapped time-series are shown in Figure 5.37. Overall a northward trend is observed in the models, albeit reduced in magnitude and significance from SRES-A1B. Figure 5.38 shows the distribution of linear trends and Figure 5.39 shows the distribution of correlation with time and significance of trend shown in Figure 5.39p. Here in addition to the reduction in magnitude of the trend we note that the GISS model no longer shows a southward trend in this scenario, rather it shows a weak northward trend. The statistics associated with the trend analysis are seen in Table 5.12. Nine of ten models show a northward trend in W_ϕ, although only eight of the nine models are significant at alpha equal to 10% and only four of the eight are significant at the more stringent alpha equal to 2%. The significance of the linear regressions are summarized in Table 5.12.

Winter Means

The majority of models identify north to south changes in phase of the WACZ as the primary mode of variability in an EOF analysis of 925 hPa divergence as seen in Figure 5.41. As with SRES-A1B and AMIP there is an increase in relative magnitude over West Africa, relative to summer.

The climatology of 925 hPa divergence for winter means is shown in Figure 5.42. An east to west band of convergence is visible across North Africa, generally near to 8° N. Table 5.13 shows the median, interquartile range and skewness of W_ϕ. Half of models (five of ten) show either no shift or a small northward shift in the position of the W_ϕ relative to the AMIP scenario. Only one model has a large southward shift in position (IAP), and only four models have a large northward shift in position (CNRM, IPSL, MIROC-h, MPI). These results are verified in Figure 5.43 which shows the varied shifts in mean divergence relative to the 20th century.

The winter mean position of W_ϕ and W_λ are shown in Figure 5.44. North to south spread between models is evident, and summarized in Table 5.13, but is consistent with position in SRES-A1B. A graphical comparison between models is shown in Figure 5.45, with maximum and minimum of the median of the models shown in horizontal lines. MIROC-m is nearly always beneath the minimum median W_ϕ and IPSL is entirely outside of the maximum median W_ϕ. The median position and variability of W_ϕ is comparable to that seen in SRES-A1B.

The time-series of W_ϕ is shown in Figure 5.46, similar to SRES-A1B we note reduced inter-annual and decadal variability compared to AMIP. A slight trend is noticeable in some models, but less evident than in SRES-A1B. To assess the significance of the trend bootstrapping was applied to linear regression analysis of W_ϕ. The means and standard deviations associated with the bootstrap are shown in Figure 5.47. While models suggest there could be a weak northern trend in the data (Figure 5.48), the magnitude of the trend is reduced as is the correlation coefficient between W_ϕ and time (Figure 5.49). Significance of the trend is shown in Figure 5.50 and Table 5.14 relative to SRES-A1B. Seven of ten models show a positive phase that is significant at alpha of 2%, one of ten models (GISS) shows a southward trend that is significant at an alpha of 10%. Overall less models indicate significant northward trends in SRES-B1 compared to SRES-A1B.

5.4 Discussion

5.4.1 Model Specific Results

By quantifying their bias in W_ϕ relative to reanalysis in the 20th century, in Chapter 4 we ranked model performance in the AMIP scenario identifying models as performing well (IPSL, MIROC-hres, MPI, CNRM) , middling (MRI, GFDL, UKMO, CCSM, GISS) or poorly (MIROC-mres, IAP). Based on these findings the question arises if models ranked poor or strong project similar changes in the position of the WACZ in 21st century climate runs.

Median values of W_ϕ in each scenario and model run for the 21st century are shown in Table 5.15 for both summer and winter. Model biases appear to be consistent from AMIP to SRES-A1B and SRES-B1. For example, the poorly performing model MIROC-mres represented a southern outlier in winter consistently in AMIP, SRES-A1B and SRES-B1. Likewise, the poorly performing IAP represents the northern outlier in summer in all of AMIP, SRES-A1B and SRES-B1. Model biases relative to reanalysis appear to extend from AMIP into both SRES-A1B and SRES-B1 scenarios. With no observations of the 21st century available to compare to, it is more difficult to identify models that perform well. Therefore we can only identify models that behave similarly to other models and those that are outliers (as in the above case). As such we can clearly define IAP and MIROC-mres as outliers as they are clearly different than their companion models, as they were in the AMIP case as well.

The IQR (inter-quartile range) represents the range in value of W_ϕ between the 75th and 25th percentiles, and as such represents the spread of W_ϕ, although constrained to the middle 50% of data. The IQR does not include any information about the upper and lower 25% of data, data in which comprises the northernmost and southernmost years of W_ϕ. As such the IQR is not suitable to examine true inter-annual variability, as much of the geophysical impacts of W_ϕ are related to values outside of the middle 50%. As shown previously the variability of the extreme 25% of data is less than that observed in 20th century reanalysis. However, as seen in Table 5.16, variability of the middle 50% of data is generally larger in SRES-A1B and SRES-B1, than in AMIP. For our poorly performing model both IAP and MIROC-hres see at least doubling of the IQR from AMIP to both SRES scenario in summer, and doubling of the IQR for MIROC-hres in winter (IAP does not change greatly in winter). However this large increase (doubling or more) in IQR from AMIP to the SRES scenarios is not seen in any models identified as strong performers, suggesting that this phenomenon is limited to models that performed poorly in the 20th century and may be indicative of weaker models.

The key finding of this work is the clear northward trend in W_ϕ in both winter and summer, which was strongest in Scenario SRES-A1B suggesting a strengthening of the trend with increased climate forcing. Table 5.17 shows a side by side comparison of linear trends in each of the GCMs for all scenarios. No relationship between model bias in position of W_ϕ with respect to reanalysis and linear trend in future scenarios is evident. The GISS model is the outlier in terms of linear trend suggesting a southward migration of the WACZ in three of four future scenarios; the GISS model was defined as a middle performing model in the AMIP scenario. The two poor-performance models indicate a northward trend (significant in three of four scenarios). Models that did poorly, in the middle or well placing the WACZ in the 20th century all show a significant northward movement of W_ϕ in the 21st century.

In summary we examine the two models that did worst at placing the WACZ in the 20th century. These models exhibit large deviations from other models with placement of W_ϕ in the 21st century. The IQR of both the poorly performing models at least doubles, suggesting quite a bit of variability about the mean value, although we note a lack of variability in extreme values (few far-north and far-south years). However despite poor performance in mean and variability poorly performing models support the premise of northward migration of W_ϕ in the 21st century.

5.4.2 Model Shift in Divergence

Tables 5.3, 5.5, 5.9, and 5.11 all highlight the large southern shift in model divergence from AMIP to SRES-A1B and SRES-B1 in both annual and summer means compared to the 20th century. The observed shift was also seen in DJFM of SRES-A1B and to a lesser degree in SRES-B1. Significant northward trends were observed in both scenarios in summer and annual W_ϕ during the 21st century. The superposition of this trend suggests W_ϕ was at its most southern point at the start of the 21st century, and that its difference from AMIP (20th century) was largest at this point as well. Visual comparison between the position of W_ϕ in

2000 in reanalysis (e.g. Figure 5.12) to the position of W_ϕ in 2000 in any GCM simulations of the 21st century (e.g. Figure 5.11) confirms this abrupt southward shift, followed by a northward trend.

The observed shift is likely due to differences between coupled and non-coupled ocean-atmosphere in CMIP-SRES and AMIP respectively. In the AMIP scenarios the sea surface temperature and sea ice coverage are prescribed. Models then are free to produce an atmospheric response to the oceanic conditions. In both the SRES-A1B and SRES-B1 the models are based on the same physics and parameterizations but predict their own SST and sea ice coverage. In both scenarios, in the year 2000 greenhouse gas forcing must be similar to greenhouse gas forcing at the end of the 20th century AMIP scenario. The discontinuity in the placement of the WACZ from the end of the 20th century to the start of the 21st century, which is of the order of 2.5° in extreme cases, is due to model differences in the treatment of SST and ocean processes.

5.4.3 Implications for Mineral Dust Emission and Transport

In Chapters 2 and 3 the critical relationship between W_ϕ and mineral dust transport to Barbados is shown. W_ϕ drives dust transport by controlling the strength and direction of wind over critical dust hot spot emission regions in the Sahel and Sahara in both winter and summer seasons. We also found that in summer W_ϕ impacts dust transport via precipitation and in turn soil moisture and vegetative cover. The relationship between W_ϕ and mineral dust at Barbados holds on inter-annual timescales by examining seasonal means of dust load and seasonal means of W_ϕ.

Model predictions for the 21st century show reduced inter-annual variability in W_ϕ compared to 20th century reanalysis products. This reduction in variability is shown in both 21st century scenario SRES-A1B and SRES-B1 and holds for annual, winter and summer means. Model runs in the AMIP scenario also showed reduced inter-annual variability, and showed no skill in reproducing the time-series of W_ϕ from reanalysis. As such we conclude that the models likely are unable to predict inter-annual or even decadal changes in mineral dust emission and transport. Additionally the models' inability to replicate temporal variability in the 20th century suggests that current models may lack some key physical processes necessary to accurately predict the position of the WACZ, and also climate-dust feedbacks are excluded in CMIP3 models.

Prior work has suggested an expansion of the Hadley Circulation as the Earth's climate warms which could have implications for the positioning of the WACZ with time and in turn mineral dust emission and transport. A northward trend is predicted in the annual and summer position of the WACZ in the 21st century in this study. Northward migration of the WACZ could lead to reduced transport of mineral dust to Barbados, as a result of shifting of surface winds away from key source regions and increased precipitation in general in the Sahel. Such a projection would be of low confidence as source regions could experience significant change over the coming century due to climatic shifts and anthropogenic land uses changes with time. To estimate how northward migration of the WACZ could impact mineral dust transport we first establish the relationship between the WACZ and mineral dust in Barbados in the 20th century via linear regression. For a one degree northward shift mineral dust at Barbados is reduced by by $-6.52\ \mu\mathrm{g\,m^{-3}}$ $-3.75\ \mu\mathrm{g\,m^{-3}}$ and for summer and winter respectively. Next we estimate the change in the position of the WACZ over the 21st century in SRES-A1B and SRES-B1. To do so we calculate the trend of the median seasonal value of every model output (shown in Tables 5.6, 5.8, 5.12, 5.14). To assess uncertainty of the trend we repeat this calculation for the 2.5 and 97.5 percentiles to create a 95% confidence interval about our projection. To calculate the change in dust load the trends are multiplied by 100 years to calculate the 100 year change in WACZ position, and then multiplied through by the dust per degree of WACZ shift as calculated in the 20th century. Results are shown in Table 5.18. For SRES-A1b we expect a change of $-3.8\ \mu\mathrm{g\,m^{-3}}$ in summer ($-3.0\ \mu\mathrm{g\,m^{-3}}$ to $-4.7\ \mu\mathrm{g\,m^{-3}}$ confidence interval) and a change of $-2.2\ \mu\mathrm{g\,m^{-3}}$ in winter ($-1.3\ \mu\mathrm{g\,m^{-3}}$ to $-2.4\ \mu\mathrm{g\,m^{-3}}$ confidence interval). The predicted change in mean dust load from the end of the 20th century to the 21st century is of the same order of magnitude as the inter-annual variance in the 20th century, or put another way, the predicted reduction is expected to be nearly as large as the current year-to-year changes in dust load. As previously noted SRES-B1 produced smaller northward trends than SRES-A1b, so reductions in dustload are less; $-1.9\ \mu g\,m^{-3}$ in summer ($-1.1\ \mu g\,m^{-3}$ to $-2.7\ \mu g\,m^{-3}$ confidence interval) and $-1.5\ \mu g\,m^{-3}$ in winter ($-1.0\ \mu g\,m^{-3}$ to $-2.0\ \mu g\,m^{-3}$ confidence interval). A fully coupled vegetation-land surface and climate model would be necessary to determine the magnitude of change of mineral dust transport in the 21st century, but here we show based on shifts in the WACZ expected changes in mineral dust emission and transport on the order of inter-annual variability of mineral dust in the 20th century.

5.5 Conclusions

This work examined changes in divergence over West Africa at 925 hPa in the 21st century in GCMs from the CMIP3 experiment for the SRES-A1B and SRES-B1 scenarios. Climate models captured the annual migration of the WACZ and identified north-south shifts in the annual position of the WACZ as the dominant mode of variability. However models showed reduced inter-annual and decadal variability of W_ϕ particularly in the north and south quartiles, quartiles previously identified as playing key roles in determining precipitation, wind and in turn mineral dust transport. A southward shift of up to 2.5° in W_ϕ from the AMIP/20th century to the 21st century GCM runs was identified. Northward migration of W_ϕ over the 21st century is seen in annual, winter and summer means.

Overall GCM output for the 21st century showed reduced variability compared to 20th century reanalysis. Reductions in inter-annual variability in W_ϕ we shown for summer and winter means. Additionally no decadal variability in W_ϕ was seen, in contrast to 20th century in which decadal shifts in W_ϕ were observed.

Compared with the 20th century, a southward shift in the WACZ is evident in both 21st century scenarios. Concurrently over the 21st century a clear northward trend is evident. A northward trend in time combined with an overall southward bias suggests the largest southward displacement occurred nearest to the year 2000 and decreased over the 21st century. Such a large discontinuity cannot be the result of changes in greenhouse gas forcing (as forcing near to 2000 are identical). The apparent conflict must be related to oceanic model variability. In the AMIP 20th century scenario the models were forced with prescribed SST and sea ice conditions based on observation, in contrast in the 21st century models were free to develop their own SST conditions. As weak northward trends were observed in the 20th century summer and annual means it appears the northward trend is robust over varied scenarios, and the southward discontinuity near the year 2000 a model artifact.

Northward trends in W_ϕ were seen in annual, winter and summer means and significance of the trends was assessed by bootstrapping. Northward trends were larger in SRES-A1B than SRES-B1; the median linear trend of W_ϕ was 5.88 $\times10^{-3}$ $^\circ$yr^{-1} and 5.48 $\times10^{-3}$ $^\circ$yr^{-1} for summer and winter respectively in SRES-A1B and 2.92 $\times10^{-3}$ $^\circ$yr^{-1} and 3.83 $\times10^{-3}$ $^\circ$yr^{-1} for summer and winter respectively in SRES-B1.

While reductions in inter-annual and decadal variability render predictions of dust load moot for the 21st century, estimates for changes in dust load at Barbados over the 21st century were performed. In SRES-A1b mean dust load is expected by -3.8 μg m^{-3} and -2.2 μg m^{-3} in summer and winter respectively. For SRES-B1 expected reductions in dust load were -1.9 μg m^{-3} and -1.5 μg m^{-3} in summer and winter respectively. This is consistent with northward migration of the WACZ leading to reduced dust emission and transport to Barbados.

Prior work has suggested a poleward expansion of the Hadley Cell as the climate warms [*Fu et al.*, 2006; *Hu and Fu*, 2007; *Frierson et al.*, 2007; *Gastineau et al.*, 2008; *Johanson and Fu*, 2009]. Our work focuses on the equatorial ascending branch of the Hadley Cell over West Africa, the WACZ. Our work in general supports the hypothesis of poleward expansion of the Hadley cell on annual, summer and winter means as we identify clear northward trends in the latitudinal position over the 21st century. We note that prior work in general focuses on the northern extent of the Hadley Cell, which is subsidence generally well north of the WACZ. Our work contrasts the findings of *Gastineau et al.* [2008] who found a southward migration in the equatorial-ascending branch of the Hadley Cell by examining 500 hPa streamfunction in GCM simulations, as here we find a northward migration of the ascending branch in the 21st century in divergence nearer to the surface.

The results of this project raise a number of questions that could be addressed as future work. We hypothesize that changes in the WACZ would reduce transport of dust to Barbados in the 21st century. A detailed land-surface model could be coupled to a GCM to assess how long-term shifts in the position of the WACZ would affect surface conditions, which could lead to marked changes in mineral dust emission. We suggest that the large shift in position of the WACZ from the end of AMIP to the start of the SRES scenarios is attributable to changes in ocean conditions. A study should be performed to analyze differences in SST in GCMs and note how the WACZ responds to such changes. Lastly, here we note a northward trend in the position of the ascending branch of the Hadley Cell. The center of action approach could be inverted to examine movement of areas of near surface divergence associated with the poleward descending branch of the Hadley Cell. It would be of interest to note if changes in position of the divergence zone are related to changes in the position of the convergence zone.

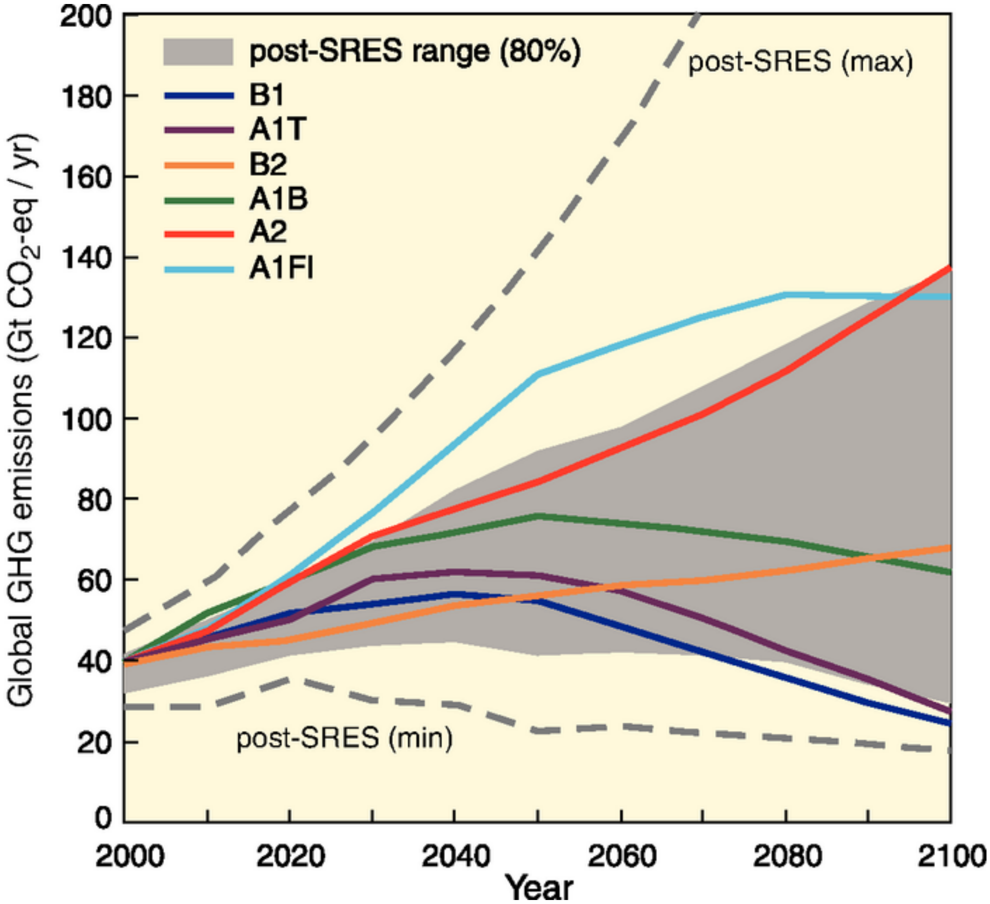

Figure 5.1: Time-series of emissions of greenhouse gases in multiple SRES Scenarios. Image from *Solomon et al.* [2007].

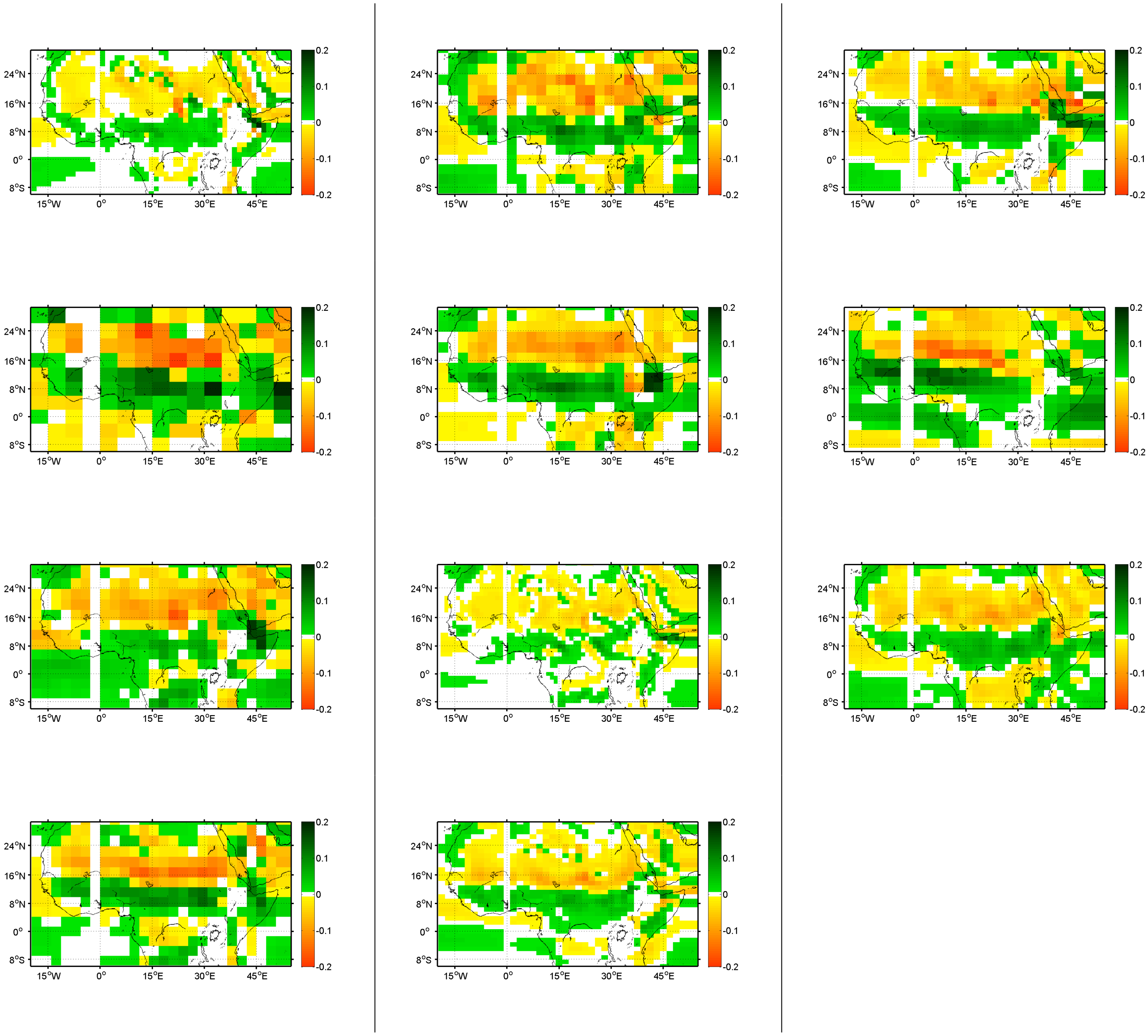

Figure 5.2: First mode of the EOF of 925 hPa divergence of all months in the period 2000–2100 for SRESA1-B. Top row: (a) CCSM, (b) CNRM, (c) GFDL. Second row: (d)GISS, (e)IAP, (f)IPSL Third row: (g) MIROC-mres, (h) MIROC-hires, (i) MPI. Fourth row: (j) MRI and (k) UKMO-HADGEM.

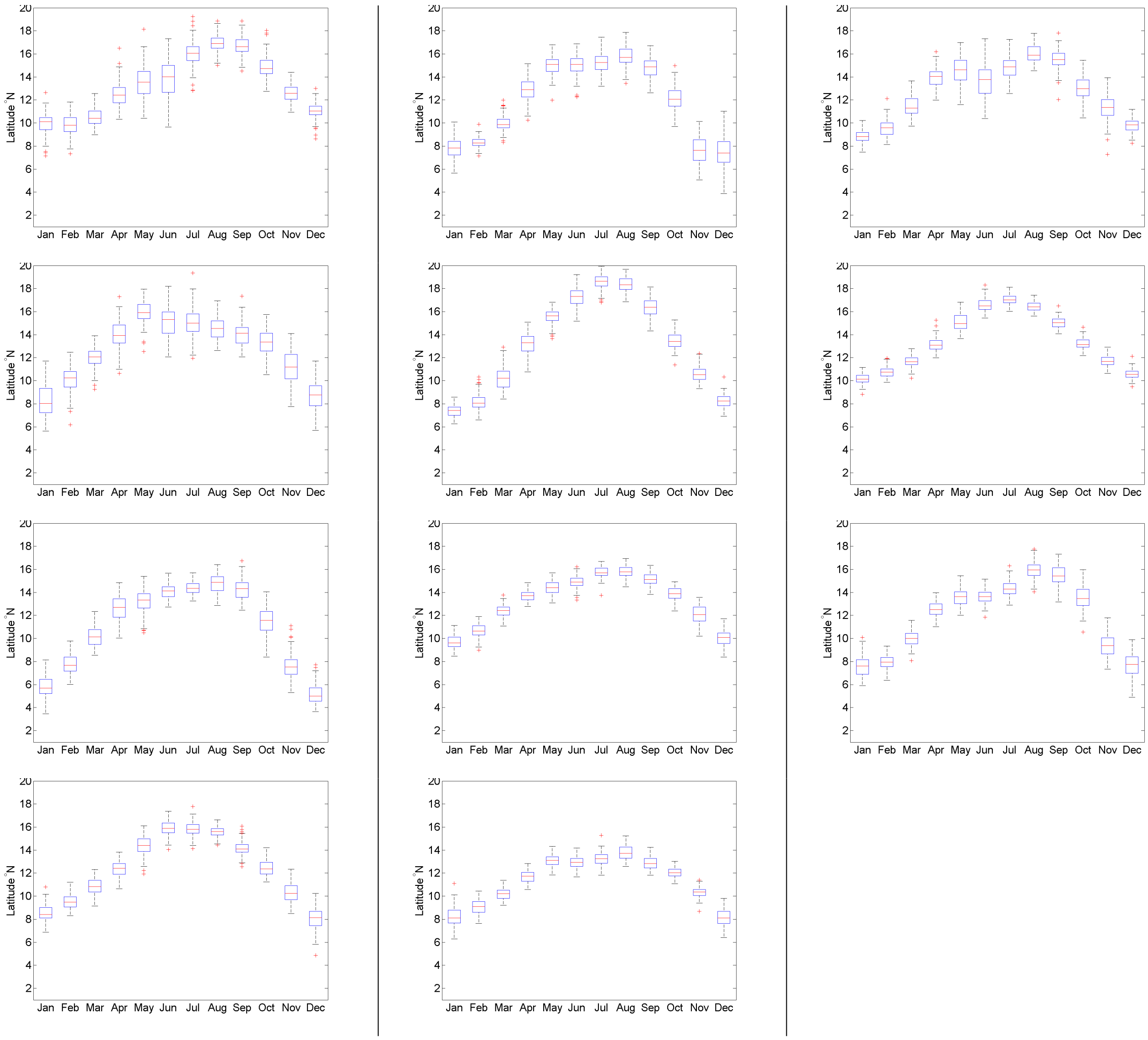

Figure 5.3: Annual south to north migration of WACZ as illustrated by boxplot of monthly means of W_ϕ over the period 2000–2100 for SRES-A1b. Red center line represents median, blue lines above and below median represent the 75th and 25th percentiles respectively. Red crosses represents outliers. Black lines extend 1.5 times the interquartile range out from the median. Top row: (a) CCSM, (b) CNRM, (c) GFDL. Second row: (d)GISS, (e)IAP, (f)IPSL Third row: (g) MIROC-mres, (h) MIROC-hires, (i) MPI. Fourth row: (j) MRI and (k) UKMO-HADGEM.

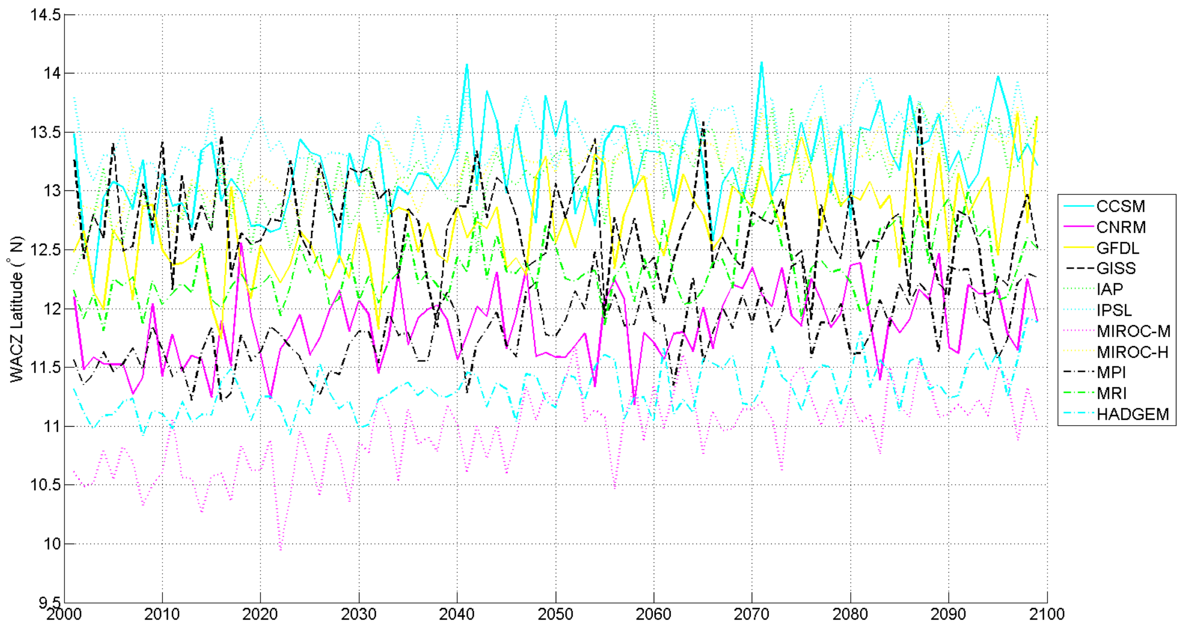

Figure 5.4: Time-series of annual means of W_ϕ over the period 2000–2100 for SRES-A1b.

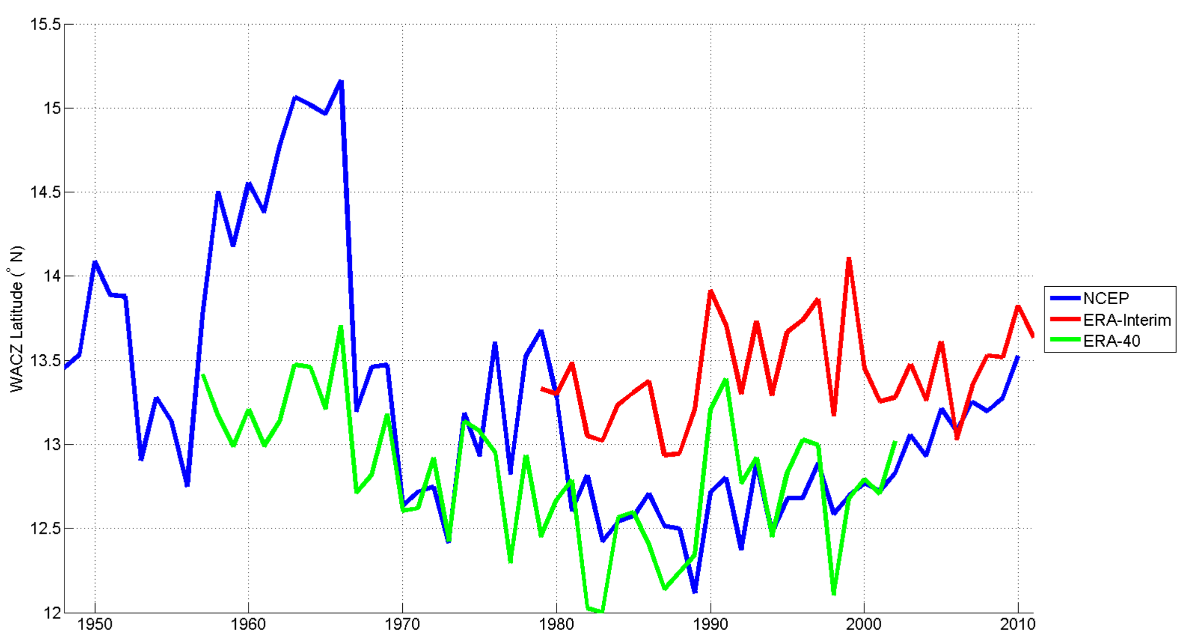

Figure 5.5: Time-series of annual means of W_ϕ over the period 1948 to 2011 in reanalysis.

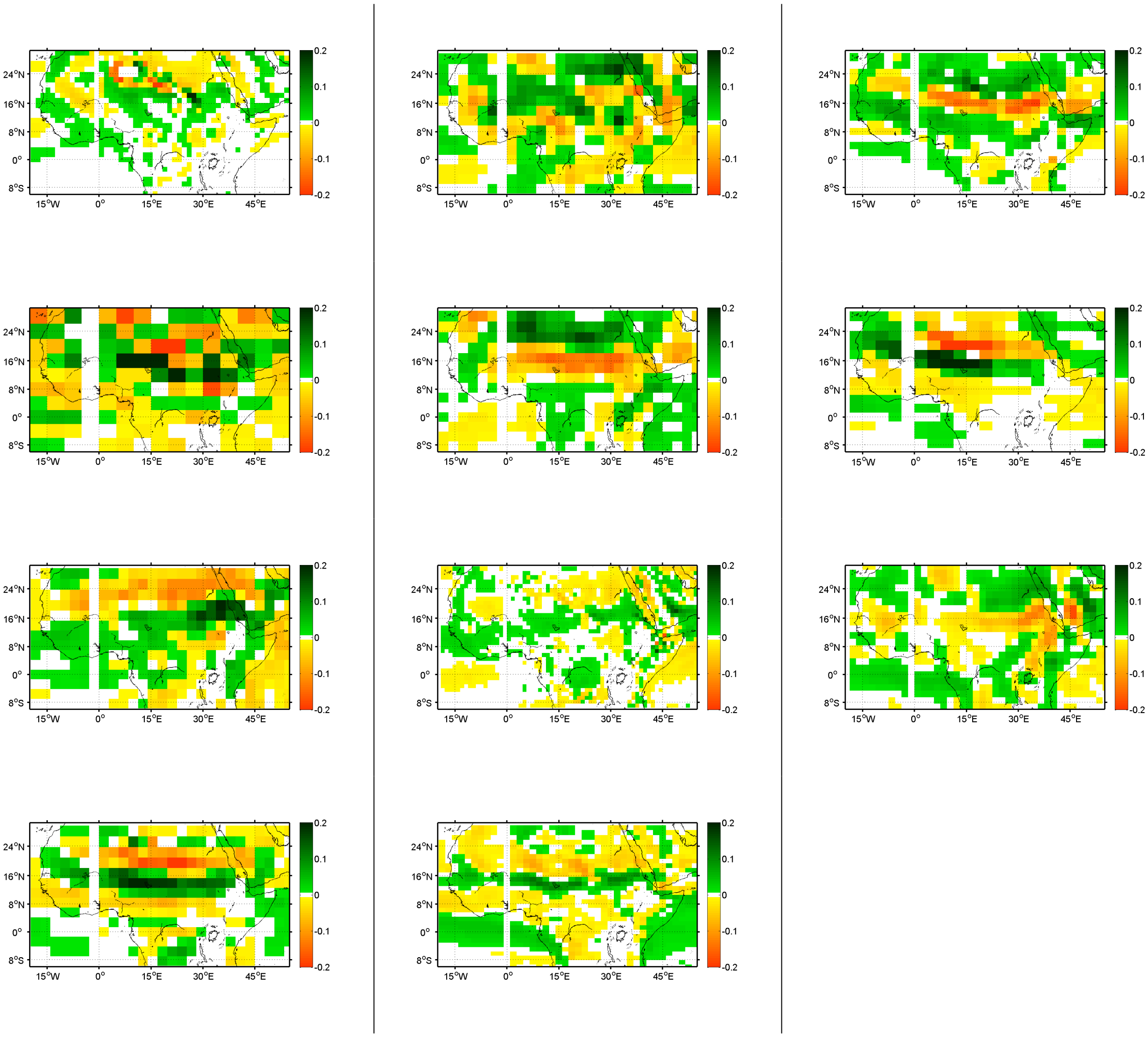

Figure 5.6: First mode of the EOF of 925 hPa divergence during summer (JJAS) in the period 2000–2100 for SRESA1-B. Top row: (a) CCSM, (b) CNRM, (c) GFDL. Second row: (d)GISS, (e)IAP, (f)IPSL Third row: (g) MIROC-mres, (h) MIROC-hires, (i) MPI. Fourth row: (j) MRI and (k) UKMO-HADGEM.

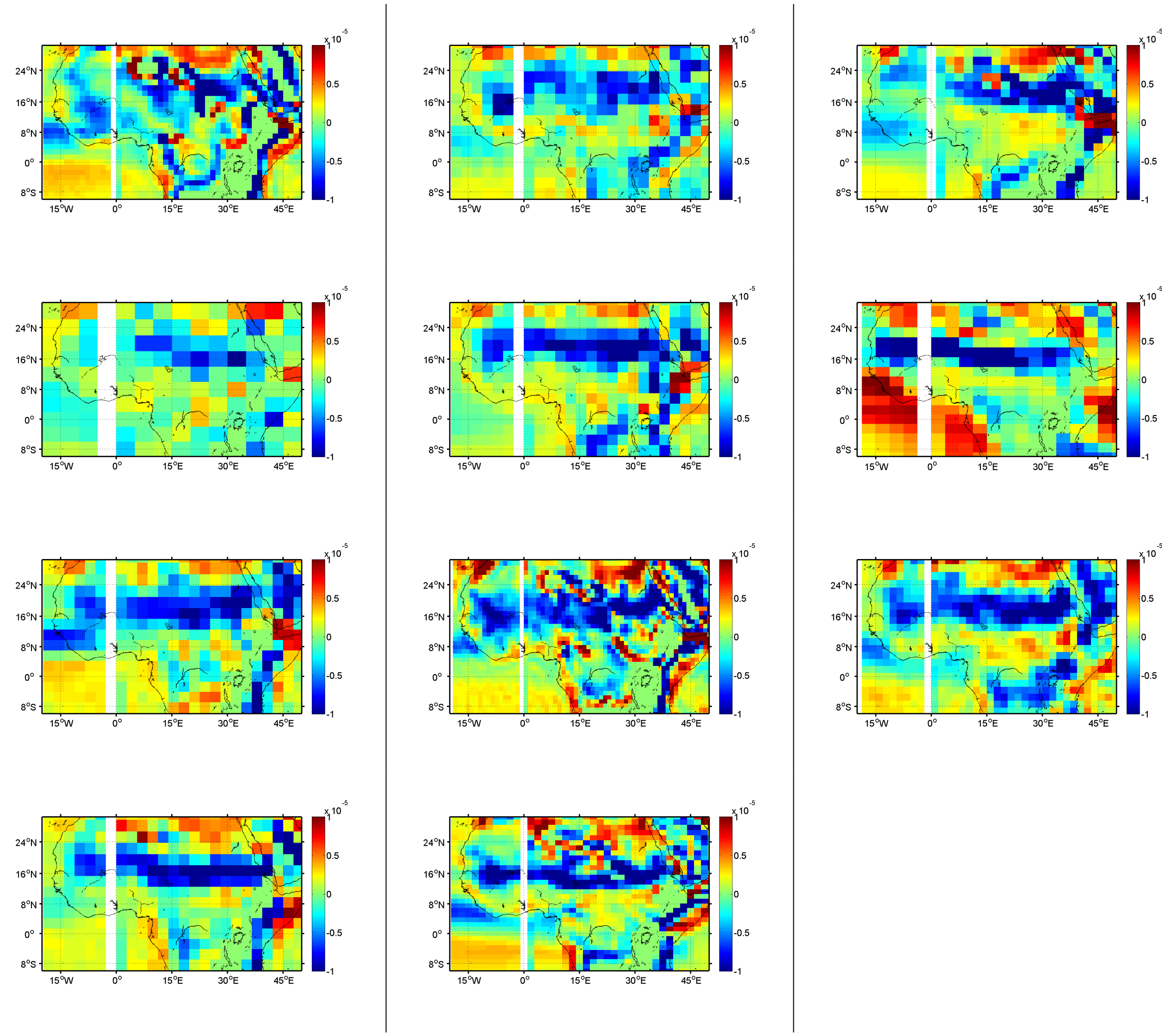

Figure 5.7: Long-term mean of 925 hPa divergence during summer (JJAS) in the period 2000–2100 for SRESA1-B. Top row: (a) CCSM, (b) CNRM, (c) GFDL. Second row: (d)GISS, (e)IAP, (f)IPSL Third row: (g) MIROC-mres, (h) MIROC-hires, (i) MPI. Fourth row: (j) MRI and (k) UKMO-HADGEM.

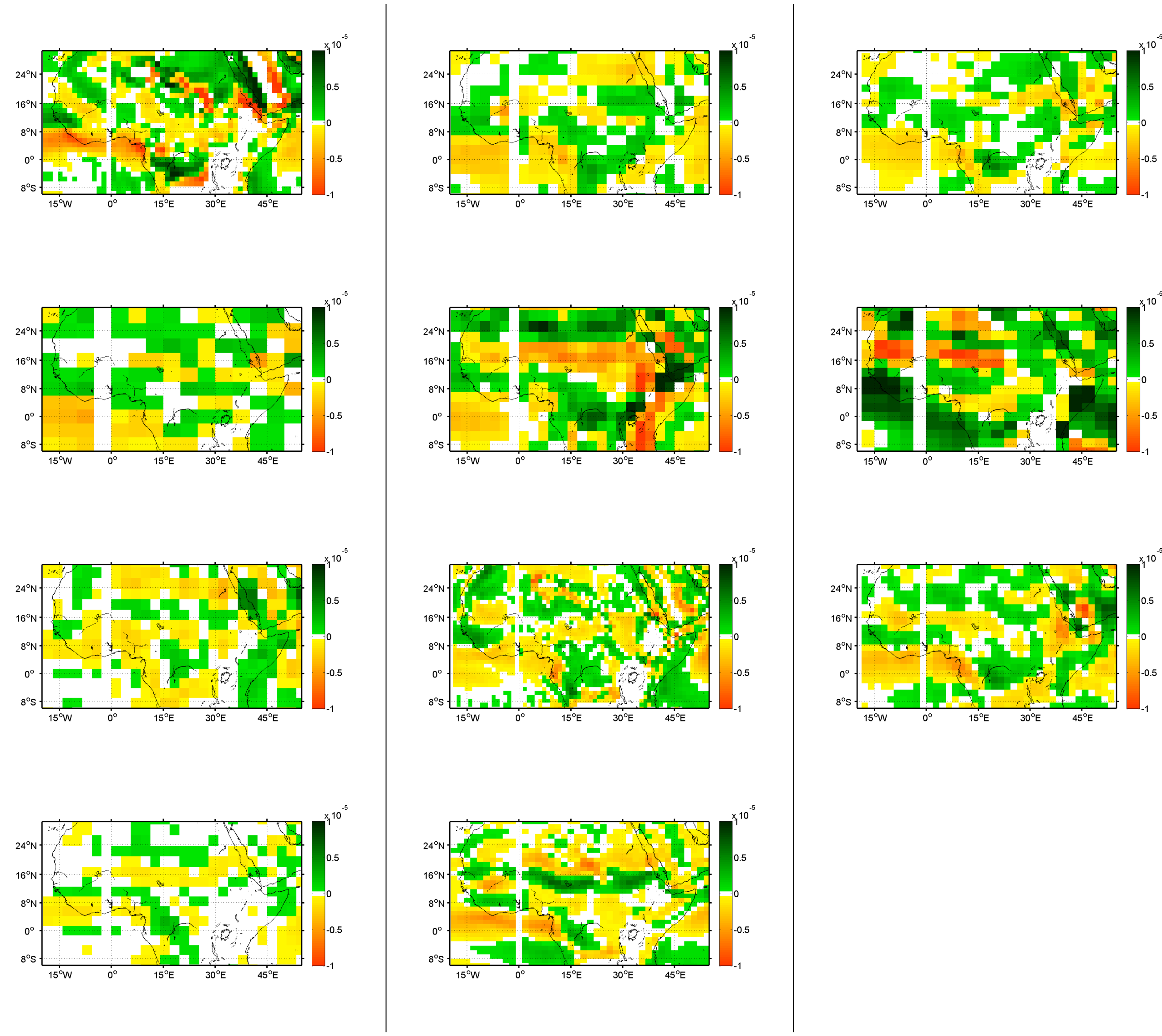

Figure 5.8: Long-term mean divergence over the period 2000–2100 for SRESA1-B minus long term mean divergence over the period 1978–2002 for AMIP. Divergence calculated at 925 hPa for summer months. Top row: (a) CCSM, (b) CNRM, (c) GFDL. Second row: (d)GISS, (e)IAP, (f)IPSL Third row: (g) MIROC-mres, (h) MIROC-hires, (i) MPI. Fourth row: (j) MRI and (k) UKMO-HADGEM.

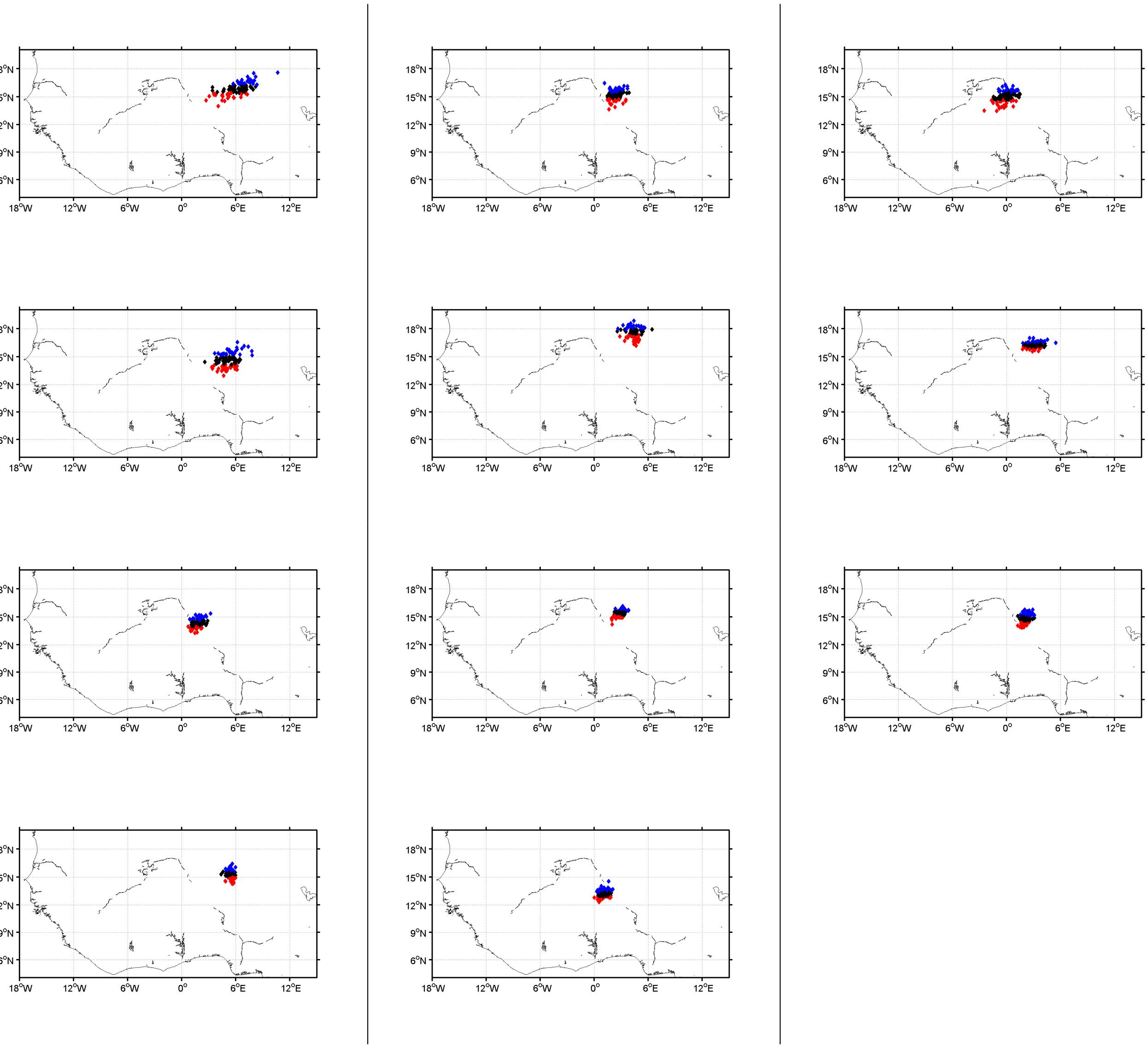

Figure 5.9: Position of WACZ as determined by W_λ and W_ϕ. Each summer mean position is plotted. The quarter of years that are furthest north are blue diamonds, the quarter of years that are furthest south are red diamonds and the interquartile range are black diamonds. COA plotted over the period 2000–2100 for SRESA1-B. Top row: (a) CCSM, (b) CNRM, (c) GFDL. Second row: (d)GISS, (e)IAP, (f)IPSL Third row: (g) MIROC-mres, (h) MIROC-hires, (i) MPI. Fourth row: (j) MRI and (k) UKMO-HADGEM.

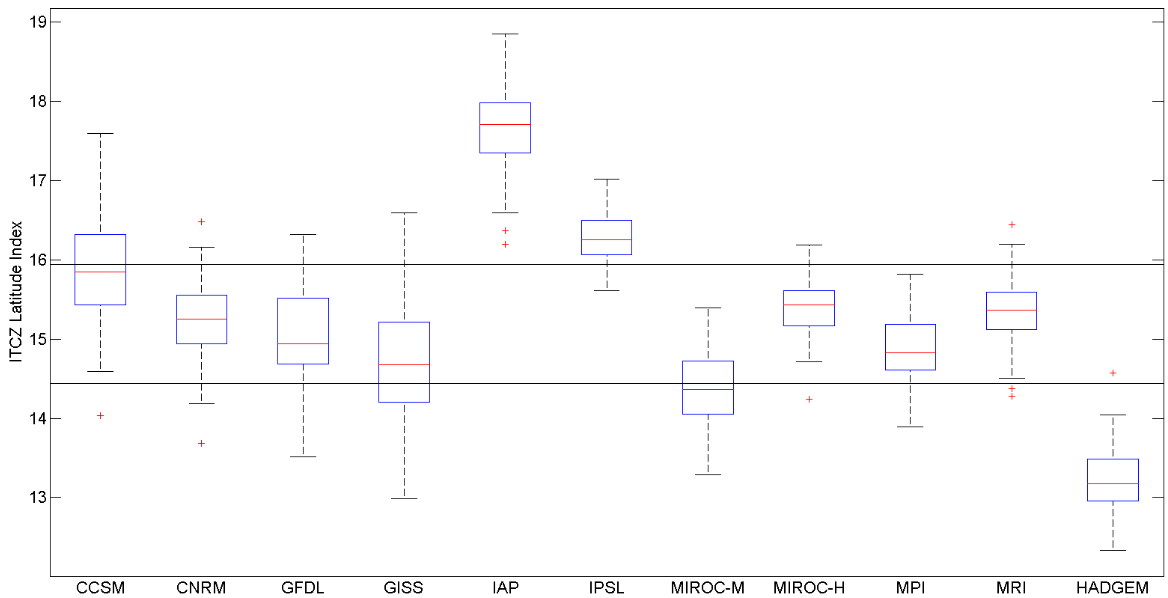

Figure 5.10: Boxplot of summer means of W_ϕ over the period 2000–2100 for SRES-A1b. Red center line represents median, blue lines above and below median represent the 75th and 25th percentiles respectively. Red crosses represents outliers. Black lines extend 1.5 times the interquartile range out from the median.

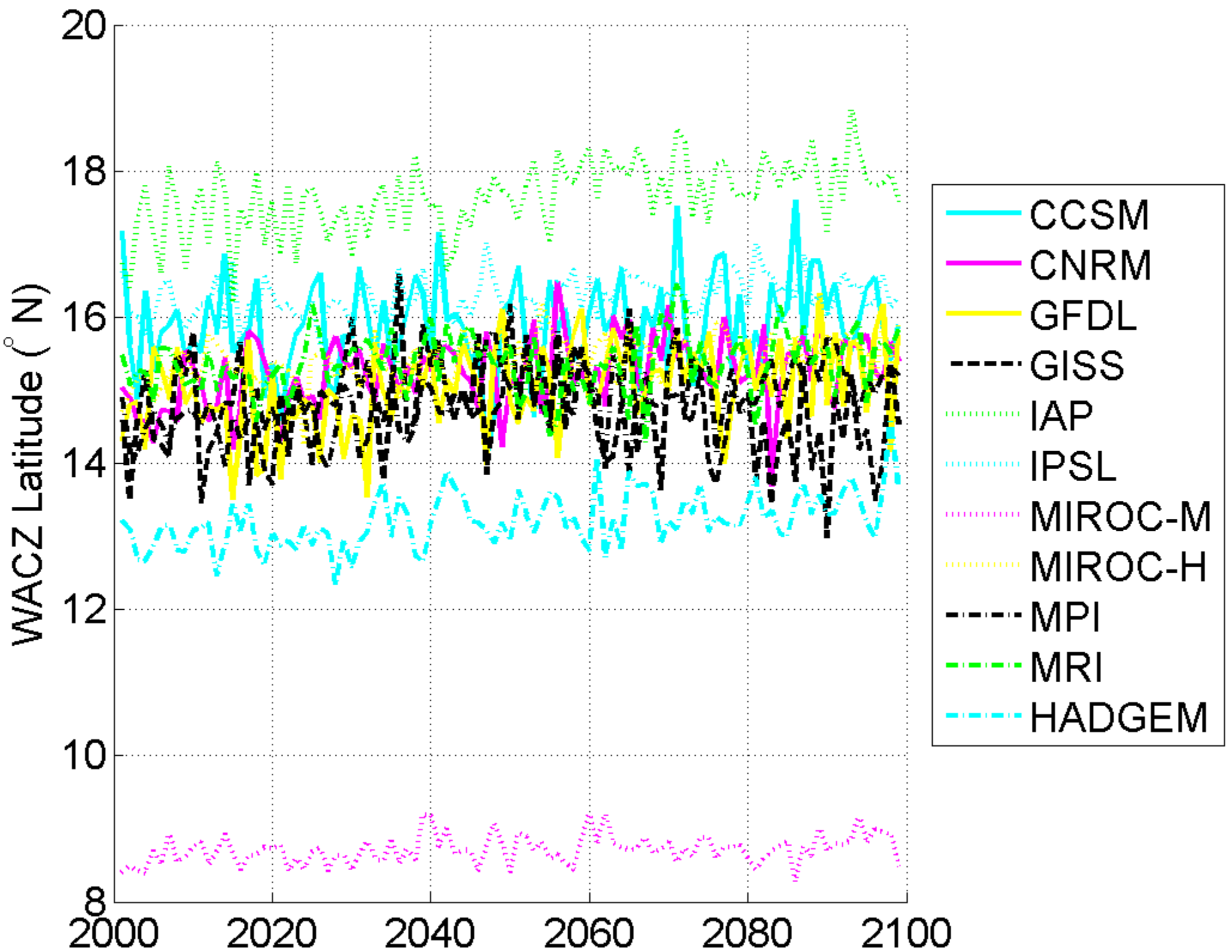

Figure 5.11: Time-series of summer means of W_ϕ over the period 2000–2100 for SRES-A1b.

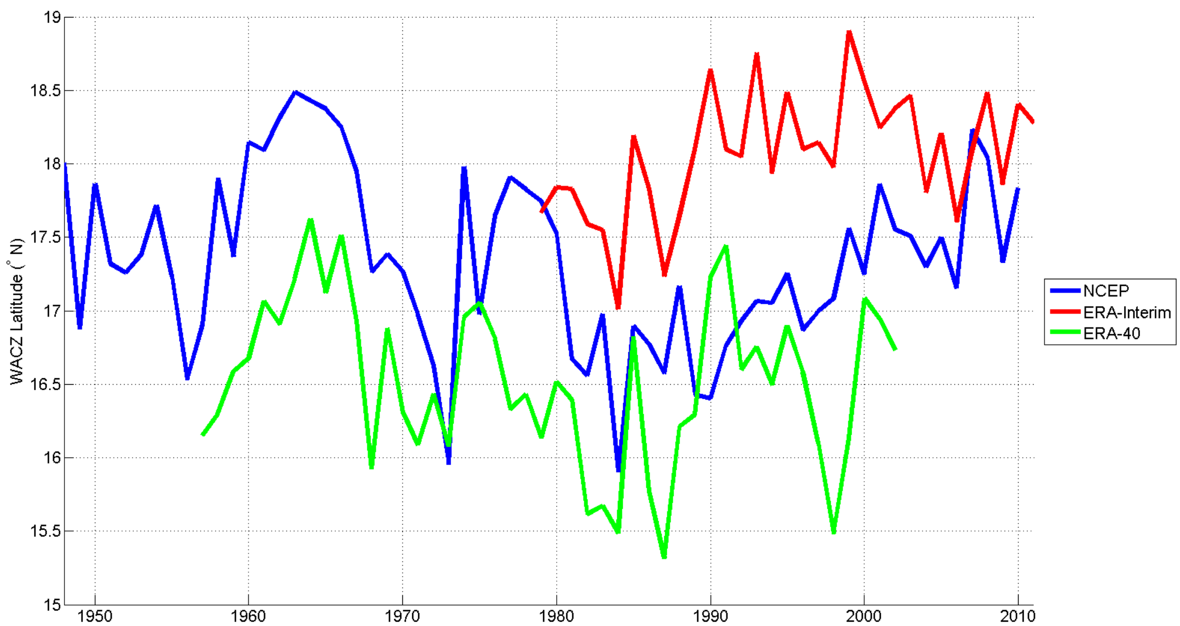

Figure 5.12: Time-series of summer means of W_ϕ over the period 1948 to 2011 in reanalysis.

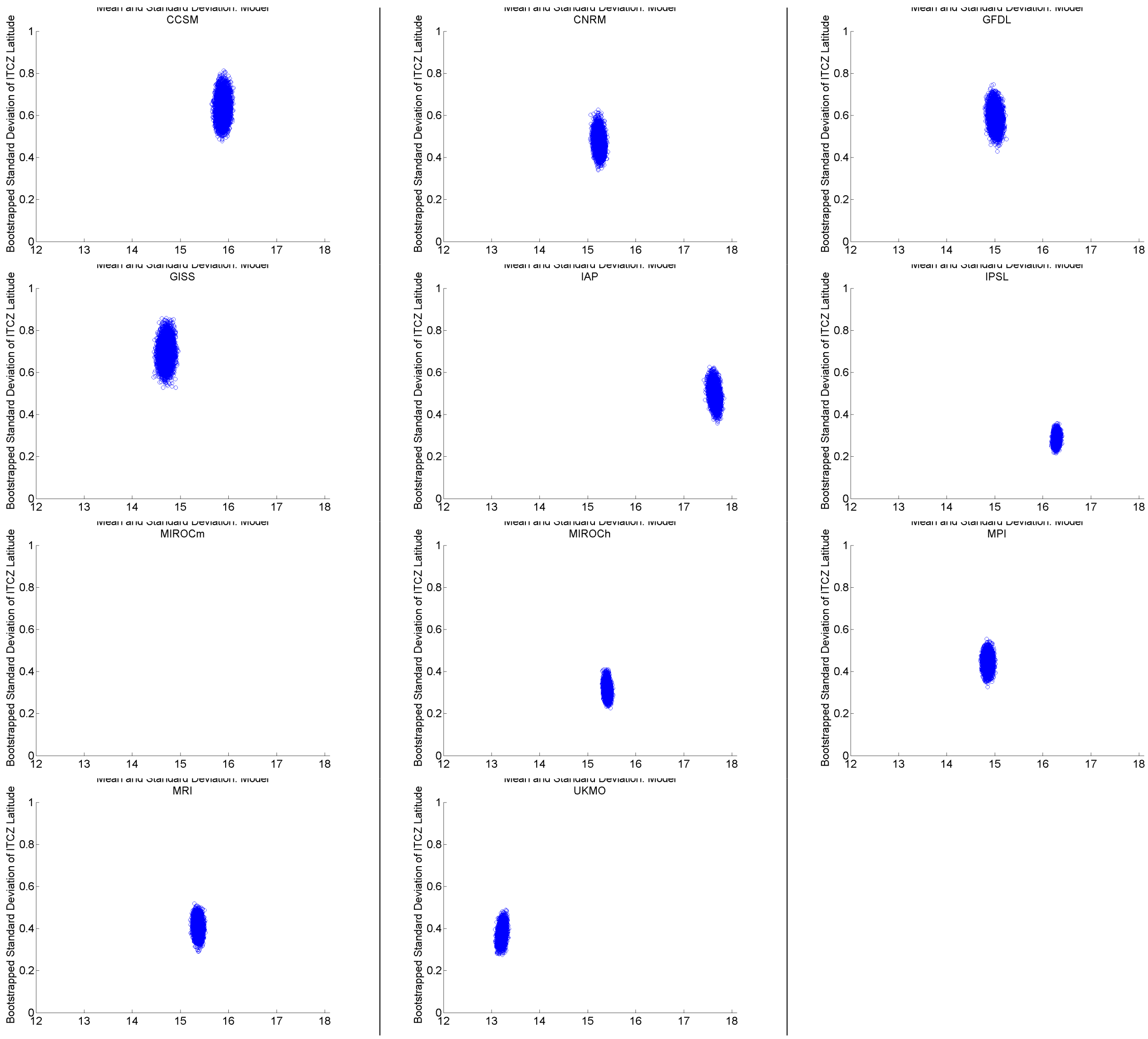

Figure 5.13: Mean (x-axis) and standard deviation (y-axis) of W_ϕ in 10,000 resamplings via bootstrapping over period 2001–2099 in SRES-A1B scenario in summer (JJAS). Top row: (a) CCSM, (b) CNRM, (c) GFDL. Second row: (d) GISS, (e) IAP, (f) IPSL Third row: (g) MIROC-mres, (h) MIROC-hires, (i) MPI. Fourth row: (j) MRI and (k) UKMO-HADGEM.

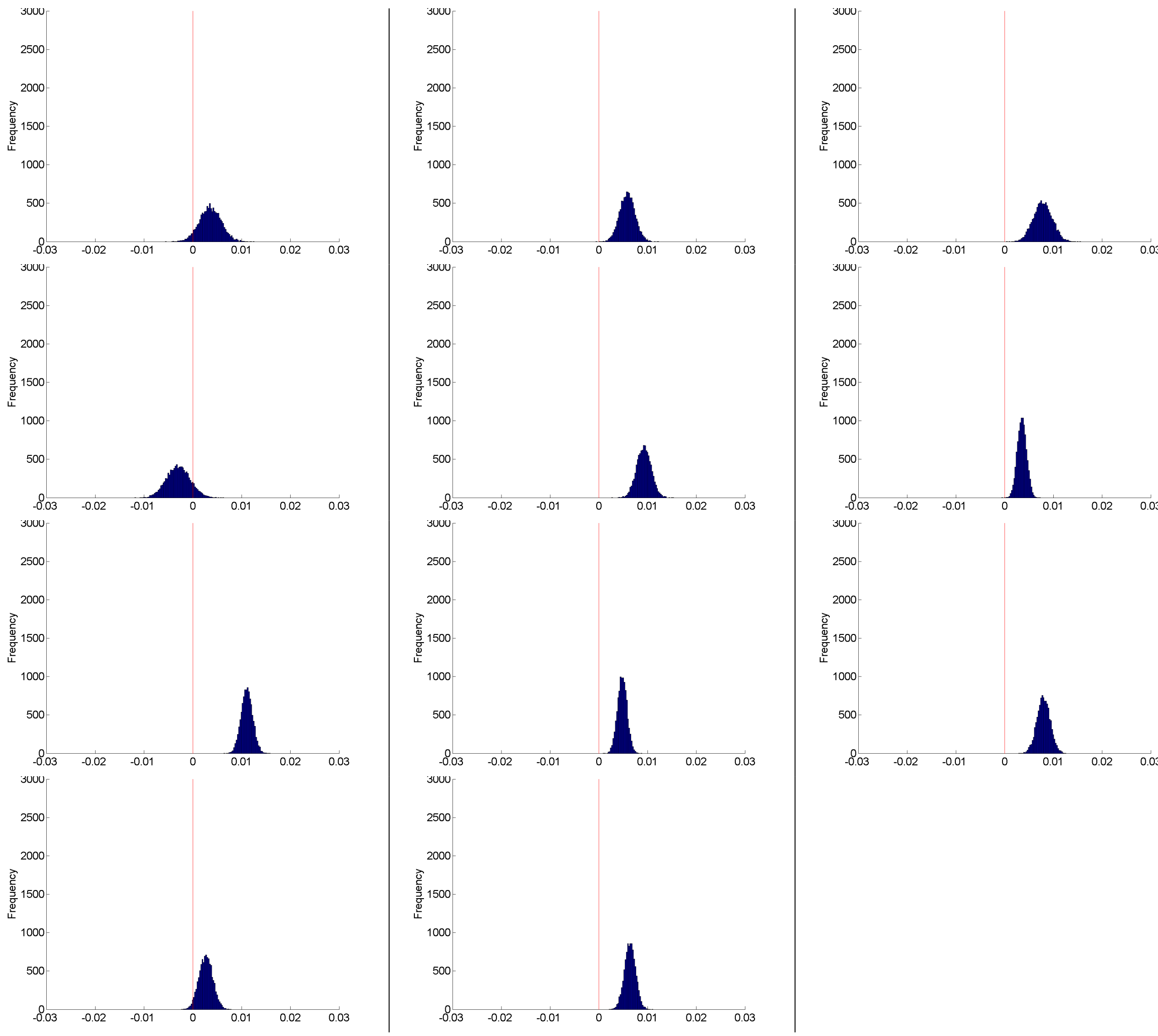

Figure 5.14: Linear trend of W_ϕ in 10,000 resamplings via bootstrapping over period 2001–2099 in SRES-A1B scenario in summer (JJAS). Top row: (a) CCSM, (b) CNRM, (c) GFDL. Second row: (d)GISS, (e)IAP, (f)IPSL Third row: (g) MIROC-mres, (h) MIROC-hires, (i) MPI. Fourth row: (j) MRI and (k) UKMO-HADGEM.

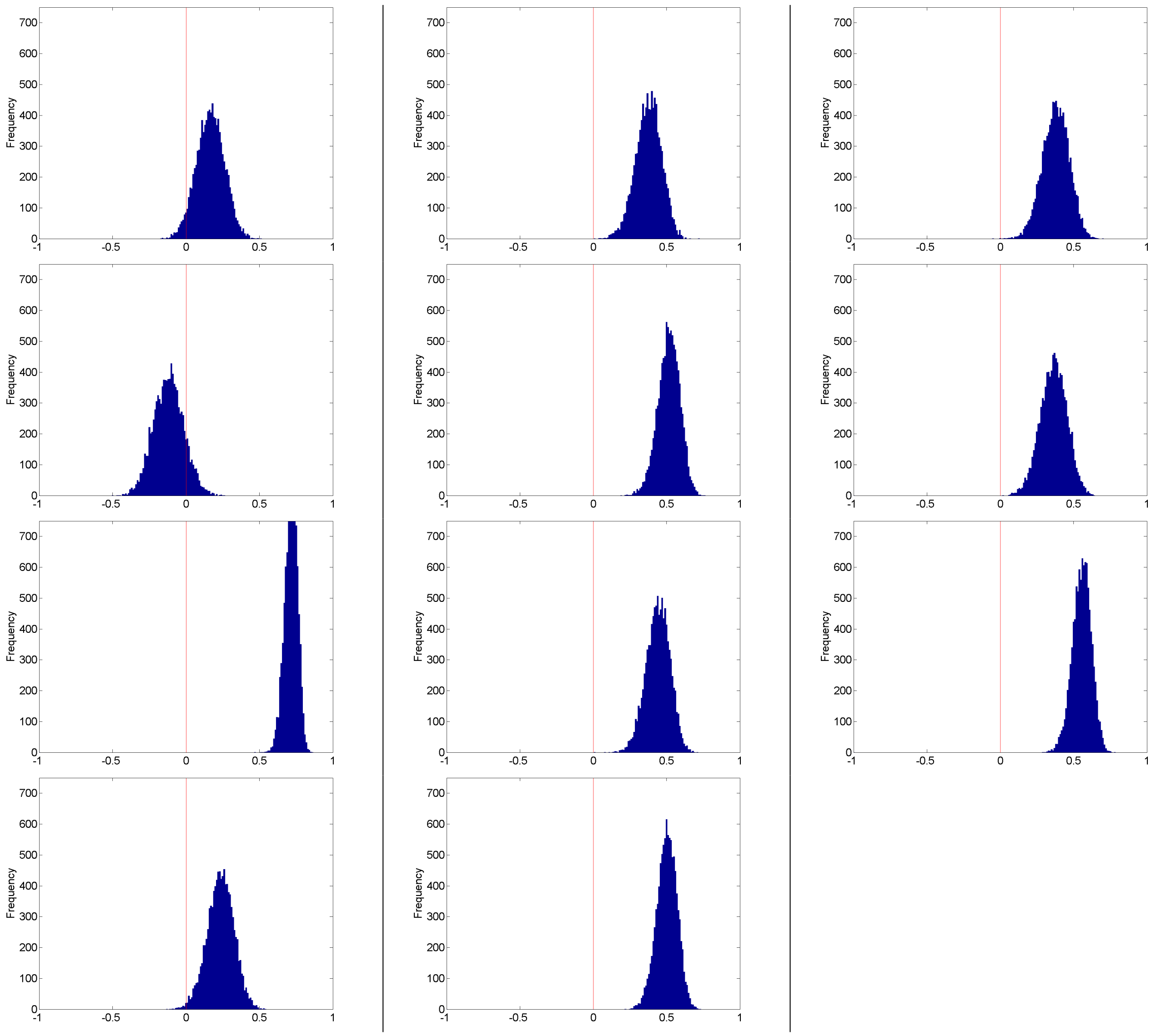

Figure 5.15: Pearson product moment correlation coefficients between W_ϕ and time in 10,000 resamplings via bootstrapping over period 2001–2099 in SRES-A1B scenario in summer (JJAS). Top row: (a) CCSM, (b) CNRM, (c) GFDL. Second row: (d)GISS, (e)IAP, (f)IPSL Third row: (g) MIROC-mres, (h) MIROC-hires, (i) MPI. Fourth row: (j) MRI and (k) UKMO-HADGEM.

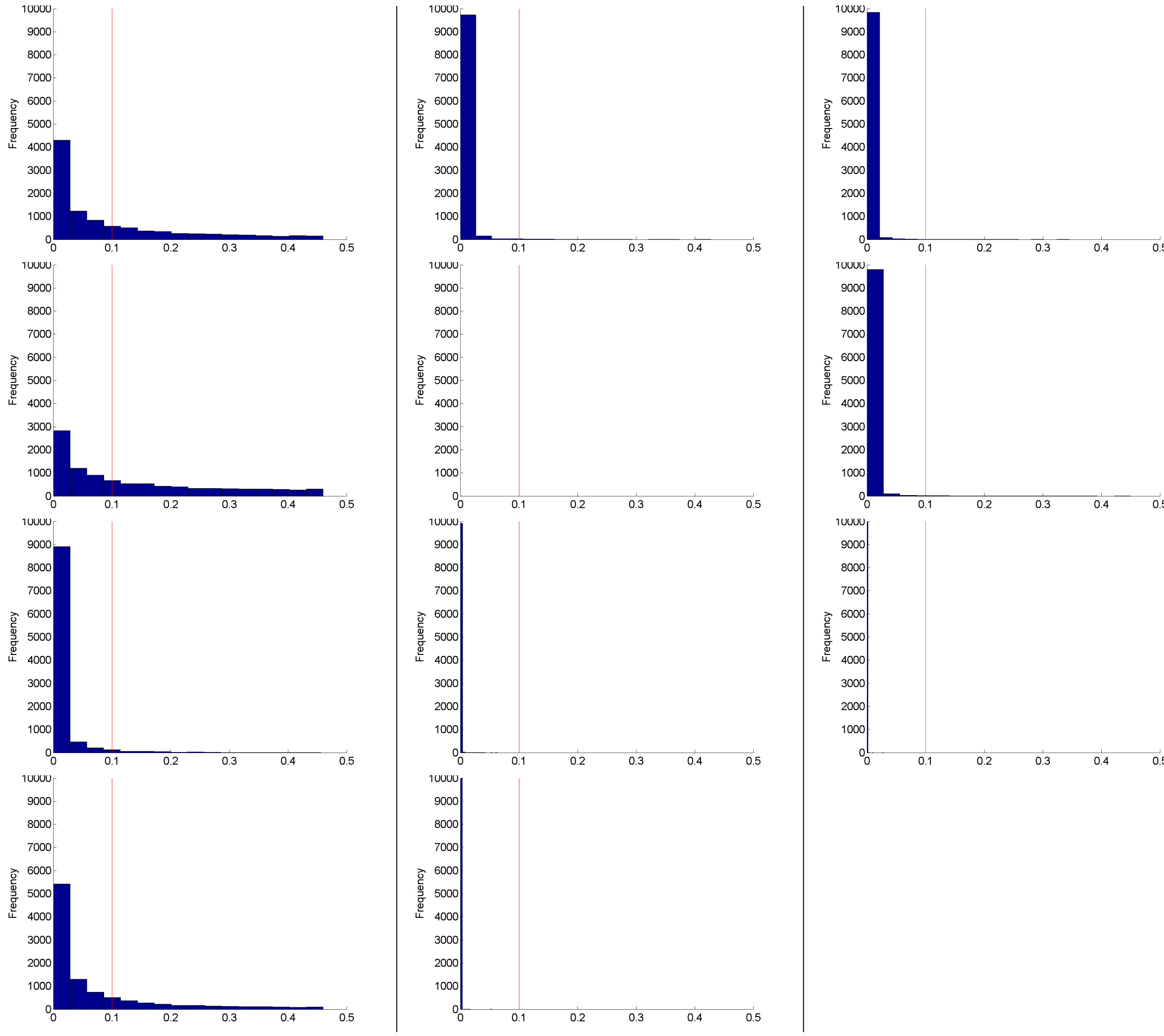

Figure 5.16: Probability to reject the hypothesis that there is a significant linear trend of W_λ in 10,000 resamplings via bootstrapping over period 2001–2099 in SRES-A1B scenario in summer (JJAS). Top row: (a) CCSM, (b) CNRM, (c) GFDL. Second row: (d)GISS, (e)IAP, (f)IPSL Third row: (g) MIROC-mres, (h) MIROC-hires, (i) MPI. Fourth row: (j) MRI and (k) UKMO-HADGEM.

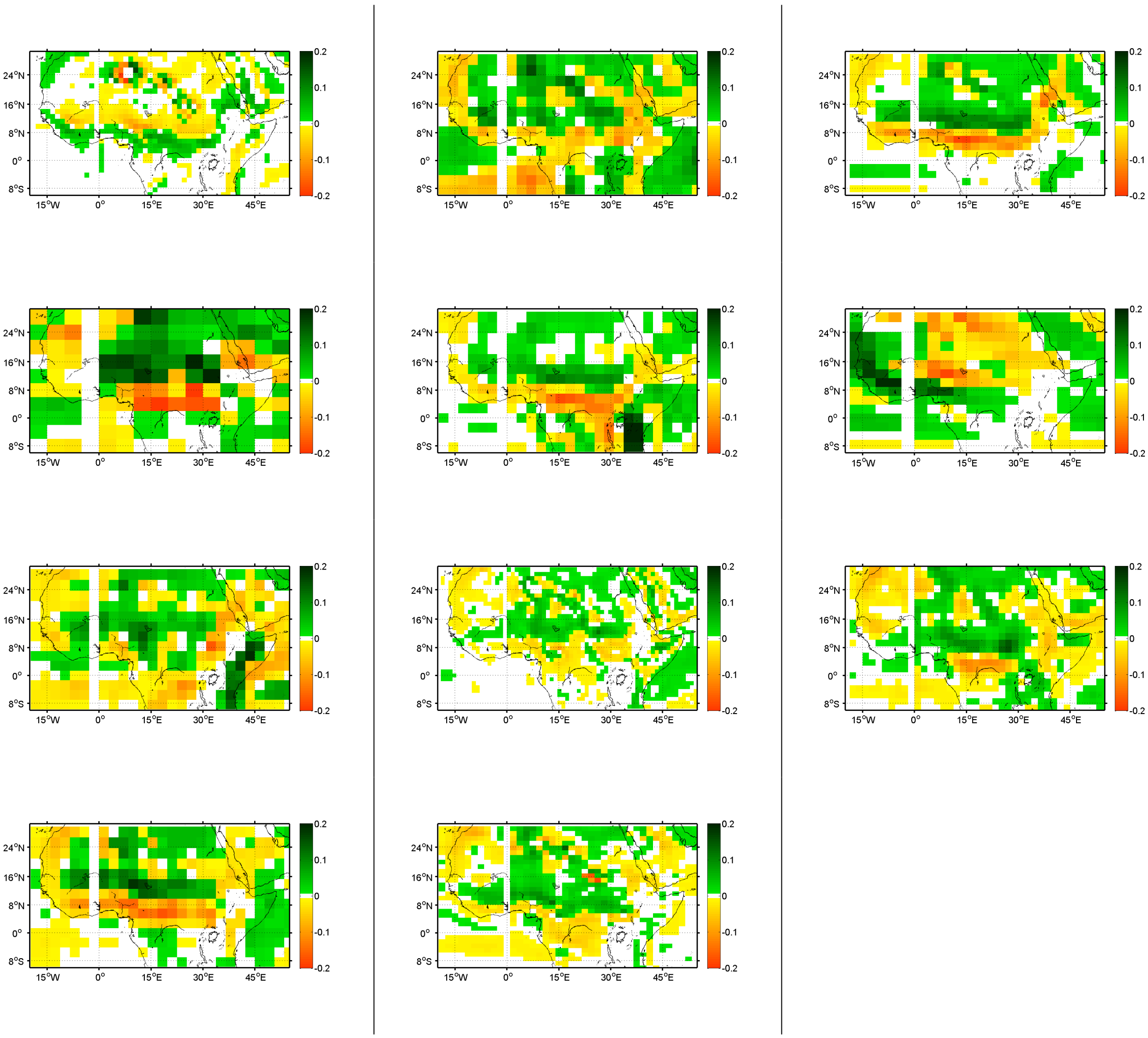

Figure 5.17: First mode of the EOF of 925 hPa divergence during winter (DJFM) in the period 2000–2100 for SRESA1-B. Top row: (a) CCSM, (b) CNRM, (c) GFDL. Second row: (d)GISS, (e)IAP, (f)IPSL Third row: (g) MIROC-mres, (h) MIROC-hires, (i) MPI. Fourth row: (j) MRI and (k) UKMO-HADGEM.

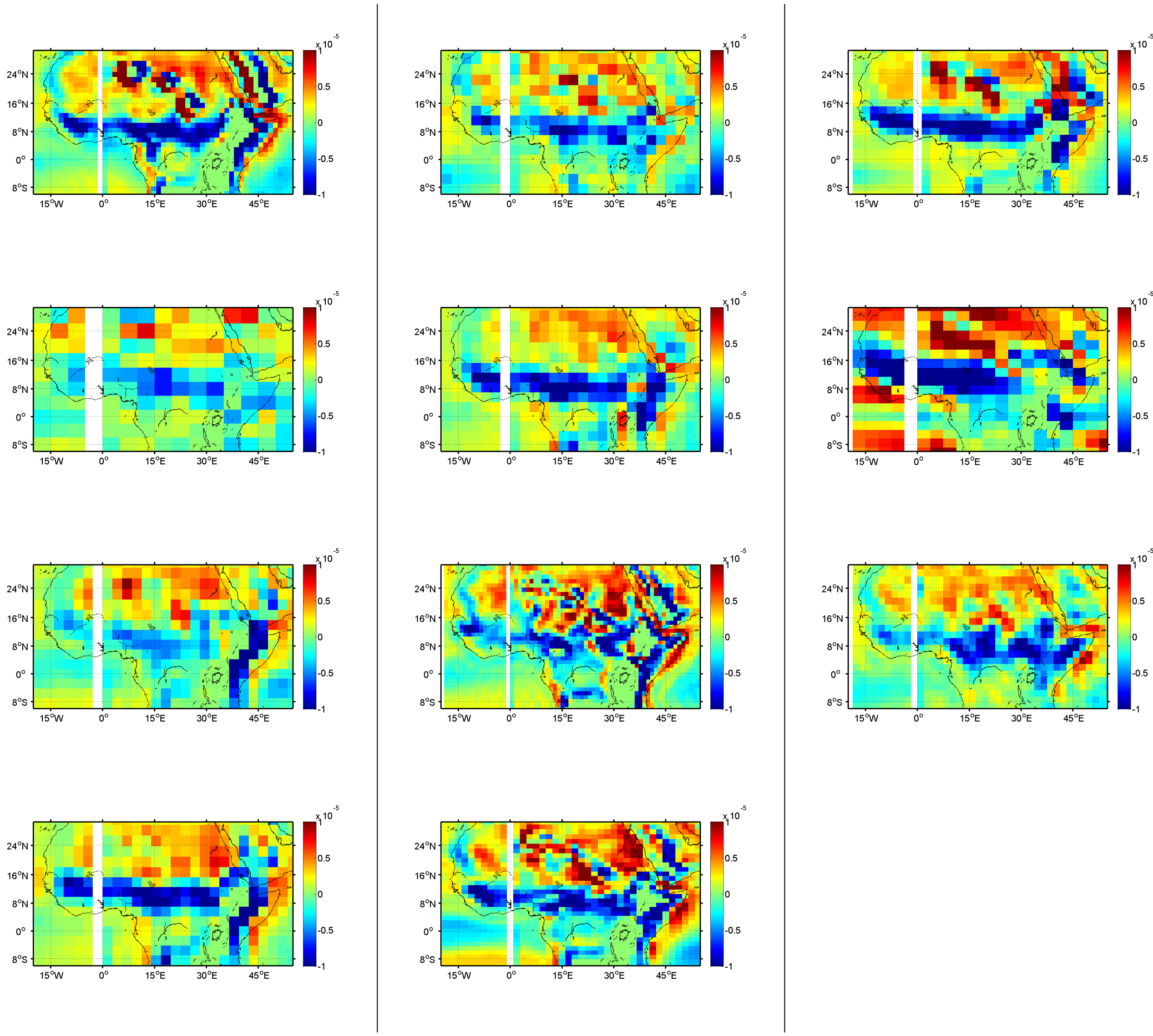

Figure 5.18: Long term mean of 925 hPa divergence during winter (DJFM) in the period 2000–2100 for SRESA1-B. Top row: (a) CCSM, (b) CNRM, (c) GFDL. Second row: (d) GISS, (e) IAP, (f) IPSL Third row: (g) MIROC-mres, (h) MIROC-hires, (i) MPI. Fourth row: (j) MRI and (k) UKMO-HADGEM.

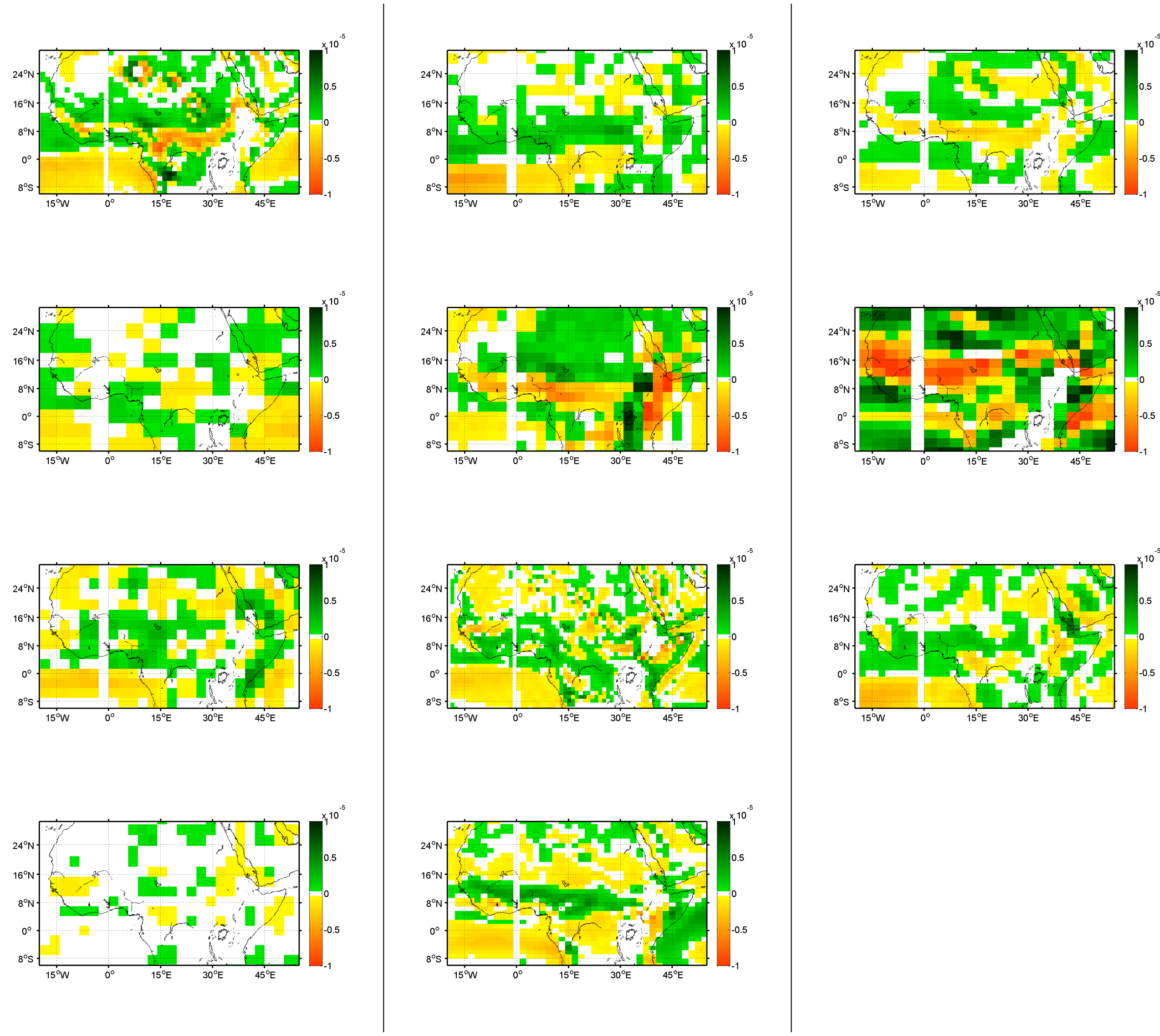

Figure 5.19: Long term mean divergence over the period 2000–2100 in winter (DJFM) for SRESA1-B minus long term mean divergence over the period 1978–2002 for AMIP. Divergence calculated at 925 hPa for winter months. Top row: (a) CCSM, (b) CNRM, (c) GFDL. Second row: (d) GISS, (e) IAP, (f) IPSL Third row: (g) MIROC-mres, (h) MIROC-hires, (i) MPI. Fourth row: (j) MRI and (k) UKMO-HADGEM.

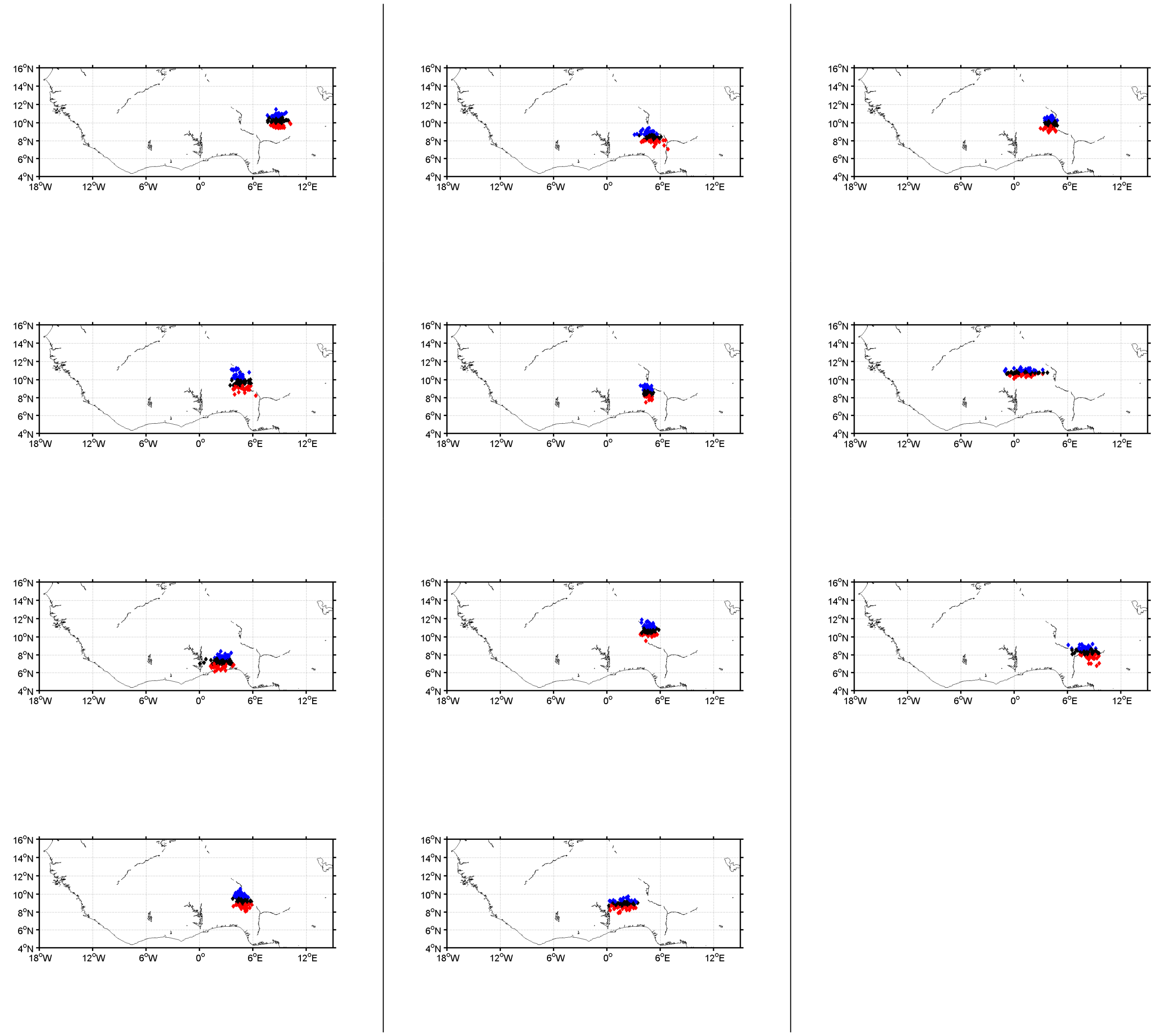

Figure 5.20: Position of WACZ as determined by W_λ and W_ϕ. Each winter mean position is plotted. The quarter of years that are furthest north are blue diamonds, the quarter of years that are furthest south are red diamonds and the interquartile range are black diamonds. COA plotted over the period 2000–2100 for SRESA1-B. Top row: (a) CCSM, (b) CNRM, (c) GFDL. Second row: (d)GISS, (e)IAP, (f)IPSL Third row: (g) MIROC-mres, (h) MIROC-hires, (i) MPI. Fourth row: (j) MRI and (k) UKMO-HADGEM.

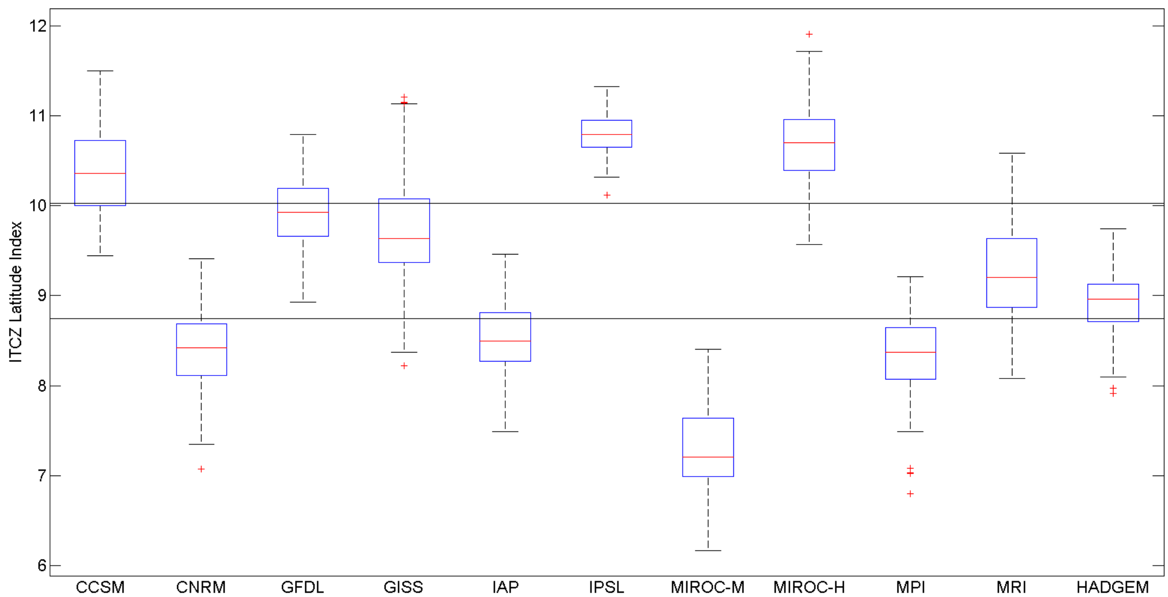

Figure 5.21: Boxplot of winter means of W_ϕ over the period 2000–2100 for SRES-A1b. Red center line represents median, blue lines above and below median represent the 75th and 25th percentiles respectively. Red crosses represents outliers. Black lines extend 1.5 times the interquartile range out from the median.

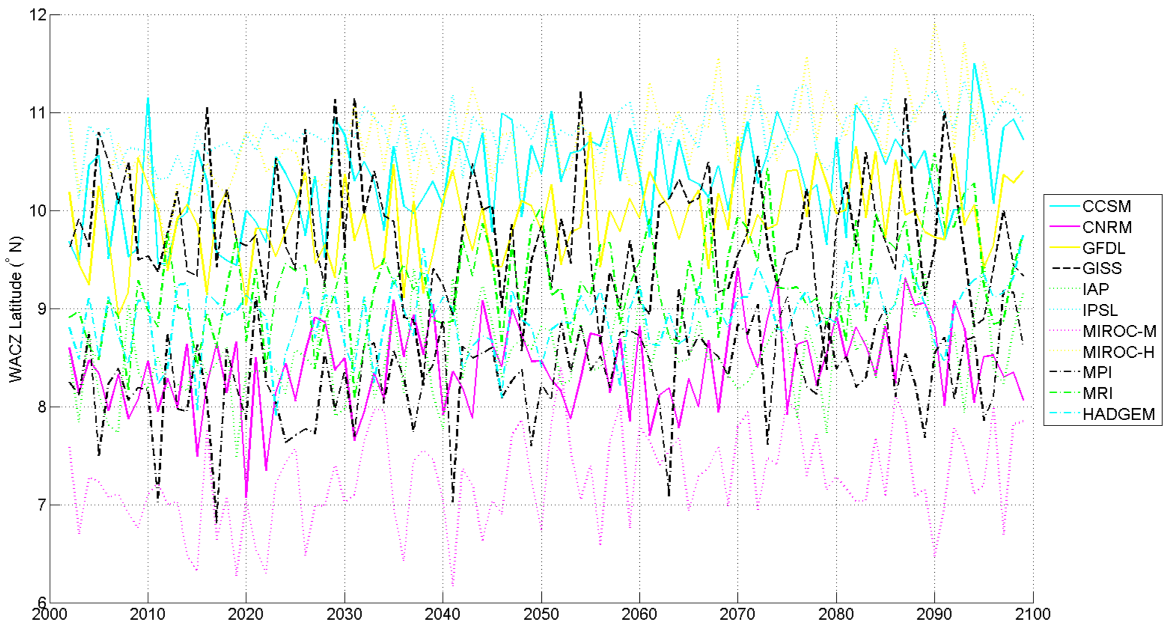

Figure 5.22: Time-series of winter means of W_ϕ over the period 2000–2100 for SRES-A1b.

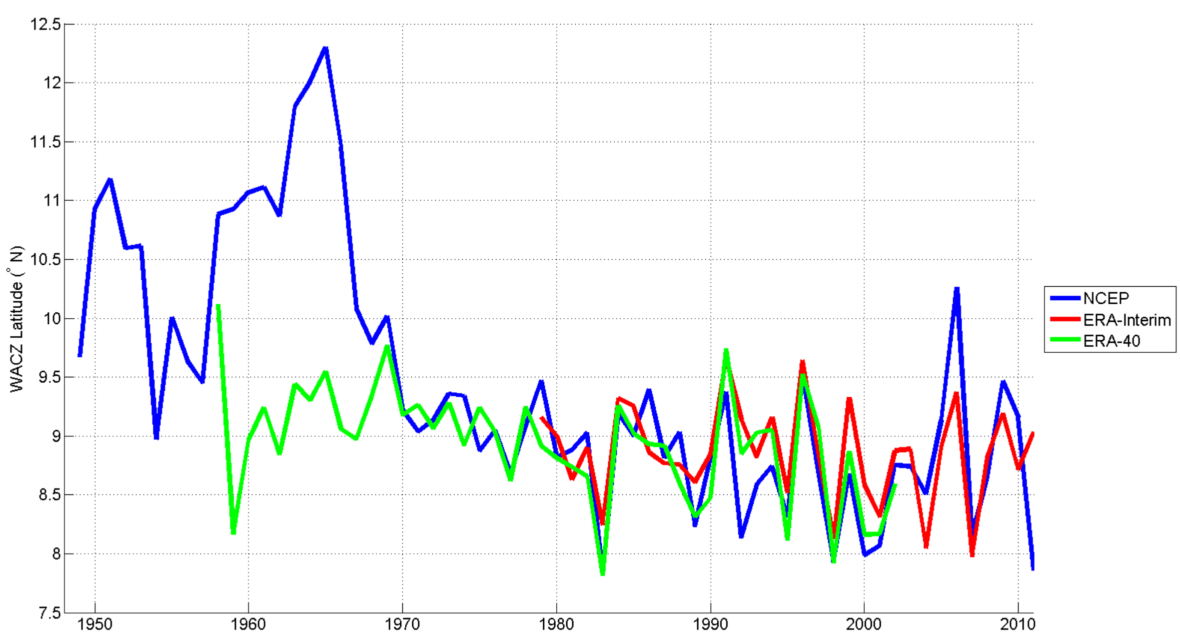

Figure 5.23: Time-series of winter means of W_ϕ over the period 1948 to 2011 in reanalysis.

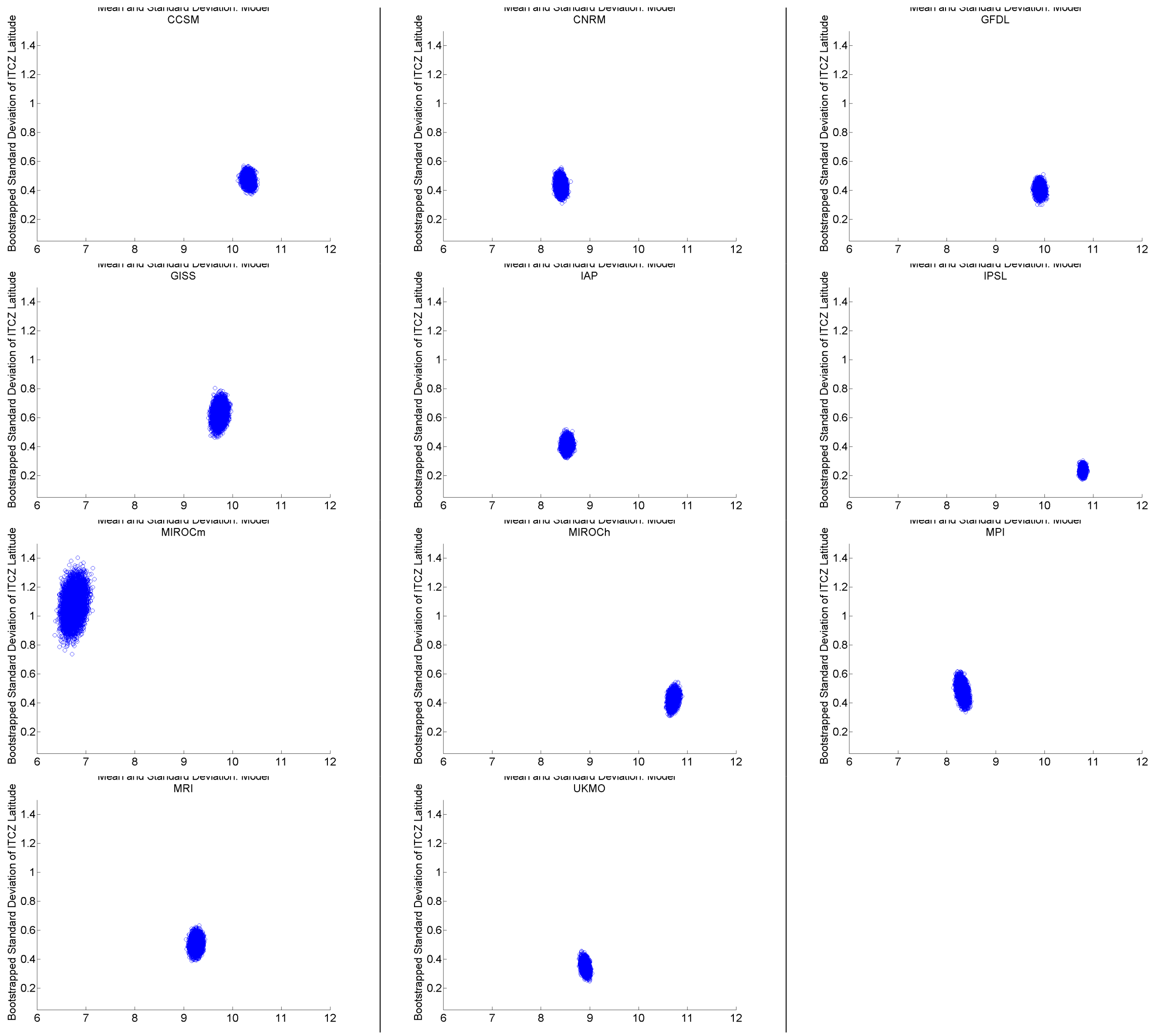

Figure 5.24: Mean (x-axis) and standard deviation (y-axis) of W_ϕ in 10,000 resamplings via bootstrapping over period 2001–2099 in SRES-A1B scenario for winter (DJFM). Top row: (a) CCSM, (b) CNRM, (c) GFDL. Second row: (d)GISS, (e)IAP, (f)IPSL Third row: (g) MIROC-mres, (h) MIROC-hires, (i) MPI. Fourth row: (j) MRI and (k) UKMO-HADGEM.

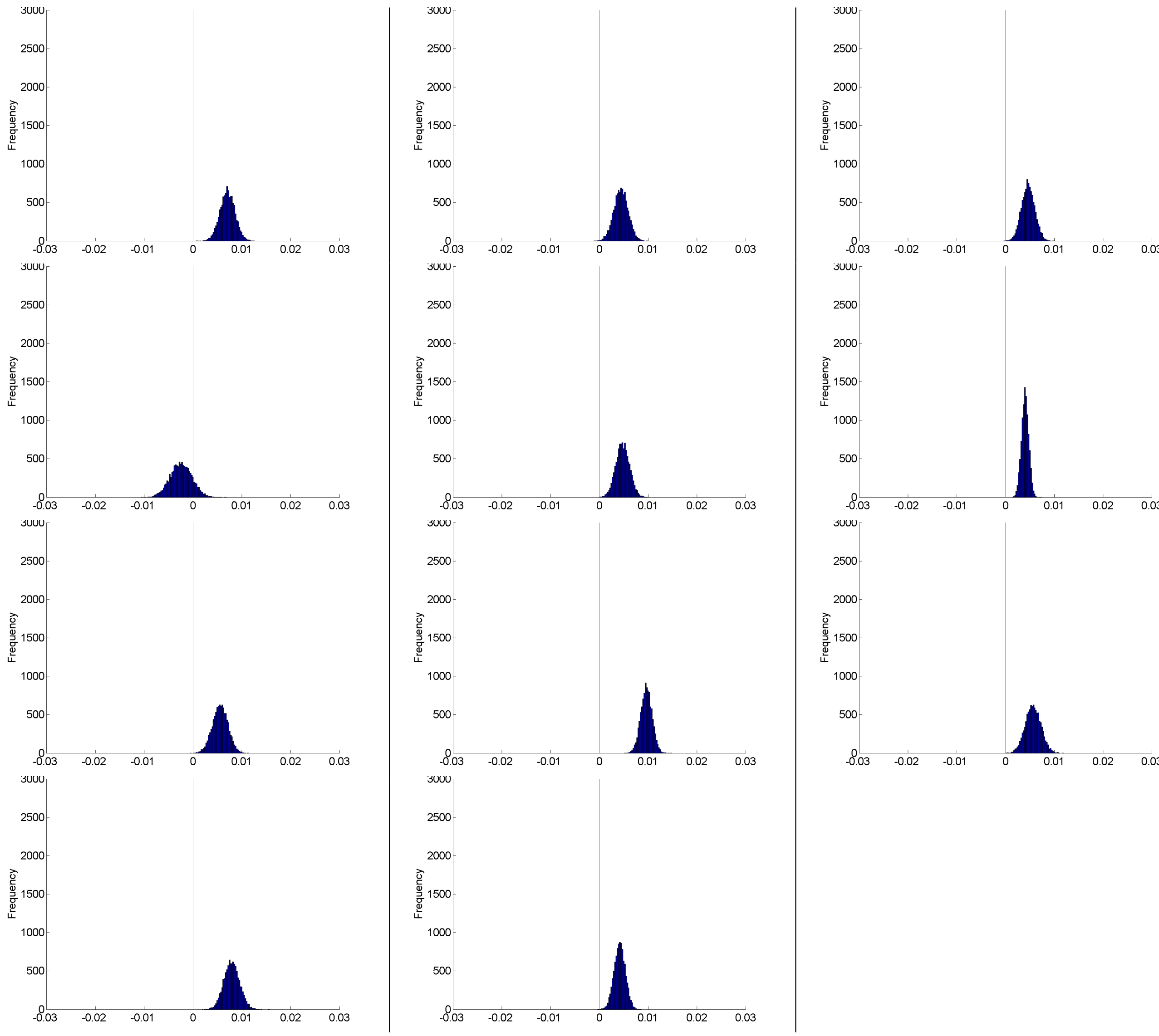

Figure 5.25: Linear trend of W_ϕ in 10,000 resamplings via bootstrapping over period 2001–2099 in SRES-A1B scenario in winter (DJFM). Top row: (a) CCSM, (b) CNRM, (c) GFDL. Second row: (d)GISS, (e)IAP, (f)IPSL Third row: (g) MIROC-mres, (h) MIROC-hires, (i) MPI. Fourth row: (j) MRI and (k) UKMO-HADGEM.

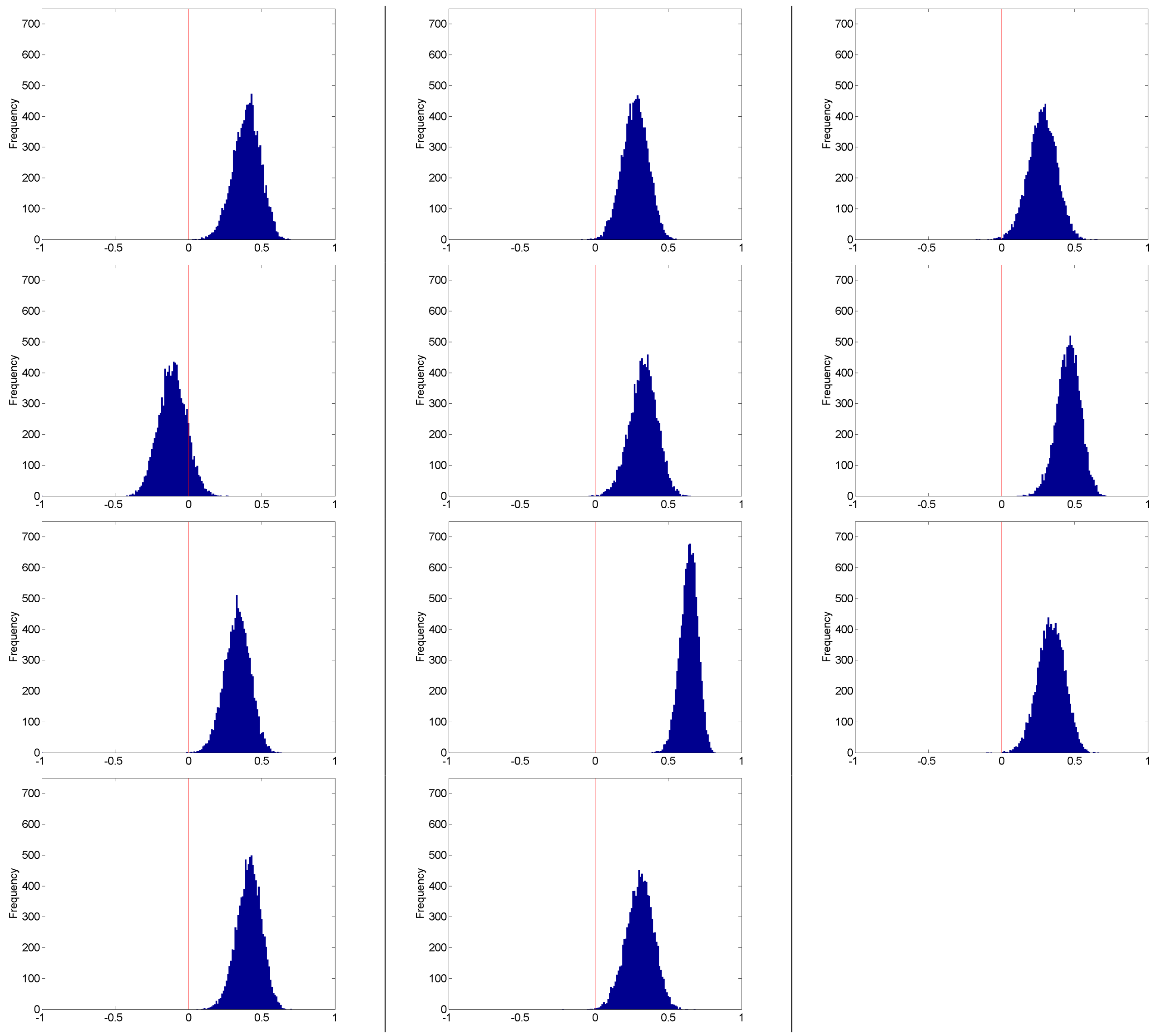

Figure 5.26: Pearson product moment correlation coefficients between W_ϕ and time in 10,000 resamplings via bootstrapping over period 2001–2099 in SRES-A1B scenario in winter (DJFM). Top row: (a) CCSM, (b) CNRM, (c) GFDL. Second row: (d)GISS, (e)IAP, (f)IPSL Third row: (g) MIROC-mres, (h) MIROC-hires, (i) MPI. Fourth row: (j) MRI and (k) UKMO-HADGEM.

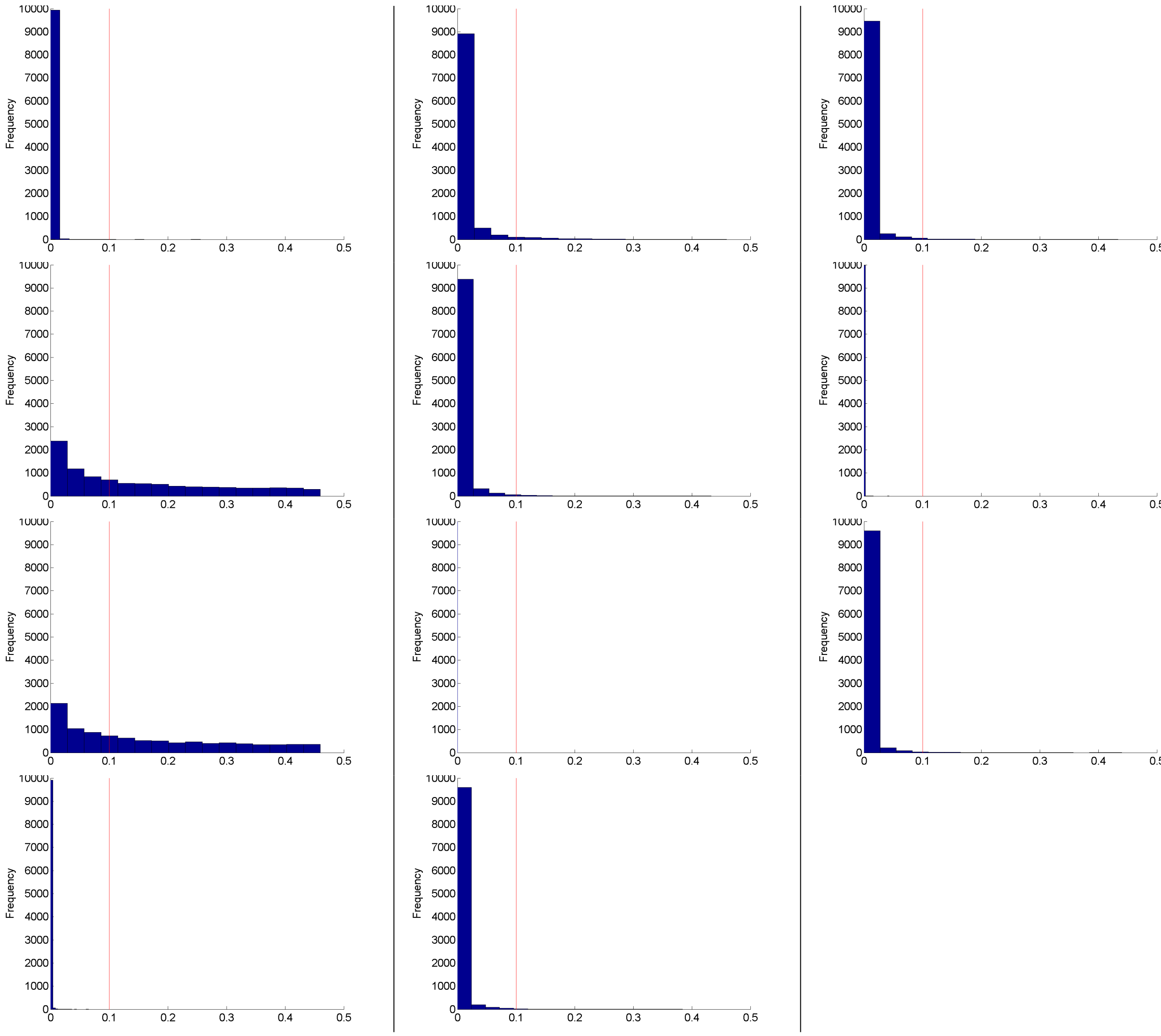

Figure 5.27: Probability to reject the hypothesis that there is a significant linear trend of W_ϕ in 10,000 resamplings via bootstrapping over period 2001–2099 in SRES-A1B scenario in winter (DJFM). Top row: (a) CCSM, (b) CNRM, (c) GFDL. Second row: (d)GISS, (e)IAP, (f)IPSL Third row: (g) MIROC-mres, (h) MIROC-hires, (i) MPI. Fourth row: (j) MRI and (k) UKMO-HADGEM.

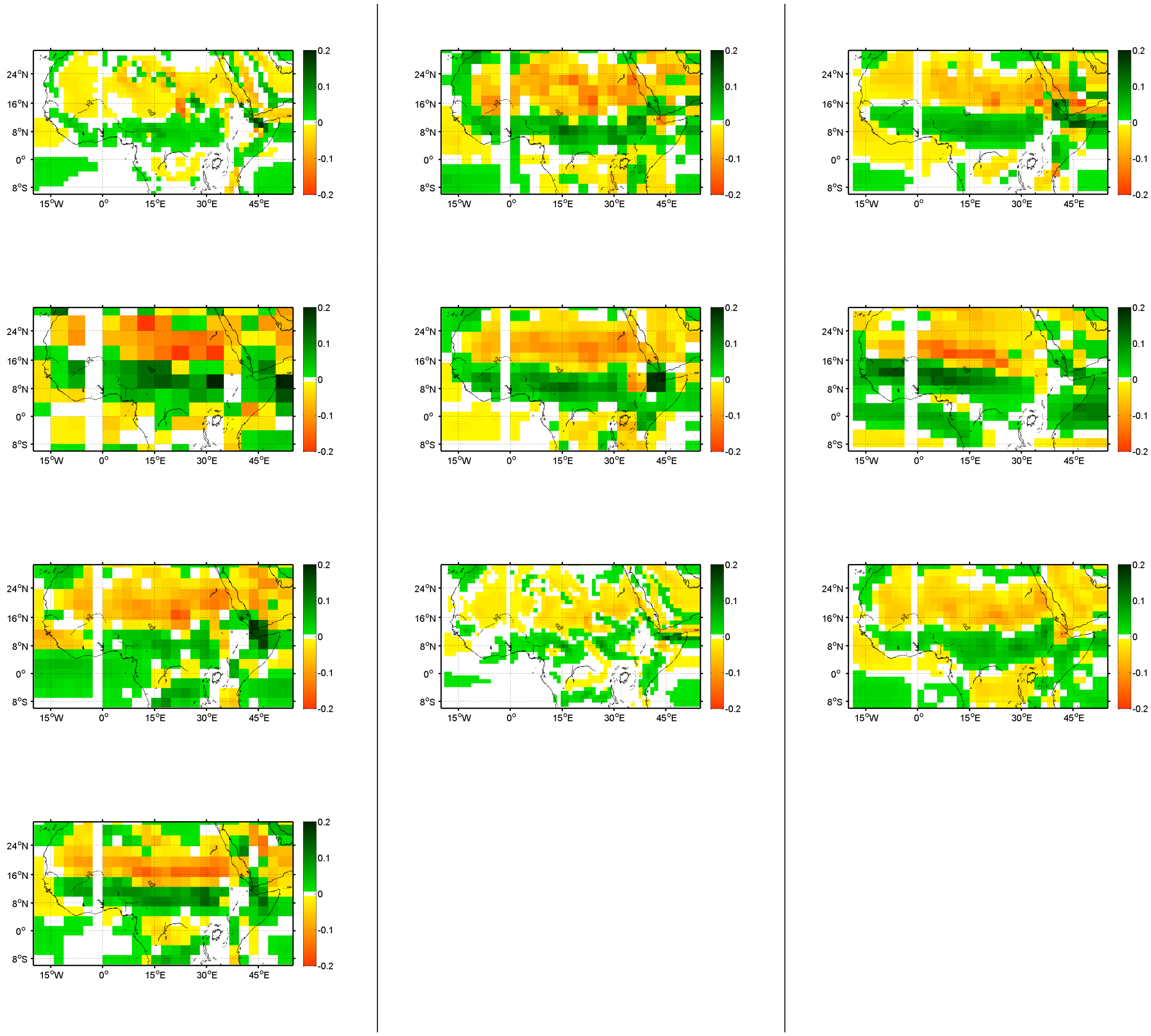

Figure 5.28: First mode of the EOF of 925 hPa divergence of all months in the period 2000–2100 for SRESB1. Top row: (a) CCSM, (b) CNRM, (c) GFDL. Second row: (d)GISS, (e)IAP, (f)IPSL Third row: (g) MIROC-mres, (h) MIROC-hires, (i) MPI. Fourth row: (j) MRI

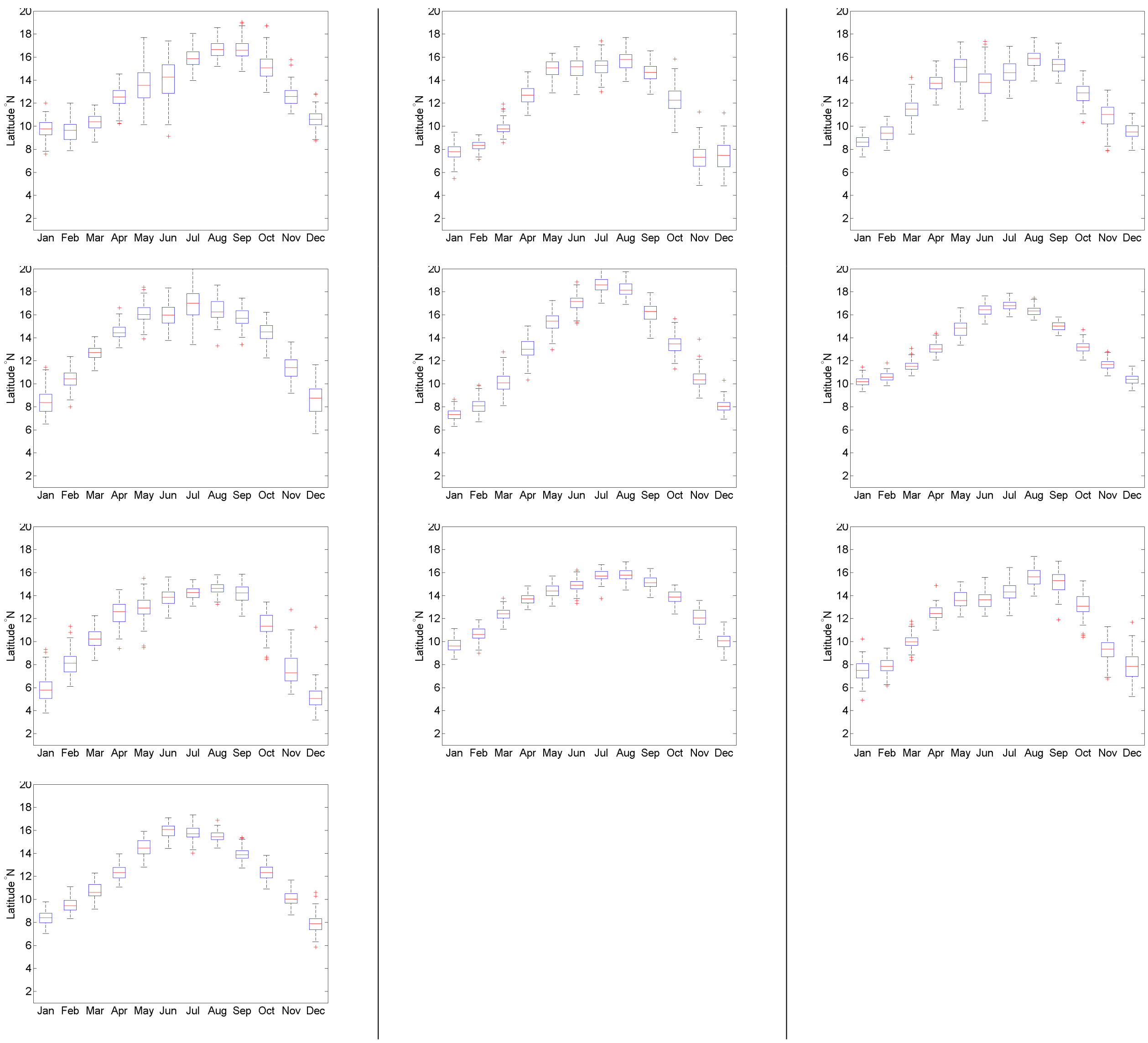

Figure 5.29: Annual south to north migration of WACZ as illustrated by boxplot of monthly means of W_ϕ over the period 2000–2100 for SRES-A1b. Red center line represents median, blue lines above and below median represent the 75th and 25th percentiles respectively. Red crosses represents outliers. Black lines extend 1.5 times the interquartile range out from the median. Top row: (a) CCSM, (b) CNRM, (c) GFDL. Second row: (d)GISS, (e)IAP, (f)IPSL Third row: (g) MIROC-mres, (h) MIROC-hires, (i) MPI. Fourth row: (j) MRI

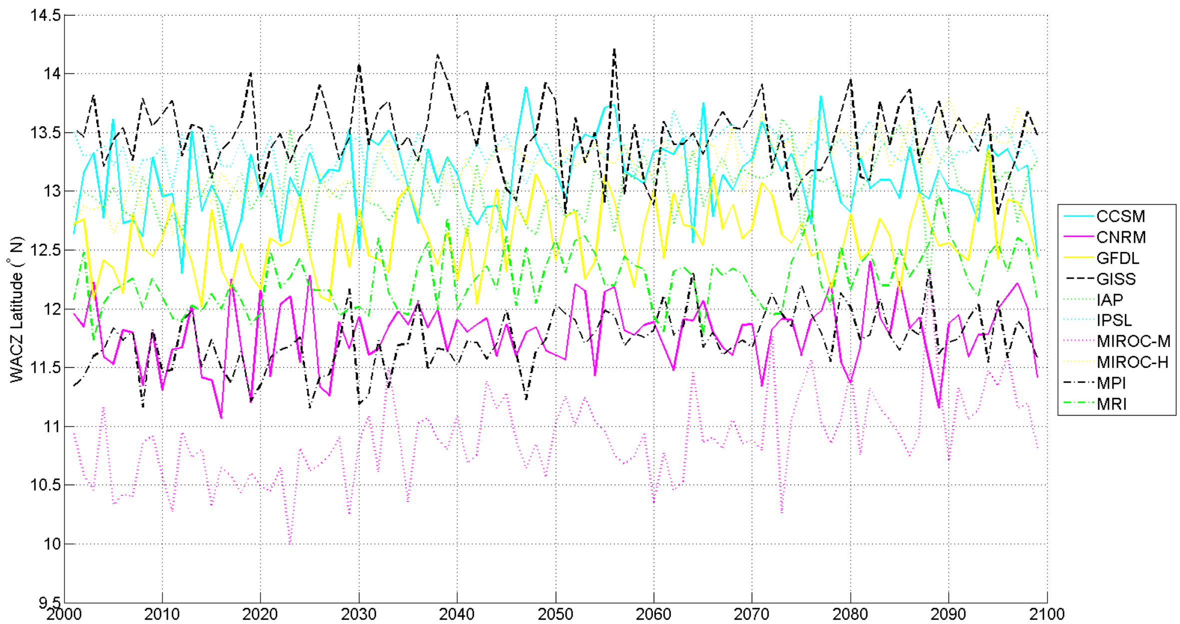

Figure 5.30: Time-series of annual means of W_ϕ over the period 2000–2100 for SRES-A1b.

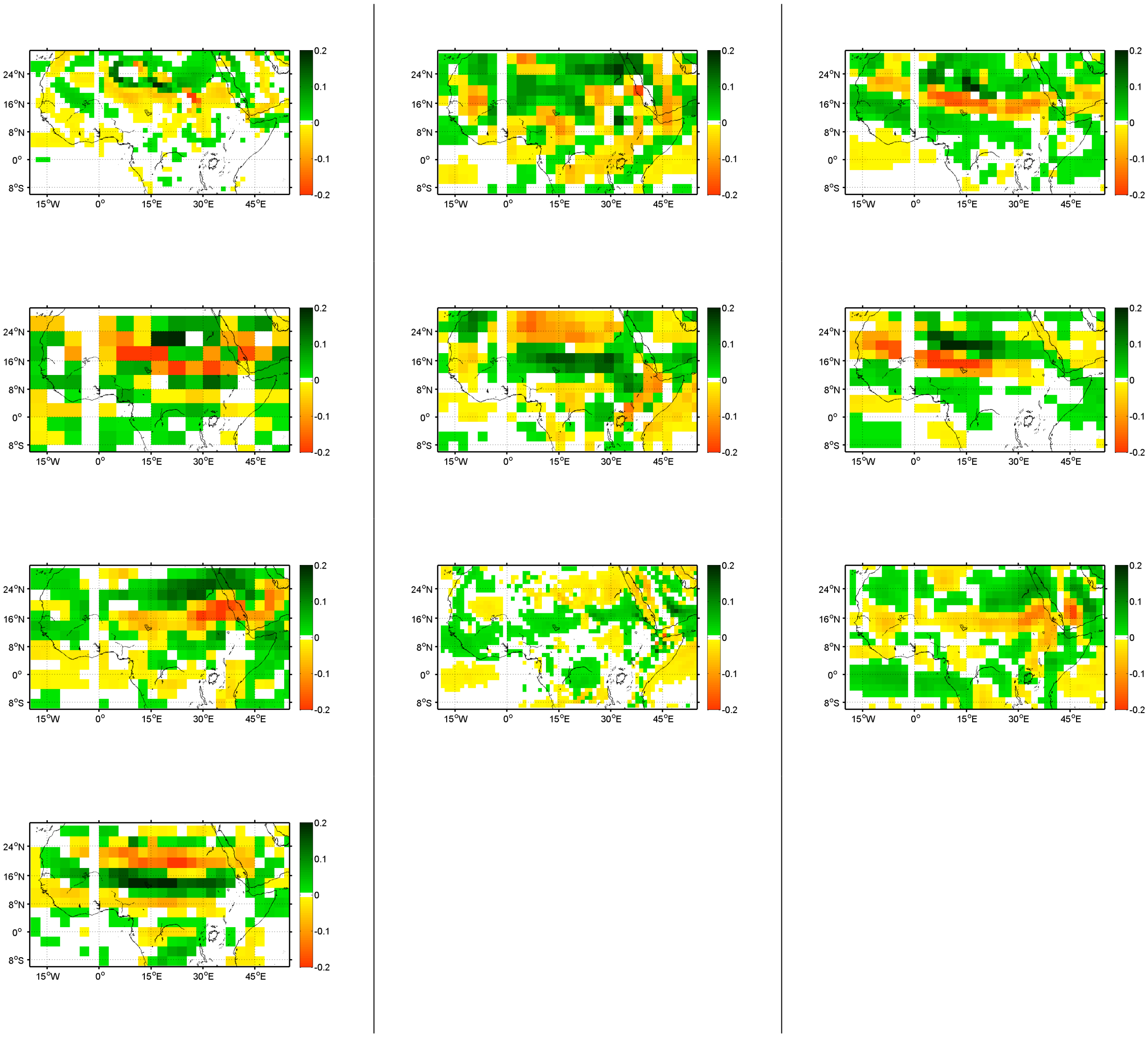

Figure 5.31: First mode of the EOF of 925 hPa divergence during summer (JJAS) in the period 2000–2100 for SRESB1. Top row: (a) CCSM, (b) CNRM, (c) GFDL. Second row: (d)GISS, (e)IAP, (f)IPSL Third row: (g) MIROC-mres, (h) MIROC-hires, (i) MPI. Fourth row: (j) MRI and (k) UKMO-HADGEM.

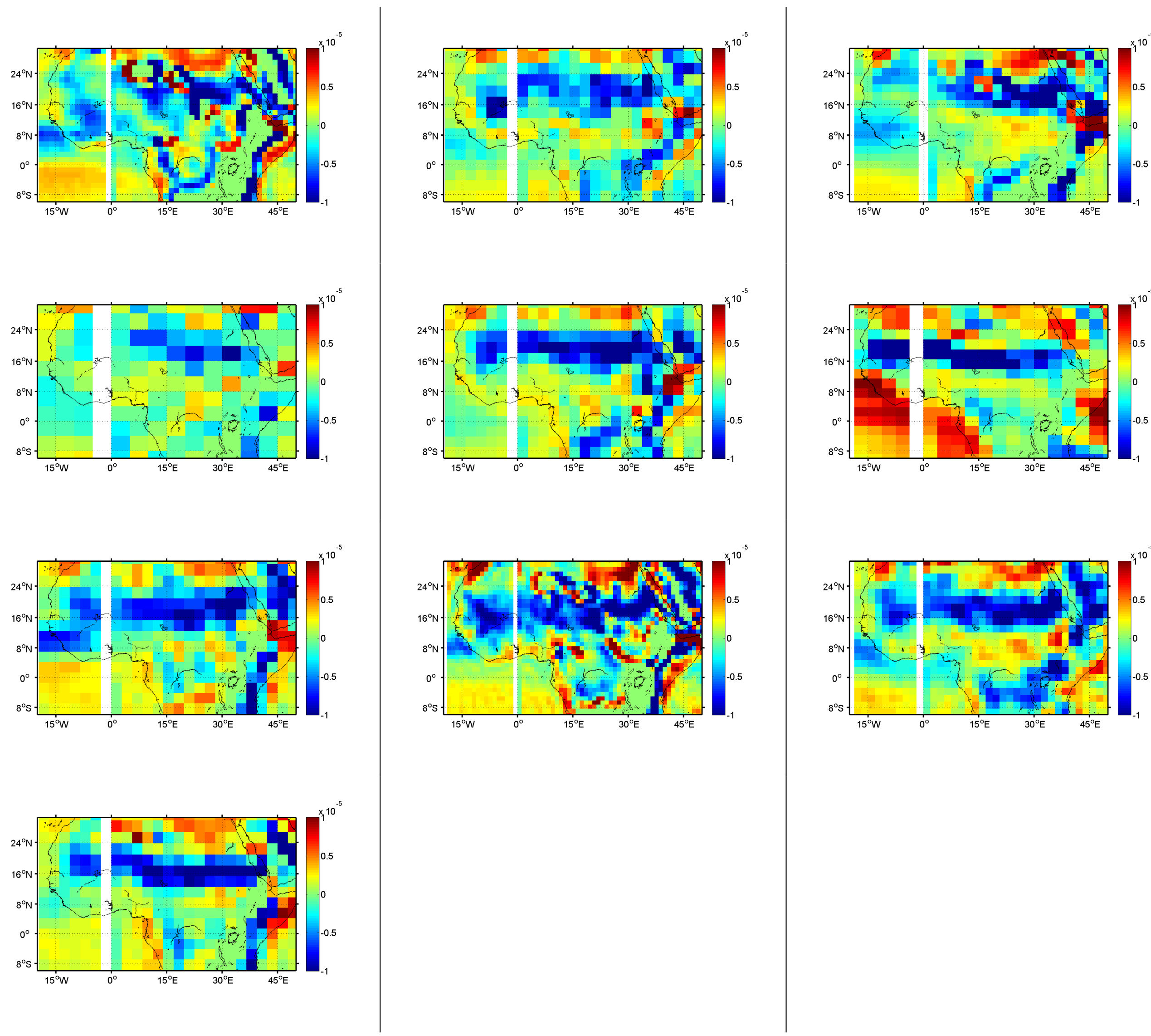

Figure 5.32: Long term mean of 925 hPa divergence during summer (JJAS) in the period 2000–2100 for SRESB1. Top row: (a) CCSM, (b) CNRM, (c) GFDL. Second row: (d)GISS, (e)IAP, (f)IPSL Third row: (g) MIROC-mres, (h) MIROC-hires, (i) MPI. Fourth row: (j) MRI.

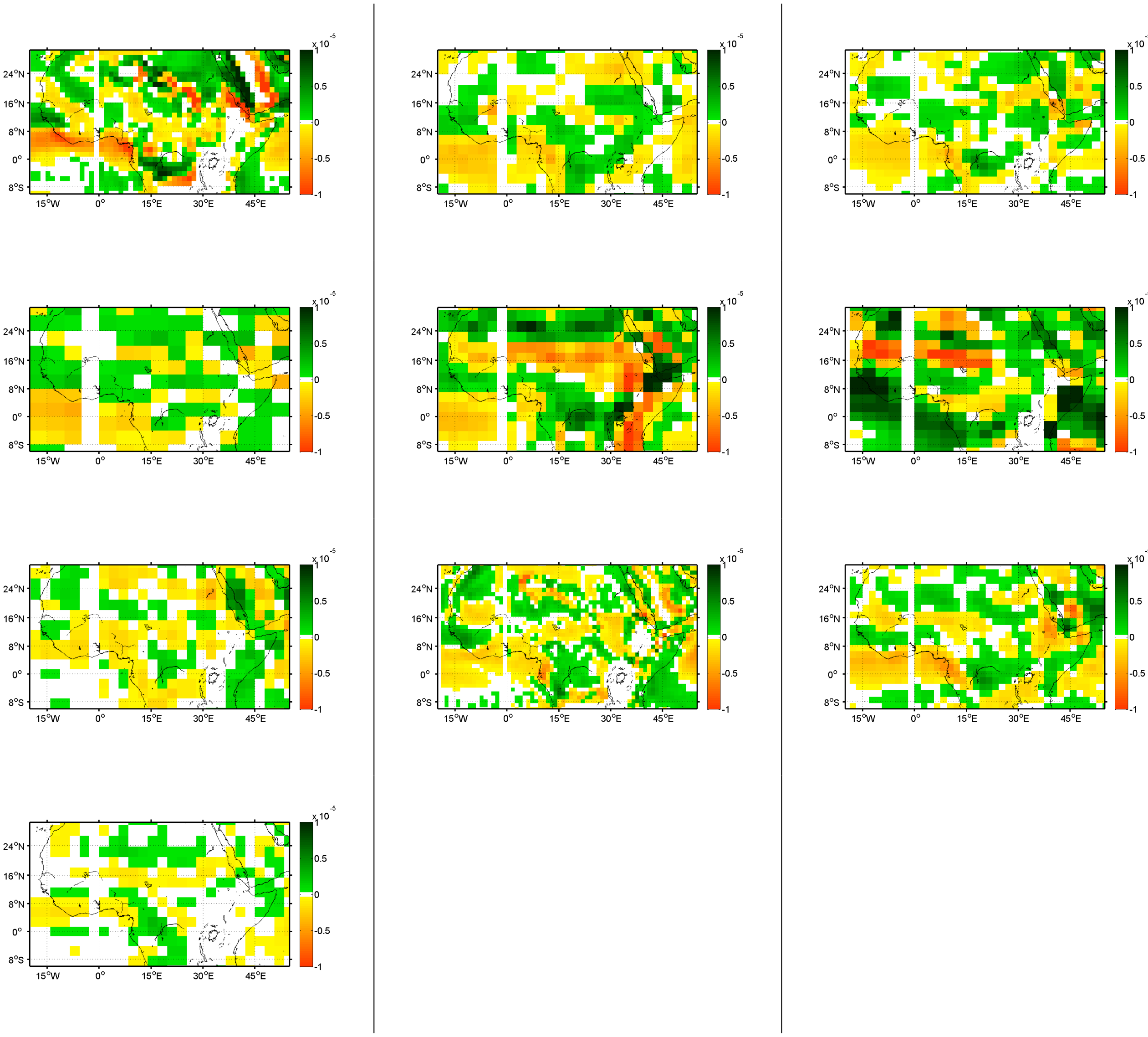

Figure 5.33: Long term mean divergence over the period 2000–2100 for SRESB1 minus long term mean divergence over the period 1978–2002 for AMIP. Divergence calculated at 925 hPa for summer months. Top row: (a) CCSM, (b) CNRM, (c) GFDL. Second row: (d)GISS, (e)IAP, (f)IPSL Third row: (g) MIROC-mres, (h) MIROC-hires, (i) MPI. Fourth row: (j) MRI.

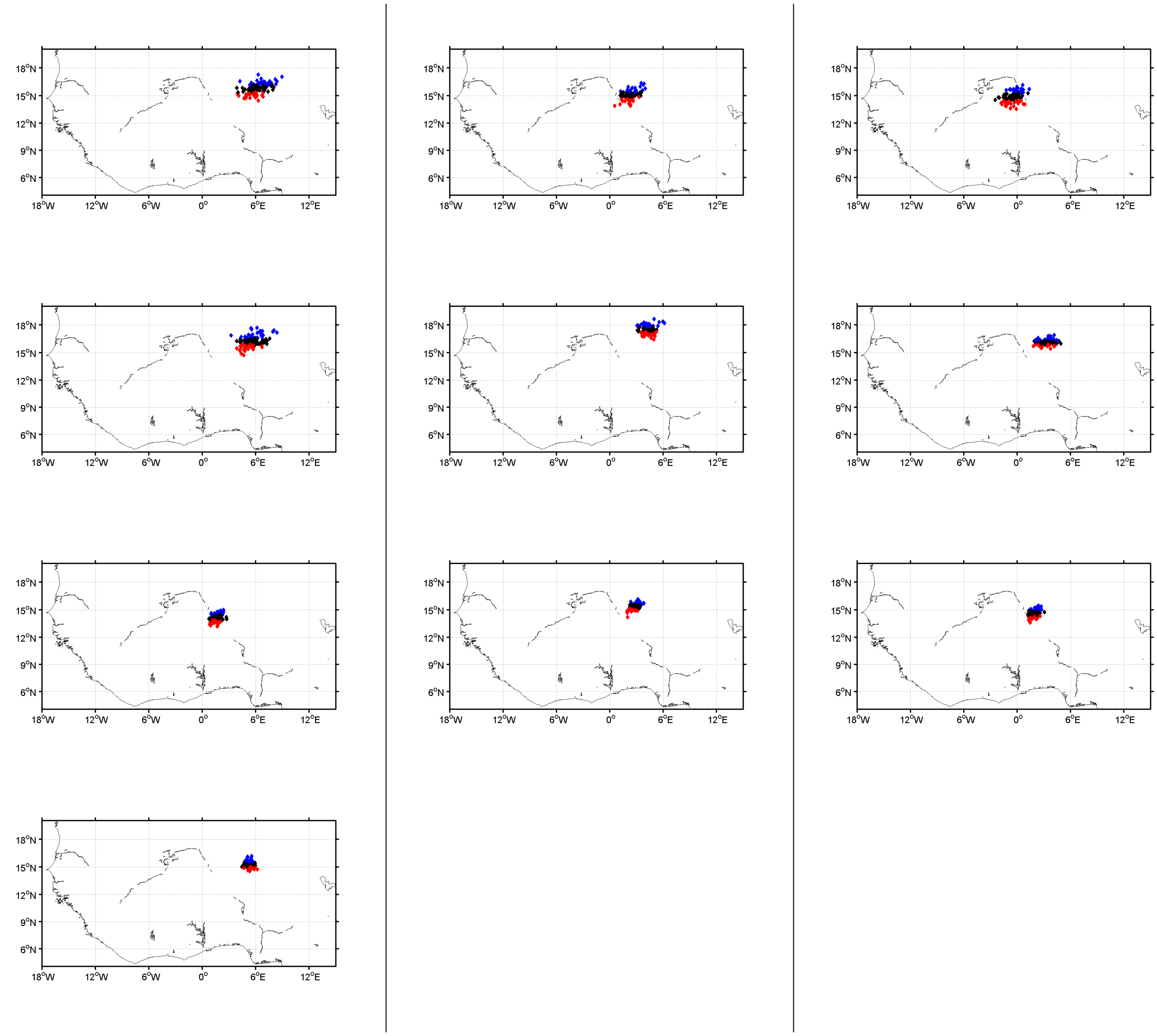

Figure 5.34: Position of WACZ as determined by W_λ and W_ϕ. Each summer mean position is plotted. The quarter of years that are furthest north are blue diamonds, the quarter of years that are furthest south are red diamonds and the interquartile range are black diamonds. COA plotted over the period 2000–2100 for SRESb1. Top row: (a) CCSM, (b) CNRM, (c) GFDL. Second row: (d)GISS, (e)IAP, (f)IPSL Third row: (g) MIROC-mres, (h) MIROC-hires, (i) MPI. Fourth row: (j) MRI.

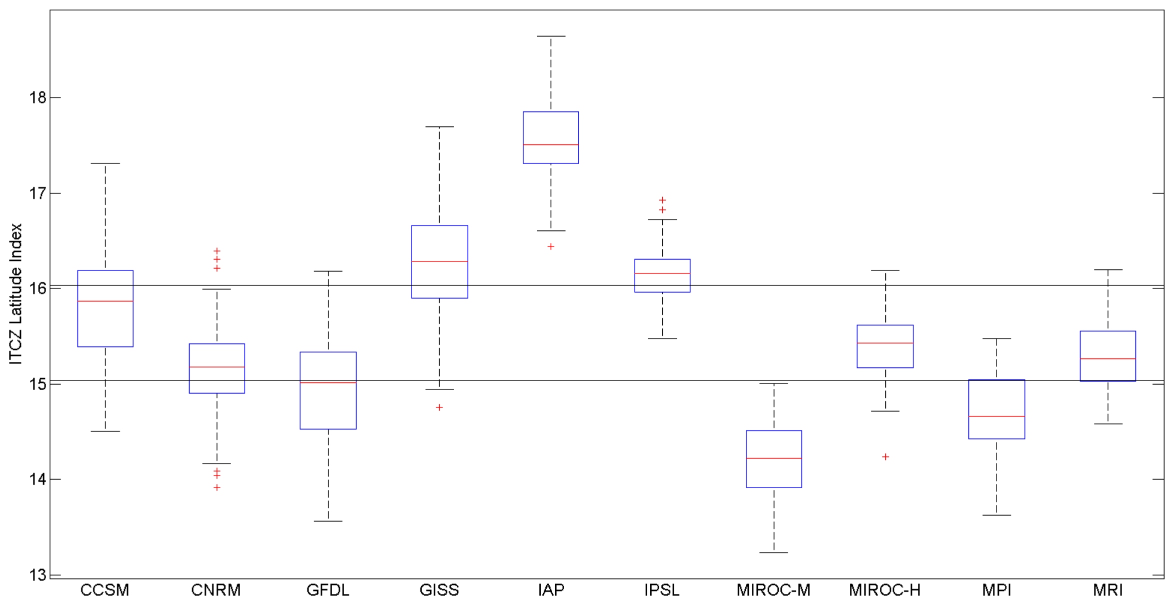

Figure 5.35: Boxplot of summer means of W_ϕ over the period 2000–2100 for SRES-A1b. Red center line represents median, blue lines above and below median represent the 75th and 25th percentiles respectively. Red crosses represents outliers. Black lines extend 1.5 times the interquartile range out from the median.

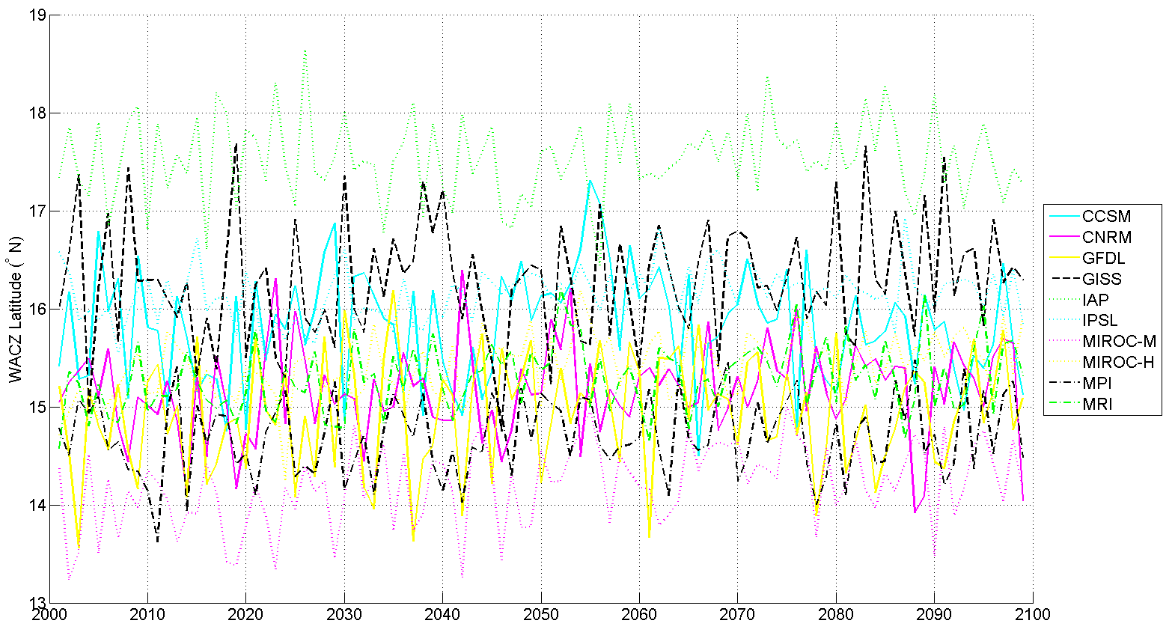

Figure 5.36: Time-series of summer means of W_ϕ over the period 2000–2100 for SRES-A1b.

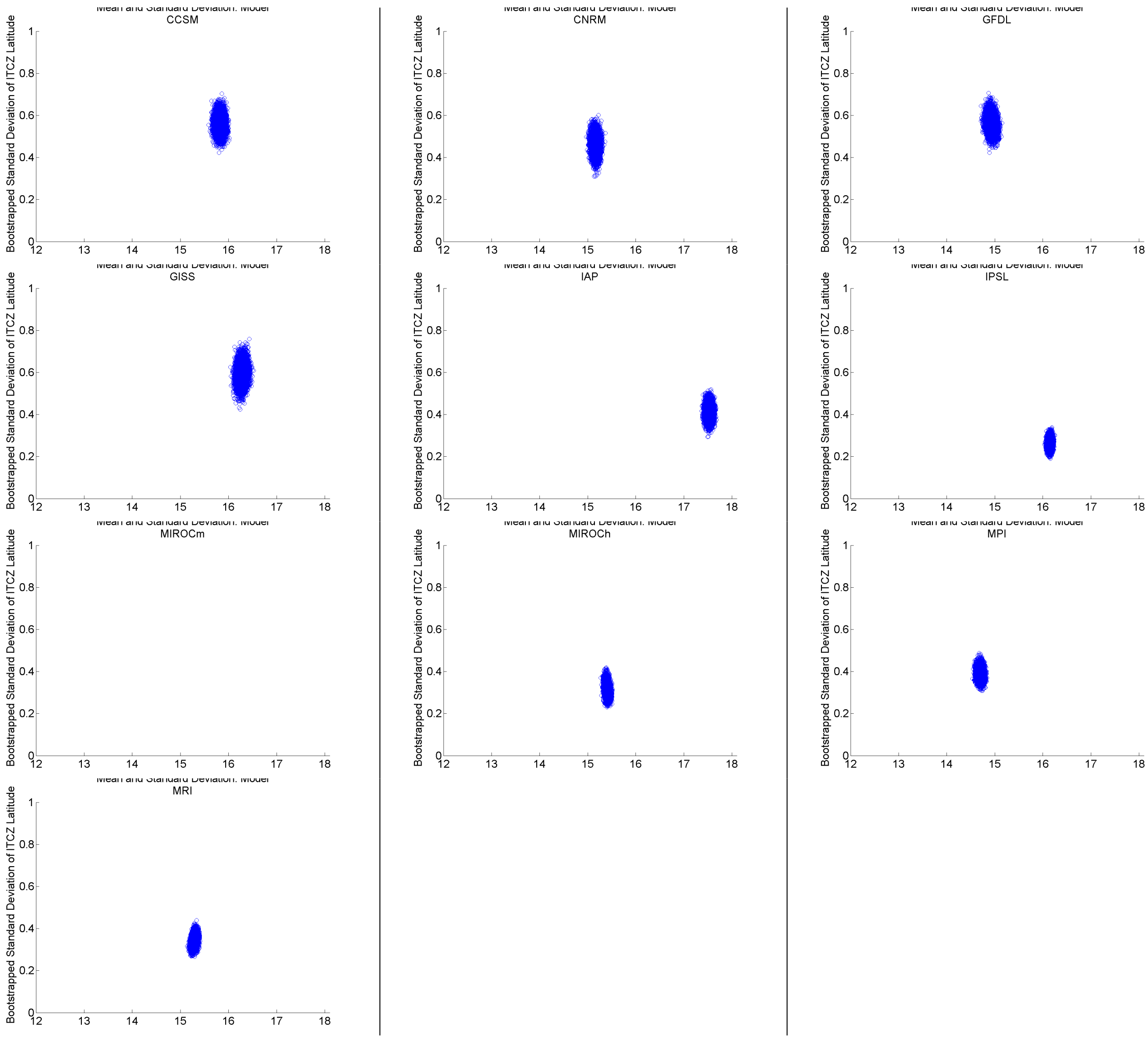

Figure 5.37: Mean (x-axis) and standard deviation (y-axis) of W_{ϕ} in 10,000 resamplings via bootstrapping over period 2001–2099 in SRESB1 scenario in summer (JJAS). Top row: (a) CCSM, (b) CNRM, (c) GFDL. Second row: (d)GISS, (e)IAP, (f)IPSL Third row: (g) MIROC-mres, (h) MIROC-hires, (i) MPI. Fourth row: (j) MRI.

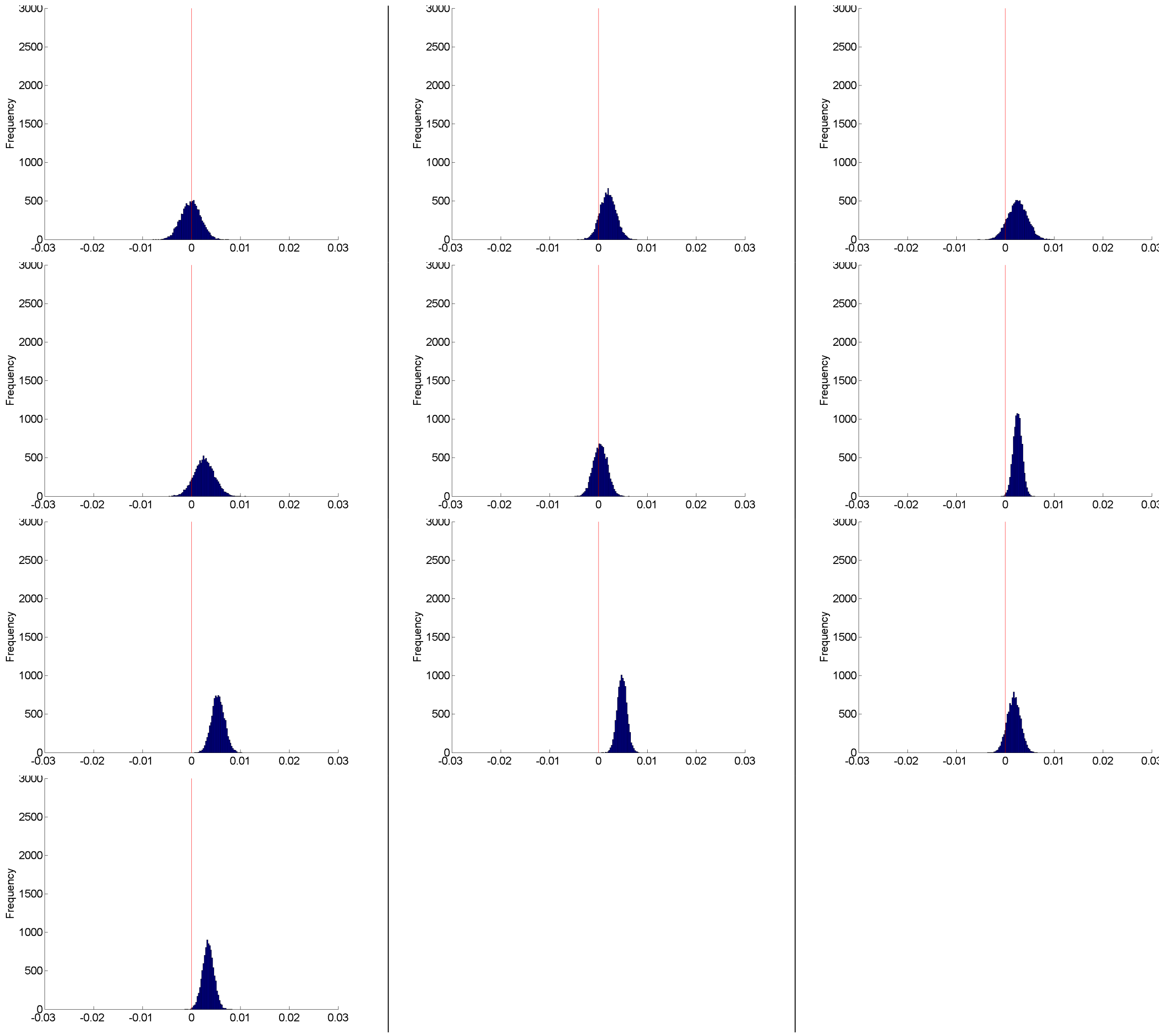

Figure 5.38: Linear trend of W_ϕ in 10,000 resamplings via bootstrapping over period 2001–2099 in SRESB1 scenario in summer (JJAS). Top row: (a) CCSM, (b) CNRM, (c) GFDL. Second row: (d)GISS, (e)IAP, (f)IPSL Third row: (g) MIROC-mres, (h) MIROC-hires, (i) MPI. Fourth row: (j) MRI.

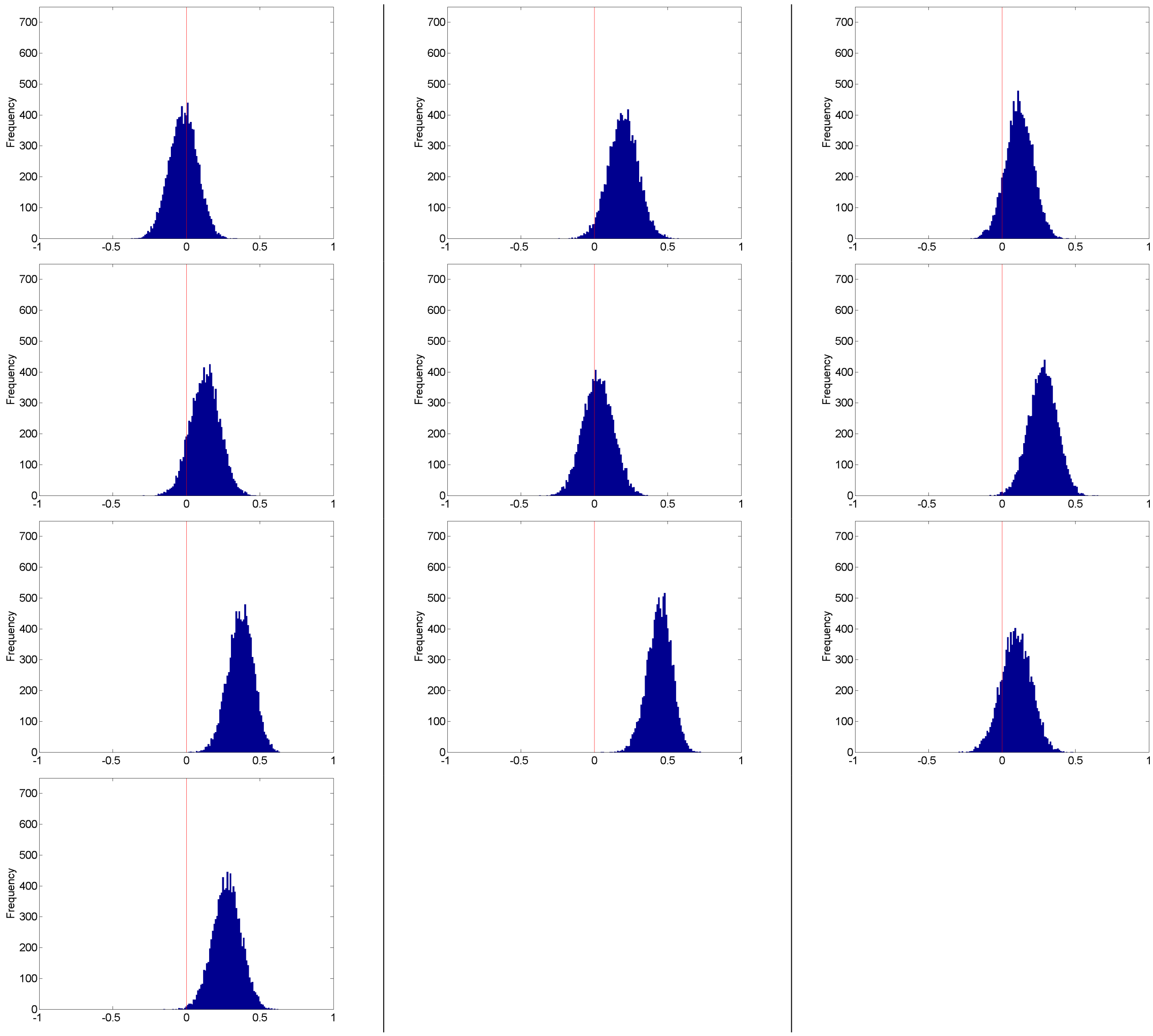

Figure 5.39: Pearson product moment correlation coefficients between W_ϕ and time in 10,000 resamplings via bootstrapping over period 2001–2099 in SRESB1 scenario in summer (JJAS). Top row: (a) CCSM, (b) CNRM, (c) GFDL. Second row: (d)GISS, (e)IAP, (f)IPSL Third row: (g) MIROC-mres, (h) MIROC-hires, (i) MPI. Fourth row: (j) MRI.

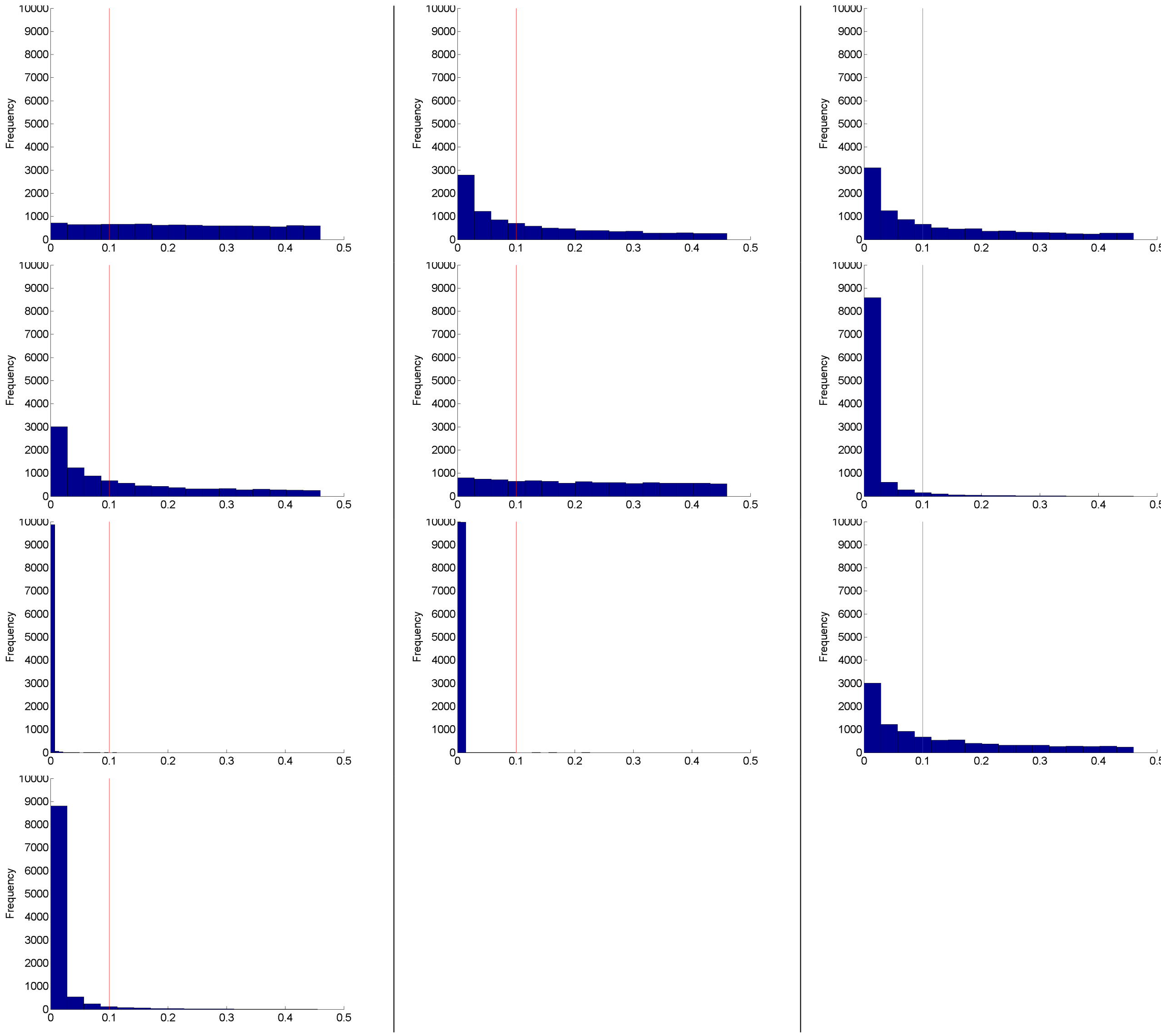

Figure 5.40: Probability to reject the hypothesis that there is a significant linear trend of W_ϕ in 10,000 resamplings via bootstrapping over period 2001–2099 in SRESB1 scenario in summer (JJAS). Top row: (a) CCSM, (b) CNRM, (c) GFDL. Second row: (d)GISS, (e)IAP, (f)IPSL Third row: (g) MIROC-mres, (h) MIROC-hires, (i) MPI. Fourth row: (j) MRI.

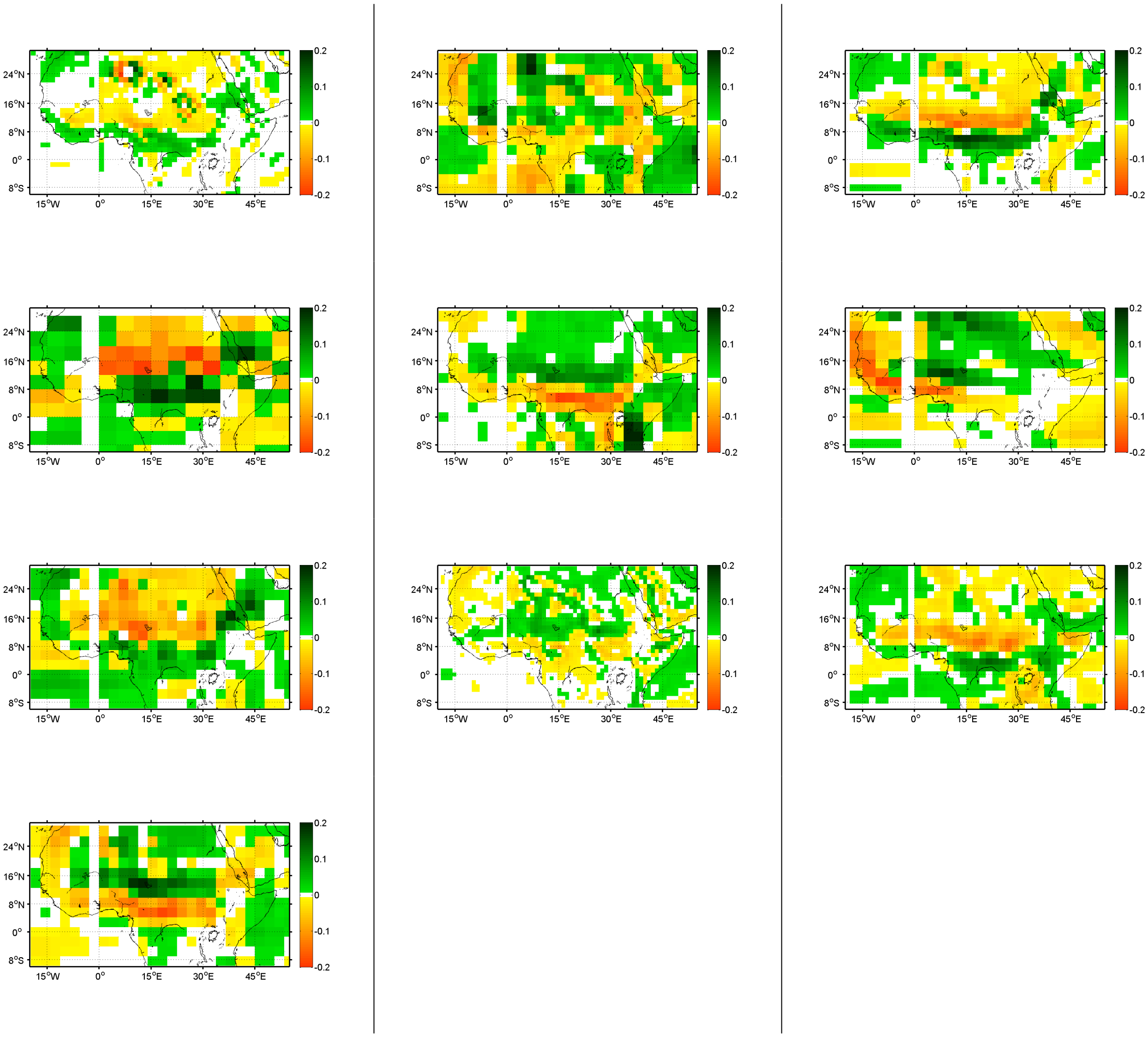

Figure 5.41: First mode of the EOF of 925 hPa divergence during winter (DJFM) in the period 2000–2100 for SRESB1. Top row: (a) CCSM, (b) CNRM, (c) GFDL. Second row: (d)GISS, (e)IAP, (f)IPSL Third row: (g) MIROC-mres, (h) MIROC-hires, (i) MPI. Fourth row: (j) MRI.

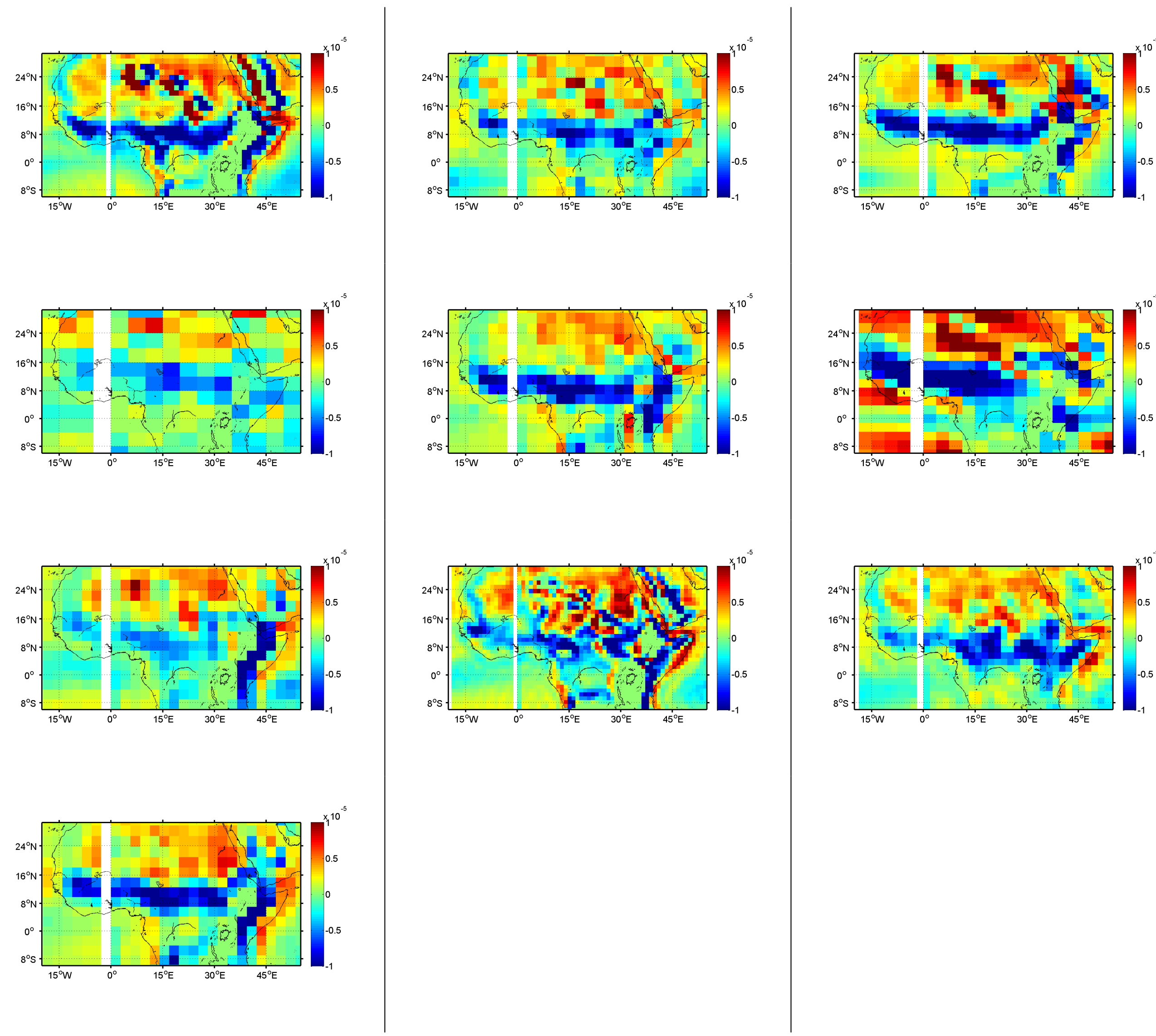

Figure 5.42: Long term mean of 925 hPa divergence during winter (DJFM) in the period 2000–2100 for SRESB1. Top row: (a) CCSM, (b) CNRM, (c) GFDL. Second row: (d)GISS, (e)IAP, (f)IPSL Third row: (g) MIROC-mres, (h) MIROC-hires, (i) MPI. Fourth row: (j) MRI.

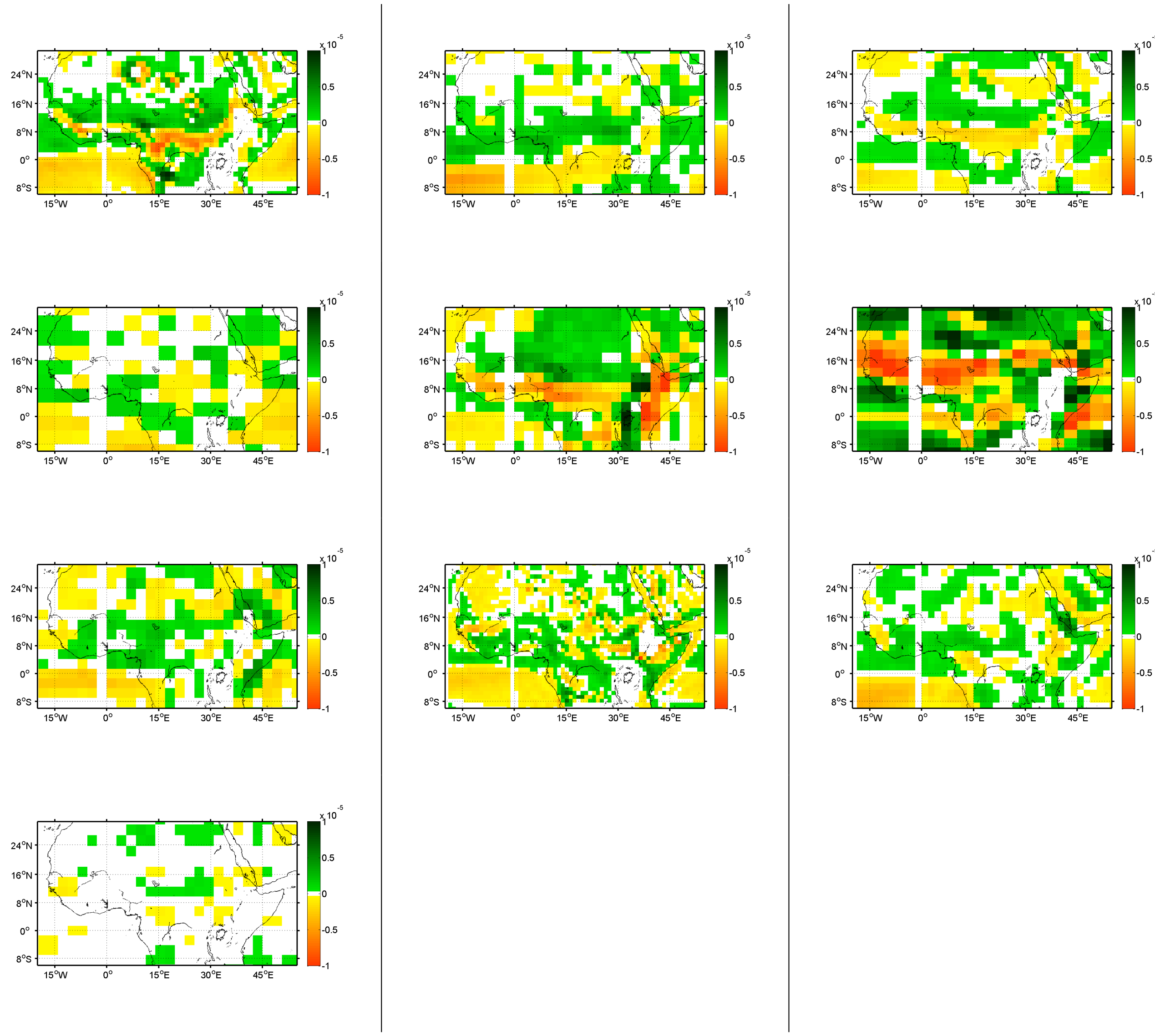

Figure 5.43: Long term mean divergence over the period 2000–2100 for SRESB1 minus long term mean divergence over the period 1978–2002 for AMIP. Divergence calculated at 925 hPa for winter months. Top row: (a) CCSM, (b) CNRM, (c) GFDL. Second row: (d)GISS, (e)IAP, (f)IPSL Third row: (g) MIROC-mres, (h) MIROC-hires, (i) MPI. Fourth row: (j) MRI.

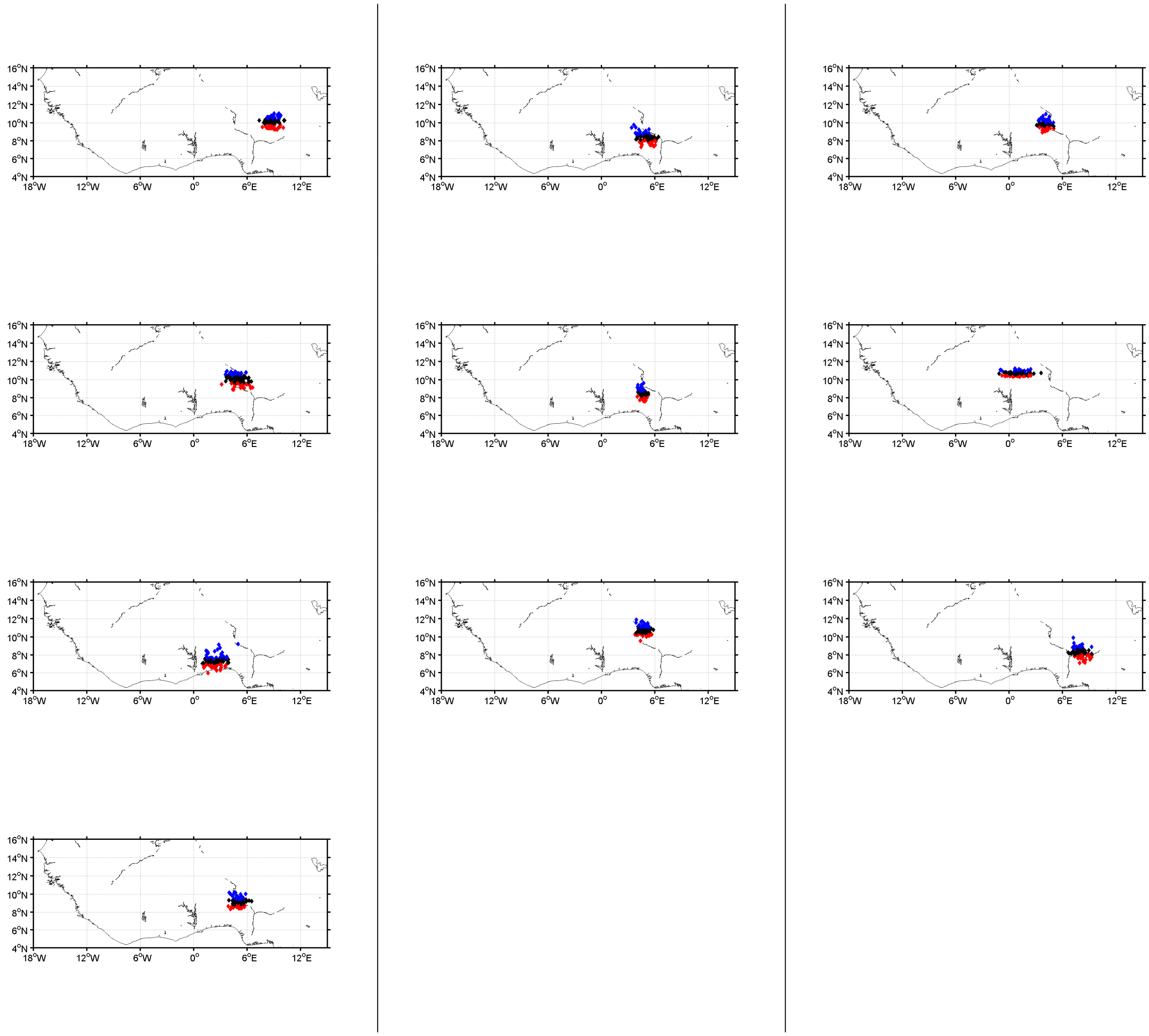

Figure 5.44: Position of WACZ as determined by W_λ and W_ϕ. Each winter mean position is plotted. The quarter of years that are furthest north are blue diamonds, the quarter of years that are furthest south are red diamonds and the interquartile range are black diamonds. COA plotted over the period 2000–2100 for SRESb1. Top row: (a) CCSM, (b) CNRM, (c) GFDL. Second row: (d)GISS, (e)IAP, (f)IPSL Third row: (g) MIROC-mres, (h) MIROC-hires, (i) MPI. Fourth row: (j) MRI.

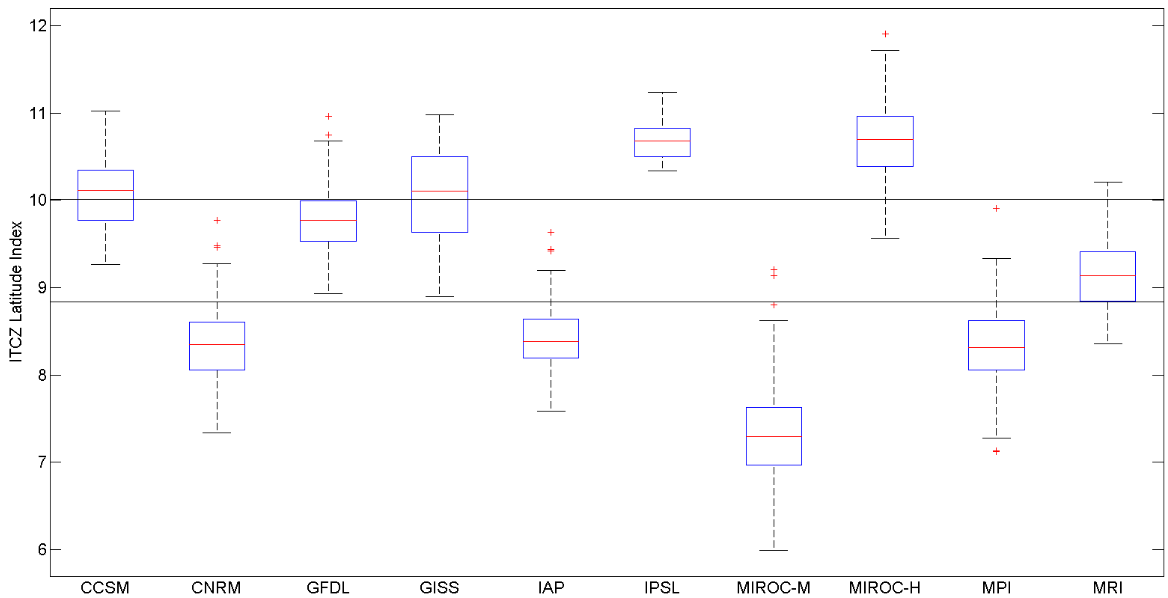

Figure 5.45: Boxplot of winter means of W_ϕ over the period 2000–2100 for SRES-A1b. Red center line represents median, blue lines above and below median represent the 75th and 25th percentiles respectively. Red crosses represents outliers. Black lines extend 1.5 times the interquartile range out from the median.

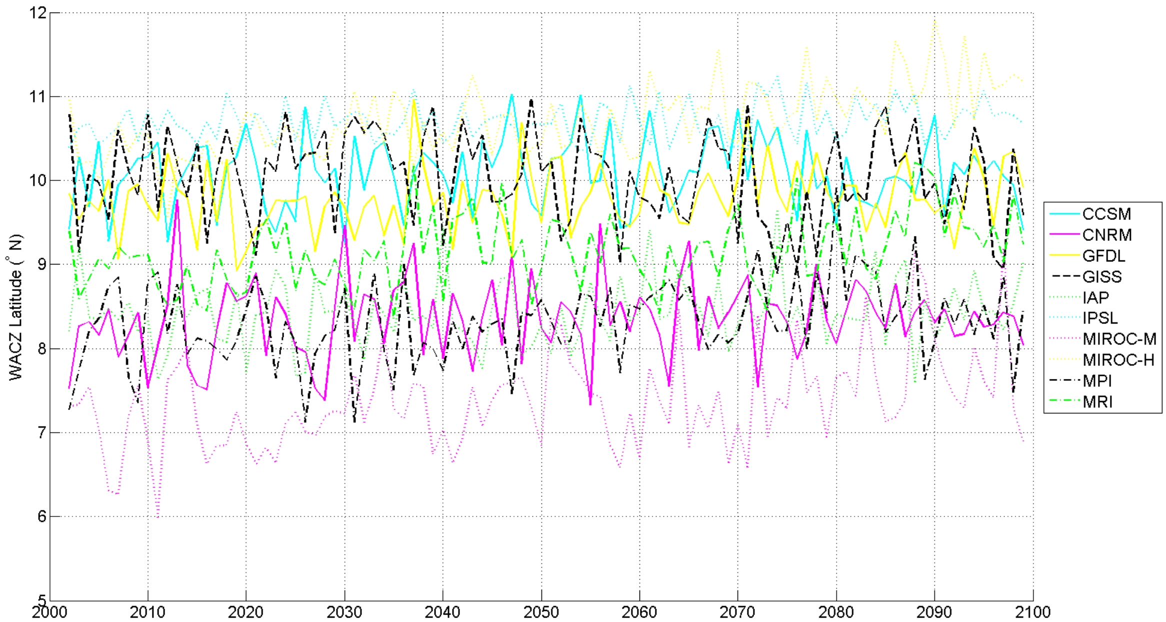

Figure 5.46: Time-series of winter means of W_ϕ over the period 2000–2100 for SRES-A1b.

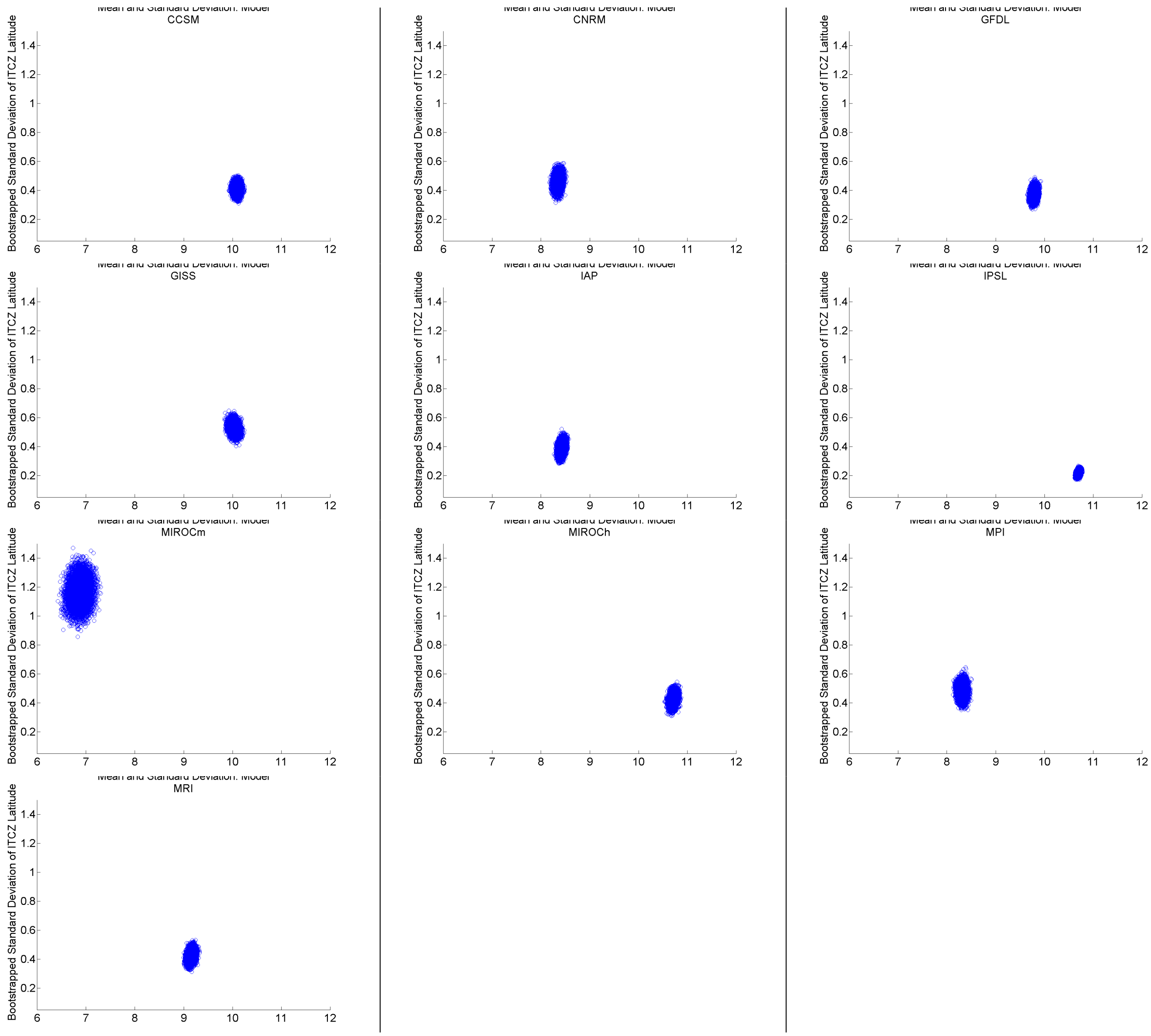

Figure 5.47: Mean (x-axis) and standard deviation (y-axis) of W_λ in 10,000 resamplings via bootstrapping over period 2001–2099 in SRESB1 scenario. Top row: (a) CCSM, (b) CNRM, (c) GFDL. Second row: (d)GISS, (e)IAP, (f)IPSL Third row: (g) MIROC-mres, (h) MIROC-hires, (i) MPI. Fourth row: (j) MRI.

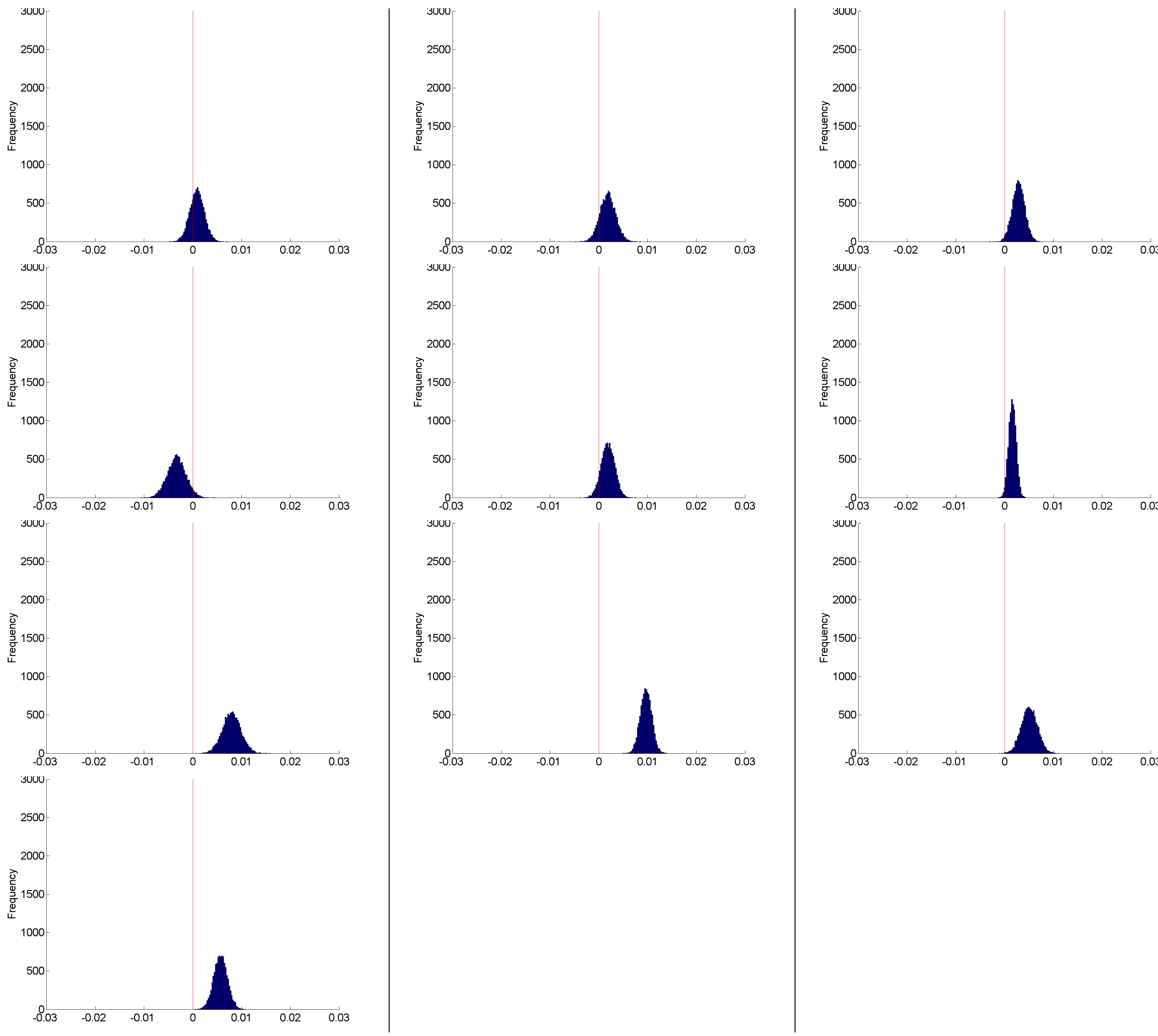

Figure 5.48: Linear trend of W_ϕ in 10,000 resamplings via bootstrapping over period 2001–2099 in SRESB1 scenario in winter (DJFM). Top row: (a) CCSM, (b) CNRM, (c) GFDL. Second row: (d)GISS, (e)IAP, (f)IPSL Third row: (g) MIROC-mres, (h) MIROC-hires, (i) MPI. Fourth row: (j) MRI.

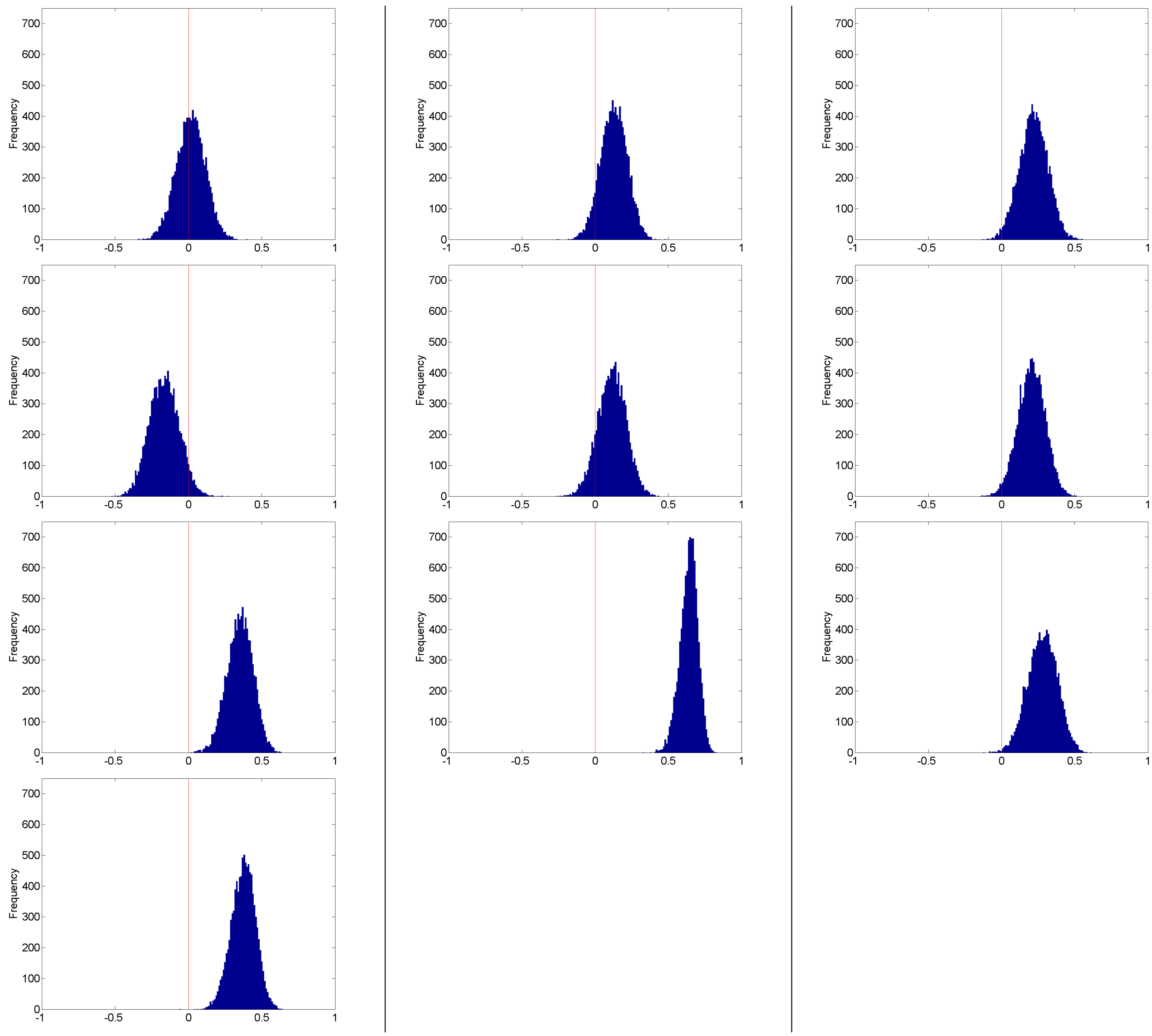

Figure 5.49: Pearson product moment correlation coefficients between W_ϕ and time in 10,000 resamplings via bootstrapping over period 2001–2099 in SRESB1 scenario in winter (DJFM). Top row: (a) CCSM, (b) CNRM, (c) GFDL. Second row: (d)GISS, (e)IAP, (f)IPSL Third row: (g) MIROC-mres, (h) MIROC-hires, (i) MPI. Fourth row: (j) MRI.

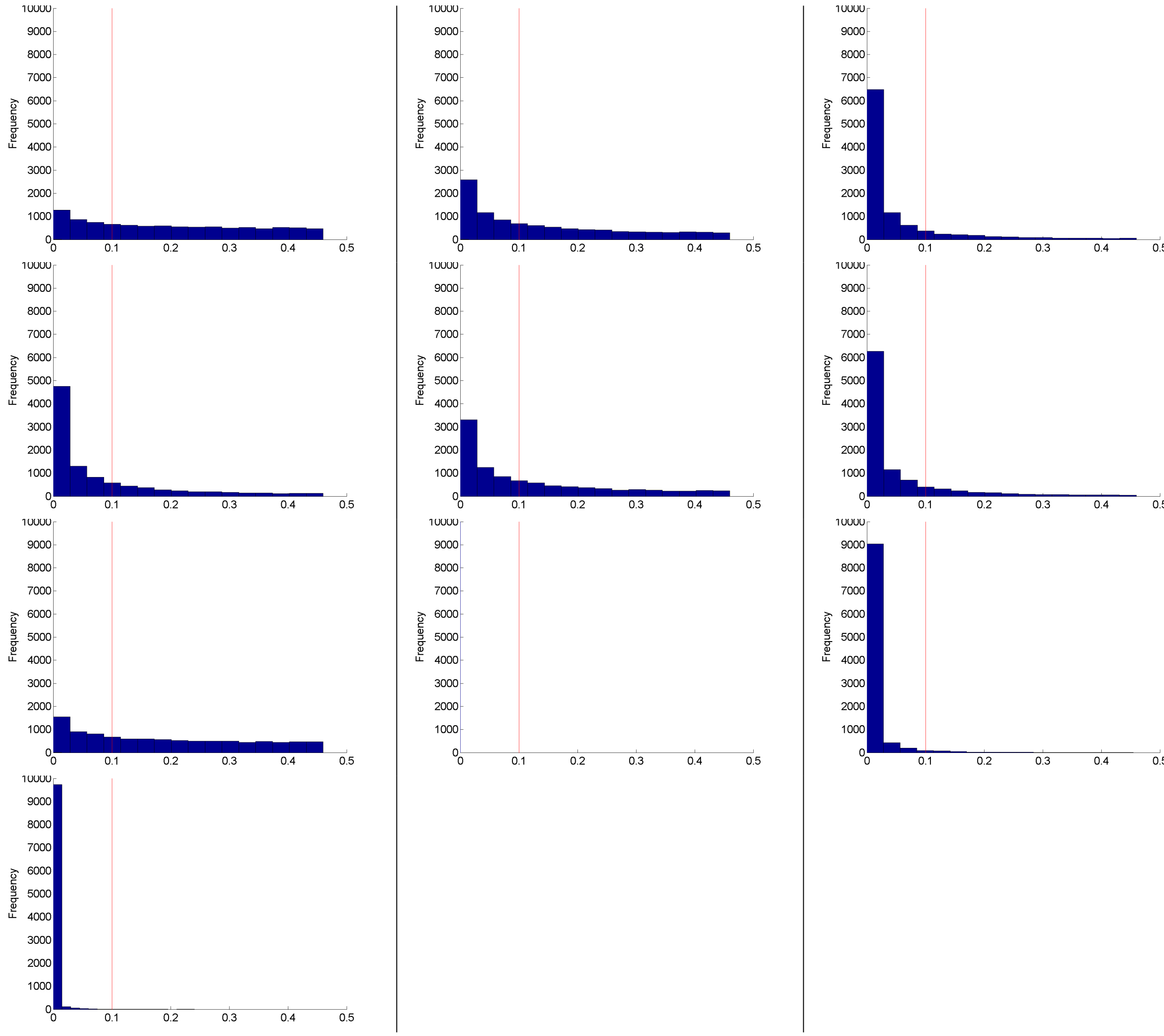

Figure 5.50: Probability to reject the hypothesis that there is a significant linear trend of W_λ in 10,000 resamplings via bootstrapping over period 2001–2099 in SRESB1 scenario in winter (DJFM). Top row: (a) CCSM, (b) CNRM, (c) GFDL. Second row: (d)GISS, (e)IAP, (f)IPSL Third row: (g) MIROC-mres, (h) MIROC-hires, (i) MPI. Fourth row: (j) MRI.

Table 5.1: Summary of key information on CMIP GCMs used, including acronyms, resolution, start and end times for SRES-A1b and SRES-B1 scenarios, and number of complete years simulated. Additional information on models available in prior chapter. UKMO model only available for SRES-A1b.

Model Acronym	Resolution	Start	End	Total Years
CCSM	1.40625°× 1.40625°	Jan 2000	Dec 2099	100
CNRM	2.8125°× 2.8125°	Jan 2000	Dec 2099	100
GFDL	2°× 2.5°	Jan 2001	Dec 2100	100
GISS	4°× 5°	Jan 2000	Dec 2099	100
IAP	3°× 2.8125°	Jan 2000	Dec 2099	100
IPSL	2.5°× 3.75°	Jan 2000	Dec 2100	101
MIROC (mres)	2.8125°× 2.8125°	Jan 2001	Dec 2100	100
MIROC (hires)	1.125°× 1.125°	Jan 2001	Dec 2100	100
MPI	1.875°× 1.875°	Jan 2001	Dec 2100	100
MRI	2.8125°× 2.8125°	Jan 2001	Dec 2100	100
UKMO	1.25°× 1.875°	Jan 2000	Nov 2099	99

Table 5.2: Overview of socioeconomic conditions contributing to SRES emission scenarios used. Adapted after *Solomon et al.* [2007].

	Scenario A1B	Scenario B1
Population growth	low	low
GDP growth	very high	high
Energy use	very high	low
Land- use changes	low	high
Resource availability	medium	low
Pace and direction of technological change favoring	rapid balanced	medium efficiency and dematerialization

Table 5.3: Overview of W_ϕ for annual means in SRESA1 over period 2001–2099.

Model	Median	IQR	Skewness	AMIP Median	SRESA1 - AMIP
CCSM	12.88	4.71	0.12	14.05	-1.17
CNRM	12.39	6.56	-0.20	12.07	0.32
GFDL	12.99	4.48	-0.14	14.48	-1.48
GISS	13.19	4.28	-0.45	15.15	-1.96
IAP	13.36	7.61	-0.04	14.82	-1.45
IPSL	13.10	4.78	0.14	13.20	-0.10
MIROCm	11.91	6.36	-0.44	12.63	-0.72
MIROCh	13.74	3.65	-0.41	14.24	-0.50
MPI	12.73	5.52	-0.21	12.70	0.03
MRI	12.36	5.13	-0.13	11.86	0.50
UKMO	11.86	3.29	-0.42	12.60	-0.74
remean	13.03	5.22	-0.25	13.40	-0.36
remedian	13.02	5.01	-0.27	13.36	-0.33

Table 5.4: Summary of statistics associated with the bootstrap analysis of linear trend of annual means for SRESA1 over the period 2001 to 2099. $\text{Trend}_{0.5}$ is the median of the linear trend ($^\circ\text{yr}^{-1}$). $r_{\min}$ and $r_{\min}$ are the 95 % confidence interval of the correlation between W_ϕ. $r_{0.5}$ is the median correlation coeffient. $p_{0.5}$ is the median probability to reject the hypothesis that a trend exists using a t-test.

	$\text{Trend}_{0.5}$	$r_{\min}$	$r_{\max}$	$r_{0.5}$	$p_{0.5}$
CCSM	5.57×10^{-3}	0.28	0.58	0.44	5.88×10^{-7}
CNRM	4.21×10^{-3}	0.25	0.58	0.43	4.37×10^{-6}
GFDL	7.92×10^{-3}	0.46	0.72	0.60	8.60×10^{-15}
GISS	-3.53×10^{-3}	-0.44	-0.08	-0.26	2.89×10^{-3}
IAP	7.57×10^{-3}	0.56	0.77	0.67	2.67×10^{-20}
IPSL	3.93×10^{-3}	0.39	0.68	0.56	1.49×10^{-10}
MIROCm	7.80×10^{-3}	0.58	0.77	0.68	3.28×10^{-19}
MIROCh	7.19×10^{-3}	0.75	0.88	0.82	8.16×10^{-46}
MPI	6.22×10^{-3}	0.47	0.72	0.61	1.60×10^{-14}
MRI	4.52×10^{-3}	0.29	0.62	0.47	2.30×10^{-8}
UKMO	4.29×10^{-3}	0.43	0.69	0.57	1.59×10^{-13}
remean	4.64×10^{-3}	0.82	0.92	0.87	4.97×10^{-63}
remedian	5.17×10^{-3}	0.69	0.85	0.78	7.84×10^{-33}

Table 5.5: Overview of W_ϕ for summer means in SRESA1 over period 2001–2099.

Model	Median	IQR	Skewness	AMIP Median	SRESA1 - AMIP
CCSM	15.84	0.88	0.08	17.07	-1.22
CNRM	15.25	0.61	-0.27	17.79	-2.53
GFDL	14.94	0.83	-0.25	17.80	-2.85
GISS	14.67	1.00	0.14	18.49	-3.81
IAP	17.71	0.63	-0.48	19.32	-1.61
IPSL	16.25	0.43	0.15	16.74	-0.48
MIROCm	14.36	0.67	0.03	15.05	-0.68
MIROCh	15.42	0.44	-0.39	16.61	-1.18
MPI	14.82	0.57	-0.01	17.09	-2.26
MRI	15.36	0.47	-0.14	15.46	-0.09
UKMO	13.17	0.53	0.46	15.04	-1.86
remean	15.29	0.29	-0.20	16.90	-1.60
remedian	15.24	0.31	-0.36	16.9	-1.65

Table 5.6: Summary of statistics associated with the bootstrap analysis of linear trend of summer means in SRESA1 over the period 2001 to 2099. $\mathrm{Trend}_{0.5}$ is the median of the linear trend ($^\circ\mathrm{yr}^{-1}$). $r_{\min}$ and $r_{\min}$ are the 95 % confidence interval of the correlation between W_ϕ. $\mathrm{r}_{0.5}$ is the median correlation coeffient. $p_{0.5}$ is the median probability to reject the hypothesis that a trend exists using a t-test.

	$\mathrm{Trend}_{0.5}$	$r_{\min}$	$r_{\max}$	$r_{0.5}$	$p_{0.5}$
CCSM	3.57×10^{-3}	-0.03	0.35	0.17	4.41×10^{-2}
CNRM	5.88×10^{-3}	0.20	0.54	0.38	4.96×10^{-5}
GFDL	7.83×10^{-3}	0.20	0.54	0.38	2.14×10^{-5}
GISS	-2.99×10^{-3}	-0.31	0.09	-0.12	8.89×10^{-2}
IAP	9.27×10^{-3}	0.36	0.65	0.52	9.25×10^{-11}
IPSL	3.57×10^{-3}	0.18	0.53	0.37	4.67×10^{-5}
MIROCm	1.11×10^{-2}	0.62	0.80	0.72	1.81×10^{-22}
MIROCh	4.83×10^{-3}	0.28	0.59	0.45	2.97×10^{-7}
MPI	8.01×10^{-3}	0.42	0.67	0.60	7.98×10^{-10}
MRI	2.71×10^{-3}	0.56	0.41	0.24	2.11×10^{-2}
UKMO	6.42×10^{-3}	0.36	0.63	0.51	6.72×10^{-9}
remean	5.49×10^{-3}	0.71	0.86	0.79	3.45×10^{-35}
remedian	5.88×10^{-3}	0.56	0.78	0.68	1.51×10^{-19}

Table 5.7: Overview of W_ϕ for winter means in SRESA1 over period 2001–2099.

Model	Median	IQR	Skewness	AMIP Median	SRESA1 - AMIP
CCSM	10.35	0.72	-0.15	10.19	0.15
CNRM	8.42	0.57	-0.19	7.37	1.04
GFDL	9.92	0.52	-0.10	9.72	0.20
GISS	9.63	0.70	0.31	9.79	-0.15
IAP	8.49	0.54	0.08	9.69	-1.19
IPSL	10.79	0.30	-0.07	8.83	1.95
MIROCm	7.21	0.64	-0.08	7.69	-0.48
MIROCh	10.69	0.56	0.39	10.11	0.57
MPI	8.36	0.57	-0.71	7.43	0.92
MRI	9.20	0.76	0.18	8.70	0.49
UKMO	8.96	0.41	-0.52	9.15	-0.19
remean	9.28	0.29	-0.15	8.99	0.28
remedian	9.28	0.38	0.19	9.14	0.14

Table 5.8: Summary of statistics associated with the bootstrap analysis of linear trend of winter means in SRESA1 over the period 2001 to 2099. $\text{Trend}_{0.5}$ is the median of the linear trend ($^\circ\text{yr}^{-1}$). $r_{\min}$ and $r_{\min}$ are the 95 % confidence interval of the correlation between W_ϕ. $r_{0.5}$ is the median correlation coeffient. $p_{0.5}$ is the median probability to reject the hypothesis that a trend exists using a t-test.

	$\text{Trend}_{0.5}$	$r_{\min}$	$r_{\max}$	$r_{0.5}$	$p_{0.5}$
CCSM	7.10×10^{-3}	0.21	0.57	0.40	1.57×10^{-6}
CNRM	4.43×10^{-3}	0.10	0.44	0.27	9.02×10^{-4}
GFDL	4.67×10^{-3}	0.09	0.46	0.28	2.32×10^{-4}
GISS	-2.42×10^{-3}	-0.29	0.08	-0.11	1.11×10^{-1}
IAP	4.76×10^{-3}	0.14	0.51	0.33	2.51×10^{-4}
IPSL	4.06×10^{-3}	0.29	0.61	0.46	1.18×10^{-8}
MIROCm	5.60×10^{-3}	0.16	0.49	0.33	1.35×10^{-4}
MIROCh	9.67×10^{-3}	0.52	0.75	0.64	2.46×10^{-17}
MPI	5.73×10^{-3}	0.15	0.51	0.34	1.10×10^{-4}
MRI	7.97×10^{-3}	0.24	0.57	0.42	2.45×10^{-7}
UKMO	4.22×10^{-3}	0.12	0.48	0.31	1.19×10^{-4}
remean	4.90×10^{-3}	0.46	0.77	0.68	3.55×10^{-20}
remedian	5.48×10^{-3}	0.45	0.71	0.59	3.71×10^{-14}

Table 5.9: Overview of W_ϕ for annual means in SRESB1 over period 2001–2099.

Model	Median	IQR	Skewness	AMIP Median	SRESB1 - AMIP
CCSM	12.98	5.01	0.05	14.05	-1.06
CNRM	12.44	6.56	-0.21	12.07	0.37
GFDL	12.91	4.56	-0.14	14.48	-1.57
GISS	14.32	5.11	-0.46	15.15	-0.83
IAP	13.19	7.67	-0.03	14.82	-1.63
IPSL	13.12	4.54	0.12	13.20	-0.08
MIROCm	11.80	5.93	-0.51	12.63	-0.83
MIROCh	13.74	3.65	-0.41	14.24	-0.50
MPI	12.61	5.29	-0.25	12.70	-0.08
MRI	12.33	5.27	-0.12	11.86	0.47
remean	13.11	5.42	-0.23	13.51	-0.39
remedian	13.06	5.22	-0.25	13.53	-0.47

Table 5.10: Summary of statistics associated with the bootstrap analysis of linear trend of annual means in SRESB1 over the period 2001 to 2099. $\mathrm{Trend}_{0.5}$ is the median of the linear trend ($^\circ\mathrm{yr}^{-1}$). $r_{\min}$ and $r_{\min}$ are the 95 % confidence interval of the correlation between W_ϕ. $\mathrm{r}_{0.5}$ is the median correlation coeffient. $p_{0.5}$ is the median probability to reject the hypothesis that a trend exists using a t-test.

	$\mathrm{Trend}_{0.5}$	$r_{\min}$	$r_{\max}$	$r_{0.5}$	$p_{0.5}$
CCSM	1.76×10^{-3}	-0.06	0.33	0.14	4.57×10^{-2}
CNRM	1.52×10^{-3}	-0.06	0.36	0.16	4.53×10^{-2}
GFDL	2.59×10^{-3}	0.06	0.41	0.24	3.29×10^{-3}
GISS	-1.27×10^{-3}	-0.28	0.07	-0.11	9.26×10^{-2}
IAP	2.92×10^{-3}	0.23	0.56	0.40	1.30×10^{-4}
IPSL	2.04×10^{-3}	0.19	0.52	0.37	1.61×10^{-5}
MIROCm	6.79×10^{-3}	0.37	0.61	0.53	3.01×10^{-10}
MIROCh	7.20×10^{-3}	0.75	0.88	0.82	3.39×10^{-46}
MPI	3.80×10^{-3}	0.25	0.58	0.43	3.56×10^{-7}
MRI	3.51×10^{-3}	0.25	0.57	0.42	3.15×10^{-6}
remean	3.09×10^{-3}	0.68	0.86	0.79	3.97×10^{-35}
remedian	3.36×10^{-3}	0.55	0.78	0.67	1.06×10^{-19}

Table 5.11: Overview of W_ϕ for summer means in SRESB1 over period 2001–2099.

Model	Median	IQR	Skewness	AMIP Median	SRESB1 - AMIP
CCSM	15.86	0.80	-0.04	17.07	-1.20
CNRM	15.17	0.51	-0.15	17.79	-2.61
GFDL	15.01	0.80	-0.26	17.80	-2.79
GISS	16.28	0.75	0.14	18.49	-2.20
IAP	17.50	0.53	0.02	19.32	-1.81
IPSL	16.15	0.34	0.10	16.74	-0.58
MIROCm	14.22	0.60	-0.38	15.05	-0.82
MIROCh	15.42	0.44	-0.39	16.61	-1.18
MPI	14.66	0.62	-0.08	17.09	-2.43
MRI	15.25	0.52	0.30	15.46	-0.20
remean	15.54	0.19	0.02	17.07	-1.52
remedian	15.47	0.30	0.38	17.13	-1.66

Table 5.12: Summary of statistics associated with the bootstrap analysis of linear trend of summer means in SRESB1 over the period 2001 to 2099. $\text{Trend}_{0.5}$ is the median of the linear trend ($^\circ\text{yr}^{-1}$). $r_{\min}$ and $r_{\min}$ are the 95 % confidence interval of the correlation between W_ϕ. $\text{r}_{0.5}$ is the median correlation coeffient. $p_{0.5}$ is the median probability to reject the hypothesis that a trend exists using a t-test.

	$\text{Trend}_{0.5}$	$r_{\min}$	$r_{\max}$	$r_{0.5}$	$p_{0.5}$
CCSM	-7.10×10^{-5}	-0.21	0.17	-0.02	2.12×10^{-1}
CNRM	1.96×10^{-3}	-0.01	0.39	0.20	8.86×10^{-2}
GFDL	2.56×10^{-3}	-0.07	0.30	0.12	7.99×10^{-2}
GISS	2.61×10^{-3}	-0.06	0.32	0.13	8.47×10^{-2}
IAP	3.97×10^{-4}	-0.17	0.23	0.03	2.10×10^{-1}
IPSL	2.56×10^{-3}	0.09	0.46	0.28	1.51×10^{-3}
MIROCm	5.43×10^{-3}	0.19	0.53	0.37	1.60×10^{-5}
MIROCh	4.84×10^{-3}	0.27	0.59	0.44	2.89×10^{-7}
MPI	1.78×10^{-3}	-0.11	0.29	0.10	7.89×10^{-2}
MRI	3.43×10^{-3}	0.09	0.46	0.28	1.05×10^{-3}
remean	2.55×10^{-3}	0.34	0.64	0.50	9.42×10^{-9}
remedian	2.92×10^{-3}	0.26	0.57	0.43	1.17×10^{-6}

Table 5.13: Overview of W_ϕ for winter means in SRESB1 over period 2001–2099.

Model	Median	IQR	Skewness	AMIP Median	SRESB1 - AMIP
CCSM	10.11	0.56	-0.01	10.19	-0.08
CNRM	8.34	0.54	0.25	7.37	0.97
GFDL	9.77	0.46	0.35	9.72	0.04
GISS	10.10	0.87	-0.25	9.79	0.31
IAP	8.38	0.44	0.45	9.69	-1.31
IPSL	10.67	0.33	0.40	8.83	1.84
MIROCm	7.29	0.66	0.77	7.69	-0.40
MIROCh	10.69	0.56	0.39	10.11	0.57
MPI	8.31	0.56	0.01	7.43	0.87
MRI	9.13	0.57	0.39	8.70	0.42
remean	9.29	0.24	0.06	8.95	0.33
remedian	9.30	0.30	0.36	9.12	0.18

Table 5.14: Summary of statistics associated with the bootstrap analysis of linear trend of winter means in SRESB1 over the period 2001 to 2099. $\text{Trend}_{0.5}$ is the median of the linear trend ($^\circ\text{yr}^{-1}$). $r_{\min}$ and $r_{\min}$ are the 95 % confidence interval of the correlation between W_ϕ. $\text{r}_{0.5}$ is the median correlation coeffient. $p_{0.5}$ is the median probability to reject the hypothesis that a trend exists using a t-test.

	$\text{Trend}_{0.5}$	$r_{\min}$	$r_{\max}$	$r_{0.5}$	$p_{0.5}$
CCSM	8.87×10^{-4}	-0.18	0.21	0.02	1.85×10^{-1}
CNRM	1.86×10^{-3}	-0.06	0.30	0.13	1.02×10^{-1}
GFDL	2.88×10^{-3}	0.02	0.40	0.22	1.12×10^{-2}
GISS	-3.30×10^{-3}	-0.36	0.03	-0.17	3.16×10^{-2}
IAP	1.88×10^{-3}	-0.08	0.30	0.12	6.86×10^{-2}
IPSL	1.62×10^{-3}	0.02	0.38	0.20	1.33×10^{-2}
MIROCm	7.93×10^{-3}	0.17	0.52	0.36	6.34×10^{-6}
MIROCh	9.69×10^{-3}	0.51	0.75	0.65	1.28×10^{-17}
MPI	5.10×10^{-3}	0.08	0.48	0.28	6.16×10^{-4}
MRI	5.71×10^{-3}	0.20	0.52	0.38	1.68×10^{-5}
remean	3.44×10^{-3}	0.49	0.74	0.63	3.48×10^{-16}
remedian	3.98×10^{-3}	0.33	0.62	0.48	1.54×10^{-9}

Table 5.15: Side-by-side summary of median W_ϕ in AMIP or 20th Century, SRES-A1B and SRES-B1 scenarios for various reanalysis and CMIP GCMs. Median W_ϕ shown for summer mean (JJAS) and winter mean (DJFM).

	JJAS			DJFM		
Model	AMIP or 20th	SRES-A1B	SRES-B1	AMIP or 20th	SRES-A1B	SRES-B1
NCEP	15.03	-	-	9.26	-	-
ERA-40	14.66	-	-	8.46	-	-
ERA-Interim	16.35	-	-	8.88	-	-
CCSM	14.96	15.84	15.86	9.74	10.35	10.11
CNRM	16.09	15.25	15.17	7.73	8.42	8.34
GFDL	14.87	14.94	15.01	10.37	9.92	9.77
GISS	17.35	14.67	16.28	9.56	9.63	10.10
IAP	16.24	17.71	17.50	10.17	8.49	8.38
IPSL	14.87	16.25	16.15	9.13	10.79	10.67
MIROC-mres	14.13	14.36	14.22	7.69	7.21	7.29
MIROC-hres	15.71	15.42	15.42	9.96	10.69	10.69
MPI-ECHAM	16.23	14.82	14.66	8.24	8.36	8.31
MRI	14.97	15.36	15.25	9.23	9.20	9.13
UKMO-HADGEM	14.47	13.17	-	9.39	8.96	-

Table 5.16: Side-by-side summary of iqr W_ϕ in AMIP or 20th Century, SRES-A1B and SRES-B1 scenarios for various reanalysis and CMIP GCMs. IQR of W_ϕ shown for summer mean (JJAS) and winter mean (DJFM).

	JJAS			DJFM		
Model	AMIP or 20th	SRES-A1B	SRES-B1	AMIP or 20th	SRES-A1B	SRES-B1
NCEP	0.45	-	-	0.37	-	-
ERA-40	0.52	-	-	0.30	-	-
ERA-Interim	0.54	-	-	0.48	-	-
CCSM	0.41	0.88	0.80	0.24	0.72	0.56
CNRM	0.74	0.61	0.51	0.57	0.57	0.54
GFDL	0.47	0.83	0.80	0.44	0.52	0.46
GISS	0.55	1.00	0.75	0.61	0.70	0.87
IAP	0.29	0.63	0.53	0.68	0.54	0.44
IPSL	0.36	0.43	0.34	0.34	0.30	0.33
MIROC-mres	0.21	0.67	0.60	0.34	0.64	0.66
MIROC-hres	0.34	0.44	0.44	0.37	0.56	0.56
MPI-ECHAM	0.37	0.57	0.62	0.71	0.57	0.56
MRI	0.46	0.47	0.52	0.72	0.76	0.57
UKMO-HADGEM	0.39	0.53	-	0.40	0.41	-

Table 5.17: Side-by-side summary of the linear trend ($^{\circ}yr^{-1}$) in W_{ϕ} in AMIP or 20th Century, SRES-A1B and SRES-B1 scenarios for various reanalysis and CMIP GCMs. Linear trend of W_{ϕ} shown for summer mean (JJAS) and winter mean (DJFM).

	JJAS			DJFM		
Model	AMIP or 20th	SRES-A1B	SRES-B1	AMIP or 20th	SRES-A1B	SRES-B1
NCEP	0.013	-	-	-0.029	-	-
ERA-40	0.026	-	-	-0.011	-	-
ERA-Interim	0.042	-	-	-0.007	-	-
CCSM	0.052	0.004	0.000	-0.019	0.007	0.001
CNRM	0.014	0.006	0.002	0.007	0.004	0.002
GFDL	0.023	0.008	0.003	0.048	0.005	0.003
GISS	-0.004	-0.003	0.003	0.011	-0.002	-0.003
IAP	-0.023	0.009	0.000	-0.012	0.005	0.002
IPSL	0.002	0.004	0.003	-0.014	0.004	0.002
MIROC-mres	-0.003	0.011	0.005	0.018	0.006	0.008
MIROC-hres	0.001	0.005	0.005	-0.014	0.010	0.010
MPI-ECHAM	0.006	0.008	0.002	-0.022	0.006	0.005
MRI	0.024	0.003	0.003	-0.033	0.008	0.006
UKMO-HADGEM	-0.015	0.006	-	-0.010	0.004	-

Table 5.18: Projection of expected change in mean seasonal mineral dust ($\mu g\, m^{-3}$) in Barbados from 2000 to 2099 based on median of all model runs for SRES-A1B and SRES-B1 scenarios via linear regression. Expected change calculated from the product of linear regression of 20th century between observed mineral dust at Barbados and WACZ Latitude index and the expected change in position of the WACZ from the year 2000 to the year 2099. Expected change shown for 2.5th and 97.5th percentiles to represent at 5% confidence interval about the median (50th percentile) of linear trend of median bootstrapped seasonal value of all model runs.

	SRES-A1B		SRES-B1	
	JJAS	DJFM	JJAS	DJFM
2.5^{th} Percentile	-3.0	-1.3	-1.1	-1.0
50^{th} Percentile	-3.8	-2.2	-1.9	-1.5
97.5^{th} Percentile	-4.7	-2.4	-2.7	-2.0

Chapter 6

Source Apportionment of Collected Mineral Dust in the Southeastern United States and Verification With Atmospheric Data

[1]

6.1 Introduction

That the composition of mineral dust could inform as to the origins of the dust is a long established principle, dating back to *Darwin* [1846] who noted the presence of fossils from aquatic micro-organisms as evidence for the origins of the dust likely being lake bed sediment. Despite growing attention to mineral dust over the Tropical North Atlantic in the late 1960's [*Prospero et al.*, 1970; *Carlson and Prospero*, 1972] Darwin's simple hypothesis on the sources of mineral dust in North Africa was not much improved upon until higher resolution satellite

[1]This work is presented as a dissertation chapter but is expected to be published with co-authors A. Beck, J.K. Cochran and E.T. Rasbury.

imagery began to become available and key source regions from mineral dust in North Africa clearly identified.

While mineral dust is often treated as a homogeneous, spherical object with a simple size distribution in global climate and theoretical models, in reality the composition, shape and size vary greatly from source region to source region and on occasion within source regions. Furthermore such compositions, shapes and sizes can change rapidly in the atmosphere as the airmass ages, with heavier mineral dust particles settling near to the source and lighter mineral dust particles persisting in the atmosphere for long periods of time. Changes in composition of mineral dust have been shown to be of great importance for both atmospheric and marine chemistry processes, in particular the solubility of iron has been shown to both vary greatly in time and location and be of critical importance to biogeochemical processes in the surface ocean. Much attention has been paid to the solubility of iron accounting to its critical importance as a trace nutrient necessary for primary productivity, however other metals may undergo similar chemical changes in the atmosphere (e.g. titanium) highlighting the complexity of the composition of mineral dust in the atmosphere. Similar to composition, the size and shape of mineral dust can be an important control on both atmospheric and oceanographic chemical processes.

While the complexity of mineral dust as a function of its source creates challenges for environmental chemists, the complexity represents an opportunity to apportion source of mineral dust observed long distances from its source; mineralogical, elemental and isotopic composition of mineral dust can all be used as tracers for mineral dust aerosols source. For example, as elemental analysis was being developed it was nearly immediately applied to determine the composition of dusts. Baron Nordenskjold in 1869 [*Hartley and Ramage*, 1901] used the elemental composition of dust in snowpack in Upsala, Sweden to determine if dust deposited in snowpack may have originated from a meteorite shower that occurred concurrently with its detection. More recently *Perry et al.* [1997] have shown the utility of using elemental ratios to identify the source of mineral dust. In intervening years analyses have been performed on surface soils and sands, ocean and ice core sediments and mineral dust collected in the atmosphere; including major international aerosol sampling projects (e.g ACE-Asia and SHADE). Much of this work has been summarized in two review papers by *Formenti et al.* [2011] and *Grousset and Biscaye* [2005].

Previous work has assessed the mineral composition of mineral dust near to sources in Africa [*Glaccum and Prospero*, 1980; *Paquet et al.*, 1984; *Avila et al.*, 1997; *Caquineau et al.*, 1998; *Falkovich et al.*, 2001; *Caquineau et al.*, 2002; *Khiri*, 2004; *Alastuey et al.*, 2005; *OHara et al.*, 2006; *Kandler et al.*, 2009] and Asia [*Biscaye et al.*, 1997; *Svensson et al.*, 2000; *Shen et al.*, 2005; *Wang et al.*, 2005; *Shen et al.*, 2006; *Li et al.*, 2007; *Jeong*, 2008; *Wang et al.*, 2008]. Samples in these analyses vary in collection methods from mechanically operated surface impactors, passive collection on surfaces and collection from near-surface, tower-based and aircraft retrievals. Furthermore methods to determine mineral composition vary widely, from single particle techniques such as x-ray diffraction or microscopy to bulk analytical methods. Additional differences between studies originate from minerals studied and how mineral composition was reported, (e.g. percentage of weight, percentage of volumes or ratios of minerals). In some cases single particle analysis is not quantitative but rather results are reported in a semi-quantitative manner (e.g. counts or relative counts) [*Falkovich et al.*, 2001; *Reid et al.*, 2003; *Zhang et al.*, 2005; *Kandler et al.*, 2007; *Jeong*, 2008; *Matsuki et al.*, 2010]. Differences in sample collection, analysis techniques and what minerals were reported lead to difficulties in direct comparisons to study to study. A summary of mineralogical composition by region from *Formenti et al.* [2011] is given in Table 6.1.

Elemental composition of mineral dust near to sources has also been extensively studied in both Africa [*Chester et al.*, 1984; *Bergametti et al.*, 1989a,b; *Borg and Banner*, 1996; *Chiapello et al.*, 1997; *Guieu et al.*, 2002; *Formenti et al.*, 2003; *Alastuey et al.*, 2005; *Formenti et al.*, 2008] and Asia [*Alfaro and Gomes*, 2001; *Makra et al.*, 2002; *Zhang et al.*, 2003; *Zhang et al.*, 2003; *Xu et al.*, 2004; *Cheng et al.*, 2005; *Sun et al.*, 2005; *Arimoto et al.*, 2006; *Shen et al.*, 2007]. Elemental composition is commonly determined by x-ray fluorescence, or mass spectroscopy. Many spectroscopic analyses, such as the commonly used inductively coupled plasma mass spectrometry (ICP-MS) require chemical digestion of mineral dust via strong acids. Chemical digestion methods vary widely between studies and the choice of chemical digestion methods can impact results. For example hydrofluoric acid (HF) is necessary to completely break down aluminosilicates. However HF in the presence of silicon dioxide (SiO_2) can react to produce silicon tetrafluoride (SiF_4) which is a gas at room temperature and can thus artificially reduce measurements of Si, an element which is an important geochemical marker. Furthermore for analysis involving rare earth elements (REE) fluorine ions are known to attach to and remove REE from solution. Thus choice of digestion methods can affect elemental ratios, making comparisons between studies challenging. Despite aforementioned challenges *Formenti et al.* [2011] summarized a wide array of elemental analysis of mineral dust from North Africa and Asia and these are summarized in Tables 6.2.

Isotopic analysis of Nd and Sr (e.g. *Borg and Banner* [1996]; *Grousset and Biscaye* [2005]; *Cole et al.* [2009]) has been used to identify mineral dust source regions in marine sediments, ice cores, soils, and in transported aerosols. Earth-derived particles found in the atmosphere as mineral dust originate from soils and rocks generally of crustal origin. The isotopes ^{87}Sr and ^{143}Nd are radiogenic and are produced continuously from their naturally occurring parents, ^{87}Rb and ^{147}Sm, respectively. The proportion at which these two isotopes are found is a function of age of a rock, and the initial $\frac{\mathrm{Rb}}{\mathrm{Sr}}$ and $\frac{\mathrm{Sm}}{\mathrm{Nd}}$ ratios imprinted by chemical processes affected by temperature and pressure at the time of rock formation. The isotopic composition of Sr and Nd varies from the mantle-derived material to the crustal material. Thus $\frac{^{87}Sr}{^{86}Sr}$ and $\frac{^{143}Nd}{^{144}Nd}$ ratios vary from place to place on Earth's surface as a consequence of the unique ages and composition of local rocks. While isotopic ratios are strong indicators of provenance there are challenges with such an analysis. In general isotopic ratios are more resistant to issues associated with digestion of mineral dust, however isotopic ratios are often paired with elemental concentrations so digestion techniques can be important. Furthermore the isotopic ratio has been shown to change with the size of mineral dust [*Grousset and*

Biscaye, 2005], in turn the size of mineral dust has been shown to change with distance from source [*Pye and Tsoar*, 1987].

Having outlined challenges associated with using geochemical from previous studies next we examine if it is possible to use simple mineralogical and elemental ratios to apportion sources. [*Formenti et al.*, 2011] in a review paper present a useful regional framework and overview of mineralogy literature for much of the previous work done to apportion source. North Africa is subdivided into regional basins that are identified as key sources of mineral dust, such as the aforementioned Bodele Depression shown as NAF-5 in Figure 6.1a. Asia is similarly treated in Figure 6.1b. Next we present a brief overview of mineralogy, elemental and trace metal composition and isotopic ratios observed in the literature that can be utilized to separate source regions analytically; first we look for differences between continents and second we determine if differences in North African sources can be assessed.

Some differences between Asian and African dust are evident in simple mineralogical and elemental ratios. Asian dust sources show higher illite to kaolinite ratios (1.1 to 13.9) than African dust sources (0.2 to 2.0, Table 6.1). Similarly the ratio of chlorite to kaolinite is higher in Asia (1.3 to 3.3) than African dust sources (0.0 to 2.6). In contrast Asian dust (0 to 35%) appears to have lower carbonate content per unit weight than African dust sources (0 to 70%). We note a wide range in carbonate content on sub-continental scales and between studies. The ratio of Ca to Al has been used by *Perry et al.* [1997] and others to assess sources of mineral dust: Asian mineral dust (0.31 to 4.14) is enhanced relative to African sources (0.36 to 0.92) as also shown in Table 6.1. For K to Al, Asian dust (0.20 to 1.00) is also shown to be enhanced relative to African sources (0.11 to 0.3). The ratio of Fe to Al is similar between Asia (0.36 to 3.53) and Africa (0.43 to 1.08).

As the Bodele depression is thought to be the source of nearly one-quarter the total dust emitted from North Africa [*Koren et al.*, 2006] much attention has been paid to the mineralogy of the depression [*Mounkaila*, 2006; *Bristow et al.*, 2010]. Previously Chapters 2 and 3 of this dissertation have highlighted the key role that the Bodele depression plays in responding to changes in the position of the WACZ. The ratios of carbonate and illite to kaolinite have been used to fingerprint sources previously in the Bodele [*Schütz and Sebert*, 1987; *Caquineau et al.*, 2002]. Fe has in general higher values in southern Africa including the Sahel and Bodele than northern locations [*Lázaro et al.*, 2008; *Formenti et al.*, 2008]. While the ratio of Si to Al is in many places not useful in discriminating between sources, the relatively constant high values of Si to Al in the Bodele (near 4) may make it a good tracer of Bodele originated mineral dust relative to other North African sources (near to 2.3) [*Formenti et al.*, 2008]. *Cole et al.* [2009] note that plagorskite is common in sediments originally formed in lakebeds, such as that of the Bodele Depression. Plagorskite is rich in Mg, so elemental ratios in which Mg is enriched could suggest a lakebed source.

While mineralogy and elemental ratios appear to be good indicators of source, it is not clear if samples taken thousands of kilometers from source regions will maintain source region signals. For example *Trapp et al.* [2010] analyzed mineral dust collected in Miami and Barbados and found that although trace metal concentrations varied tightly with the concentration of mineral dust, the ratios between metals did not change greatly with time. It is unclear from this work if this implies a constant source region or if the fine mode of mineral dust that remains as a mineral dust layer ages does not maintain geochemical tracers with time and distance from the source regions.

The above literature review, Tables 6.1 and 6.2 and Figures 6.1a and 6.1b highlight both the challenges associated with assimilating multiple analysis performed with differing sample collection and analytical techniques and the potential utility of such analysis in apportioning sources. Variability between measurements in a region or continent is often of similar magnitude as the variability between regions or continents. In particular we note that previous studies have focused either on a specific region (e.g. Bodele Depression or Gobi Desert) or on an individual continental source, and no studies perform analysis of samples from varying sources. To address the issue associated with sample and analytical technique disparities in previous analyses, we collect samples from four different continents

(North Africa, Europe, Asia and Australia) and present a unified analysis via a qualitative mineralogy and a quantitative elemental composition of the mineral dust samples. As a test of this analysis five samples of mineral dust with unknown origins collected in the Southeastern United States are analyzed and their sources assessed. This study seeks answers to three main questions: (1) Is continental source apportionment possible with trace metal analysis? (2) Is regional source apportionment possible with trace metal analysis? (3) Do North African regional sources change as a function of the position of the WACZ?

The structure of the chapter is as follows. In Section 6.2 we introduce the samples acquired and analyzed in this project. In Section 6.3 the digestion, analysis and statistical techniques used in this project are introduced. In Section 6.4 the results of this project are shown. Sections 6.5 and 6.6 we summarize and discuss our findings in the context of prior results, linking these results to findings in Chapters 2 and 3 of this dissertation in which the role of the WACZ in controlling mineral dust emission and transport was established. In addition we discuss the potential utility of isotopic analysis, how this future work will augment our findings and how this analysis can be used in near-real time to determine the sources of mineral dust to the southeastern United States.

6.2 Materials and Data

Samples of mineral dust were collected from Africa, Europe, Australia, North America and Asia at varying distances from source regions. To characterize mineral dust sources by continent we acquired samples near to major source regions of Asia, Africa and Australia. To test our characterization scheme we include filter samples of mineral dust of unknown origins in the Southeastern United States.

6.2.1 Source Sample Collection

Table 6.3 summarizes the origins of mineral dust samples acquired for this study. All samples were collected at the Earth's surface in the form of deposited mineral dust. In most cases samples were simply swept off a surface (e.g. board on a rooftop for samples collected in Spain or car window in the case of samples collected in Australia) and sent for analysis. All samples captured in Europe are assumed to be of North African origin, as North African dust storms impacting Spain and the coastal Mediterranean have been well established in the literature.

6.2.2 SEARCH Project

Our filters for analysis come from Pensacola, Florida collected as part of the South-Eastern Aerosol Research and Characterization Study experiment (SEARCH project: `http://www.atmospheric-research.com/studies/SEARCH/index.html`.) sponsored by the EPA. Figure 6.2 shows the location of aerosol filter collection stations in the SEARCH project. Atmospheric-Research, a subcontractor with the EPA provided five - 47mm Tefon filters with mineral dust loadings of 25-125 μg of mineral dust. Pensacola, FL receives mineral dust periodically during the spring and summer months. The location of the sample site is shown in Figure 6.2.

6.3 Methods

Here we focus on the two analytical techniques used to determine mineralogy and elemental composition of mineral dust samples. Before being chemically digested, samples were analyzed at the National Synchrotron Light Source (NSLS) at Brookhaven National Lab to determine mineralogy. Samples were then chemically digested in the clean-room of the Isotope Laboratory under the direction of Dr. Troy Rasbury at the Department of Geosciences at Stony Brook University, then analyzed by ICP-MS in the lab of Dr. Aaron Beck at the

Virginia Insitute of Marine Science. Next we detail the analytical methods utilized in each aforementioned step.

6.3.1 μX-ray Diffraction and Fluorescence

A major advantage of μx-ray diffraction (XRD) and μx-ray fluorescence (XRF) performed at the National Synchrotron Light Source (NSLS) Brookhaven National Lab is that the analyses do not require destruction, meaning that the mineral dust samples (in particular on filters) could be later digested and further analyzed. XRD measures x-rays scattering from a sample that has been bombarded with x-rays or gamma rays containing high levels of energy. X-rays of different energy levels are scattered from the individual mineral dust particle and re-emitted from the bombarded sample, then both the rate and shape of scatter are measured. The intensity and pattern of scattered radiation are determined by the crystalline physical structure of atoms, thus individual minerals have unique scattering properties that can aid in identification. XRF requires bombardment with high energy particles, in the process dust molecules are excited and based on elemental composition emit radiation at discrete wavelengths and intensities which can be used to identify composition of the dust. While both processes require high energy radiation and then measure reflectance/scatter (XRD) or emission (XRF), the analytical techniques for the two are different. XRF analysis of a sample produces a two dimensional map of the sample, showing changes in elemental concentrations. In contrast XRD is a single particle analysis, requiring that each individual mineral dust grain be analyzed individually.

Samples were handled as follows. Pure dust samples were mounted in a thin layer onto kaptron adhesive tape, chosen for its lack of diffraction. In an attempt to produce a layer of one particle thick samples were mounted from vials onto the tape, then tapped repeatedly to dislodge excess dust. XRF mapping was performed on the samples, along with XRD on individual grains. As mineral dust was spread evenly across the tape XRD was performed randomly on discrete spots along the kaptron tape. Because the beam of radiation was on the order of 15 μm in width it was impossible to always identify and analyze individual grains, often multiple mineral dust particles were captured in one image. In contrast to mineral dust mounted on kaptron tape, mineral dust on collected filters was not evenly distributed but rather preferentially settled into depressions on filter surface (see Figure 6.4). In this case XRD could not be performed randomly, but rather in a semi-random location. XRF was used to identify locations in which metals associated with mineral dust were present and XRD was performed at this location.

Once a location was selected for XRD, the standard method for collection an analysis of XRD patters for NSLS-BNL beamline x26 was followed. Here briefly we highlight the approach. The standard software, Fit-2D was used for diffraction imaging. Two standards were first analyzed to calibrate the software alumina (Al_2O_3, NIST X-Ray Powder Diffraction Intensity Set SRM 674a) and silver behenate ($AgC_{22}H_{43}O_2$). Using Fit-2d, power diffration patterns were calculated for each sample. A kaptron blank was taken and subtracted from observed intensities for pure dust samples. For filters a Teflon filter blank was taken and subtracted, however the blank signal was large and often overwhelmed the signal of the mineral itself. Calibrated, blank-corrected outputs were imported into Match! software for comparison to a mineralogical database; samples that did not have a clear match were discounted. We consider the results from this analysis to be semi-quantitative at best, and are probably best characterized as qualitative. Filter concentrations of mineral dust were low and diffraction signals were weak while the diffraction patterns from the Teflon filter were often quite strong. *Formenti et al.* [2011] note challenges in limited diffraction databases for mineral dust particles as observed in previous studies [*Moore et al.*, 1989; *Caquineau et al.*, 2002]. That the results of this analysis are qualitative rather than quantitative is not rare for diffraction studies [*Falkovich et al.*, 2001; *Reid et al.*, 2003; *Zhang et al.*, 2006; *Kandler et al.*, 2007; *Jeong*, 2008; *Matsuki et al.*, 2010] because of low abundance of atmospheric aerosols and limited diffraction database resources. In this study, the mineralogy serves as useful supplemental information to the metal analysis.

6.3.2 Elemental Analysis via ICP-MS

Analysis of elemental composition is performed via ICP-MS, which requires complete chemical digestion of samples so that metals are dissolved into an acid solution which can be injected for analysis. Si is thought to be a key element for identifying mineral dust originating in the Bodele depression and in digestions utilizing HF Si can be lost via evaporation of SiF_4 in a gaseous compound. We performed digestions without HF in order to preserve Si. However without HF we cannot be assured of complete digestion of aluminosilicate clays, potentially reducing yields of elements commonly contained in these materials (such as: Al, Si, REE) and making comparison of our results to other analyses difficult. We used two digestion methods, one to digest pure dust samples and the other to digest filters that contain mineral dust. Both digestions were performed in the clean lab of the Isotope Laboratory in the Geosciences Department of Stony Brook University. Unless otherwise noted all materials used were acid washed and subjected to sequential HCl, HNO_3 and DI water baths for over a month before utilization. All solvents used in this analysis were trace metal grade, low blank, SEASTAR™ rated acids.

Pure mineral dust samples were weighed on a Mettler micro-balance (Table 6.3). Sample masses were chosen to be of the order of mineral dust expected to be on the filters (25 to 100 μg). Dust was placed in Teflon vials for digestion (see Figure 6.3a). Initially 3mL aqua regia was applied to the sample for two days, then the sample was brought to dryness on a hotplate. After cooling, 2mL of HNO_3 (16 N) were added to the samples, after two days the samples were again brought to dryness on a hotplate. Lastly 1.6 mL of HNO_3 (1 N) was used to pick up dissolved metals and centrifuged to remove non-dissolved refractory material (not quantified).

Filter samples were treated as similarly as possible to the pure mineral dust samples. However in contrast to the pure dust samples, the mass of mineral dust on the filters is unknown, so it is impossible to calculate elemental concentration in parts per million or similar notation. Filters were placed in Teflon vials for digestion and 6mL aqua regia was applied to the samples for two days, then the sample was brought to dryness on a hotplate. After cooling the filters were flipped with acid washed tongs (see Figure 6.3c) and 3mL of HNO_3 (16 N) were added to the samples, then after two days the samples were again brought to dryness on a hotplate. To allay concerns of metal ions attaching to the non-Teflron edges of of filters, they were rinsed with 2 to 3 mL of HNO_3 (1 N) then dried to completeness before being treated as pure-dust samples for the remaining steps, including pick-up in 1.6 mL followed by centrifuging.

While samples were treated to reduce trace metal contamination, some contamination is unavoidable. For example we expect contamination would be possible during collection and μx-ray analysis at BNL. All other digestion and analysis steps were performed in clean-lab environments, however despite this precaution blanks can be encountered in non-properly cleaned vessels and in the acids used in digestion. To account for blank or contamination during digestion, three blanks were run for both the pure dust and filter examples, and treated exactly as described above for actual samples.

Fully digested, centrifuged samples were then taken to the Virginia Institute of Marine Science for ICP-MS analysis. While elements such as Fe, Al, Ca, K and Si are commonly found in crustal material and are in relatively high abundance [*Taylor et al.*, 1983] other elements which can be used to apportion source via natural variability such as REE or through trace metal indicators of anthropogenic activity such as As, Cd, Cu, Cr, Ni, Pb, V, and Zn [*Trapp et al.*, 2010] are often many orders of magnitude lower in abundance. To account for such a large range of natural variability, standards were run over six orders of magnitude (a range of 0.003 ppm to 31.9 ppm). The calibration curves are generally reliable at over 5 orders of magnitude higher than the highest value of the calibration curve. Based on calibration curves we discount values less than 0.001 ppm (or 1 ppb) as unreliable, although for some metals higher cutoffs are applied where necessary based on blank problems.

To account for instrument drift, indium was used as an internal standard, as it is not found in nature. We cannot quantify contamination associated with sample collection, or contamination encountered during x-ray analysis, but blanks were measured for machine/instrument (25), digestion of pure dust (3), digestions with filters (3). Digestion variability was further assessed, quantified and corrected for by use of digestion replicates (3) and matrix issues addressed via standard additions (6). Table 6.4 summarizes the blanks calculated in this analysis.

In general instrument blanks were small compared to signal from pure dust samples (Table 6.4). Only Si had a machine blanks in excess of 10% (11.7%) of the median pure dust signal. As the signals on the filters were lower than those of pure dust, the ratio of instrument blank to filter signal is higher. However only three elements had banks of between 10% and 50% (Si, Eu, Gd). Other elements exhibited an instrument blank between 1% and 10% (U, Mg, S, Ca, Rb, Sr, Ba, Sm, Ho, Er, Tm, Yb, Lu, Th).

However, in general, instrument blanks were small compared to digestion blanks. In all cases digestion blanks were high for Fe, Ni, Cu, Zn many of which have been historically used for provenance. The digestion blank was calculated individually for pure dust and filter, as the digestion process differed slightly in the quantity of acid used in digestion. For pure dust a number of key elements had a digestion blank between 1% and 10% of the dust signal (Si, S, V, Mn, Fe, Cu), no elements fell into the range of 10% to 50% and two others far exceeded 50% (Ni, Zn). Rare earth element blanks were extremely low, well below 1% for all elements, and often well below 0.1%. The filter digestion process introduced large blanks, likely coming from the filter itself. Few elements had filter digestion blanks between 1% and 10% (Si, S, Rb). Many major elements commonly found in crustal materials had filter digestion blanks between 10% and 50% (Pb, U, Mg, Al, Ti, V, Sr, Ba). Multiple elements had filter digestion blanks in excess of 50% (Ca, Mn, Ni, Cu, Zn). In particular the filter digestion process provided more metal than the sample did (ratio greater than 100%) for many elements which are used to establish provenance (Ca, Mn, Ni, Cu, Zn). Blanks represent a challenge to the analysis, in particular Ni and Zn appear to be likely unusable. Thus for these filter samples the list of elements which could be reliably estimated is greatly reduced.

6.4 Results

6.4.1 Mineralogy

Table 6.5 to Table 6.5 shows minerals identified in pure dust samples from two African, two Asian and one Australian sample. Samples that did not have a match in the mineral database are included to give a sense of mineral representation.

Two samples from North Africa were analyzed (POLS 3, 4GOST) and 16 diffraction patterns were taken and analyzed. Five of 16 patterns were matched to known minerals, the remaining 11 patterns in general had no match in the database. It has been previously noted that mineral dust diffraction patterns, in particular North African samples are under represented. Of the five patterns identified, calcite, muscovite, kaolinite, and dolomite were dominant.

Three samples from Asia were analyzed (Nanjing, Inner Mongolia, Nandon) for a total of 17 diffraction patterns. Twelve of 17 patterns were matched, a much higher ratio than for the North African minerals. Dolomite and calcite were observed 3 of 17 times. Aluminosilicates (biotite, muscovite and generic aluminosilicate, aluminum oxide) were observed 4 of 17 times. Iron and titanium oxides were common in the Asian samples (iron-titanium hydrate, iron oxide, titanium oxide, rutile, magnetite); identified in 7 of 17 patterns. Additionally quartz with iron impurities was observed. This is largely different from North African mineral dust where iron and titanium oxides were not observed. Silica and quartz were observed in 2 of 17 measurements.

The Australian sample yielded six diffraction patterns. Muscovite and a generic aluminosilicate were observed in 2 of 6 diffractions, titanium oxide and magnetite were observed in 2 of 6 diffractions and silica was observed in 1 of 6 diffractions.

While the mineralogy cannot be considered to be quantitative, it does allow us to place the source minerals three loose groupings, a calcium carbonate group (calcite, dolomite), a titanium-iron oxide group (iron oxides, titanium oxides, iron-titanitum hydrates, magnetite, rutile) and an aluminosilicate group (kaolinite, muscovite, aluminosiciate (generic) and aluminum oxide). Silica and quartz were also identified but may not be dissolved in our digestive approach, thus may not contribute to our elemental analysis.

6.4.2 Trace Metal Chemistry of Mineral Dust

In Figures 6.5 and 6.6 elements of interest normalized by their concentration of Al are plotted. Normalization to Al is performed for two reasons; continuity to prior studies [*Formenti et al.*, 2011] and as filters contain unknown masses of dust, elemental concentrations ($\frac{massofelement}{massofsample}$) cannot be directly determined. The utility of Ca, Fe and Si are described in our review of [*Formenti et al.*, 2011]. V and Pb have been shown to be tracers of anthropogenic activity [*Sedwick et al.*, 2007; *Trapp et al.*, 2010] and in turn sources as African mineral dust passes through fewer industrialized locations than does Asian dust. Mn has been shown to track tightly with the total quantity of mineral dust in aerosols collected near to the Caribbean [*Trapp et al.*, 2010]. In each figure the mineral dust source is shown by color: Asian dust is blue, African dust is red and Australian dust is green.

Figures 6.5 and 6.6 are complimentary figures acting as a matrix of each individual ratio plotted against each other to best visually separate continental sources. Ca/Al shows clear separation in continental dust sources; African mineral samples exhibit higher ratios, generally in excess of 4. Asian samples have significantly lower ratios of Ca to Al, with values below 4. Ti to Al also is able to parse continents. Asian samples exhibit Ti/Al ratios in excess of 0.02, while the majority of African samples fall below 0.01 (although some do fall in the Asian range). Other ratios are less successful in separating sources. In both Mn/Al and V/Al, Asian and African samples overlap each other. For both Si/Al and Pb/Al some discrimination is evident, but enough samples are in mixed ranges that cause problems. Plotting Ca/Al vs Ti/Al is the most successful in separating Asian and African sources

(Figure 6.5). Asian dust is found in the upper left quadrant of the plot, corresponding to Ti/Al ratios in excess of 0.02 and Ca/Al ratios below 4 ((Figure 6.5)). African dust is clearly visible outside of the narrow Asian window. Australian dust is also clearly separated, falling nearest to the origin.

However due to concerns with possible contamination during the digestion process with Al, it is not clear if ratios normalized with Al to appropriate. We repeat the analysis normalizing with Ti, which had significantly less contamination (Table 6.4). While normalization to Ti is less common in the literature, doing so yields clearer separation between continents. Figures 6.7 and 6.8 present the matrix of ratios normalized by Ti. The ratio of Pb to Ti is not helpful in separating Asian and African sources, but Australian dust is easily identified by its high concentration of Pb. Asian dust appears to be depleted in both Ca and Mn relative to African dust, with ratios of Ca/Ti of an two orders of magnitude less than Asian dust and ratios of Mn/Ti less than 2, while the majority of African samples show ratios in excess of 2. Al/Ti, Si/Ti and V/Ti all show the same general trend: Australian dust shows high ratios, African dust has medium ratios and Asian dust has low ratios. Values of 1 for Si/Ti, 50 for Al/Ti and 0.25 for V/Ti can roughly be used to separate African-Asian source regions.

Cole et al. [2009] suggest that Mg may be a useful element in identifying dust originating in dried lakebeds, such as the Bodele Depression. However we do not show Mg Figures 6.5, 6.6, 6.7 and 6.8 as Mg is not useful in separating continental sources. All Asian dust is depleted in Mg (ratios near to zero), while Mg ratios in African dust ranges over orders of magnitude. Here we hypothesize that Mg could be useful in separating regional sources, however it is not useful in separating continental sources.

We have identified a number of ratios by which continental sources can be separated, however to a large extent this approach is subjective and only includes analysis of six of the thirty elements analyzed for. To better quantify the relationships and include all elements analyzed, we use a principal component analysis.

Principal Component Analysis Using Metal Data

principal component analysis (PCA) can be used to identify which elements are coupled together over varying source regions. We first perform PCA using elemental ratios normalized to Al, which is the most common normalized element. We repeat the analysis using ratios normalized to Ti to account for potential Al contamination.

Figure 6.9 shows the results of the PCA for ratios normalized by Al. Figure 6.9a shows the magnitude first principal component (PC1) and second principal component (PC2) with the sample value plotted as a color blue for Asia, red for Africa and green for Australian. Asian dust samples are found only in the top right quadrant of the figure, corresponding to values of PC1 below -1 and PC2 values above 0. In contrast African samples are uniformly distributed across PC1, but generally fall below a values of PC2 of 1. Figure 6.9b shows the second and third principal (PC3) components plotted against each other. In summary Asian dust can be identified by PC1 values above 1, PC2 values above 0 and PC3 values near 0. African dust can be identified by PC2 values below 1 and PC3 values above 0.5 (with a notable outliers). Figure 6.9c attempts to visualize the three-dimensional relationship; separation between sources is visible. Figure 6.9d shows the biplot of elements that correspond to the principal components. Weight of the individual element is shown in blue by the distance from the origin. Each element is labeled on the biplot. Red dots represent the samples. Three key groupings are identified; Ti-Fe-Pb-Mn are grouped together, possibly representing an iron-oxide grouping. A Ca-Rb-Sr-Si group is seen possibly corresponding to a carbonate group. To the right REE elements are grouped together tightly.

Figure 6.10 shows the results of the PCA for ratios normalized by Ti. The first and second principal components are featured in Figure 6.10a with sample values again plotted as color blue for Asia, red for Africa and green for Australian. PC2 discriminates little between African and Asian dust, as most values are near to a value of zero. In PC1 however Asian dust is shown to have values of less than -3, and African dust has values greater than -3. Figure 6.10b shows the third principal component which also can be used to separate

Asian and African dust. In PC3 Asian dust have values less than -0.5, while African dust has values greater than -0.5. Figure 6.10c combines all three principal components, and visually African and Asian dust can be discriminated. Australian dust is disparate to Afrian and Asian dust in all three PC. Figure 6.10d shows the biplot for the principal components normalized by Ti, again three groups are evident a Ca-Sr group, a Fe-Pb-Mn group and a REE-Al-Si group.

We have highlighted two approaches to separate African and Asian dust, using elemental composition of a few select metals and principal component analysis of multiple metals. In the next section we seek to test our separation methods on filters of mineral dust with unknown origins.

6.4.3 Apportionment of Unknown Filters

First we consider metals ratios normalized by Al. Ca/Al and Ti/Al were both shown to separate Asian and African sources. The Ti/Al of all five filters fall within the range of African samples, with all filters having ratios near 0.01. Ca quantities measured on filters were low, with 3 of 5 falling below detection limits. Of the two remaining filters the Ca/Al ratios fell into the Asian range. Little can be concluded from this analysis as normalizing by Al yields conflicting results.

More elemental ratios were able to separate continental sources when ratios were normalized by Ti than Al; Ca/Ti, Mn/Ti, Al/Ti, Si/Ti and V/Ti all were able to clearly separate Asian and African dust sources. Ca/Ti ratios for filters were low, but as previously noted 3 of 5 filter samples had Ca levels below detection. Mn/Ti filters ratios were low, similar to Asian signals. Al/Ti ratios of filters fell in medium range, closer to African dust than Asian dust. Si/Ti values for filters varied widely and had values near both Asian and African ranges. V/Ti values for filters fell in the middle of the African source values. Two metal ratios (Al/Ti, V/Ti) suggested African sources and one ratio (Mn/Ti) suggested Asian sources for the filters. This analysis, similar to the results using ratios normalized to Al, yielded conflicting results for sources.

Next we repeat the PCA, including filter samples normalized by both Al and Ti. In this analysis the loading patterns are re-defined as the variance of all samples is greatly changed by the inclusion of filter samples. To avoid biases from variable concentrations all samples are normalized before the PCA is performed. Of interest here are two questions; can source regions still be separated and do the filter samples group with any source region.

First we examine the PCA for elements normalized to Al as shown in Figure 6.11. Figure 6.11a shows the first and second principal components, with filter samples shown in black. Filter samples are separated from source samples along the first principal component. The majority of source samples are bunched together in the lower right quadrant of Figure 6.11a with negative values of the 2nd principal component, and positive values of the 1st principal component. It is difficult to use Figure 6.11a to separate sources, as African and Asian mineral dust appear to be intermingled tightly. The 2nd and 3rd principal components are plotted on Figure 6.11b. Here sources are better separated: Australian dust have higher values of the 3rd principal component than others, while Asian dust has higher values of 2nd principal component compared to African dust. However filters values range greatly over the 3rd and 2nd principal components, not matching with any source group clearly. Combining all three components in Figure 6.11c filter samples are clearly distinct from other source regions. Additionally no clear geochemical explanation for principal component loading patterns (Figure 6.11d) is evident. Rare earth elements do group tightly in the lower right quadrant, but other previously identified groupings such as Fe-Ti (iron and titanium oxides) and Ca-Sr-Rb (carbonates) are now disparate and randomly grouped.

Figure 6.12 is as Figure 6.11 but with data normalized to Ti. Figure 6.12a shows the first and second principal components, where each major source region is clearly separated along the first principal component with Asian samples falling below -3, African samples falling between -3 and 4 and Australian samples falling above values of 8. Figure 6.12b shows the 2nd and 3rd components, where additional separation is evident along both the 2nd and 3rd components. Along the 2nd component, values increase from Australian samples (-2 to -1.5) to Asian samples (-1 to -0.5) to African samples (-0.75 to 5). Along the 3rd component, values decline from Australian samples (near to 1.5), towards Asian samples (0 to 0.5) and into African samples (0 to -2). However along each principal component, filter samples are clearly distinct and separate from nearly all source signals, as summarized in Figure 6.12c. Geochemical groupings by loading pattern are not as clear when filter samples are included as seen in Figure 6.12d. Rare earth elements appear to be tightly clustered again, with aluminum suggesting an aluminosilicate source. However carbonates (Ca, Sr) and iron oxides (Fe) are not clearly separated.

In summary principal component analysis shows that with filters included separation of sources is possible, particularly when looking at data normalized to Ti. Signals are not distinct when looking at data normalized to Al, possibly due to variability induced by extremely large blanks in Al in filter analysis (blank is 37% of Al median filter signal). In comparison Ti had relatively small blanks (11%) and showed more skill in separating source regions. Additionally while we are able to separate continental sources, we note that our clear geochemical separation by aluminosilicate vs. carbonate vs. iron oxide disappears, possibly due to high blanks associated with filter digestion in key tracers such as Fe (84%), Ca (256%), Sr (48%).

6.5 Discussion

6.5.1 Back Trajectory Analysis

Geochemical sourcing of mineral dust is a useful tool to apportion source, however it not the only tool available. In this section we couple geochemical tracers with back-trajectory analysis and satellite data.

Figure 6.13a and 6.13b are aerosol absorbing data from TOMS/Earth-Probe for the day before and day of collection respectively. A pulse of dust is evident near Bermuda, extending southward toward Hispanola in Figure 6.13a, the next day the dust appears to move over Florida towards the collection site. Figure 6.13c and 6.13d show back trajectory analysis during morning (12z) and early afternoon (18z) during the day of collection. Trajectories were run at three heights at 1,000 (red), 10,000 (blue) and 15,000 (green) meters above ground level and run back in time for ten days prior to sample collection. In both morning and afternoon, air from near the surface has its origins over the Tropical North Atlantic Ocean. For air at highest heights in both morning and afternoon the air originates from over the Pacific Ocean. Air at intermediate height switches from Atlantic to Pacific origins. Satellite measurements of dust appear to suggest a Saharan source, as does near-surface air, however back trajectory analysis of air aloft leaves open the potential of Asian influence.

Filter 03-T9329 shows similar satellite imagery to the last case, on the day prior to collection Figure 6.14a dust particles appear over the Bahamas south towards Puerto Rico extending into South Florida. The next day dust appears to spread west over the remainder of Florida. Trajectory analysis is shown in Figure 6.14c and 6.14d for morning (12z) and afternoon (18z) the day of collection. Low level flow again shows a source over the Tropical Atlantic near to the coast of Africa. Upper level flow again shows a source over the Pacific, with middle levels swapping sources over the duration of the day. Based on satellite measurements a North African source would be assumed, supported by low level flow, however again air arriving aloft, suggests the possibility of Asian aerosols.

In contrast to the previous two cases satellite imaginary for the day prior to (Figure 6.15a) and of collection (Figure 6.15b) for Filter 04-T11260 no clear dust plumes are evident approaching Florida, although Figure 6.15b suggests that some dust may passed over Florida between images. Figure 6.15c and 6.16d show that both in morning and afternoon near surface air has origins in the Tropical North Atlantic, and air aloft has origins over the Pacific.

Filter 04-T11261 has the least indication of mineral dust from satellite imagery as shown in Figure 6.16a and 6.16b. On the day of collection (Figure 6.16b) some indication of dust may be approaching Florida, but the signal is weak. Trajectories are shown for the morning and afternoon of collection in Figures 6.16c and 6.16d. Low level air has its origins near to Africa and air aloft has origins from near to Asia in the Pacific.

Satellite images associated with Filter 04-T9429 are shown in Figures 6.17a and 6.17b for the day preceding collection and the day of collection. On both days a pulse of dust appears to be near to Florida, either just south and west of the collection station or to the east on respective days. Trajectories for Filter 04-T9429 are shown in Figures 6.17c and 6.17d for morning and afternoon of the day of collection respectively. Here no clear source of air masses is evident, suggesting something of a stagnant wind pattern. No Asian of African influence of air masses is evident.

In general satellite imagery confirms the expectation that mineral dust appears to be coming from points east in its path passing over Florida. Trajectory analysis suggest that air at low levels is originating over the Tropical Atlantic near to Africa, however air aloft appears to have its origins in most cases over the Pacific.

The above analysis comes with a number of caveats. The satellite analysis as presented is both qualitative and subjective. The satellite in use here has known calibration issues over this time-period [*Kiss et al.*, 2007] and is likely over-estimating aerosol load. The trajectory analysis is run using low resolution NCEP reanalysis data, the only data available for analysis over this period. As such there is a large degree of uncertainty of air mass source, and this uncertainty likely grows over the ten-day back trajectory presented here. None the less, this analysis suggests that the Sahara is the likely source of mineral dust to Florida but Asian influence cannot be ruled out.

6.5.2 Geochemical Tracers and the WACZ

Previous chapters introduced the hypothesis that changes in the position of the WACZ changes the quantity of Saharan mineral dust transported across the Atlantic, specifically by activating preferred hot spots such as the Bodele Depression in years in which the WACZ is south. Filters were subjectively selected to include the largest mineral dust events over the period 2003 to 2004, thus the events included in this analysis are like major Saharan dust events. Previous studies have indicated timespans of approximately a week to reach the Caribbean, and thus additional time to reach Florida. As such here we assume the dust took between 7 and 14 days to reach Florida. To examine if the position of the WACZ plays a role in the quantity of mineral dust reaching Pensacola, FL we calculate the mean position of the WACZ over the period 7 to 14 days preceding the sample collection. This information is summarized in Table 6.6 along with the anomaly of the week long period for the trend corrected climatological mean. In four of five events the WACZ was south of its climatological position.

6.6 Conclusions

In this work we analyze dust samples collected over four continents for mineralogy via diffraction and elemental ratios via ICP-MS. Principal component analysis, a novel approach in geochemistry, is applied to elemental data and, combined with elemental ratios, clear separation of source regions is demonstrated, representing a validation of the method.

Blanks, for the filter samples are problematic. High blanks in elements previously identified via PCA as being important in discriminating between key mineral groupings, e.g. (Fe, Ca, Sr and Al) reduce the ability to apportion source of filter samples. Similarly in all treatments blanks on elements which could be used as anthropogenic signal identifiers, such as Zn, Cu and Ni are high and reduce the usefulness of these elements to discriminate sources. Instrument blanks associated with Si may be reduce its utility in identifying alumniosilicate rich materials. However, Ti is shown to be a resistant element with low blanks and is useful in each analysis.

The elemental composition of pure dust samples expressed as ratios to Al and Ti showed the ability to separate African and Asian dust sources for specific elemental ratios. However when many of these elemental ratios were examined for filter samples of unknown origin, they showed ratios dissimilar to both African and Asian samples, or some ratios were similar to African and others similar to Asian samples. This ambiguity leaves open that possibility that problems with the digestion method could be the cause. As the initial quantities of mineral dust on filters are unknown, recovery during the digestion process is not known. Metals could be dissolved into acid and then resorb onto the edges of the filter which were not Teflon. It is also possible that mineral dust could be deposited deep into the Teflon and thus not exposed to the acid, or simply not fully digested. If the digestion process was not the same between pure dust and filter samples, comparisons made here are not appropriate.

Only three samples from Asian sources were used in this analysis, and less than the seven African sources utilized. African samples in general exhibited wider spread than Asian samples, possibly due to under-representation of Asian sources in this study. An additional four samples from Asia have been procured but these samples arrived after this analysis was performed. Results would have been strengthened by including theses additional samples.

6.6.1 Filter Handling

Blanks associated with filter samples were unacceptably high. This experimental set up does not allow for us to quantify or account for blanks arising from sample collection in the field or handling during μ-XRF and μ-XRD analysis. Filter samples were collected in impacters exposed to the elements for prolonged period of times. After collection it is unclear how filters were handled or processes. In future studies sample collection blanks must be accounted for. Furthermore the advantage of non-destructive techniques such as μ-XRF and μ-XRD is offset by possible contamination induced during processing. Future analyses should be designed for two samples to be taken, one directly sent for μ-XRF and μ-XRD analysis and the other for trace metal analysis.

6.6.2 North American Mineral Dust

While samples were procured from four continents, no North American dust samples were used in this analysis. The Sahara is the dominant global source of mineral dust aerosols, with the Asian continent the second largest source of mineral dust aerosols. In general North America is not a major source of mineral dust on the global scale, but regionally North American dust sources can be important. We cannot rule out North American dust sources as unimportant for the Southeastern United States so samples from North American desert bases should be acquired and included in future analysis. Local sources of mineral dust mixing in with long-range dust on filters could explain why observed ratios varied from "pure" end-member samples.

6.6.3 Isotope Analysis

As discussed in the introduction, isotopic analysis is a powerful tool to apportion source. Samples used in this study have been treated in a way that isotopic analysis is the next step in the analysis, however due to multiple lab setbacks this analysis cannot be included this dissertation. We anticipate performing this isotopic analysis in the near future, as isotopic ratios should complement findings from the principal component analysis.

6.6.4 Rare Earth Elements

Analysis of rare earth elements (REE) may represent a strong method for apportioning source, as shown in *Taylor and McLennan* [1985] and subsequent work. Blanks associated with instrument and digestion techniques are low for rare earth elements. Although REE are found in low abundance in crustal material and thus signals are low on filters that contain only milligrams of mineral dust, signals were detectable for most REE for most filter samples and were well above detection for pure dust samples. *Trapp et al.* [2010] highlighted the potential utility of such elements in an analysis of mineral dust at Miami, noting that elemental ratios change little between dust storms with the exception of REE. As such REE likely have utility in apportioning source, potentially on subcontinental scales. In this analysis not all REE were available for analysis in available calibration fluids, so a complete analysis was not possible. In future analyses REE should be fully run.

6.6.5 SEARCH Utilization

The ability to use principal component analysis to separate source regions on elemental ratios will be applied near real time to samples from the SEARCH network in 2013 during mineral dust outbreaks in the Southeastern United States. Aliquots from pure dust samples used in this study are being sent to Atmospheric-Research in Cary, NC for complete digestion and analysis via ICP-MS receiving the same treatment that field filters samples receives. This data will be analyzed and PCA performed and a predictive schemed develop to identify dust sources in near real time as ICP-MS analysis is performed on field samples.

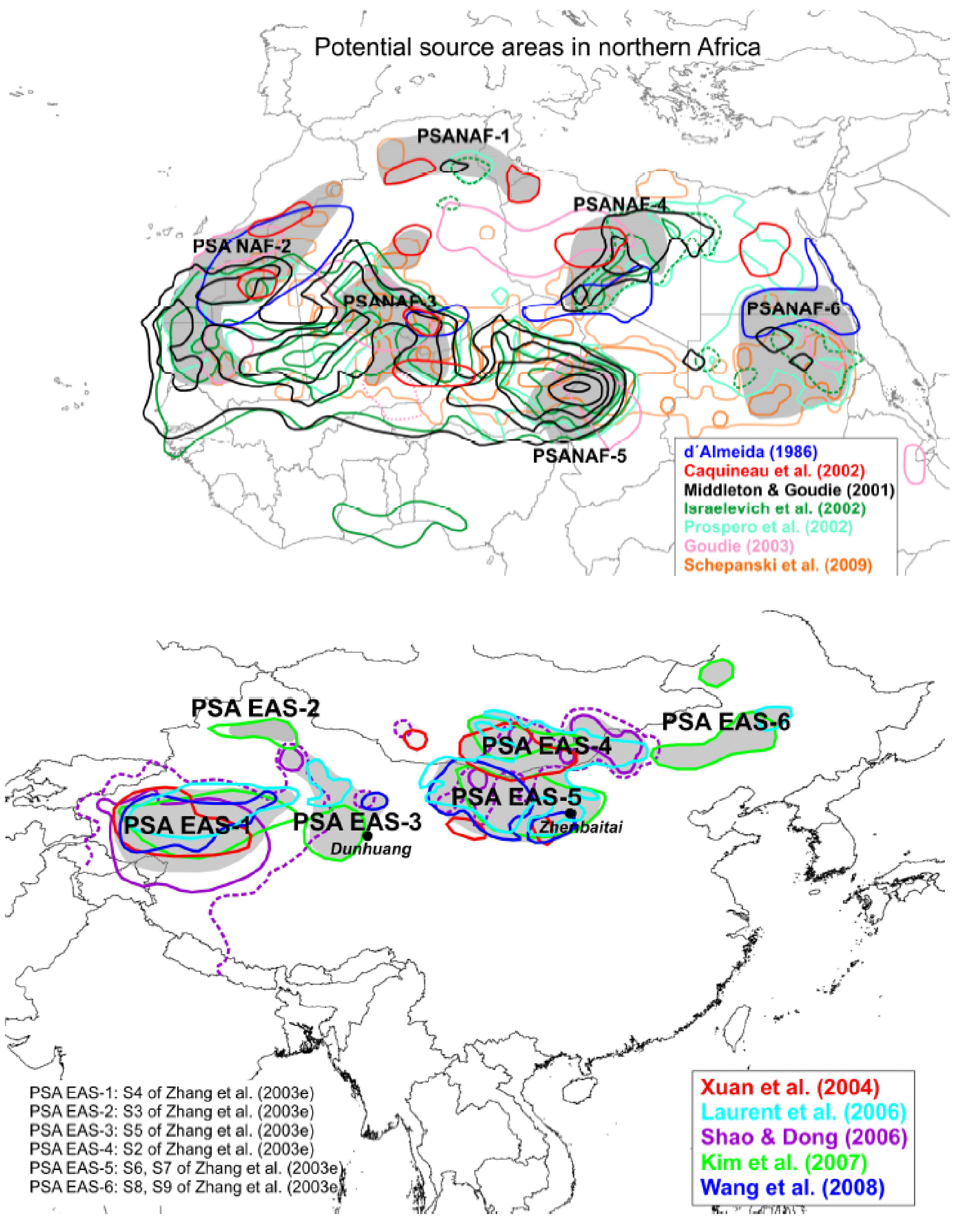

Figure 6.1: Regions as separated in *Formenti et al.* [2011] and shown in Table 6.1 and 6.2.

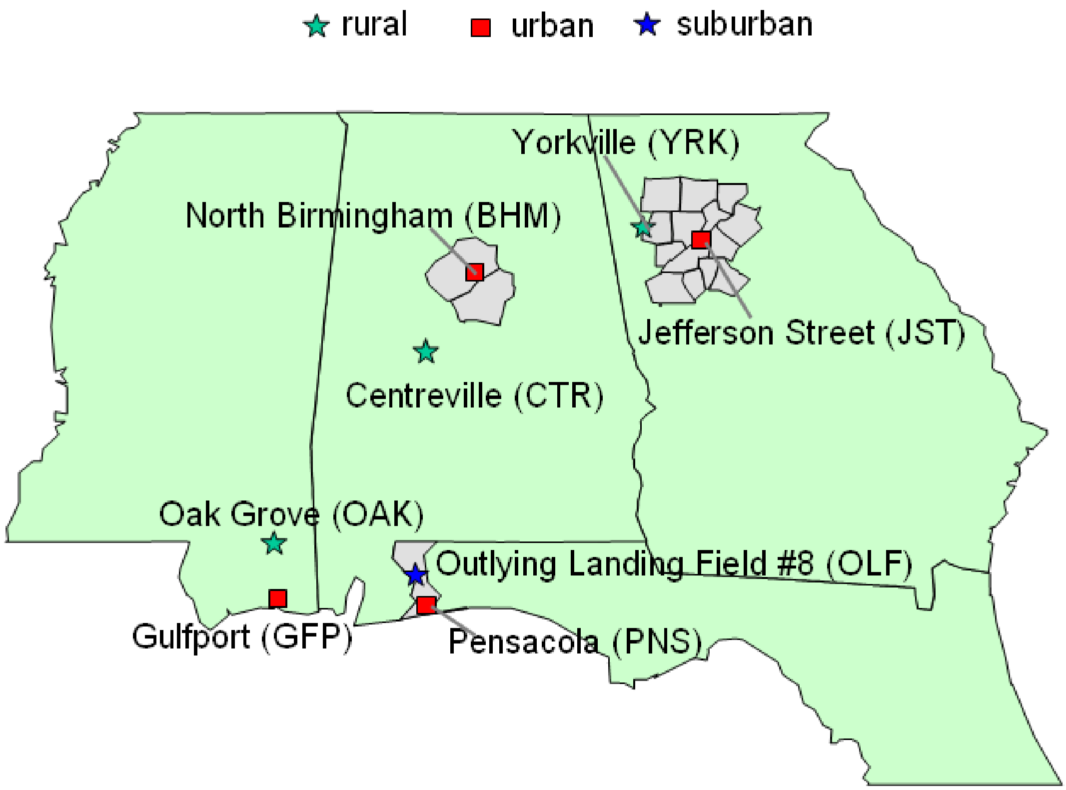

Figure 6.2: Position of sampling stations for the SEARCH project.

Figure 6.3: (top left) Digestion set-up both pure dust and filter samples placed in acid-washed Teflon beakers covered with Teflon eye glasses. (top right) Pure dust sample in aqua regia digestion phase. (bottom left) Pure dust sample after dry down, black carbon shown as residual. (bottom right) Teflon filter after acid digestion before final rinse.

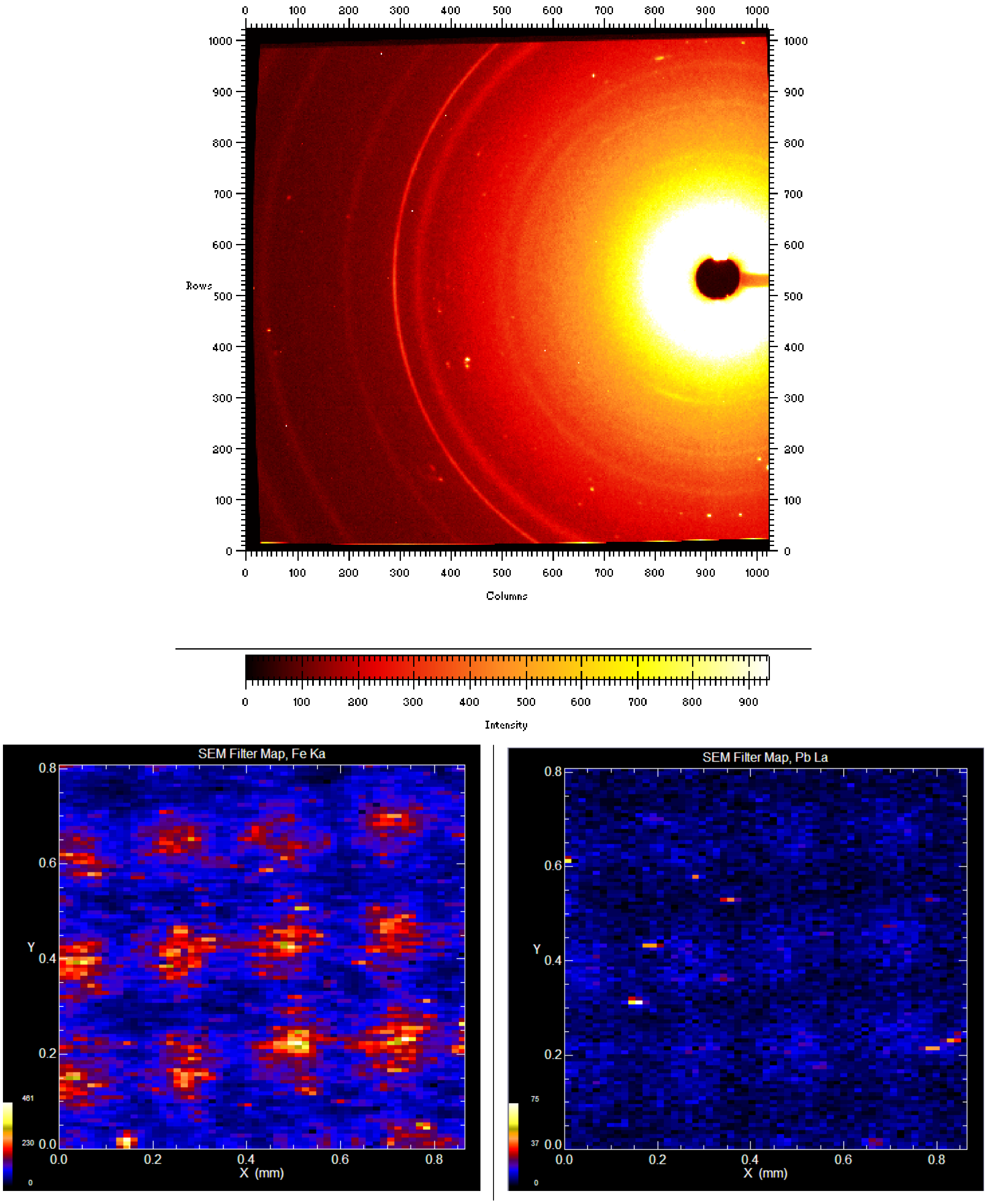

Figure 6.4: Sample images from NSLS at BNL. (top) Example of intensity patterns from μ x-ray diffraction. (bottom) Examples of μx-ray refraction of sample Teflon filters (left) Fe, (right) Pb.

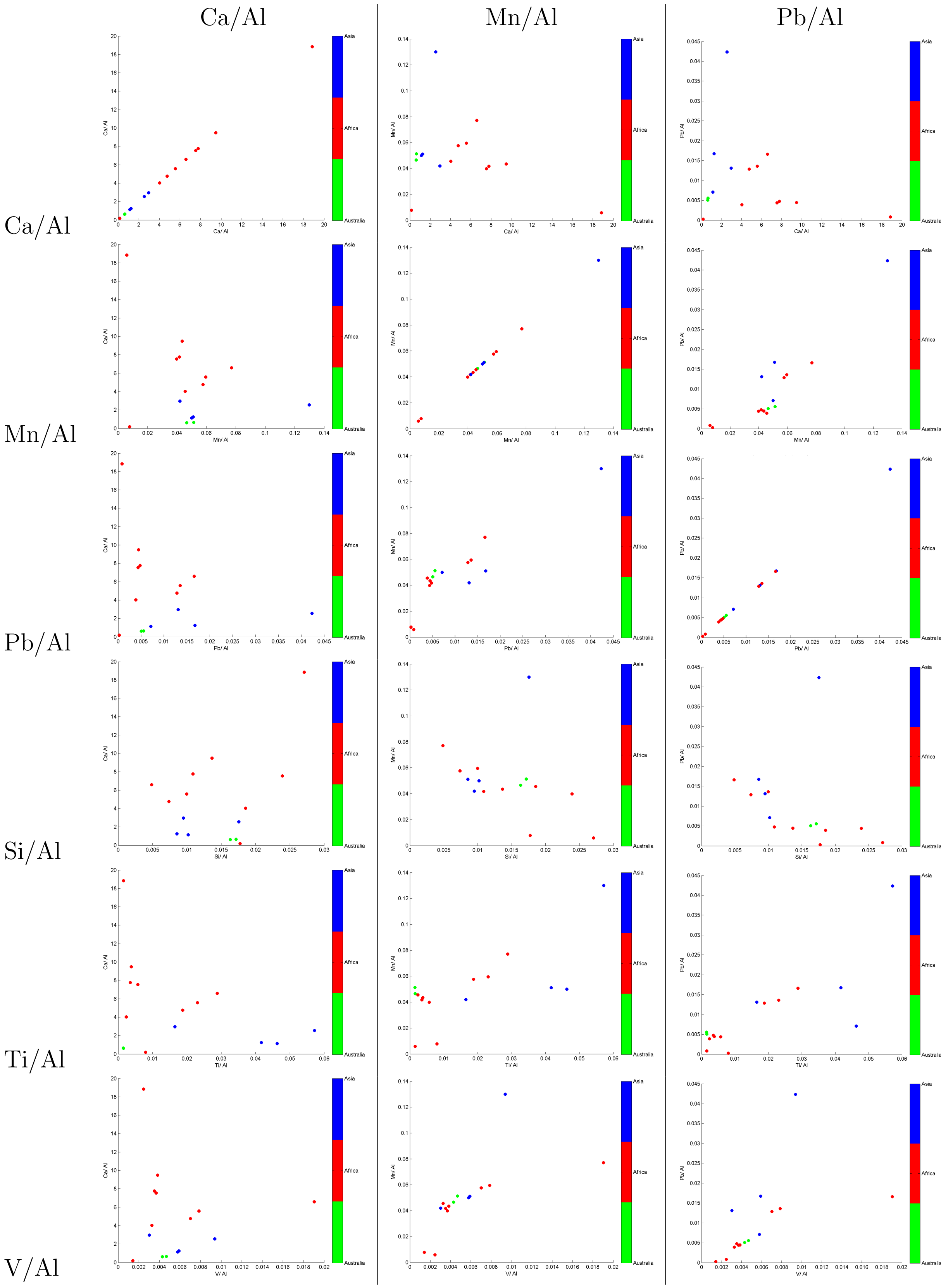

Figure 6.5: Matrix of scatterplots showing elemental ratios normalized to Al. Asian samples are blue, African samples are red and Australian samples are green.

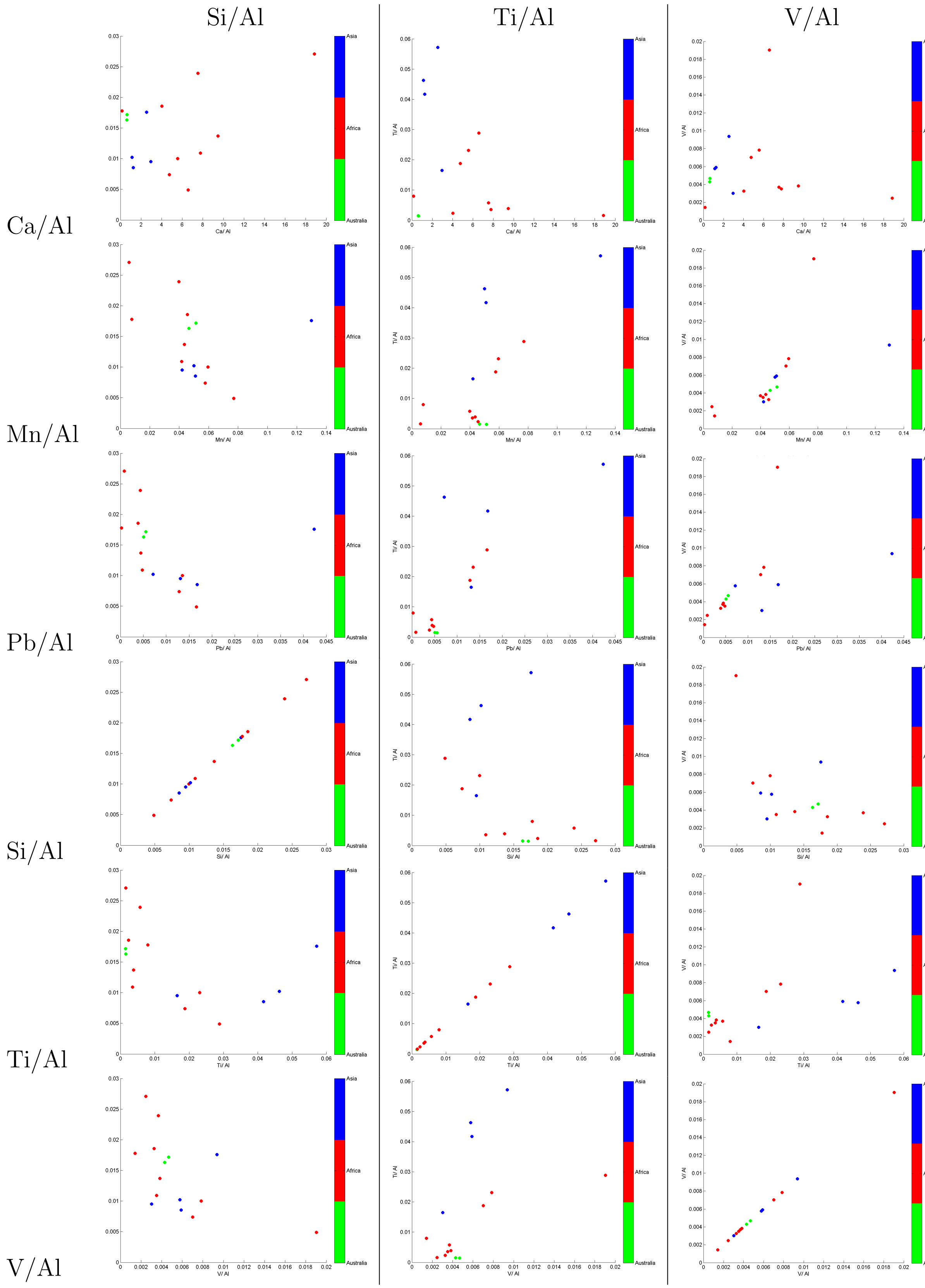

Figure 6.6: Matrix of scatterplots showing elemental ratios normalized to Al. Asian samples are blue, African samples are red and Australian samples are green

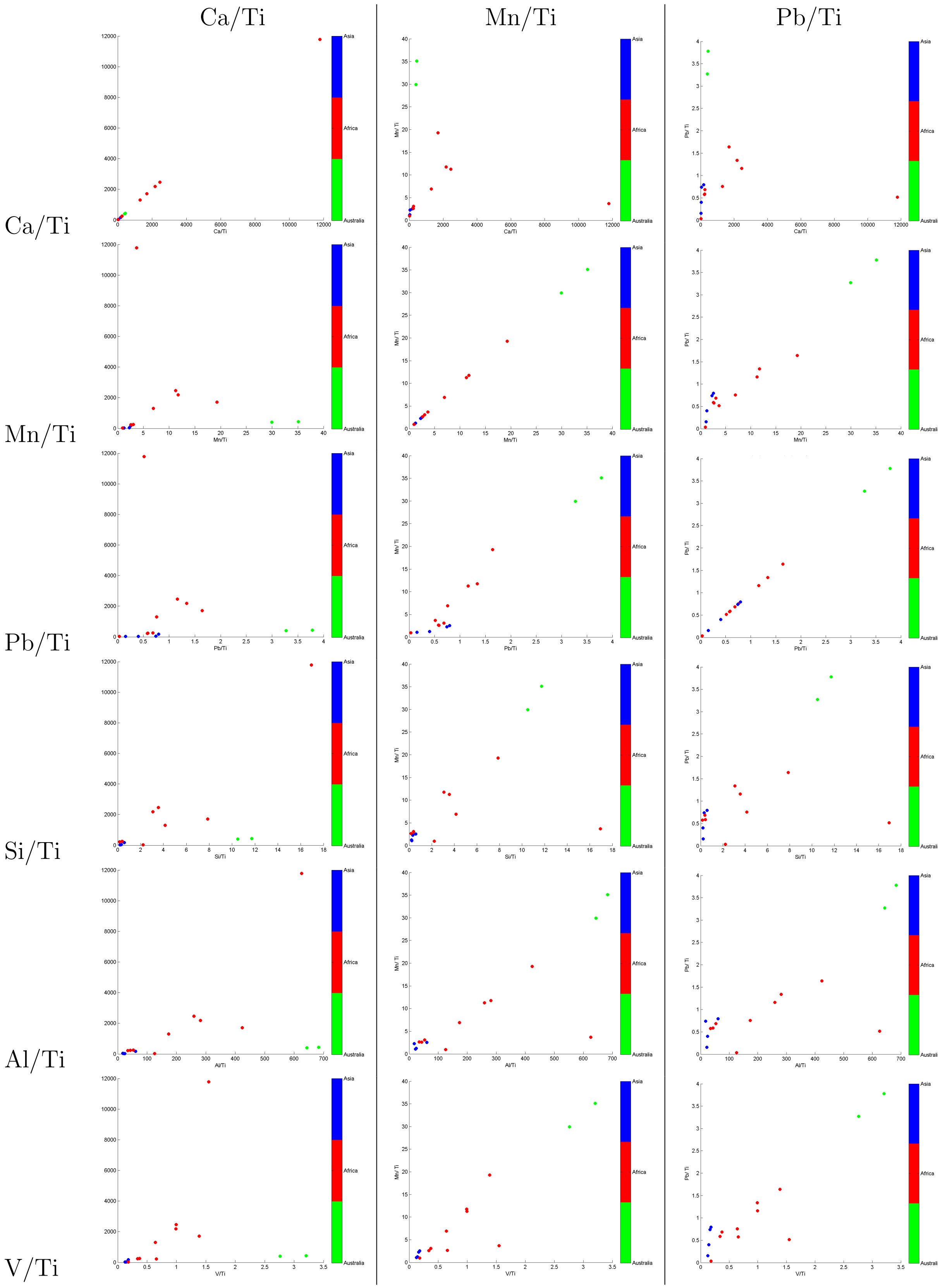

Figure 6.7: Matrix of scatterplots showing elemental ratios normalized to Ti. Asian samples are blue, African samples are red and Australian samples are green

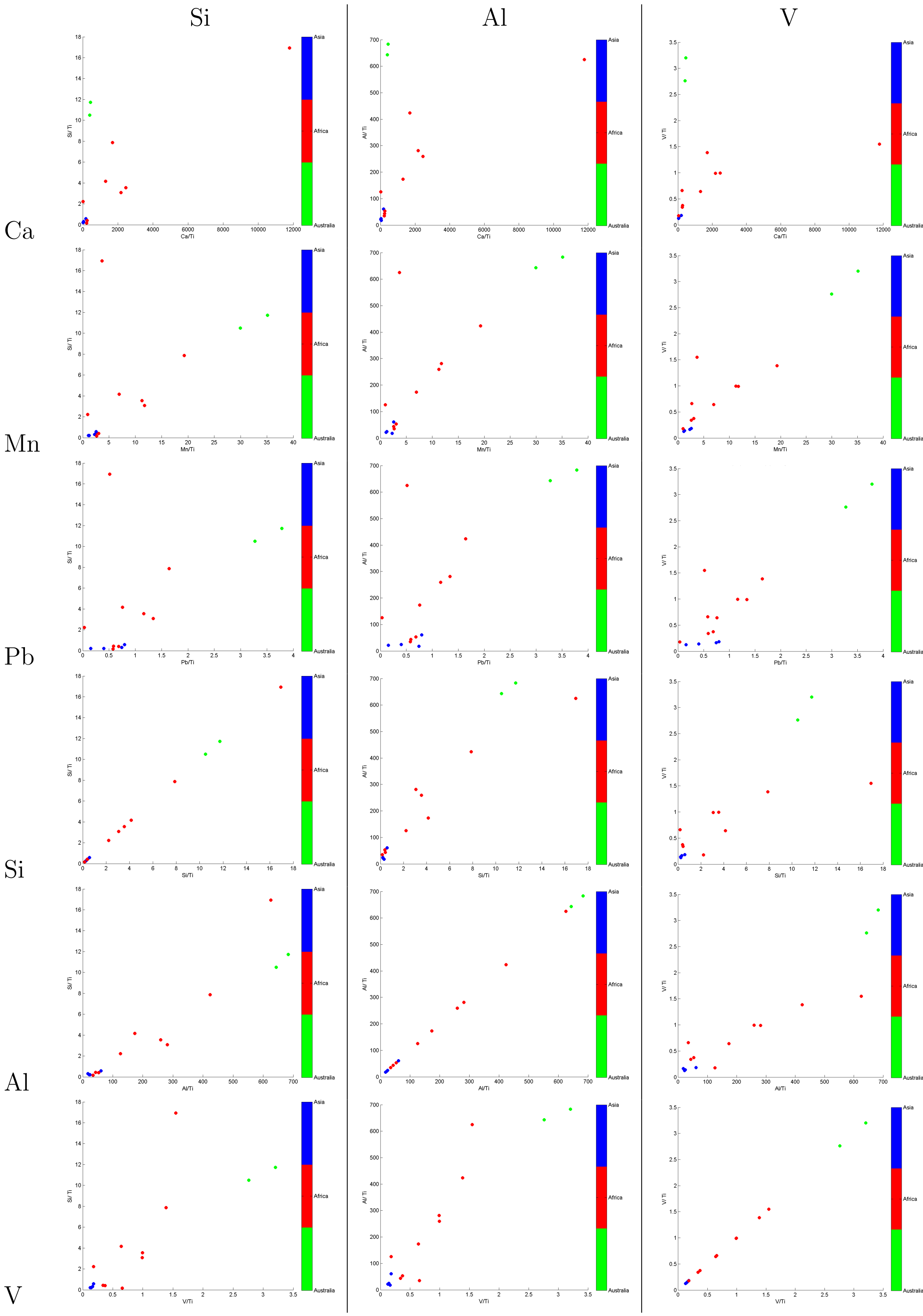

Figure 6.8: Matrix of scatterplots showing elemental ratios normalized to Ti. Asian samples are blue, African samples are red and Australian samples are green

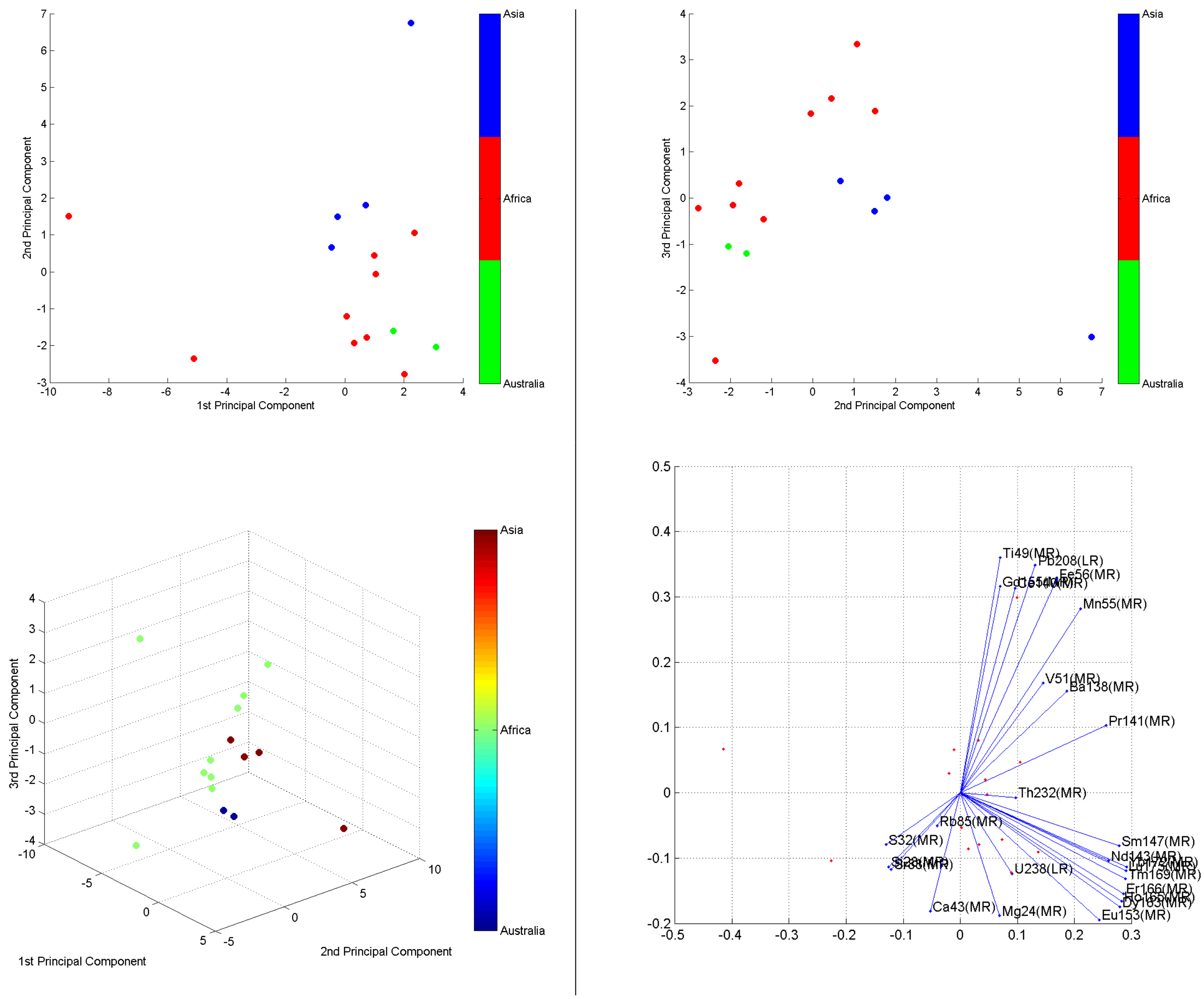

Figure 6.9: PCA on elemental ratios normalized to Al. (a) The first and second principal components. (b) The second and third principal components. (c) A three-dimensional visualization of the principal components. (d) A biplot of the relative magnitudes of the principal components and their grouping. The three principal components express 75% of the total variance of the elemental data.

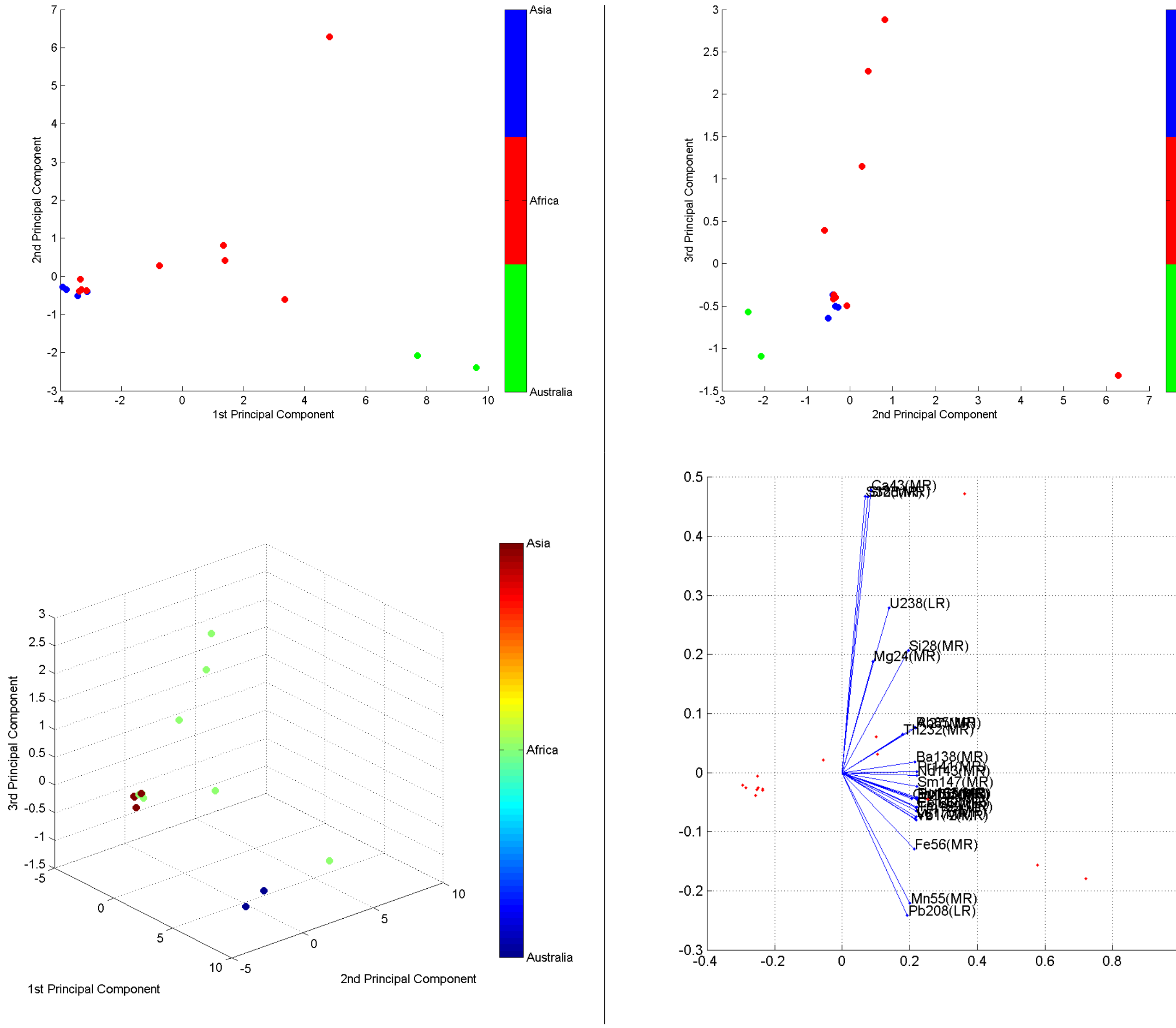

Figure 6.10: PCA on elemental ratios normalized to Ti. (a) The first and second principal components. (b) The second and third principal components. (c) A three-dimensional visualization of the principal components. (d) A biplot of the relative magnitudes of the principal components and their grouping. The three principal components express over 95% of the total variance of the elemental data.

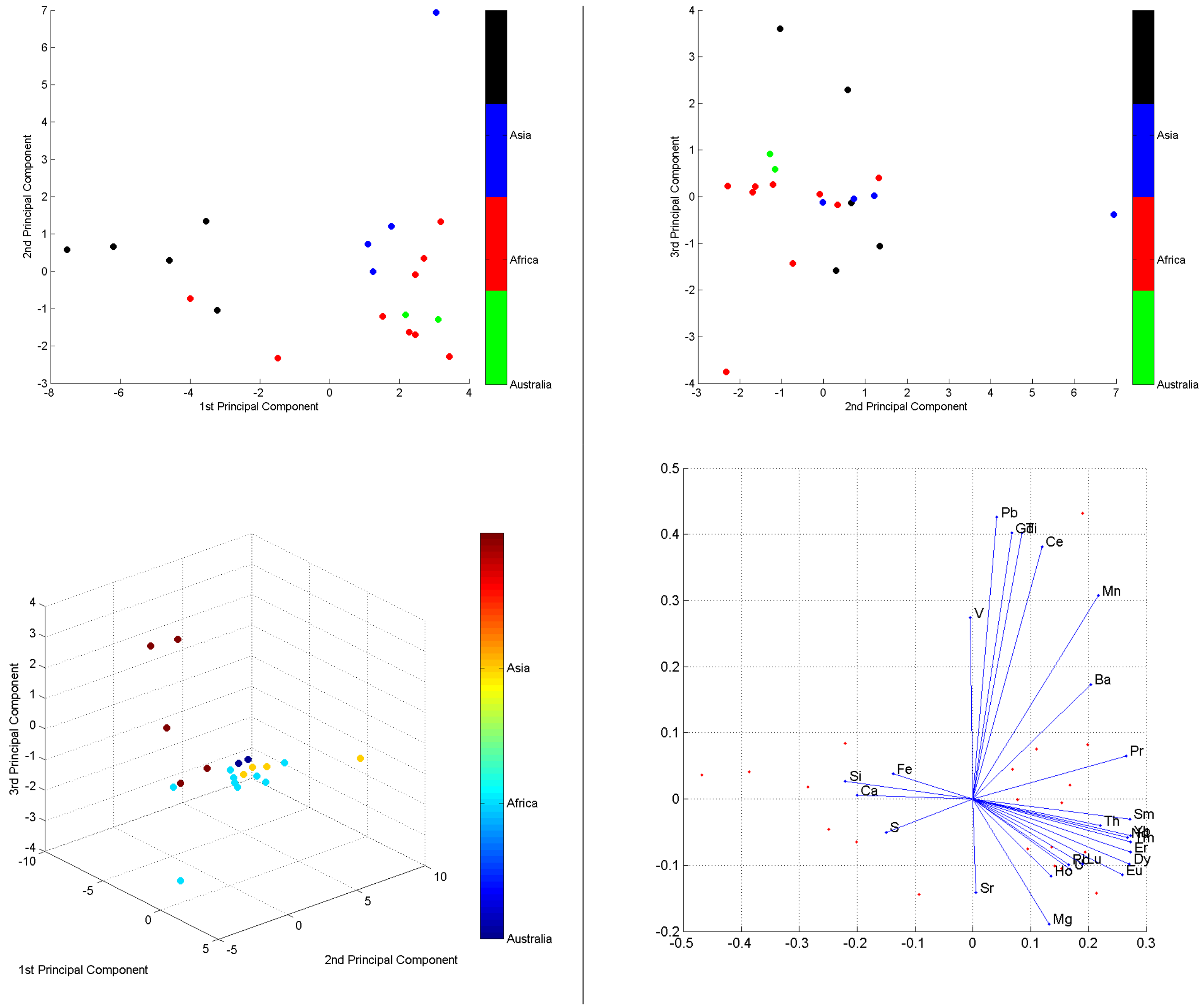

Figure 6.11: As in Figure 6.9 PCA on elemental ratios normalized to Al, with filter samples included. The three principal components express over 68% of the total variance of the elemental data.

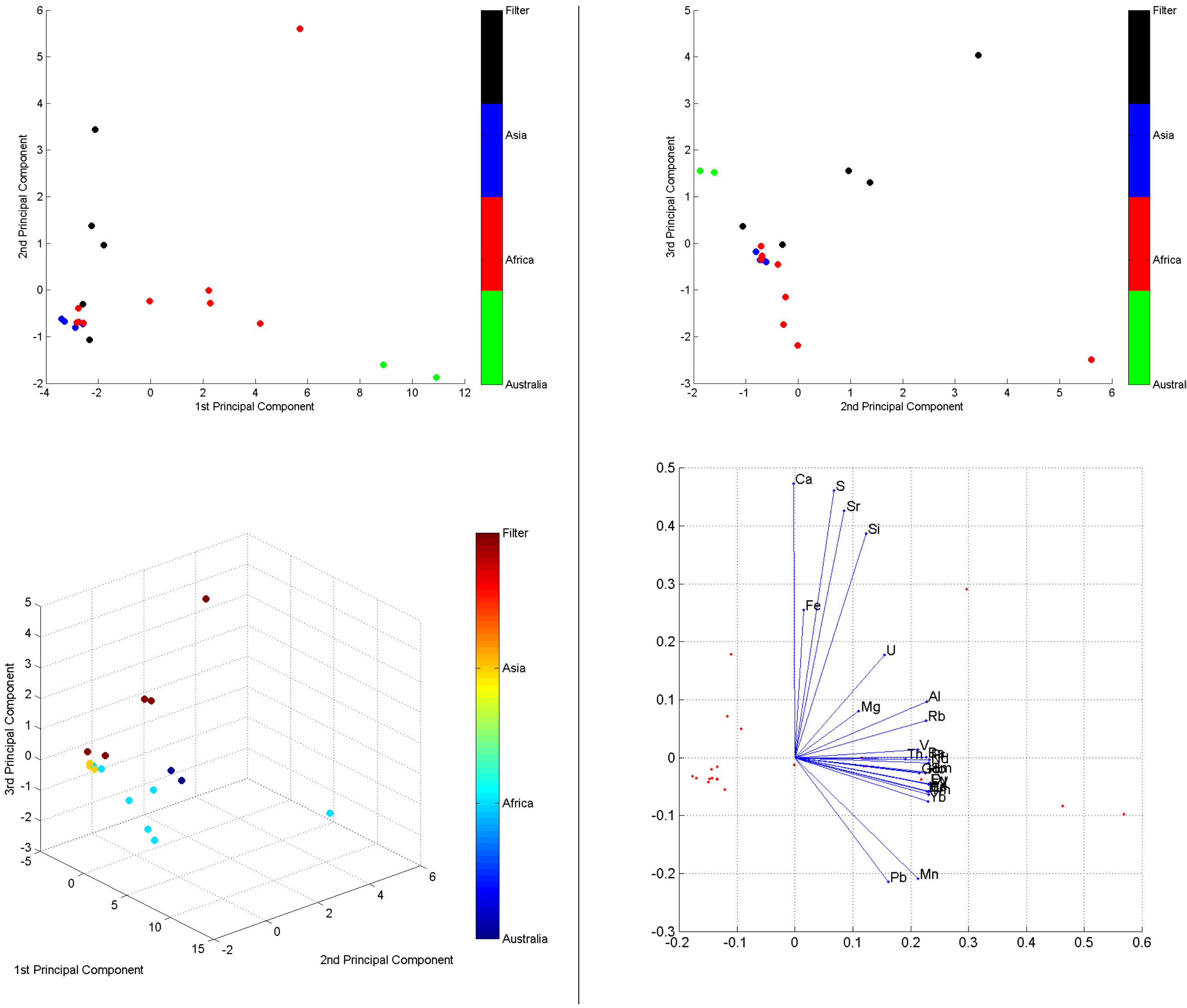

Figure 6.12: As in Figure 6.9 PCA on elemental ratios normalized to Ti, with filter samples included. The three principal components express over 90% of the total variance of the elemental data.

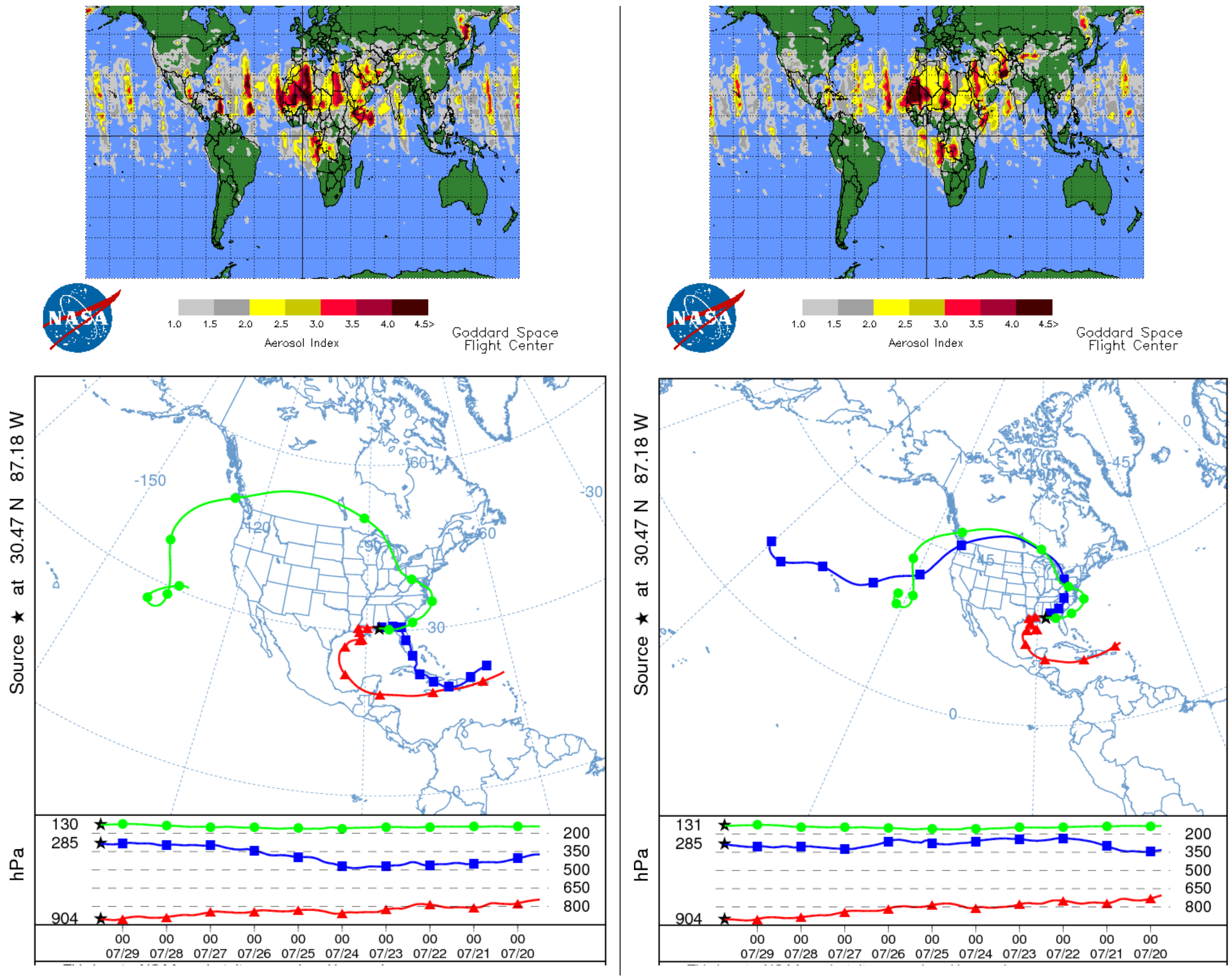

Figure 6.13: (top) Absorbing Index (AI) from TOMS/Earth-Probe for July 29 and July 30, 2003. (bottom) Back-trajectories for 12z July 29, 2003 (left) and 18z July 29, 2003 (right). These images correspond to filter 03-T10914.

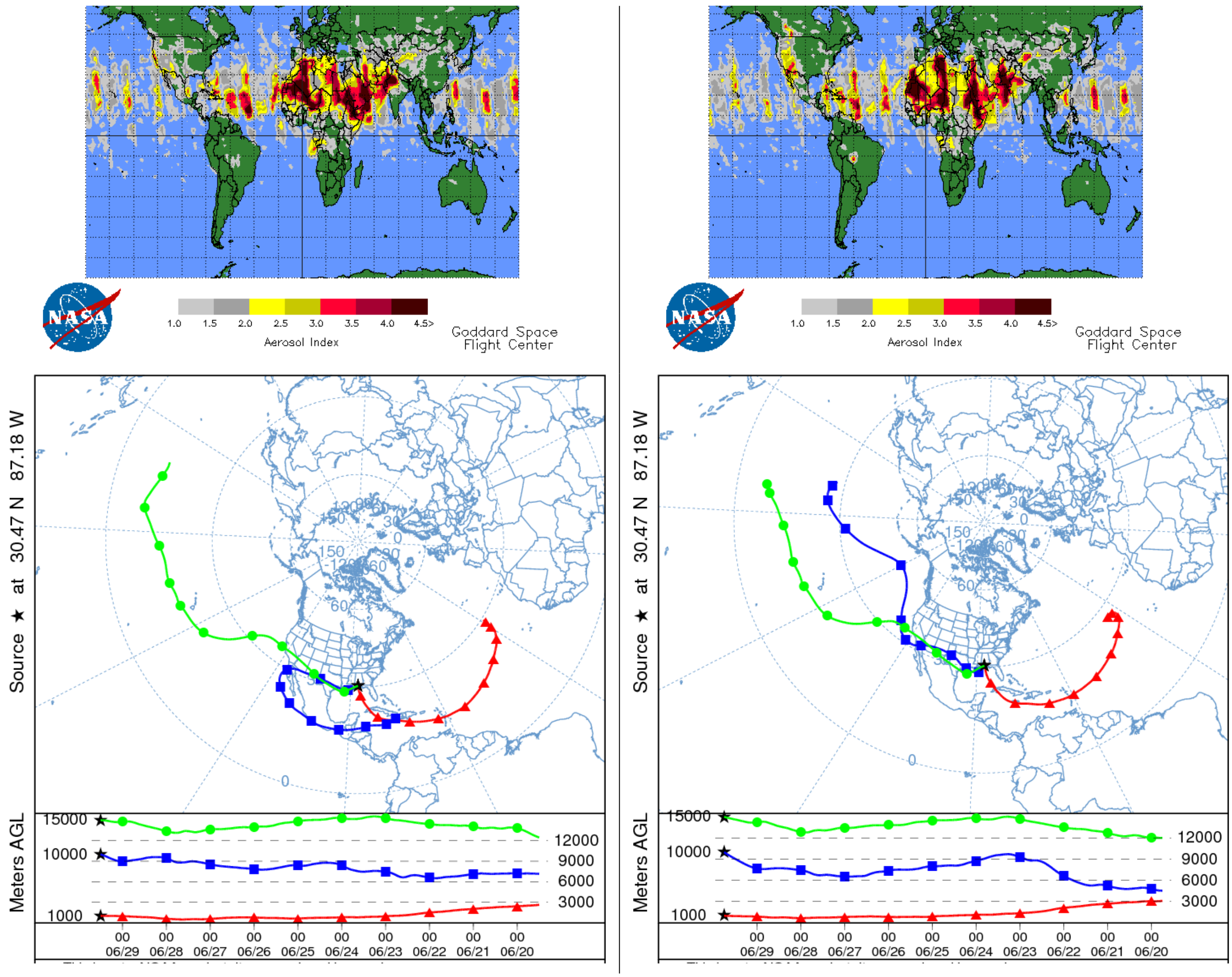

Figure 6.14: (top) Absorbing Index (AI) from TOMS/Earth-Probe for June 29 and June 30, 2003. (bottom) Back-trajectories for 12z June 29, 2003 (left) and 18z June 29, 2003 (right). These images correspond to filter 03-T9329.

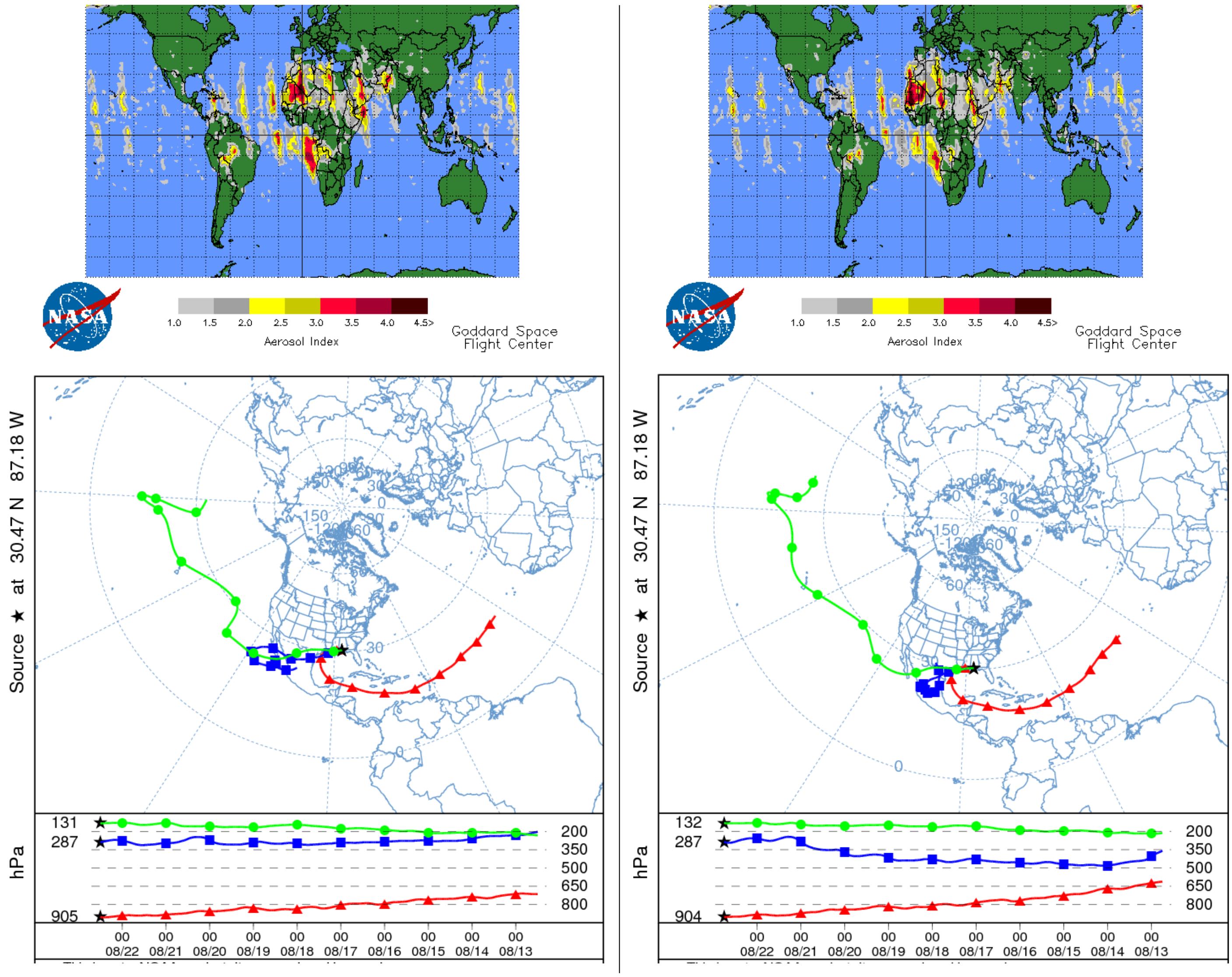

Figure 6.15: (top) Absorbing Index (AI) from TOMS/Earth-Probe for August 22 and August 23, 2004. (bottom) Back-trajectories for 12z August 22, 2004 (left) and 18z August 22, 2004 (right). These images correspond to filter 04-T11260.

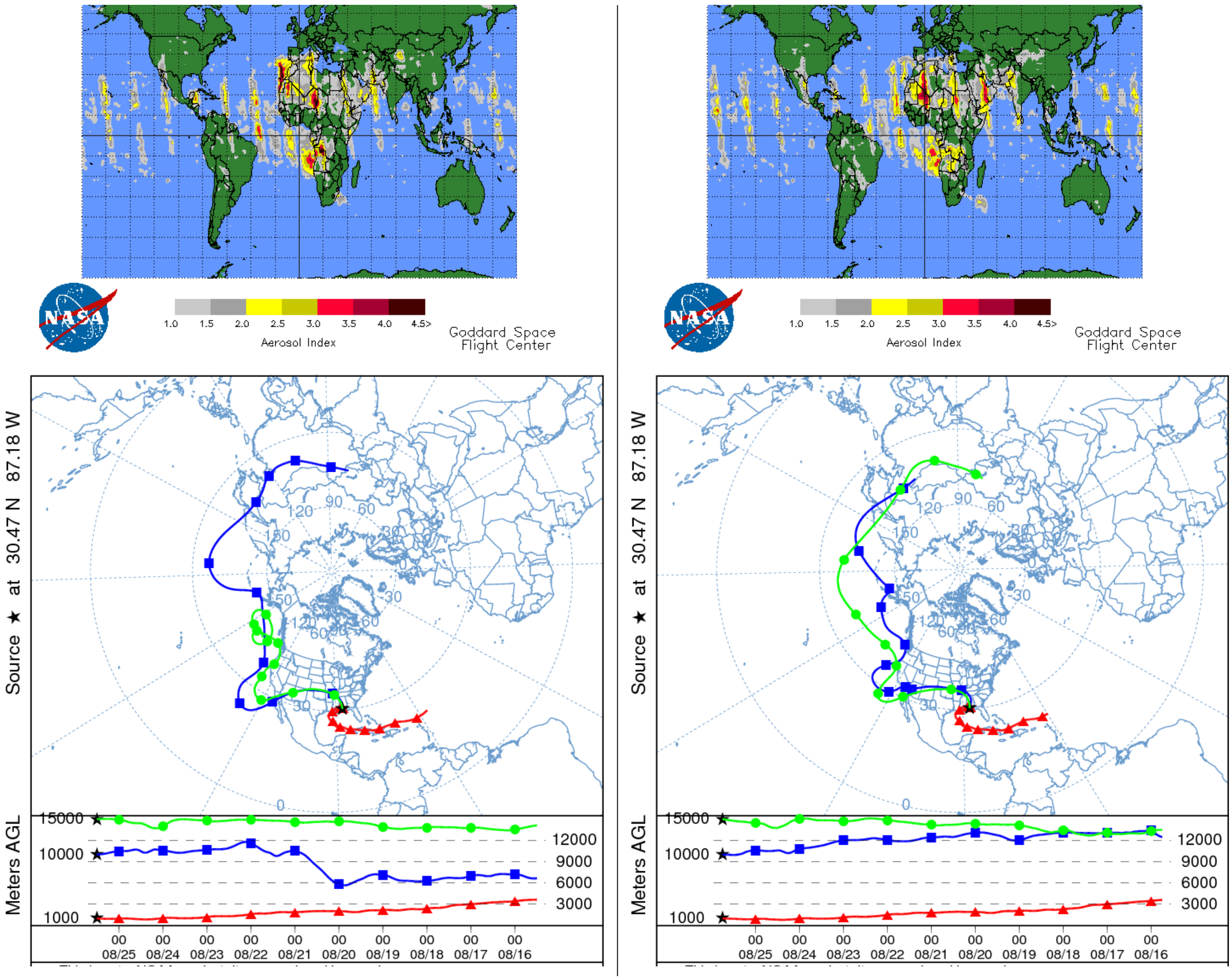

Figure 6.16: (top) Absorbing Index (AI) from TOMS/Earth-Probe for August 25 and August 26, 2004. (bottom) Back-trajectories for 12z August 25, 2004 (left) and 18z August 25, 2004 (right). These images correspond to filter 04-T11261.

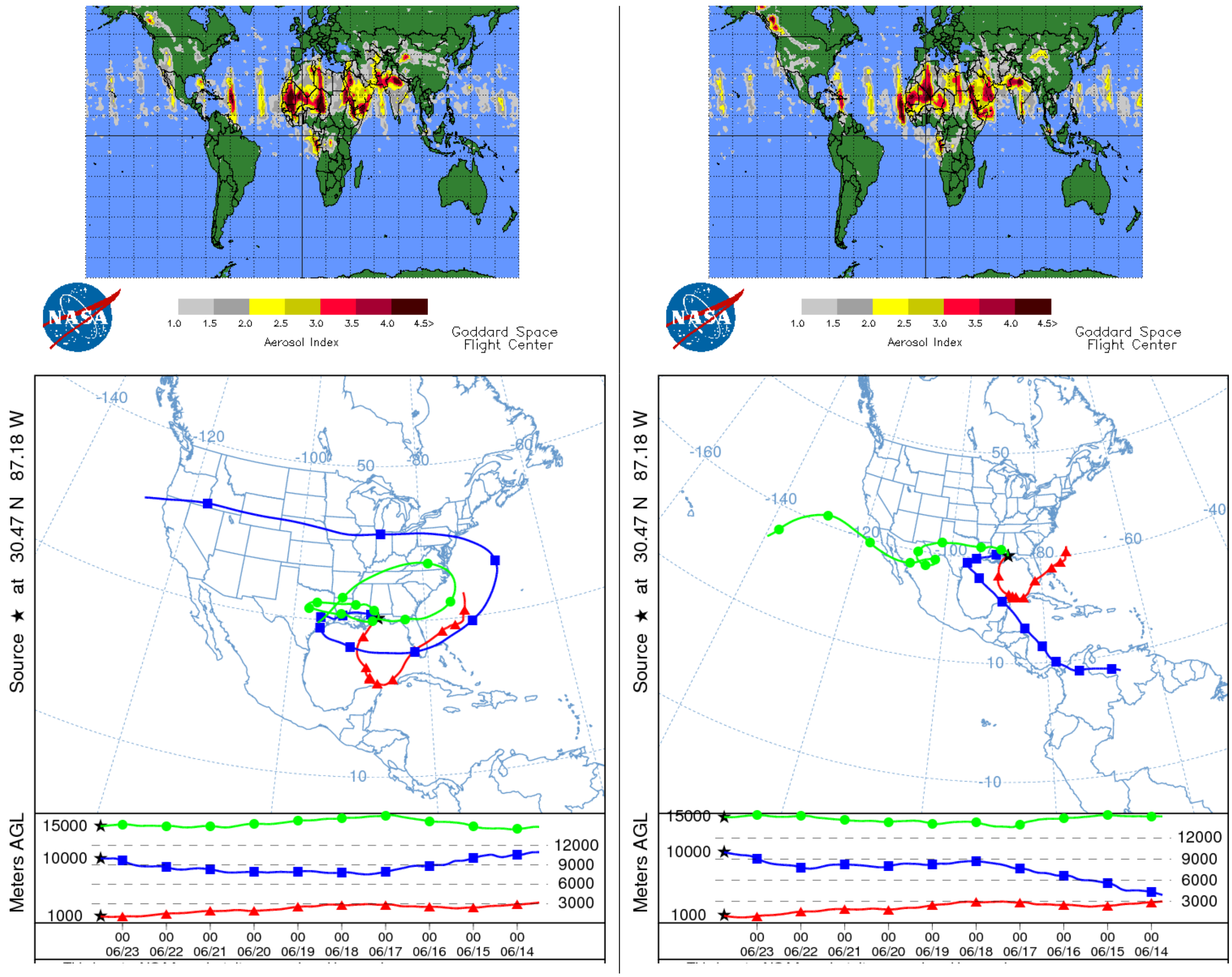

Figure 6.17: (top) Absorbing Index (AI) from TOMS/Earth-Probe for June 23 and Jun 24, 2004. (bottom) Back-trajectories for 12z June 23, 2004 (left) and 18z June 23, 2004 (right). These images correspond to filter 04-T9429.

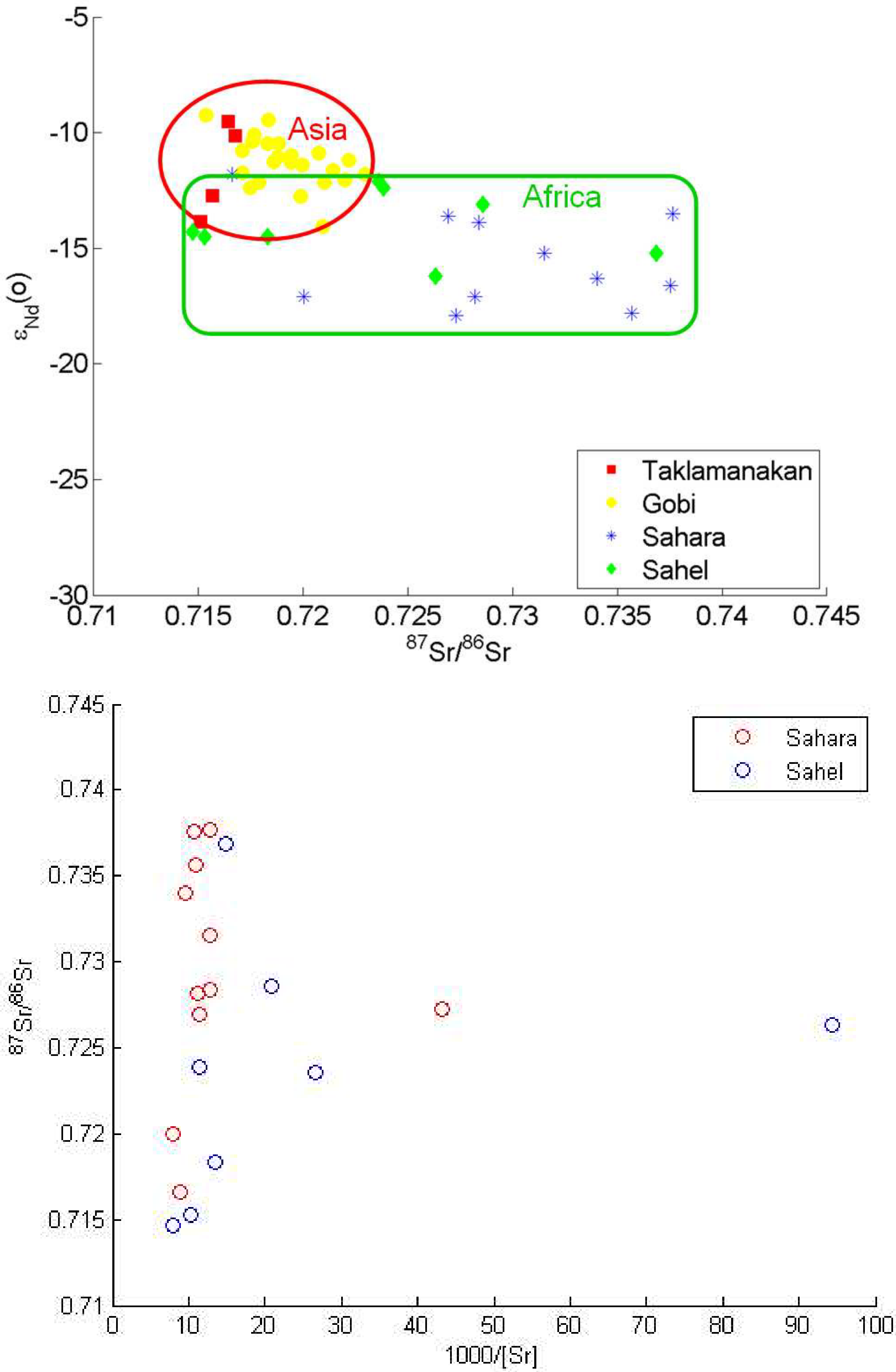

Figure 6.18: Example of separation of continental sources (top) and regional sources (bottom) using isotopic ratios of Nd and Sr after *Grousset and Biscaye* [2005]

North Africa				Asia			
Source area	$\frac{\text{Illite}}{\text{kaolinite}}$ ratio	$\frac{\text{Chlorite}}{\text{kaolinite}}$ ratio	Carbonate (wt%)	Source area	$\frac{\text{Illite}}{\text{kaolinite}}$ ratio	$\frac{\text{Chlorite}}{\text{kaolinite}}$ ratio	Carbonate (wt%)
NAF-1	1.0–2.0 [PA, C2]	1.5 [PA]	10–50 [PA]	EAS-1	12.5–13.9 [S5]	3.3 [S5]	6–35 [W5, LI, W8]
NAF-2	> 1.6 [AV, C2, KA]	0.0–0.8 [GL, AV, KA]	5–70 [AV, KH, KA]	EAS-2	— —	— —	0–10 [W5, S6, LI, W8]
NAF-3	0.3–0.7 [PA, C8]	0.2–0.9 [PA, AL]	0–55 [PA, FA, A5]	EAS-3	7.0–8.0 [S6]	2.0–2.2 [S6]	4–13 [W5, S6, LI, W8]
NAF-4	0.2–1.9 [OH]	0.0–2.6 [OH]	1–25 [OH]	EAS-4	1.1–6.0 [BI, SV]	1.3–3.0 [BI, SV]	0–5 [W5, JE]
NAF-5	0.0–0.4 —	b.d. —	b.d —	EAS-5	5.0–5.6 [S5]	1.4 [S5]	0–10 [W5, LI, JE, W8]
NAF-6	0.7 [C2]	— —	— —	EAS-6	7.5–9.7 [S5]	1.7–2.0 [S5]	< 1 [W5, LI, JE]

Table 6.1: Table of mineralogy by region from [*Formenti et al.*, 2011]. The references are: AL: *Alastuey et al.* [2005], AV: *Avila et al.* [1997], BI: *Biscaye et al.* [1997], C8: *Caquineau et al.* [1998], C2: *Caquineau et al.* [2002], FA: *Falkovich et al.* [2001], GL: *Glaccum and Prospero* [1980], JE: *Jeong* [2008], KA: *Kandler et al.* [2009], KH: *Khiri* [2004], LI: *Li et al.* [2007], OH: *OHara et al.* [2006], PA: *Paquet et al.* [1984], S5: *Shen et al.* [2005], S6: *Shen et al.* [2006], SV: *Svensson et al.* [2000], W5: *Wang et al.* [2005], W8: *Wang et al.* [2008].

North Africa				Asia			
Source	Ca/Al	Fe/Al	K/Al	Source	Ca/Al	Fe/Al	K/Al
NAF-1	—	0.43–0.70 [CS, B2]	—	EAS-1	2.04–4.14 [Z2, MA]	0.87–1.74 [Z2, MA]	0.54–0.94 [Z2, MA]
NAF-2	0.60–0.92 [B1, CI, F3, F8]	0.54–1.24 [B1, B2, CI, F3, F8]	0.1–0.3 [B1, CI, F3, F8]	EAS-2	1.69 —	0.48 —	0.43 —
NAF-3	0.36–0.40 [CI, AL]	0.35–1.69 [B2, CI, AL]	0.22 [CI, AL]	EAS-3	0.94–1.80 [Z1, Z2]	0.65–3.53 [Z1, Z2]	0.26–0.44 [Z1, Z2]
NAF-4	—	0.55–0.65 [GU]	—	EAS-4	0.42 [SU]	0.55 [SU]	—
NAF-5	0.4 [F8]	0.6 [F8]	0.3 [F8]	EAS-5	0.67–2.43 [AF, Z1, Z2, AR, XU, SU]	0.36–1.60 [AF, Z1, Z2, AR, XU, SU]	0.20–1.00 [AF, Z1, Z2, AR, XU, SU]
NAF-6	0.75 [EL]	1.08 [EL]	0.24 [EL]	EAS-6	0.31–0.94 [CG, SH]	0.70–1.07 [CG, SH]	0.36–0.80 [CG, SH]

Table 6.2: Table of elemental ratios by region from *Formenti et al.* [2011]. The references are: AL: *Alastuey et al.* [2005], AF: *Alfaro and Gomes* [2001], AR: *Arimoto et al.* [2006], B1: *Bergametti et al.* [1989a], B2: *Bergametti et al.* [1989b], CG: *Cheng et al.* [2005], CS: *Chester et al.* [1984], CI: *Chiapello et al.* [1997], EL: *Eltayeb et al.* [1993], F3: *Formenti et al.* [2003], F8: *Formenti et al.* [2008], GU: *Guieu et al.* [2002], MA: *Makra et al.* [2002], SH: *Shen et al.* [2007], SU: *Sun et al.* [2005], XU: *Xu et al.* [2004], Z1: *Zhang et al.* [2003], Z2: *Zhang et al.* [2003].

Sample	Sample Mass (g)	Sample Location	Sample Origin
Australia	0.0191	Australia	Australia
Australia Rep	0.01114	Australia	Australia
BCN	0.01554	Europe	N. Africa
GOST	0.01707	Europe	N. Africa
Green	0.01119	Europe	N. Africa
Green Rep	0.01065	Europe	N. Africa
Handan	0.01691	Asia	Asia
Inner Mongolia	0.01198	Asia	Asia
Inner Mongolia Rep	0.01774	Asia	Asia
Nanjing	0.01369	Asia	Asia
POLS1	0.01423	Europe	N. Africa
POLS2	0.01152	Europe	N. Africa
POLS3	0.01598	Europe	N. Africa
RED	0.01259	Europe	N. Africa
Sahara Bulk	0.02128	Africa	N. Africa
03-T10914	-	N. America	Unknown
03-T9329	-	N. America	Unknown
04-T11260	-	N. America	Unknown
04-T11261	-	N. America	Unknown
04-T9429	-	N. America	Unknown

Table 6.3: Table of samples analyzed. Columns are sample names as used in this study, mass of sample used in digestion (g), where the sample was acquired and the assumed source of the sample. Bottom five rows represent filters of unknown provenance.

	Instrument Blank to Pure Dust	Instrument Blank to Filter	Pure Dust Digestion Blank to Pure Dust	Filter Digestion Blank to Filter
Pb	0.00%	0.06%	0.40%	27.28%
U	0.03%	1.81%	0.14%	17.58%
Mg	0.01%	1.03%	0.28%	37.27%
Al	0.00%	0.09%	0.05%	36.65%
Si	11.71%	45.54%	4.44%	9.57%
S	0.42%	1.41%	1.94%	4.94%
Ca	0.01%	1.97%	0.20%	265.56%
Ti	0.02%	0.17%	0.42%	10.92%
V	0.02%	0.17%	2.87%	27.57%
Mn	0.00%	0.03%	6.85%	544.82%
Fe	0.00%	0.01%	9.34%	83.80%
Ni	0.00%	0.00%	93.02%	261.57%
Cu	0.01%	0.08%	9.47%	116.42%
Zn	0.00%	0.01%	71.26%	134.56%
Rb	0.07%	2.32%	0.09%	5.24%
Sr	0.05%	3.66%	0.21%	48.22%
Ba	0.04%	1.50%	0.25%	21.61%
Ce	0.00%	0.18%	0.03%	4.83%
Pr	0.01%	0.36%	0.03%	4.77%
Nd	0.00%	0.29%	0.03%	4.87%
Sm	0.01%	1.10%	0.03%	4.22%
Eu	0.81%	41.69%	0.77%	21.23%
Gd	0.41%	16.18%	0.15%	-3.71%
Dy	0.01%	0.67%	0.03%	4.95%
Ho	0.04%	2.88%	0.03%	4.94%
Er	0.02%	1.15%	0.04%	4.59%
Tm	0.09%	6.29%	-0.01%	1.65%
Yb	0.03%	2.06%	0.04%	9.63%
Lu	0.07%	5.33%	0.03%	9.07%
Th	0.03%	5.65%	0.05%	6.24%

Table 6.4: Table of procedural and analytical blanks by metal. The second and third columns shows the ratio of instrument blanks to median pure dust and filters samples as a percentage respectively. The fourth and fifth columns show the ratio of the digestion blanks to median pure dust and filter samples as a percentage respectively.

Sample Source	Dust ID	Mineral
North Africa	1	no match
	2	no match
	3	no match
	4	no match
	5	no match
(POLS 3)	6	calcite
	7	muscovite
	8	no match
	9	no match
	10	no match
N. Africa	11	kaolenite
	12	no match
	13	no match
(4GOST)	14	no match
	15	dolomite
	16	dolomite
Asia	17	no match
	18	FeTi hydrate
	19	FeO
	20	no match
	21	no match
(Nanjing)	22	biotite
	23	dolomite
	24	Al oxide
	25	Quartz (w/ Fe impurities)
	26	no match
	27	muscovite
	28	aluminosilicate
(Australia)	29	silica
	30	TiO
	31	magnesite
Asia	32	no match
	33	no match
(Inner Mongolia)	34	Aluminosilicate, TiO
	35	dolomite
	36	iron oxide
Asia	37	no match
	38	calcite
(Handon)	39	rutile (TiO)
	40	magnetite

Table 6.5: Table of mineralogy from μ-XRD. Columns are samples, sample number, and mineral as identified by MATCH! software. A value of "no match" indicates a pattern which could not be matched to any known mineral diffraction pattern.

Samples	W_ϕ	W_ϕ'
T9329	18.031	1.55
T10914	18.13	-0.08
T11260	17.56	-1.26
T11261	18.49	-0.33
T9492	17.86	-0.36

Table 6.6: Position of WACZ (W_ϕ) for each sample over the period 7 to 14 days prior. The anomaly (W_ϕ') calculated relative to trend corrected climatological position of WACZ over 20th century.

Chapter 7

Conclusion

7.1 Summary of Key Findings

The reasons for the inter-annual variability of dust transport from the Sahara across the Atlantic were previously not well-understood. This work has provided insight into the mechanisms that govern the interannual variability of mineral dust transport. To obtain these results it was necessary to develop a new climate index that tracks the north and south migration of the ITCZ over West Africa. The utility of this index was demonstrated by applying it in three different ways; (1) to the record of mineral dust load at Barbados, (2) to reanalysis and GCM products of the 20th century and (3) to projections of the 21st century in GCM output. We found a; (1) robust relationship between the latitude of the ITCZ and dustload at Barbados, (2) varying degrees of skill at GCM at recreating the 20th century record as seen in reanalysis and a northward trend in the latitude of the ITCZ in summer and (3) a strong northward trend in all seasons in the 21st century, with implications for a reduction in mineral dust transport. Last (4) using mineralogical and elemental ratios of collected mineral dust samples from multiple continents we constructed a framework for separating continental sources of mineral dust.

In this work we addressed this issue of variability by creating a new climate index that captures the position and intensity of the zone of near-surface convergence over West Africa, a part of the global Intertropical Convergence Zone (ITCZ). We then related this index to a 38-year record of mineral dust concentrations at Barbados first focusing on the winter season. The results showed that the latitudinal displacement of the ITCZ over West Africa and the dust load in Barbados are statistically significantly correlated with a correlation coefficient of $r = -0.69$. A southward movement of the ITCZ corresponds to an increased dust load at Barbados. This correlation represented an improvement upon previous results, which focused on traditional teleconnection indices such as the North Atlantic Oscillation or the El-Niño-Southern Oscillation. From analyzing composites of wind and precipitation we concluded that for the winter season, the inter-annual variability of the Barbados dust load is related to changes in near-surface northeasterly winds in semi-arid regions in North Africa coincident with the movement of the ITCZ. Changes in precipitation appear to only play a minor role.

We next extended the "center of action" indices for the ITCZ over West Africa to the inter-annual variability of dust transport from the Sahara to Barbados in summer. As in the winter case, previous efforts to explain the variability of summer season mineral dust amount focused on teleconnection indices such as ENSO and the NAO. However only weak relationships between such climate indices and the abundance of mineral dust were found. The latitudinal position of the ITCZ is significantly correlated with the quantity of mineral dust at Barbados over the period 1965 to 2003 ($r = -0.47$) in summer. A southward displacement of the ITCZ is associated with both increased near-surface flow and decreased precipitation over the dust emitting regions of the southern Saharan desert, Sahel and Lake Chad. This in turn reduces soil moisture and vegetation furthering the potential for dust emission. In contrast, the intensity of the ITCZ is not correlated with dust concentration at Barbados. Analyzing this "null case," we conclude that the coupling of changes in near-surface winds with changes in precipitation in emission regions driven by a southward movement of the ITCZ most directly influence dust load at Barbados and the

Caribbean during summer.

Having shown that the latitudinal position of the ITCZ over West Africa is important for mineral dust emission and transport in both winter and summer seasons, we next examined how multiple reanalysis products and global climate models from CMIP3 compared in determining in the latitude of the ITCZ over the period 1978 to 2002. Reanalysis products performed similarly to each other in the abstract, but when temporal variability is compared significant differences emerged. Substantial differences in the spatial field of 925 hPa divergence between reanalysis and GCM were identified over North Africa. The ITCZ index was calculated using the output of each model and the each reanalysis product, which allowed for a quantitative comparison. Analysis of ITCZ in both reanalysis and model showed a significant northward trend in the position of the ITCZ over the 20th century in summer.

While reanalysis products were similar in their representation of the ITCZ latitude, our analysis showed that there was a large range in performance of the global climate models in representing this quantity. In particular we found global climate models were unable to accurately quantify the interannual variability of the ITCZ and did not replicate trends observed in reanalysis. Lastly we provided an overview of each models performance and potential suitability for future projections. We identified two models that performed consistently with reanalysis products, and three models which exhibited poor skill at placing the latitude of the ITCZ over West Africa.

Further, we calculated the ITCZ latitude index using CMIP GCM model output from simulations of the 21st century. Two scenarios were considered; SRES-A1B, in which greenhouse gases levels continued to rise steadily in the 21st century, and SRES-B1 in which greenhouse gas emission was moderated. A large southward discontinuity in the divergence field was noted when model results were compared to the 20th century, which was attributable to changes in ocean conditions in GCMs. A strong northward trend of the WACZ was identified for all seasons in both scenarios for the whole of the 21st century. We extrapolated the trend in WACZ to observed variability between W_ϕ and mineral dust at Barbados and predicted reductions of mineral dust between $-1.9\ \mu g\,m^{-3}$ and $-3.8\ \mu g\,m^{-3}$ in summer and $-1.5\ \mu g\,m^{-3}$ and $-2.2\ \mu g\,m^{-3}$ in winter. Model performance in the 20th century was not related to the trend predicted in the 21st century.

Last, we attempted to verify our hypothesis by applying geochemical techniques to mineral dust samples. Mineral dust samples from Africa, Asia, Europe and Australia were acquired and analyzed for their mineralogy and elemental composition. Filter samples of unknown provenience collected in Florida were similarly analyzed. To differentiate source regions principal component analysis was applied to elemental composition. The results showed that African, Asian and Australian dust can be separated in this manner. Principal components were shown to correspond to three mineral groupings; carbonate, aluminosilicates and iron/titanium oxides. Filter samples from Florida were shown to be dissimilar to the pure African, Asian and Australian signals, possibly because high blanks obscured the dust source signal.

7.2 Implications of Research

Our key finding that the latitude of the WACZ controls a large fraction of the variability of mineral dust transport to Barbados in both winter and summer represents a new paradigm for explaining seasonal dust transport. It also represents a major improvement on prior results utilizing other teleconnection indices such as the NAO and ENSO. This finding confirms other previous studies; for example the improvement over ENSO is consistent with *Mahowald et al.* [2003] who did not find correlations in West Africa between dust and ENSO. Our results indirectly confirm the findings of *Engelstaedter and Washington* [2007] who found a spatial correlation over North Africa between 10 m-divergence and satellite estimates of dustload. Our results directly confirm the hypothesis of *Schwanghart and Schütt* [2008] who argued that northward movement of the ITCZ could diminish NE winds over the Sahara and Sahel.

While this work focuses on the role of the WACZ in explaining mineral dust transport, such an index has been applied by *Taylor et al.* [2012] to biogeochemical and primary productivity data in the Cariaco Basin and find meaningful relationships. This index likely can be applied to many other environmental datasets in North Africa and surrounding regions.

In the summer during the 20th century a clear northward trend of the WACZ was observed in reanalysis and GCM output; this northward trend continued in the 21st century, extending to both summer and winter over this period. This finding agrees with basic theory surrounding the Hadley Cell, which posits a poleward expansion of the Hadley Cell in a warming climate [*Polvani and Kushner*, 2002; *Hu and Fu*, 2007]. Here our work focuses on the ascending branch of the Hadley Cell over West Africa. Our finding of poleward expansion of the ascending branch compliments the work of *Gastineau et al.* [2008] who found evident for equatorward and poleward contraction/expansion of the ascending branch of the Hadley Cell in climate models.

As northward migration of the WACZ leads to reduced dust transport, and the WACZ is expected to drift northward as the climate warms in the 21st century, then mineral dust transport should be expected to diminish in the warming climate. Paleoclimatologists have long argued for the paradigm that cold, glacial periods are dusty and warm, interglacial periods are less dusty. Here our new paradigm is a direct mechanism for which this argument can be explained on a regional scale, with a proven physical mechanism.

Utilizing the mineralogy and elemental composition of dust samples procured from source regions, a framework has been developed to separate continental sources. This result supports the supposition made in *Formenti et al.* [2011] that mineralogy on regional and continental scales can be useful in identifying dust sources. *Trapp et al.* [2010] found unchanging elemental ratios of major metals in Barbados and Miami dust samples, our results suggest that this implies a single continental source for this dust. The framework of continental source separation has practical applications; this analysis will be repeated and applied real time to suspected mineral dust outbreaks across the Southeastern United States moving forward.

7.3 Future Work

This work has opened up new opportunities for further research in the following areas:

7.3.1 Timescale

Mineral dust is directly emitted to the atmosphere via turbulent wind gusts, which occur on the timescale of seconds to minutes. Emitted dust is lofted above the boundary layer over the course of hours. A particularly dusty air layer can form a Saharan Air Layer over the course of days. A dust layer can be transported across the Atlantic Ocean from Africa over the course of 1 to 2 weeks. Each of these processes responsible for the emission, persistence and transport of mineral dust occurs on timescales shorter than the seasonal timescale that is the focus of this work. A natural extension of this work would be to examine how the location of the WACZ is related to physical drivers associated with short timescales such as gustiness and stability. One potential mechanism would be to examine if the WACZ is in some way related to African Easterly Waves, which represent a potential mechanism by which to relate short term variability to seasonal scale variability.

7.3.2 Assessment of more recent CMIP model results

The global climate models analyzed in this work are products of the Climate Model Intercomparison Project 3 (CMIP3). At the time this work was initiated CMIP3 represented the best choice for analysis. In the interim CMIP5 has been released. CMIP5 utilizes, in general, higher resolution models (in both space and time) as well as an improvement on model physics. CMIP5 may include some dust-climate feedbacks which could be of importance in setting the position of the WACZ. Before this work can be prepared for publication, it should be repeated with CMIP5 model products.

7.3.3 Mechanism for control of WACZ in Climate Models

We have found both a large southward shift in the WACZ in 21st century model runs and large biases relative to reanalysis in many 20th century model runs. This work could be extended to the mechanisms by which these shifts and biases occur and begin to investigate how changes in model SST impact the WACZ and how cross-equatorial pressure gradients impact the WACZ.

7.3.4 Geochemistry Analysis

From the beginning it was expected that the geochemistry section of this work would be an analytical challenge, accounting for the small quantities of mineral dust expected to be found on the filters of unknown provenance. Below are four suggestions for improving such a study in the future.

North American Samples

Filter samples, in general, did not fall within the envelope of elemental composition as seen in Asian, African or Australian mineral dust samples. While this result could be due to method or analysis errors, it could also be indicative of a local source of mineral dust not captured by our source region. Future analysis should include mineral dust samples both from North American desert sources and local soil sources.

Comparing Different Digestions

Elemental composition as measured by ICP-MS is no doubt strongly influenced by the acids and digestion methods selected. A comprehensive study should include a sensitivity analysis to digestion method. Filters should be prepared with a known quantity of mineral dust applied to the surface. In this way recovery the digestion method could be quantified.

Isotopic Analysis

This work is substantially weakened by the absence of an isotopic analysis. Samples are prepared and waiting for chemical separation of Pb, Sr and Nd. Once separation is performed and a suitable instrument is found, such information will be invaluable in overcoming blank issues associated with the elemental analysis. In addition to traditional geochemical mixing curve analysis isotope data can be included as a predictor in the principle component analysis. It is anticipated that this work will be performed prior to publication of this work.

Blank Reduction

Filters were taken to the National Synchrotron Light Source at Brookhaven National Lab for micro x-ray diffraction and florescence studies. These methods were chosen as they are non-destructive, the filters could subsequently be digested an analyzed for elemental composition. However in this process, the filters were exposed in a non-clean environment, and contamination could possibly have been introduced. This could represent a major source of trace metals, and in turn register erroneous elemental composition. In future work two filters should be taken side by side, one preserved in a clean environment for digestion and the other taken for diffraction studies. Alternatively captured filters could be physically split for different analyses.

Bibliography

Adler, R. F., G. J. Huffman, A. Chang, R. Ferraro, P.-P. Xie, J. Janowiak, B. Rudolf, U. Schneider, S. Curtis, D. Bolvin, A. Gruber, J. Susskind, P. Arkin, and E. Nelkin (2003), The Version-2 Global Precipitation Climatology Project (GPCP) Monthly Precipitation Analysis (1979 Present), *J. Hydrometeor.*, *4*, 1147.

Alastuey, A., X. Querol, S. Castillo, M. Escudero, A. Avila, E. Cuevas, C. Torres, P.-M. Romero, F. Exposito, O. Garca, J. P. Diaz, R. V. Dingenen, and J. P. Putaud (2005), Characterisation of TSP and PM2.5 at Izaa and Sta. Cruz de Tenerife (Canary Islands, Spain) during a Saharan Dust Episode (July 2002), *Atmospheric Environment*, *39*(26), 4715 – 4728, doi:10.1016/j.atmosenv.2005.04.018.

Albrecht, B. A. (1989), Aerosols, Cloud Microphysics, and Fractional Cloudiness, *Science, Volume 245, Issue 4923, pp. 1227-1230*, *245*, 1227–1230, doi:10.1126/science.245.4923.1227.

Alfaro, S. C., and L. Gomes (2001), Modeling mineral aerosol production by wind erosion: Emission intensities and aerosol size distributions in source areas, *J. Geophs. Res.*, *106*, 18,075–18,084, doi:10.1029/2000JD900339.

Andreae, M. (1996), Raising dust in the greenhouse, *Nature*, *380*, 389 – 390.

Angell, J., and J. Korshover (1982), Comparison of year-average latitude, longitude and pressure of the four centers of action with air and sea temperature, 1899–1978, *Monthly Weather Rev.*, *110*, 300–303.

Angell, J., and T. Korshover (1974), Quasi-Biennial and Long-Term Fluctuations in the Centers of Action, *Mont. Weather Rev.*, *102*, 669–678.

Arimoto, R. (2001), Eolian dust and climate: relationships to sources, tropospheric chemistry, transport and deposition, *Earth-Sci. Rev.*, *54*, 29–42.

Arimoto, R., Y. J. Kim, Y. P. Kim, P. K. Quinn, T. S. Bates, T. L. Anderson, S. Gong, I. Uno, M. Chin, B. J. Huebert, A. D. Clarke, Y. Shinozuka, R. J. Weber, J. R. Anderson, S. A. Guazzotti, R. C. Sullivan, D. A. Sodeman, K. A. Prather, and I. N. Sokolik (2006), Characterization of Asian Dust during ACE-Asia, *Global and Planetary Change*, *52*, 23–56, doi:10.1016/j.gloplacha.2006.02.013.

Avila, A., I. Queralt-Mitjans, and M. Alarcón (1997), Mineralogical composition of African dust delivered by red rains over northeastern Spain, *J. Geophs. Res.*, *102*, 21,977–21,996, doi:10.1029/97JD00485.

Bakalian, F., S. Hameed, and R. Pickart (2007), Influence of the Icelandic Low latitude on the frequency of Greenland tip jet events: Implications for Irminger Sea convection, *Journal of Geophysical Research (Oceans)*, *112*(C11), C04020, doi:10.1029/2006JC003807.

Baker, A., T. Jickells, M. Witt, and K. Linge (2006), Trends in the solubility of iron, aluminium, manganese and phosphorus in aerosol collected over the Atlantic Ocean, *Mar. Chem.*, *98*(1), 43 – 58, doi:10.1016/j.marchem.2005.06.004.

Bauer, S., Y. Balkanski, M. Schulz, D. Hauglustaine, and F. Dentener (2004), Global modeling of heterogeneous chemistry on mineral aerosol surfaces: Influence on tropospheric ozone chemistry and comparison to observations, *J. Geophys. Res.*, *109*, D02,304, doi:10.1029/2003JD003868.

Ben-Ami, Y., I. Koren, and O. Altaratz (2009), Patterns of North African dust transport over the Atlantic: winter vs. summer, based on CALIPSO first year data, *Atmos. Chem. Phys.*, *9*, 7867–7875, doi:{10.5194/acp-9-7867-2009}.

Ben-Ami, Y., I. Koren, O. Altaratz, A. B. Kostinski, and Y. Lehahn (2011), Discernible rhythm in the spatio/temporal distributions of transatlantic dust, *Atmospheric Chemistry & Physics Discussions*, *11*, 23,513–23,539, doi:10.5194/acpd-11-23513-2011.

Bergametti, G., L. Gomes, G. Coude-Gaussen, P. Rognon, and M.-N. Le Coustumer (1989a), African dust observed over Canary Islands: source-regions identification and transport pattern for some summer situations, *J. Geophs. Res.*, *94*, 14,855–14,864, doi:10.1029/JD094iD12p14855.

Bergametti, G., A.-L. Dutot, P. Buat-Ménard, R. Losno, and E. Remoudaki (1989b), Seasonal variability of the elemental composition of atmospheric aerosol particles over the northwestern Mediterranean, *Tellus Series B Chemical and Physical Meteorology B*, *41*, 353–361, doi:10.1111/j.1600-0889.1989.tb00314.x.

Bian, H., and C. Zender (2003), Mineral dust and global tropospheric chemistry: Relative roles of photolysis and heterogeneous uptake, *J. Geophys. Res.*, *108*, 4672, doi:10.1029/2002JD003143.

Biscaye, P. E., F. E. Grousset, M. Revel, S. Van der Gaast, G. A. Zielinski, A. Vaars, and G. Kukla (1997), Asian provenance of glacial dust (stage 2) in the Greenland Ice Sheet Project 2 Ice Core, Summit, Greenland, *J. Geophs. Res.*, *102*, 26,765–26,782, doi:10.1029/97JC01249.

Borg, L., and J. Banner (1996), Neodymium and strontium isotopic constraints on soil sources in barbados, west indies, *Geochimica et Cosmochimica Acta*, *60*(21), 4193–4206.

Braun, S. A. (2010), Reevaluating the Role of the Saharan Air Layer in Atlantic Tropical Cyclogenesis and Evolution, *Monthly Weather Review*, *138*, 2007–2037, doi:10.1175/2009MWR3135.1.

Bristow, C., K. Hudson-Edwards, and A. Chappell (2010), Fertilizing the Amazon and equatorial Atlantic with West African dust, *Geophysical Research Letters*, *37*(14), L14,807.

Camberlin, P., S. Janicot, and I. Poccard (2001), Seasonality and atmospheric dynamics of the teleconnection between African rainfall and tropical sea-surface temperature: Atlantic vs. ENSO, *International Journal of Climatology*, *21*(8), 973–1005.

Caquineau, S., A. Gaudichet, L. Gomes, M. Magonthier, and B. Chatenet (1998), Saharan dust: Clay ratio as a relevant tracer to assess the origin of soil-derived aerosols, *Geophysical research letters*, *25*(7), 983–986.

Caquineau, S., A. Gaudichet, L. Gomes, and M. Legrand (2002), Mineralogy of Saharan dust transported over northwestern tropical Atlantic Ocean in relation to source regions, *Journal of Geophysical Research (Atmospheres)*, *107*, 4251, doi:10.1029/2000JD000247.

Carlson, T. (1979), Atmospheric turbidity in Saharan dust outbreaks as determined by analyses of satellite brightness data, *Monthly Weather Rev.*, *107*, 322–335.

Carlson, T., and J. Prospero (1972), The large-scale movement of Saharan air outbreaks over the northern equatorial Atlantic, *J. Applied Met.*, *11*, 283–297.

Chen, J., B. E. Carlson, and A. D. Del Genio (2002), Evidence for Strengthening of the Tropical General Circulation in the 1990s, *Science*, *295*, 838–841, doi:10.1126/science.1065835.

Cheng, T., D. Lu, G. Wang, and Y. Xu (2005), Chemical characteristics of asian dust aerosol from Hunshan Dake Sandland in northern China, *Atmospheric Environment*, *39*(16), 2903–2911.

Chester, R., E. Sharples, G. Sanders, and A. Saydam (1984), Saharan dust incursion over the Tyrrhenian Sea, *Atmospheric Environment*, *18*(5), 929 – 935, doi:10.1016/0004-6981(84)90069-6.

Chiapello, I., and C. Moulin (2002), TOMS and METEOSAT satellite records of the variability of Saharan dust transport over the Atlantic during the last two decades, *Geophys. Res. Letters*, *29*(8), 1176, doi:10.1029/2001GL013767.

Chiapello, I., G. Bergamietti, L. Gomes, B. Chatenet, F. Dulac, J. Pimenta, and E. Suares (1995), An additional low layer transport of Sahelian and Saharan dust over the north-eastern tropical Atlantic, *Geophys. Res. Letters*, *22*, 3191–3194.

Chiapello, I., G. Bergametti, B. Chatenet, P. Bousquet, F. Dulac, and E. S. Soares (1997), Origins of African dust transported over the northeastern tropical Atlantic, *J. Geophs. Res.*, *102*, 13,701–13,710, doi:10.1029/97JD00259.

Chiapello, I., J. Prospero, J. Herman, and N. Hsu (1999), Detection of mineral dust over the North Atlantic Ocean and Africa; with the Nimbus 7 TOMS, *J. Geophys. Res.*, *104*, 9277–9291.

Chiapello, I., C. Moulin, and J. M. Prospero (2005), Understanding the long-term variability of African dust transport across the Atlantic as recorded in both Barbados surface concentrations and large-scale Total Ozone Mapping Spectrometer (TOMS) optical thickness, *J. Geophys. Res-Atmos.*, *110*(D9), D18S10, doi:10.1029/2004JD005132.

Christoforou, P., and S. Hameed (1997), Solar cycle and the Pacific ‘Centers of Action’, *Geophys. Res. Lett.*, *24*, 293–296, doi:10.1029/97GL00017.

Cole, J., S. Goldstein, P. Demenocal, S. Hemming, and F. Grousset (2009), Contrasting compositions of saharan dust in the eastern atlantic ocean during the last deglaciation and african humid period, *Earth and Planetary Science Letters*, *278*(3), 257–266.

Collins, W., C. Bitz, M. Blackmon, G. Bonan, C. Bretherton, J. Carton, P. Chang, S. Doney, J. Hack, T. Henderson, et al. (2006), The community climate system model version 3 (ccsm3), *Journal of Climate*, *19*(11), 2122–2143.

Croke, M. S., R. D. Cess, and S. Hameed (1999), Regional Cloud Cover Change Associated with Global Climate Change: Case Studies for Three Regions of the United States., *Journal of Climate*, *12*, 2128–2134, doi:10.1175/1520-0442(1999)012⟨2128:RCCCAW⟩2.0.CO;2.

Dai, A., K. E. Trenberth, and T. Qian (2004), A Global Dataset of Palmer Drought Severity Index for 1870 2002: Relationship with Soil Moisture and Effects of Surface Warming, *Journal of Hydrometeorology*, *5*, 1117, doi:10.1175/JHM-386.1.

Darwin, C. (1846), An account of this fine dust which often falls on vessels in the Atlantic Ocean, *Geol. Soc. London Q. J.*, *2*, 26–30.

Dee, D. (2012), The climate data guide: Era-interim, *Tech. rep.*, Retrieved from https://climatedataguide.ucar.edu/reanalysis/era-interim.

Dee, D., S. Uppala, A. Simmons, P. Berrisford, P. Poli, S. Kobayashi, U. Andrae, M. Balmaseda, G. Balsamo, P. Bauer, et al. (2011), The era-interim reanalysis: Configuration and performance of the data assimilation system, *Quarterly Journal of the Royal Meteorological Society*, *137*(656), 553–597.

DeMott, P. J., K. Sassen, M. R. Poellot, D. Baumgardner, D. C. Rogers, S. D. Brooks, A. J. Prenni, and S. M. Kreidenweis (2003), African dust aerosols as atmospheric ice nuclei, *Geophys. Res. Lett.*, *30*(14), 1732, doi:10.1029/2003GL017410.

Dentener, F., G. Carmichael, Y. Zhang, J. Lelieveld, and P. Crutzen (1996), Role of mineral aerosol as a reactive surface in the global troposphere, *J. Geophys. Res.*, *101*, 22,869–22,889.

Dickerson, R., S. Kondragunat, G. Stenchikov, K. Civerolo, B. Doddridge, and B. Holben (1997), The impact of aerosols on solar ultraviolet radiation and photochemical smog, *Science*, *278*, 827–830.

Diedhiou, A., S. Janicot, A. Viltard, P. De Felice, and H. Laurent (1999), Easterly wave regimes and associated convection over West Africa and tropical Atlantic: results from the NCEP/NCAR and ECMWF reanalyses, *Climate Dynamics*, *15*(11), 795–822.

Doherty, O., N. Riemer, and S. Hameed (2008), Saharan mineral dust transport into the Caribbean: Observed atmospheric controls and trends, *Journal of Geophysical Research (Atmospheres)*, *113*(D12), D07,211, doi:10.1029/2007JD009171.

Doherty, O., N. Riemer, and S. Hameed (2012a), Control of Saharan mineral dust transport to Barbados in winter by the Intertropical Convergence Zone over West Africa, *Journal of Geophysical Research*, *117*(D19), D19,117.

Doherty, O., N. Riemer, and S. Hameed (2012b), Role of the Intertropical Convergence Zone over West Africa in controlling Saharan mineral dust transport to the Caribbean in the dusty season, *In Prep for: Journal of Geophysical Research*.

Dunion, J., and C. Velden (2004), The impact of the Saharan air layer on Atlantic tropical cyclone activity, *Bull. Amer. Meteor. Soc.*, *85*, 353–365.

Eklundh, L., and L. Olsson (2003), Vegetation index trends for the African Sahel 1982-1999, *Geophys. Res. Lett.*, *30*(8), 1430, doi:10.1029/2002GL016772.

Eltayeb, M. A., C. F. Xhoffer, P. J. V. Espen, R. V. Grieken, and W. Maenhaut (1993), Sources and composition of aerosol from Khartoum, Sudan, *Atmospheric Environment. Part B. Urban Atmosphere*, *27*(1), 67 – 76, doi:10.1016/0957-1272(93)90046-9.

Engelstaedter, S., and R. Washington (2007), Atmospheric controls on the annual cycle of North African dust, *Journal of Geophysical Research (Atmospheres)*, *112*(D11), D03103, doi:10.1029/2006JD007195.

Evan, A. T., J. Dunion, J. A. Foley, A. K. Heidinger, and C. S. Velden (2006), New evidence for a relationship between Atlantic tropical cyclone activity and African dust outbreaks, *Geophys. Res. Lett.*, *33*(19), L19,813, doi:10.1029/2006GL026408.

Evan, A. T., A. K. Heidinger, and P. Knippertz (2006a), Analysis of winter dust activity off the coast of West Africa using a new 24-year over-water advanced very high resolution radiometer satellite dust climatology, *J. Geophys. R.*, *111*(D10), doi:10.1029/2005JD006336.

Evan, A. T., A. K. Heidinger, and P. Knippertz (2006b), Analysis of winter dust activity off the coast of West Africa using a new 24-year over-water advanced very high resolution radiometer satellite dust climatology, *Journal of Geophysical Research (Atmospheres)*, *111*(D10), D12210, doi:10.1029/2005JD006336.

Falkovich, A. H., E. Ganor, Z. Levin, P. Formenti, and Y. Rudich (2001), Chemical and mineralogical analysis of individual mineral dust particles, *J. Geophs. Res.*, *106*, 18,029–18,036, doi:10.1029/2000JD900430.

Folland, C., J. Owen, M. Ward, and A. Coleman (1991), Prediction of seasonal rainfall in the Sahel region using empirical and dynamical methods, *Journal of Forecasting*, *10*(1-2), 21–56.

Folland, C. K., T. N. Palmer, and D. E. Parker (1986), Sahel rainfall and worldwide sea temperatures, 1901-85, *Nature*, *320*, 602–607, doi:10.1038/320602a0.

Formenti, P., W. Elbert, W. Maenhaut, J. Haywood, and M. O. Andreae (2003), Chemical composition of mineral dust aerosol during the Saharan Dust Experiment (SHADE) airborne campaign in the Cape Verde region, September 2000, *Journal of Geophysical Research (Atmospheres)*, *108*, 8576, doi:10.1029/2002JD002648.

Formenti, P., J. L. Rajot, K. Desboeufs, S. Caquineau, S. Chevaillier, S. Nava, A. Gaudichet, E. Journet, S. Triquet, S. Alfaro, M. Chiari, J. Haywood, H. Coe, and E. Highwood (2008), Regional variability of the composition of mineral dust from western Africa: Results from the AMMA SOP0/DABEX and DODO field campaigns, *Journal of Geophysical Research (Atmospheres)*, *113*, D00C13, doi:10.1029/2008JD009903.

Formenti, P., L. Schütz, Y. Balkanski, K. Desboeufs, M. Ebert, K. Kandler, A. Petzold, D. Scheuvens, S. Weinbruch, and D. Zhang (2011), Recent progress in understanding physical and chemical properties of African and Asian mineral dust, *Atmos. Chem. Phys*, *11*(16), 8231–8256.

Frierson, D. M., J. Lu W., and G. Chen (2007), Width of the Hadley cell in simple and comprehensive general circulation models, *Geophys. Res. Lett.*, *34*, doi:doi:10.1029/2007GL031115.

Fu, Q., C. M. Johanson, J. M. Wallace, and T. Reichler (2006), Enhanced mid-latitude tropospheric warming in satellite measurements, *Science*, *312*(5777), 1179, doi:10.1126/science.1125566.

Fung, I., S. Meyn, I. Tegen, S. Doney, J. John, and J. Bishop (2000), Iron supply and demand in the upper ocean, *Global Biogeochem. Cycles*, *14*, 281–296.

Gastineau, G., H. Le Treut, and L. Li (2008), Hadley circulation changes under global warming conditions indicated by coupled climate models, *Tellus Series A*, *60*, 863–884, doi:10.1111/j.1600-0870.2008.00344.x.

Gates, W. (1992), Amip: The atmospheric model intercomparison project. program for climate model diagnosis and intercomparison: Revision 1, *Tech. rep.*, Lawrence Livermore National Lab. CA (United States).

Giannini, A., R. Saravanan, and P. Chang (2003), Oceanic Forcing of Sahel Rainfall on Interannual to Interdecadal Time Scales, *Science*, *302*, 1027–1030, doi:10.1126/science.1089357.

Ginoux, P., J.M., O. Torres, and M. Chin (2004), Long-term simulation of global dust distribution with the GOCART model: Correlation with North Atlantic Oscillation, *Environmental Modelling and Software*, *19*, 113–128.

Glaccum, R. A., and J. M. Prospero (1980), Saharan aerosols over the tropical North Atlantic Mineralogy, *Mar. Geol.*, *37*(3-4), 295 – 321, doi:10.1016/0025-3227(80)90107-3.

Grassian, V. (2002), Chemical reactions of nitrogen oxides on the surface of oxide, carbonate, soot, and mineral dust particles: Implications for the chemical balance of the troposphere, *The Journal of Physical Chemistry A*, *106*(6), 860–877.

Grousset, F., and P. Biscaye (2005), Tracing dust sources and transport patterns using Sr, Nd and Pb isotopes, *Chem. Geol.*, *222*, 149–167.

Guieu, C., Y. Bozec, S. Blain, C. Ridame, G. Sarthou, and N. Leblond (2002), Impact of high saharan dust inputs on dissolved iron concentrations in the mediterranean sea, *Geophysical Research Letters*, *29*(19), 1911.

Hameed, S., and S. Piontkovski (2004), The dominant influence of the Icelandic Low on the position of the Gulf Stream northwall, *Geophys. Res. Letters*, *31*, L0903, doi:10.029/2004GL019561.

Hameed, S., M. J. Iqbal, Saqib-ur-Rehman, and D. Collins (2011), Impact of the Indian Ocean high pressure system on winter precipitation over western and southwestern Australia, *Australian Meteorological and Oceanographic Journal*, *61*(3), 159–170.

Hartley, W., and H. Ramage (1901), The Mineral Constituents of Dust and Soot from various Sources, *The Mineral*, pp. 97–108.

Herman, J., P. Bhartia, O. Torres, B. Holben, D. Tanre, T. Eck, A. Smirnov, B. Chatenet, and F. Lavenu (1997), Comparison of the TOMS aerosol index with sun-photometer aerosol optical thickness: Results and applications, *J. Geophys. Res.*, *102*, 16,911–16,922.

Herrmann, S. M., A. Anyamba, and C. J. Tucker (2005), Recent trends in vegetation dynamics in the African Sahel and their relationship to climate, *Global Environmental Change*, *15*(4), 394 – 404, doi:10.1016/j.gloenvcha.2005.08.004.

Herwitz, S., D. Muhs, J. Prospero, S. Mahan, and B. Vaughn (1996), Origin of Bermuda's clay-rich Quaternary paleosols and their paleoclimatic significance, *J. Geophys. Res*, *101*, 23,389–23,400.

Hoerling, M., J. Hurrell, J. Eischeid, and A. Phillips (2006), Detection and Attribution of Twentieth-Century Northern and Southern African Rainfall Change, *Journal of Climate*, *19*, 3989–4008, doi:10.1175/JCLI3842.1.

Holton, J., and D. Staley (1996), An introduction to dynamic meteorology, *American Journal of Physics*, *41*, 752.

Hsieh, J., and K. Cook (2005), Generation of African easterly wave disturbances: Relationship to the African easterly jet, *Monthly weather review*, *133*(5), 1311–1327.

Hu, Y., and Q. Fu (2007), Observed poleward expansion of the Hadley circulation since 1979, *Atmospheric Chemistry & Physics Discussions*, *7*, 9367–9384.

Huang, J., C. Zhang, and J. M. Prospero (2009), Aerosol-Induced Large-Scale Variability in Precipitation over the Tropical Atlantic, *Journal of Climate*, *22*, 4970–4988, doi:10.1175/2009JCLI2531.1.

Hurrell, J. (1995), Decadal trend in the North Atlantic Oscillation: Regional temperatures and precipitation, *Science*, *269*, 676–679.

Jenkins, G., A. Gaye, and B. Sylla (2005), Late 20th century attribution of drying trends in the Sahel from the Regional Climate Model (RegCM3), *Geophysical Research Letters*, *32*(22), L22,705.

Jeong, G. Y. (2008), Bulk and single-particle mineralogy of Asian dust and a comparison with its source soils, *Journal of Geophysical Research (Atmospheres)*, *113*(D12), D02208, doi:10.1029/2007JD008606.

Jickells, T. (1999), The inputs of dust derived elements to the Sargasso sea; a synthesis, *Marine Chem.*, *68*, 5–14.

Johanson, C. M., and Q. Fu (2009), Hadley Cell Widening: Model Simulations versus Observations, *Journal of Climate*, *22*, 2713, doi:10.1175/2008JCLI2620.1.

Jones, C., N. Mahowald, and C. Luo (2003), The Role of Easterly Waves on African Desert Dust Transport., *Journal of Climate*, *16*, 3617–3628.

Jordi, A., and S. Hameed (2009), Influence of the Icelandic Low on the Variability of Surface Air Temperature in the Gulf of Lion: Implications for Intermediate Water Formation, *J. Phys. Oceanogr.*, *39*, 3228, doi:10.1175/2009JPO4194.1.

Kalnay, E., M. Kanamitsu, R. Kistler, W. Collins, D. Deaven, L. Gandin, M. Iredell, S. Saha, G. White, J. Woollen, Y. Zhu, M. Chellia, W. Ebisuzaki, W. Higgins, J. Janowiak, K. Mo, C. Ropelewski, J. Wang, A. Leetmaa, R. Reynolds, R. Jenne, and D. Joseph (1996), The NCEP/NCAR 40-year reanalysis project, *Bull. Amer. Meteor. Soc.*, *77*, 437–471.

Kandler, K., N. Benker, U. Bundke, E. Cuevas, M. Ebert, P. Knippertz, S. Rodríguez, L. Schütz, and S. Weinbruch (2007), Chemical composition and complex refractive index of Saharan mineral dust at Izana, Tenerife (Spain) derived by electron microscopy, *Atmospheric Environment*, *41*(37), 8058–8074.

Kandler, K., L. Schütz, C. Deutscher, M. Ebert, H. Hofmann, S. Jäckel, R. Jaenicke, P. Knippertz, K. Lieke, A. Massling, A. Petzold, A. Schladitz, B. Weinzierl, A. Wiedensohler, S. Zorn, and S. Weinbruch (2009), Size distribution, mass concentration, chemical and mineralogical composition and derived optical parameters of the boundary layer aerosol at Tinfou, Morocco, during SAMUM 2006, *Tellus Series B Chemical and Physical Meteorology B*, *61*, 32–50, doi:10.1111/j.1600-0889.2008.00385.x.

Kapala, A., H. Mächel, and H. Flohn (1998), Behaviour of the centres of action above the Atlantic since 1881. Part II: Associations with regional climate anomalies, *International Journal of Climatology*, *18*, 23–36.

Karyampudi, M. V., S. P. Palm, J. A. Reagen, H. Fang, W. B. Grant, R. M. Hoff, C. Moulin, H. F. Pierce, O. Torres, E. V. Browell, and S. H. Melfi (1999), Validation of the Saharan Dust Plume Conceptual Model Using Lidar, Meteosat, and ECMWF Data., *Bulletin of the American Meteorological Society*, *80*, 1045–1076.

Karyampudi, V., and H. Pierce (2002), Synoptic-scale influence of the Saharan air layer on tropical cyclogenesis over the eastern Atlantic, *Monthly Weather Review*, *130*(12), 3100–3128.

Kaufman, Y., I. Koren, L. Remer, D. Tanré, P. Ginoux, and S. Fan (2005), Dust transport and deposition observed from the Terra-Moderate Resolution Imaging Spectroradiomenter (MODIS) spacecraft over the Atlantic Ocean, *J. Geophys. Res.*, *110*, D10S12, doi:10.1029/2003JD004436.

Khiri, F. (2004), Dust deposits in Souss-Massa basin, South-West of Morocco: granulometrical, mineralogical and geochemical characterisation, *Journal of African Earth Sciences*, *39*, 459–464, doi:10.1016/j.jafrearsci.2004.07.019.

Kim, K.-M., W. K.-M. Lau, Y. C. Sud, and G. K. Walker (2010), Influence of aerosol-radiative forcings on the diurnal and seasonal cycles of rainfall over West Africa and Eastern Atlantic Ocean using GCM simulations, *Climate Dynamics, Volume 35, Issue 1, pp.115-126*, *35*, 115–126, doi:10.1007/s00382-010-0750-1.

Kiss, P., I. Janosi, and O. Torres (2007), Early calibration problems detected in TOMS Earth-Probe aerosol signal, *Geophys. Res. Lett.*, *34*, doi:10.1029/2006GL028108.

Kolker, A. S., and S. Hameed (2007), Meteorologically driven trends in sea level rise, *Geophysical Reasearch Letters*, *34*, L23616, doi:10.1029/2007GL031814.

Koren, I., and Y. J. Kaufman (2004), Direct wind measurements of Saharan dust events from Terra and Aqua satellites, *Geophysical Reasearch Letters*, *31*, L06122, doi:10.1029/2003GL019338.

Koren, I., Y. J. Kaufman, R. Washington, M. C. Todd, Y. Rudich, J. Vanderlei Martins, and D. Rosenfeld (2006), The Bodélé depression: a single spot in the Sahara that provides most of the mineral dust to the Amazon forest, *Environmental Research Letters, Volume 1, Issue 1, pp. 014005 (2006).*, *1*(1), 014,005, doi:10.1088/1748-9326/1/1/014005.

Krueger, B., V. Grassian, J. Cowin, and A. Laskin (2004), Heterogeneous chemistry of individual mineral dust particles from different dust source regions: the importance of particle mineralogy, *Atmospheric Environment*, *38*(36), 6253–6261.

Lau, K. M., and K. M. Kim (2007a), Cooling of the Atlantic by Saharan dust, *Geophys. Res. Lett.*, *34*, doi:10.1029/2007GL031538.

Lau, K. M., K. M. Kim, Y. C. Sud, and G. K. Walker (2009a), A GCM study of the response of the atmospheric water cycle of West Africa and the Atlantic to Saharan dust radiative forcing, *Annales Geophysicae*, *27*, doi:10.5194/angeo-27-4023-2009.

Lau, K. M., K. M. Kim, Y. C. Sud, and G. K. Walker (2009b), A GCM study of the response of the atmospheric water cycle of West Africa and the Atlantic to Saharan dust radiative forcing, *Annales Geophysicae*, *27*, doi:10.5194/angeo-27-4023-2009.

Lau, W. K. M., and K.-M. Kim (2007b), How nature foiled the 2006 hurricane forecasts, *EOS Transactions*, *88*, 105–106, doi:10.1029/2007EO090002.

Lázaro, F., L. Gutiérrez, V. Barrón, and M. Gelado (2008), The speciation of iron in desert dust collected in gran canaria (canary islands): Combined chemical, magnetic and optical analysis, *Atmospheric Environment*, *42*(40), 8987–8996.

Levin, Z., A. Teller, E. Ganor, and Y. Yin (2005), On the interactions of mineral dust, sea-salt particles, and clouds: A measurement and modeling study from the mediterranean israeli dust experiment campaign, *Journal of Geophysical Research (Atmospheres)*, *110*(D9), D20,202, doi:10.1029/2005JD005810.

Li, G., J. Chen, Y. Chen, J. Yang, J. Ji, and L. Liu (2007), Dolomite as a tracer for the source regions of Asian dust, *Journal of Geophysical Research (Atmospheres)*, *112*(D11), D17201, doi:10.1029/2007JD008676.

Mächel, H., A. Kapala, and H. Flohn (1998), Behaviour of the centres of action above the Atlantic since 1881. Part I: Characteristics of seasonal and interannual variability, *International Journal of Climatology*, *18*, 1–22.

Mahowald, N., C. Lou, J. del Corral, and C. Zender (2003), Interannual variability in atmospheric mineral aerosols from a 22-year model simulation and observational data, *J. Geophys Res.*, *108*, 4352, doi:10.029/2002JD002821.

Mahowald, N., D. Muhs, S. Levis, P. Rasch, M. Yoshioka, C. Zender, and C. Luo (2006), Change in atmospheric mineral aerosols in response to climate: Last glacial period, preindustrial, modern, and doubled carbon dioxide climates, *USGS Staff–Published Research*, p. 166.

Mahowald, N. M., and J.-L. Dufresne (2004), Sensitivity of TOMS aerosol index to boundary layer height: Implications for detection of mineral aerosol sources, *Geophys. Res. Lett.*, *31*, L03103, doi:10.1029/2003GL018865.

Makra, L., I. Borbély-Kiss, E. Koltay, and Y. Chen (2002), Enrichment of desert soil elements in Takla Makan dust aerosol, *Nuclear Instruments and Methods in Physics Research B*, *189*, 214–220, doi:10.1016/S0168-583X(01)01045-X.

Massie, S., O. Torres, and S. Smith (2004), Total Ozone Mapping Spectrometer (TOMS) observations of increases in Asian aerosol in winter from 1979 to 2000, *J. Geophys. Res.*, *109*, D18,211, doi:10.029/2004JD004620.

Matsuki, A., B. Quennehen, A. Schwarzenboeck, S. Crumeyrolle, H. Venzac, P. Laj, and L. Gomes (2010), Temporal and vertical variations of aerosol physical and chemical properties over west africa: Amma aircraft campaign in summer 2006, *Atmospheric Chemistry and Physics*, *10*(17), 8437–8451.

McGee, D., W. Broecker, and G. Winckler (2010), Gustiness: The driver of glacial dustiness?, *Quaternary Science Reviews*, *29*(17), 2340–2350.

McKendry, I. G., K. Stahl, and R. D. Moore (2006), Synoptic sea-level pressure patterns generated by a general circulation model: comparison with types derived from NCEP/NCAR re-analysis and implications for downscaling, *International Journal of Climatology*, *26*, 1727–1736, doi:10.1002/joc.1337.

Meehl, G., C. Covey, T. Delworth, M. Latif, B. McAvaney, J. Mitchell, R. Stouffer, and K. Taylor (2007), The WCRP CMIP3 multi-model dataset: A new era in climate change research, *Bulletin of the American Meteorological Society*, *88*, 1383–1394.

Merrill, J., M. Uematsu, and R. Bleck (1989), Meteorological analysis of long range transport of mineral aerosols over the North Pacific, *J. Geophys. Res.*, *94*, 8584–8598.

Meskhidze, N., W. L. Chameides, A. Nenes, and G. Chen (2003), Iron mobilization in mineral dust: Can anthropogenic SO_2 emissions affect ocean productivity?, *Geophys. Res. Lett.*, *30*(21), 2085, doi:10.1029/2003GL018035.

Meskhidze, N., W. L. Chameides, and A. Nenes (2005), Dust and pollution: A recipe for enhanced ocean fertilization?, *Journal of Geophysical Research (Atmospheres)*, *110*, D03301, doi:10.1029/2004JD005082.

Miller, R., J. Perlwitz, and I. Tegen (2004), Feedback upon dust emission by dust radiative forcing through the planetary boundary layer, *J. Geophys. Res.*, *109*, D24,209, doi:10.1029/2004JD004912.

Mitas, C. M., and A. Clement (2005), Has the Hadley cell been strengthening in recent decades?, *Geophys. Res. Lett.*, *32*, L03809, doi:10.1029/2004GL021765.

Mitas, C. M., and A. Clement (2006), Recent behavior of the Hadley cell and tropical thermodynamics in climate models and reanalyses, *Geophys. Res. Lett.*, *33*, L01810, doi:10.1029/2005GL024406.

Mohr, K. I., and C. D. Thorncroft (2006), Intense convective systems in West Africa and their relationship to the African easterly jet, *Quarterly Journal of the Royal Meteorological Society*, *132*, 163–176, doi:10.1256/qj.05.55.

Moore, D., R. Reynolds Jr, et al. (1989), *X-ray diffraction and the identification and analysis of clay minerals.*, Oxford University Press (OUP).

Moulin, C., C. Lambert, F. Dulac, and U. Dayan (1997), Control of atmospheric export of dust from North Africa by the North Atlantic Oscillation, *Nature*, *387*, 691–694.

Mounkaila, M. (2006), Spectral and mineralogical properties of potential dust sources on a transect from the Bodélé Depresseion (Central Sahara) to the Lake Chad in the Sahel, Ph.D. thesis, Universität Hohenheim.

Muhs, D., J. Budahn, J. Prospero, G. Skipp, and S. Herwitz (2012), Soil genesis on the island of bermuda in the quaternary: The importance of african dust transport and deposition, *Journal of Geophysical Research*, *117*(F3), F03,025.

Muhs, D. R., J. R. Budahn, J. M. Prospero, and S. N. Carey (2007), Geochemical evidence for African dust inputs to soils of western Atlantic islands: Barbados, the Bahamas, and Florida, *Journal of Geophysical Research (Earth Surface)*, *112*(F11), F02009, doi:10.1029/2005JF000445.

Nicholson, S. (2008), The intensity, location and structure of the tropical rainbelt over west Africa as factors in interannual variability, *International Journal of Climatology*, *28*(13), 1775–1785.

Nicholson, S. E. (2009), A revised picture of the structure of the "monsoon" and land ITCZ over West Africa, *Climate Dynamics*, *32*, 1155–1171, doi:10.1007/s00382-008-0514-3.

Nicholson, S. E., C. J. Tucker, and M. B. Ba (1998), Desertification, Drought, and Surface Vegetation: An Example from the West African Sahel., *Bulletin of the American Meteorological Society*, *79*, 815–829, doi:10.1175/1520-0477(1998)079⟨0815:DDASVA⟩2.0.CO;2.

OHara, S. L., M. L. Clarke, and M. S. Elatrash (2006), Field measurements of desert dust deposition in Libya, *Atmospheric Environment*, *40*(21), 3881 – 3897, doi:10.1016/j.atmosenv.2006.02.020.

Olson, L., L. Eklundh, and J. Ardo (2005), A recent greening of the Sahel-trends, patterns and potential causes, *Journal of Arid Environments*, *63*, 556–566.

Oort, A. H., and J. J. Yienger (1996), Observed Interannual Variability in the Hadley Circulation and Its Connection to ENSO., *Journal of Climate*, *9*, 2751–2767.

Osborn, T., K. Briffa, S. Tett, P. Jones, and R. Trigo (1999), Evaluation of the North Atlantic Oscillation as simulated by a coupled climate model, *Climate Dynamics*, *15*(9), 685–702.

Paquet, H., C. Coude-Gauseen, and P. Rognon (1984), Etude minralogique de poussieres sahariennes le long d'un itinraire entre 19 et 35 de latitude nord, *Rev. Geol. Dyn. Geogr. Phys.*

Parker, D. J., R. R. Burton, A. Diongue-Niang, R. J. Ellis, M. Felton, C. M. Taylor, C. D. Thorncroft, P. Bessemoulin, and A. M. Tompkins (2005), The diurnal cycle of the West

African monsoon circulation, *Quarterly Journal of the Royal Meteorological Society*, *131*, 2839–2860, doi:10.1256/qj.04.52.

Perry, K., T. Cahill, R. Eldred, D. Dutcher, and T. Gill (1997), Long-range transport of North African dust to the eastern United States, *J. Geophys. R.*, *102*, 11,225–11,238.

Petit, R., M. Legrand, I. Jankowiak, J. Molinie, C. A. de Beauville, G. Marion, and J. Mansor (2005), Transport of Saharan dust of the Caribbean Islands: Study on an event, *J. Geophys. Res.*, *110*, D18S09, doi:101.1029/2004JD0047478.

Piontkovski, S., and S. Hameed (2002), Precursors of Copepod abundance in the Gulf of Maine in atmospheric Centers of Action and see surface temperature, *The Global Atmosphere and Ocean System*, *8*, 283–291.

Poccard, I., S. Janicot, and P. Camberlin (2000), Comparison of rainfall structures between NCEP/NCAR reanalyses and observed data over tropical Africa, *Climate Dynamics*, *16*(12), 897–915.

Polvani, L. M., and P. J. Kushner (2002), Tropospheric response to stratospheric perturbations in a relatively simple general circulation model, *Geophys. Res. Lett.*, *29*(7), 1114, doi:10.1029/2001GL014284.

Prospero, J., and T. Carlson (1972), Vertical and Areal Distribution of Saharan Dust over the Western Equatorial North Atlantic Ocean, *J. Geophys. Res.*, *77*.

Prospero, J., and P. Lamb (2003), African droughts and dust transport to the Carribean: Climate change implications, *Science*, *302*, 1024–1027.

Prospero, J., and R. Nees (1986), Impact of the North African drought and El Nino on mineral dust in the Barbados trade winds, *Nature*, *320*, 735–738.

Prospero, J., and D. Savoie (1989), Effect of continental sources of nitrate concentrations over the Pacific Ocean, *Nature*, *339*, 687–689.

Prospero, J., P. Ginoux, O. Torres, S. Nicholson, and T. Gill (2002), Environmental characterization of global sources of atmospheric soil dust identified with the Nimbus 7 Total Ozone Mapping Spectromenter (TOMS) absorbing aerosol product, *Rev. Geophys.*, *40*, 1002, doi:10.029/2000RG000095.

Prospero, J. M., and T. N. Carlson (1980), Saharan air outbreaks over the tropical North Atlantic, *Pure and Applied Geophysics*, *119*, 677–691, doi:10.1007/BF00878167.

Prospero, J. M., and R. T. Nees (1977), Dust Concentration in the Atmosphere of the Equatorial North Atlantic: Possible Relationship to the Sahelian Drought, *Science*, *196*, 1196–1198, doi:10.1126/science.196.4295.1196.

Prospero, J. M., E. Bonatti, C. Schubert, and T. N. Carlson (1970), Dust in the Caribbean atmosphere traced to an African dust storm, *Earth and Planetary Science Letters*, *9*, 287–+, doi:10.1016/0012-821X(70)90039-7.

Prospero, J. M., E. Blades, R. Naidu, G. Mathison, H. Thani, and M. C. Lavoie (2008), Relationship between African dust carried in the Atlantic trade winds and surges in pediatric asthma attendances in the Caribbean, *Int. J. of Biometeorology*, *52*, 823–832, doi:10.1007/s00484-008-0176-1.

Pye, K., and H. Tsoar (1987), The mechanics and geological implications of dust transport and deposition in deserts with particular reference to loess formation and dune sand diagenesis in the northern Negev, Israel, *Geological Society, London, Special Publications*, *35*(1), 139–156.

Redelsperger, J., A. Diongue, A. Diedhiou, J. Ceron, M. Diop, J. Gueremy, and J. Lafore (2002), Multi-scale description of a Sahelian synoptic weather system representative of the West African Monsoon, *Quarterly Journal of the Royal Meteorological Society*, *128*(582), 1229–1257.

Reid, E., J. Reid, M. Meier, M. Dunlap, S. Cliff, A. Broumas, K. Perry, and H. Maring (2003), Characterization of African dust transported to Puerto Rico by individual particle and size segregated bulk analysis, *Journal of Geophysical Research*, *108*(D19), 8591.

Riemer, N., O. Doherty, and S. Hameed (2006), On the variability of African dust transport across the Atlantic, *Geophys. Res. Letters*, *33*(13).

Rosenfeld, D., Y. Rudich, and R. Lahav (2001), Desert dust suppressing precipitation: A possible desertification feedback loop, *PNAS*, *98*, 5975–5980.

Rossby, C.-G. (1939), Relation between variations in the intensity of the zonal circulation of the atmosphere and the displacement of the semi-permanent centers of actions, *J. Marine Res.*, *2*, 38–55.

Ruti, P., and A. DellAquila (2010), The twentieth century African easterly waves in reanalysis systems and IPCC simulations, from intra-seasonal to inter-annual variability, *Climate dynamics*, *35*(6), 1099–1117.

Rydell, H. S., and J. M. Prospero (1972), Uranium and thorium concentrations in wind-borne Saharan dust over the Western Equatorial North Atlantic Ocean, *Earth and Planetary Science Letters*, *14*, 397, doi:10.1016/0012-821X(72)90140-9.

Sankar-Rao, M., K. M. Lau, and S. Yang (1996), On the Relationship Between Eurasian Snow Cover and the Asian Summer Monsoon, *International Journal of Climatology*, *16*, 605–616, doi:10.1002/(SICI)1097-0088(199606)16:6⟨605::AID-JOC41⟩3.3.CO;2-G.

Sassen, K., P. J. DeMott, J. M. Prospero, and M. R. Poellot (2003), Saharan dust storms and indirect aerosol effects on clouds: CRYSTAL-FACE results, *Geophys. Res. Lett.*, *30*(12), 1633, doi:10.1029/2003GL017371.

Savoie, D. L., J. M. Prospero, and R. T. Nees (1987), Frequency distribution of dust concentration in Barbados as a function of averaging time, *Atmos. Environ.*, *21*(7), 1659 – 1663, doi:10.1016/0004-6981(87)90327-1.

Schoof, J. T., and S. C. Pryor (2006), An evaluation of two GCMs: simulation of North American teleconnection indices and synoptic phenomena, *International Journal of Climatology*, *26*, 267–282, doi:10.1002/joc.1242.

Schütz, L., and M. Sebert (1987), Mineral aerosols and source identification, *Journal of aerosol science*, *18*(1), 1–10.

Schwanghart, W., and B. Schütt (2008), Meteorological causes of Harmattan dust in West Africa, *Geomorphology*, *95*, 412–428, doi:10.1016/j.geomorph.2007.07.002.

Sedwick, P., E. Sholkovitz, and T. Church (2007), Impact of anthropogenic combustion emissions on the fractional solubility of aerosol iron: Evidence from the sargasso sea, *Geochemistry Geophysics Geosystems*, *8*(10), Q10Q06.

Shen, Z., X. Li, J. Cao, S. Caquineau, Y. Wang, and X. Zhang (2005), Characteristics of clay minerals in Asian dust and their environmental significance, *China Particuology*, *3*(5), 260 – 264, doi:10.1016/S1672-2515(07)60198-5.

Shen, Z. X., J. J. Cao, X. X. Li, T. Okuda, Y. Q. Wang, and X. Y. Zhang (2006), Mass concentration and mineralogical characteristics of aerosol particles collected at Dunhuang during ACE-Asia, *Advances in Atmospheric Sciences*, *23*, 291–298, doi:10.1007/s00376-006-0291-z.

Shen, Z. X., J. J. Cao, R. Arimoto, R. J. Zhang, D. M. Jie, S. X. Liu, and C. S. Zhu (2007), Chemical composition and source characterization of spring aerosol over Horqin sand land in northeastern China, *Journal of Geophysical Research (Atmospheres)*, *112*(D11), D14315, doi:10.1029/2006JD007991.

Sheridan, S., and C. Lee (2010), Synoptic climatology and the general circulation model, *Progress in Physical Geography*, *34*(1), 101–109.

Simmonds, I., and J. King (2004), Global and hemispheric climate variations affecting the southern ocean, *Antarctic Science*, *16*(04), 401–413.

Simpson, J., R. F. Adler, and G. R. North (1988), A Proposed Tropical Rainfall Measuring Mission (TRMM) Satellite., *Bulletin of the American Meteorological Society*, *69*, 278–295.

Sokolik, I., and O. Toon (1996), Direct radiative forcing by anthropogenic airobrned mineral aerosols, *Nature*, pp. 681–683.

Solomon, S., D. Qin, M. Manning, Z. Chen, M. Marquis, K. Averyt, M. Tignor, and H. Miller (2007), *Contribution of Working Group I to the Fourth Assessment Report of the Intergovernmental Panel on Climate Change*, Cambridge University Press, Cambridge University Press, Cambridge, United Kingdom and New York, NY, USA.

Stoner, A. M. K., K. Hayhoe, and D. J. Wuebbles (2009), Assessing General Circulation Model Simulations of Atmospheric Teleconnection Patterns, *Journal of Climate*, *22*, 4348, doi:10.1175/2009JCLI2577.1.

Stuut, J., M. Prins, R. Schneider, G. Weltje, J. Jansen, and G. Postma (2002), A 300-kyr record of aridity and wind strength in southwestern Africa: inferences from grain-size distributions of sediments on Walvis Ridge, SE Atlantic, *Marine Geology*, *180*(1), 221–233.

Sultan, B., S. Janicot, and A. Diedhiou (2003), The West African Monsoon Dynamics. Part I: Documentation of Intraseasonal Variability., *J. Climate*, *16*, 3389–3406.

Sun, J., M. Zhang, and T. Liu (2001), Spatial and temporal characteristics of dust storms in China and its surrounding regions, 1960-1999: Relations to source area and climate, *J. Geophys. Res.*, *106*, 10,325–10,333.

Sun, Y., G. Zhuang, Y. Wang, X. Zhao, J. Li, Z. Wang, and Z. An (2005), Chemical composition of dust storms in Beijing and implications for the mixing of mineral aerosol with pollution aerosol on the pathway, *Journal of Geophysical Research (Atmospheres)*, *110*(D9), D24209, doi:10.1029/2005JD006054.

Sunnu, A., G. Afeti, and F. Resch (2008), A long-term experimental study of the Saharan dust presence in West Africa, *Atmos. Res.*, *87*, 13–26.

Svensson, A., P. E. Biscaye, and F. E. Grousset (2000), Characterization of late glacial continental dust in the Greenland Ice Core Project ice core, *J. Geophs. Res.*, *105*, 4637–4656, doi:10.1029/1999JD901093.

Swap, R., M. Garstang, S. Greco, R. Talbot, and P. Kallberg (1992), Saharan dust in the Amazon basin, *Tellus B*, *44*, 133–149.

Sylla, M., A. Dell'Aquila, P. Ruti, and F. Giorgi (2010), Simulation of the intraseasonal and the interannual variability of rainfall over West Africa with RegCM3 during the monsoon period, *International Journal of Climatology*, *30*(12), 1865–1883.

Sylla, M., F. Giorgi, P. Ruti, S. Calmanti, and A. Dell'Aquila (2011), The impact of deep convection on the West African summer monsoon climate: a regional climate model sensitivity study, *Quarterly Journal of the Royal Meteorological Society*, *137*(659), 1417–1430.

Tanaka, H. L., N. Ishizaki, and A. Kitoh (2004), Trend and interannual variability of Walker, monsoon and Hadley circulations defined by velocity potential in the upper troposphere, *Tellus Series A*, *56*, 250, doi:10.1111/j.1600-0870.2004.00049.x.

Taylor, G., F. Muller-Karger, R. Thunell, M. Scranton, Y. Astor, R. Varela, L. Ghinaglia, L. Lorenzoni, K. Fanning, S. Hameed, et al. (2012), Ecosystem responses in the southern Caribbean Sea to global climate change, *Proceedings of the National Academy of Sciences*.

Taylor, S., and S. McLennan (1985), *The continental crust: its composition and evolution*, Blackwell Scientific Pub., Palo Alto, CA.

Taylor, S., S. McLennan, and M. McCulloch (1983), Geochemistry of loess, continental crustal composition and crustal model ages, *Geochimica et Cosmochimica Acta*, *47*(11), 1897–1905.

Tegen, I., and I. Fung (1994), Modeling of mineral dust in the atmosphere: Sources, transport, and optical thickness, *Geophysical Reasearch Letters*, *99*, 22,897, doi:10.1029/94JD01928.

Tegen, I., A. Lacis, and I. Fung (1996), The influence of climate forcing of mineral aerosols from disturbed soils, *Nature*, *380*, 419–422.

Tomas, R. A., J. R. Holton, and P. J. Webster (1999), The influence of cross-equatorial pressure gradients on the location of near-equatorial convection, *Quarterly Journal of the Royal Meteorological Society*, *125*, 1107–1127, doi:10.1256/smsqj.55602.

Torres, O., P. Bhartia, J. Herman, Z. Ahmad, and J. Gleason (1998), Derivation of aerosol properties from satellite measurements of backscattered ultraviolet radiation: Theoretical basis, *J. Geophys. Res.*, *103*, 17,099–17,110.

Torres, O., P. Bhartia, J. Herman, A. Sinyuk, P. Ginoux, and B. Holben (2002), A long-term record of aerosol optical depth from TOMS observations and comparison to AERONET measurements, *J. Atmos. Sci.*, *59*, 398–413.

Trapp, J. M., F. J. Millero, and J. M. Prospero (2010), Temporal variability of the elemental composition of African dust measured in trade wind aerosols at Barbados and Miami, *Mar. Chem.*, *120*(1-4), 71 – 82, doi:10.1016/j.marchem.2008.10.004.

Tucker, C., J. Pinzon, M. Brown, D. Slayback, E. Pak, R. Mahoney, E. Vermote, and N. El Saleous (2005), An extended AVHRR 8-km NDVI dataset compatible with MODIS and

SPOT vegetation NDVI data, *International Journal of Remote Sensing*, *26*, 4485–4498, doi:10.1080/01431160500168686.

Twomey, S. (1977), The Influence of Pollution on the Shortwave Albedo of Clouds., *Journal of Atmospheric Sciences*, *34*, 1149–1154.

Uppala, S., P. Kållberg, A. Simmons, U. Andrae, V. Bechtold, M. Fiorino, J. Gibson, J. Haseler, A. Hernandez, G. Kelly, et al. (2005), The ERA-40 re-analysis, *Quarterly Journal of the Royal Meteorological Society*, *131*(612), 2961–3012.

Walsh, J. J., and K. A. Steidinger (2001), Saharan dust and Florida red tides: The cyanophyte connection, *Geophys. Res. Lett.*, *106*, 11,597–11,612, doi:10.1029/1999JC000123.

Wang, B., H. Wan, Z. Ji, X. Zhang, R. Yu, Y. Yu, and H. Liu (2004), Design of a new dynamical core for global atmospheric models based on some efficient numerical methods, *Science in China Series A: Mathematics*, *47*, 4–21.

Wang, X., J. Huang, M. Ji, and K. Higuchi (2008), Variability of East Asia dust events and their long-term trend, *Atmospheric Environment*, *42*(13), 3156 – 3165, doi:10.1016/j.atmosenv.2007.07.046.

Wang, Y., X. Zhang, R. Arimoto, J. Cao, and Z. Shen (2005), Characteristics of carbonate content and carbon and oxygen isotopic composition of northern China soil and dust aerosol and its application to tracing dust sources, *Atmospheric Environment*, *39*(14), 2631 – 2642, doi:10.1016/j.atmosenv.2005.01.015.

Washington, R., and M. Todd (2005), Atmospheric controls on mineral dust emission from the Bodele Depression, Chad: The role of the low level jet, *Geophys. Res. Letters*, *32*.

Washington, R., M. Todd, and A. G. N.Middleton (2003), Dust-storm source areas determined by the Total Ozone Monitoring Spectrometer and surface observations, *Ann. Assoc. Am. Geogr.*, *93*, L17,701, doi:10.1029/2005GL023597.

Washington, R., M. C. Todd, S. Engelstaedter, S. Mbainayel, and F. Mitchell (2006), Dust and the low-level circulation over the Bodélé Depression, Chad: Observations from BoDEx 2005, *Journal of Geophysical Research (Atmospheres)*, *111*(D10), D03201, doi:10.1029/2005JD006502.

Wielicki, B. A., T. Wong, R. P. Allan, A. Slingo, J. T. Kiehl, B. J. Soden, C. T. Gordon, A. J. Miller, S.-K. Yang, D. A. Randall, F. Robertson, J. Susskind, and H. Jacobowitz (2002), Evidence for Large Decadal Variability in the Tropical Mean Radiative Energy Budget, *Science*, *295*, 841–844, doi:10.1126/science.1065837.

Wilcox, E. M., K. M. Lau, and K.-M. Kim (2010), A northward shift of the North Atlantic Ocean Intertropical Convergence Zone in response to summertime Saharan dust outbreaks, *Geophys. Res. Lett.*, *37*, doi:10.1029/2009GL041774.

Wilks, D. (1995), *Statistical methods in the atmospheric sciences: An introduction*, *International Geophysics Series*, vol. 100, Third Edition ed., Academic Press, Oxford, UK.

Wurzler, S., T. Reisin, and Z. Levin (2000), Modification of mineral dust particles by cloud processing and subsequent effect on drop size distributions, *J. Geophys. Res.*, *105*, 4501–4512.

Xu, J., M. H. Bergin, R. Greenwald, J. J. Schauer, M. M. Shafer, J. L. Jaffrezo, and G. Aymoz (2004), Aerosol chemical, physical, and radiative characteristics near a desert source region of northwest China during ACE-Asia, *Journal of Geophysical Research (Atmospheres)*, *109*(D18), D19S03, doi:10.1029/2003JD004239.

Yukimoto, S., A. Noda, A. Kitoh, M. Sugi, Y. Kitamura, M. Hosaka, K. Shibata, S. Maeda, and T. Uchiyama (2001), The new Meteorological Research Institute coupled GCM(MRI-

CGCM 2)- model climate and variability, *Papers in Meteorology and Geophysics*, *51*(2), 47–88.

Zender, C. S., H. Bian, and D. Newman (2003), Mineral Dust Entrainment and Deposition (DEAD) model: Description and 1990s dust climatology, *Journal of Geophysical Research (Atmospheres)*, *108*, 4416, doi:10.1029/2002JD002775.

Zhang, C., P. Woodworth, and G. Gu (2006), The seasonal cycle in the lower troposphere over West Africa from sounding observations, *Quarterly Journal of the Royal Meteorological Society*, *132*, 2559–2582, doi:10.1256/qj.06.23.

Zhang, D., Y. Iwasaka, and G. Shi (2005), Sea salt shifts the range sizes of Asian dust, *Eos, Transactions American Geophysical Union*, *86*(50), 523.

Zhang, X. Y., S. L. Gong, R. Arimoto, Z. X. Shen, F. M. Mei, D. Wang, and Y. Cheng (2003), Characterization and temporal variation of Asian dust aerosol from a site in the northern Chinese deserts, *Journal of Atmospheric Chemistry*, *44*, 241–257, doi:10.1023/A:1022900220357.

Zhang, X. Y., S. L. Gong, Z. X. Shen, F. M. Mei, X. X. Xi, L. C. Liu, Z. J. Zhou, D. Wang, Y. Q. Wang, and Y. Cheng (2003), Characterization of soil dust aerosol in China and its transport and distribution during 2001 ACE-Asia: 1. Network observations, *Journal of Geophysical Research (Atmospheres)*, *108*, 4261, doi:10.1029/2002JD002632.